

Nonlinear Thermoacoustic Stability Analysis of Gas Turbine Combustion Chambers

vorgelegt von
Diplom-Ingenieur
Bernhard Ćosić
geboren in Haan

Von der Fakultät V – Verkehrs- und Maschinensysteme
der Technischen Universität Berlin
zur Erlangung des akademischen Grades

Doktor der Ingenieurwissenschaften
– Dr.-Ing. –

genehmigte Dissertation

Promotionsausschuss:

Vorsitzender: Prof. Dr. rer. nat. Valentin Popov
Gutachter: Prof. Dr.-Ing. Christian Oliver Paschereit
Gutachter: Prof. Dr. Nicolas Noiray (ETH Zürich)

Tag der wissenschaftlichen Aussprache: 25. November 2014

Berlin 2015
D 83

Vorwort

Ich war gänzlich verstummt, schwieg auch vom Guten, aber mein Schmerz fraß in mir. Mein Herz entbrannte in mir, durch mein Nachsinnen wurde ein Feuer entzündet, da redete ich mit meiner Zunge: Laß mich mein Ende wissen, o Herr, und was das Maß meiner Tage ist, damit ich erkenne, wie vergänglich ich bin! Siehe, nur Handbreiten lang hast du meine Tage gemacht, und die Dauer meines Lebens ist wie nichts vor dir. Wahrlich, jeder Mensch, wie fest er auch steht, ist nur ein Hauch! Ja, als Schattenbild geht der Mensch einher; nur um Nichtigkeit machen sie so viel Lärm! Er häuft auf und weiß nicht, wer es einsammeln wird. Und nun, Herr, worauf soll ich hoffen? Meine Hoffnung gilt dir allein!

Ps 39, 3-8

Diese Dissertation fasst Teile meiner vierjährigen Forschungsarbeit am Fachgebiet für Experimentelle Strömungsmechanik der TU Berlin zusammen. Der Großteil der Arbeit entstand im Rahmen des FVV geförderten Vorhabens “Reale Brennkammerrandbedingungen”. Zunächst gilt mein herzlicher Dank meinem Betreuer Professor Paschereit, der es mir überhaupt erst ermöglicht hat zu dem spannenden Thema Thermoakustik zu promovieren. Er ließ mir stets sehr viel Freiraum für die Verwirklichung meiner Ideen und gab mir die Möglichkeit an interessanten Aufgaben abseits meines eigentlichen Projektes zu partizipieren. Ich habe sehr viel von ihm gelernt und schaue auch gerne zurück auf die sonstigen gemeinsamen Erlebnisse wie zum Beispiel die erfolgreiche Suche nach Bären in Vancouver. Ferner möchte ich Professor Noiray für die Begutachtung und die Rückmeldung zu meiner Arbeit und Professor Popov für die Übernahme des Vorsitzes der Prüfungskommission danken.

Vor knapp fünf Jahren waren es vor allem James Willie und Nils Ohlendorf, die mich ermutigt haben auf dem Gebiet der Thermoakustik eine Promotion anzustreben. Durch die Zusammenarbeit mit beiden habe ich eine positive und fruchtbare Arbeitsatmosphäre als wichtigsten Parameter für erfolgreiche Forschungsergebnisse zu schätzen gelernt. Herzlichen Dank für die Unterstützung und die Ermutigung.

Mirko Bothien und Bruno Schuermans haben mich zu der Untersuchung des Phänomens der Heißgaspenetration in Dämpfern ermuntert und inspiriert. Dafür bin ich sehr dankbar, nicht zuletzt auch, weil Teile dieser Untersuchungen mit dem “Best Paper Award” durch die ASME ausgezeichnet wurden.

Die Grundlage für aufschlussreiche Untersuchungsergebnisse waren stets quälend lange Messungen bis in die frühen Morgenstunden und ein perfekter Messaufbau. Für die Mitwirkung an beiden Bausteinen sowie für viele gute Ideen danke ich von ganzem Herzen meinen studentischen Hilfskräften sowie Studien-, Diplom-, Bachelor- und Masterstudenten: Alexander Troyke, Alexander Wooning, Tobias Schwotzer, Thoralf Reichel, Johann Vinkeloe und Olaf Bölke. Thoralf Reichel und Olaf Bölke haben beide ihre Promotion am Fachgebiet für Experimentelle Strömungsmechanik angefangen und setzen ihre exzellente Arbeit fort, was mich besonders Stolz macht.

Vielen Dank an Jonas Moeck für die vielen Diskussionen, Gespräche, Hilfen und die gute Zusammenarbeit zu jeder Tages- und Nachtzeit.

Mein Dank gilt auch Andy Göhrs. Er hat viele Untersuchungen durch seine Ideen erst ermöglicht und konnte so manche wahnwitzige Idee praktisch umsetzen. Er hat sogar Sonder schichten eingelegt und die Konstruktionen selbst gefräst und geschweißt, damit Abgabetermine eingehalten werden konnten. Ein Dankeschön auch an Heiko Stolpe für die Unterstützung

bei Elektronik und Elektrotechnik sowie an die Mitarbeiter aus der Werkstatt und dem Sekretariat für die viele Unterstützung und Hilfe in der ganzen Zeit.

Vielen Dank auch an alle meine Arbeitskollegen, die meine Promotionszeit so wertvoll gemacht haben. Herausheben möchte ich die Kollegen und Freunde, die Teile meiner Arbeit noch einmal Korrektur gelesen haben: Christoph Strangfeld, Katharina Göckeler, Sebastian Schimek, Aditya Saurabh, Steffen Terhaar, Bernhard Bobusch, Oliver Krüger, Olaf Bölke, Thoralf Reichel, Kilian Oberleithner, Phoebe Kuhn, Dominik Waßmer und Georg Mensah sowie Nils Ohlendorf.

Das Büro habe ich mir mit den drei übrigen Mitgliedern des CONFETs geteilt, die sich im Laufe der vier Jahre zu weltweit angesehenen Experten auf den jeweiligen Forschungsfeldern entwickelt haben. Gegen Ende der Promotion schien sich plötzlich ein Kreis zu schließen: Während man über die Jahre die Nervosität vor einer Abgabefrist abgelegt hatte und die Strebssamkeit einer gewissen Routine gewichen war, war es am Ende wieder wie ganz zu Beginn. Alle starrten konzentriert auf Ihren Bildschirm und es war selten Zeit für eine Partie Kicker, das Spiel, das ich durch das CONFET lieben lernte. Umso schöner, dass wir es alle geschafft haben unsere Dissertationen zu vollenden. Ich bin sehr dankbar für den Zufluss an Ideen, die Korrekturen, Meinungen und Hilfestellungen. Das tolle Umfeld hat nicht nur zu einer Vielzahl an Publikationen geführt sondern auch dazu, dass ich jeden Tag sehr gerne zur Arbeit gekommen bin. Wir sind zusammen um die Welt gereist, haben Sportereignisse ausgerichtet und uns vor allem vier Jahre lang jeden Tag gegenseitig motiviert oder manchmal auch von der Arbeit abgelenkt. Ich wünsche Bernhard Bobusch, Oliver Krüger und Steffen Terhaar von ganzem Herzen weiterhin Glück und Erfolg. Ich habe in ihnen drei wertvolle Freunde gefunden.

Meine Ehefrau und Liebe meines Lebens Anna hat mich von Anfang an bei meiner Promotion unterstützt und alle Höhen und Tiefen miterlebt. Sie hat für mich gesorgt, wenn ich mal wieder bis morgens früh bei der Arbeit war. Aber vor allem hat sie nicht zugelassen, dass ich den Glauben an mich selbst verliere.

Ich danke meinen Eltern und meinen beiden Geschwistern für ihre Liebe und Unterstützung.

Berlin, im Januar 2015

Bernhard Ćosić

Zusammenfassung

Die Gasturbine ist die Schlüsseltechnologie für eine effiziente und flexible Erzeugung von Strom und für den Antrieb von Flugzeugen. Zurzeit stellt diese Technologie bereits den höchsten elektrischen Wirkungsgrad für die Umwandlung von fossilen Brennstoffen bei gleichzeitig geringen Emissionen und schnellen Anfahrzeiten bereit. Um Schadstoffemissionen zu minimieren, ist die magere Vormischverbrennung von besonderer Bedeutung. Die größte Herausforderung bei der Verwendung dieser Technologie ist das Auftreten von thermoakustischen Instabilitäten. Bei diesen Verbrennungsinstabilitäten handelt es sich um eine Kopplung von Wärmefreisetzungsschwankungen durch die Flamme und Druckschwankungen im akustischen Feld. Thermoakustische Instabilitäten schränken den Betriebsbereich der Gasturbine ein und beeinträchtigen dadurch die Schadstoffreduktion und Effizienzerhöhung der Gesamtmaschine.

Die Flamme antwortet auf Brennstoffverhältnis- und Geschwindigkeitsschwankungen mit Wärmefreisetzungsschwankungen, die Energie in das akustische Feld übertragen. Dieser Energietransport treibt die thermoakustische Instabilität an. Durch die Sättigung der Flammenantwort stellt sich eine Grenzamplitude im eingeschwungenen Zustand ein. Folglich bildet die Kenntnis der Flammenantwort die Grundlage für die Vorhersage der Instabilitätsfrequenz und der Schalldruckamplitude. Diese nichtlineare Flammentransferfunktion wurde experimentell mit Mikrofonen, Strömungsfeld- und Wärmefreisetzungsmessungen untersucht. Neben einer phänomenologischen Untersuchung der Sättigungseffekte der Flamme wurde die nichtlineare Flammenantwort auch über einen Blackbox-Ansatz vermessen, der für das verwendete Vorhersagewerkzeug benötigt wird. Es wurden Hinweise auf bisher unbekannte nichtlineare Sättigungsmechanismen der Flamme bei dem untersuchten industrierelevanten Brenner gefunden. Außerdem wurde ein Verfahren entwickelt, das bei der Brennerentwicklung Zeit und Kosten einspart, indem der Messaufwand für die Bewertung der Mischungsinhomogenitäten für die Flammenantwort reduziert wird.

In Gasturbinenbrennkammern sind akustische Dämpfer installiert, die die Instabilitäten unterdrücken oder zumindest die Schalldruckamplituden stark reduzieren. Oft sind die Dämpfer über akustische Resonatoren realisiert und sind heißen Abgasströmen ausgesetzt, die mit dem Kühlluftstrom des Dämpfers interagieren und bei höheren Amplituden auch in den Dämpfer eindringen können. Ein Ziel der Untersuchungen im Rahmen dieser Arbeit ist es, die Auswirkungen der heißen Brennkammerabgase auf die Dämpfer experimentell zu bestimmen und theoretisch zu modellieren. Dazu wurden Mikrofon- und Geschwindigkeitsfeldmessungen unter gasturbinenbrennkammerähnlichen Randbedingungen durchgeführt. Die Messungen zeigen einen signifikanten Einfluss der heißen Querströmung in der Brennkammer auf die akustische Dämpferantwort. Die Frequenzen, bei denen der Dämpfer besonders gut funktioniert, werden verschoben und die Dämpfung verringert sich. Bei hohen Amplituden sinkt die Dämpfung noch weiter ab und die schmale Frequenzantwort verschiebt sich noch stärker vom Auslegungspunkt weg. Diese Einflüsse wurden detailliert modelliert.

Die Flammen- und Dämpferantwort wurden erfolgreich zur Vorhersage der Amplitude und Frequenz thermoakustischer Instabilitäten bei verschiedenen Randbedingungen in ein akustisches Netzwerkmodell implementiert. Aufwendige Messungen von thermoakustischen Instabilitäten bei verschiedenen Brennkammergeometrien wurden durchgeführt, um das Vorhersagewerkzeug ohne den Einfluss des Dämpfers zu verifizieren. Es wurde eine sehr gute Vorhersagegenauigkeit bezüglich der Schalldruckamplitude und Frequenz mit dem entwickelten Vorhersagewerkzeug erzielt. Abschließend wurde die Interaktion der beiden Nichtlinearitäten des Dämpfers und der Flamme theoretisch untersucht, was als Grundlage für zukünftige Untersuchungen dienen kann.

Abstract

Currently, the stationary gas turbine is the core technology for the highest energy conversion rates available. Additionally, gas turbines are very flexible and can complement the power production of wind turbines and solar power stations very well and they are widely used as propulsion engines in the aviation industry. Liquid and gaseous fuels are burnt at very high temperatures of approximately 1600°C and electricity is produced at a conversion efficiency of more than 60%. The strict emission regulations are satisfied with the help of the lean premixed combustion technology. Here, large amounts of air are mixed with the fuel prior to burning it. This drastically limits the peak temperature in the flame and thereby reduces the NO_x emissions. The major drawback of this technology is the susceptibility to thermoacoustic instabilities. These are coupled high amplitude heat release and pressure oscillations, which can significantly limit the operation range of engines.

Thermoacoustic instabilities are difficult to predict and can, in the worst case, destroy essential parts of the gas turbine. These combustion instabilities restrain the operational range of gas turbines and are a reason for increased emissions and decreased efficiency. Therefore, models and prediction tools are of high importance in the design process of combustion chambers. Moreover, the understanding of the physical effects causing nonlinear damping and the nonlinear flame response is of utmost importance.

The scope of this thesis is the prediction of limit cycle amplitudes of an industrially relevant combustion system with realistic acoustic boundary conditions and, furthermore, the improved understanding of the relevant nonlinear effects. Firstly, the nonlinear response of a perfectly and partially premixed flame is investigated by means of microphone, chemiluminescence, and flow field measurements. The degree of spatial unmixedness is varied and the impact of temporal mixture inhomogeneities is assessed. Subsequently, the amplitude-dependent acoustic response of Helmholtz dampers and of the other boundary conditions are analyzed with the help of acoustic and flow field measurements. These dampers are used by all gas turbine manufacturers in gas turbines to control and attenuate thermoacoustic instabilities. The experiments were conducted under realistic conditions by exposing the damper to hot exhaust gas. Finally, the stability map of a premixed combustor is predicted and compared to extensive stability experiments.

The present work significantly extends the state of the art in flame describing function based nonlinear network modeling in several ways. The nonlinear response of a turbulent swirl flame is studied up to extremely high excitation amplitudes. Nonlinear mechanisms of the practically relevant flame are investigated in detail allowing for a better understanding and future modeling of the complex mechanisms. The identified saturation mechanisms are associated to mixture inhomogeneities and to hydrodynamic effects. The correct assessment of the nonlinearity of the acoustic dampers is of crucial importance for the prediction of instabilities in a real engine. For the first time, the temperature differences between the grazing flow and the cross-flow emanating from a Helmholtz resonator are investigated in terms of the influence on the acoustic response of the resonator. It is shown that density gradients between the cooling flow of the damper and the combustor flow significantly affect the damper efficiency and resonance frequency. These effects are successfully modeled and explained in detail. The nonlinear flame and damper response can be used in a nonlinear stability analysis to predict the frequency and amplitude of thermoacoustic instabilities. This is done for the first time for an industrially relevant combustor for a range of combustor lengths, thus, allowing for a realistic assessment of the accuracy of the method. Additionally, a theoretical analysis of the interaction between damper and flame paves the way for encouraging investigations in the future.

Contents

Zusammenfassung	v
Abstract	vii
List of Figures	xii
Nomenclature	xv
1 Introduction	1
1.1 General Background and Motivation	1
1.2 Scope of this Thesis	4
2 Theory and Experimental Methods	7
2.1 Acoustic Fundamentals and the Multi-Microphone-Method	7
2.2 Flame Response and Stability Map Measurements	11
2.3 Repeatability and Accuracy Assessment	16
2.4 Helmholtz Resonator Measurements	24
2.5 Optical Measurement Techniques	26
3 Flame Response Saturation	29
3.1 Decomposition of Excitation Mechanisms	33
3.2 Assessment of Hydrodynamic Similarity and Vortical Growth	35
3.3 Velocity Fluctuation Based Saturation Mechanisms	36
3.4 Equivalence Ratio Fluctuation Based Saturation Mechanisms	40
3.4.1 Flow-Field–Flame Interaction Technically Premixed Flame	43
3.4.2 Flame Describing Function Analysis	47
3.4.3 Flame Describing Function Decomposition	51
4 Acoustic Boundary Conditions	63
4.1 Helmholtz Resonator	65
4.1.1 Prediction of Acoustic Response	66
4.1.2 Helmholtz Resonator Flow and Density Field	69
4.1.3 Neck-Correction	74
4.1.4 Hot-Gas Penetration	77
4.1.5 Acoustic Dissipation at High Amplitudes and Density Stratification	85
4.1.6 Application of the Detailed Impedance Model	88

4.2	System Damping	91
4.2.1	Acoustic Burner Transfer Matrix	92
4.2.2	Upstream and Downstream Reflection Coefficients	95
5	Nonlinear Stability Analysis	97
5.1	Theory and Modeling	99
5.2	Linear Stability Analysis	102
5.3	Amplitude Prediction	107
5.4	Coupling of Nonlinear Damping and Flame response	116
6	Summary and Outlook	121
	Bibliography	127

List of Figures

1.1	World population from the year 900 AD to 2014 AD [136].	2
1.2	Examples for limited growth	3
1.3	Evolution of a thermoacoustic instability. Limit cycle is established at equilibrium between energy gain and loss.	4
1.4	Time domain simulation of a thermoacoustic instability. Acoustic pressure time signal is normalized with its maximum.	5
1.5	Structure of this work: Chapter 3 deals with the nonlinear flame dynamics, Chapter 4 with the damper response and the acoustic boundary conditions, and in Chapter 5 the whole system is analyzed.	5
2.1	Schematic representation of the experimental set-up with measurement devices indicated.	14
2.2	Broke-out view of the burner.	15
2.3	Overview of the test rig	16
2.4	Gain and phase of the linear flame transfer function investigated and analyzed in Section 5.2. Markers indicate measurement points. Measurements are conducted at a constant amplitude of $ \hat{u}/\bar{u} =0.1$. Sensitivity analysis is performed in this section with respect to this flame transfer function.	17
2.5	Day-to-day variations of the flame transfer function	18
2.6	Flame transfer function fuel mass flow impact	19
2.7	Flame transfer function air mass flow impact	20
2.8	Flame transfer function swirl number impact	21
2.9	Gain of the nonlinear flame response at 158 Hz for various PMT signals compared to MMM measurement.	22
2.10	Comparison of linear acoustic flame transfer function obtained with MMM and PMT-OH* for three different downstream temperatures estimates.	22
2.11	Flame response at 180 Hz obtained with the MMM for various degrees of partial premixedness.	23
3.1	(a) Flame describing function measurement with MMM at 120 Hz for a technically premixed flame. (b) Corresponding OH* chemiluminescence time signal for an amplitude of $ \hat{u}/\bar{u} = 1.2$	30
3.2	Forced perfectly premixed flame and flow field measurements	38
3.3	Flame response and coherent fluctuation intensity at 196 Hz for various amplitudes and three swirl numbers.	39
3.4	Normalized flame describing function model results.	42
3.5	Comparison of forced mean flow field and flame of perfectly and technically premixed flame	44

3.6	Comparison of phase-averaged flow field and flame of perfectly and technically premixed flame in the linear regime	45
3.7	Comparison of phase-averaged flow field and flame of perfectly and technically premixed flame in the nonlinear regime	46
3.8	Perfectly premixed flame describing function	47
3.9	Technically premixed flame describing function	48
3.10	Flame response at 110 Hz and 158 Hz for various amplitudes and fuel splits.	49
3.11	Flame response at 166 Hz and 180 Hz for various amplitudes and fuel splits.	50
3.12	Flame describing function decomposition at 110 Hz.	52
3.13	Flame describing function decomposition at 158 Hz.	53
3.14	Flame describing function decomposition at 166 Hz.	54
3.15	Flame describing function decomposition at 180 Hz.	55
3.16	Comparison of normalized perfectly and technically premixed describing function.	57
3.17	Normalized turbulence intensity turbulent shear stress integrated over the flame and premixed zone	58
3.18	Turbulent shear stresses in the flame area	59
3.19	Turbulence intensity in the flame area	60
3.20	Gain and phase of flame describing function contributions at 196 Hz for three different fuel splits and artificially increased equivalence ratio fluctuations.	60
3.21	Linear flame transfer function gain at 155 Hz for two-frequency forcing	61
4.1	time-averaged flow fields of the emanating jet in the resonator and its vicinity for two momentum-flux ratios and forcing amplitudes.	70
4.2	Phase-averaged fluctuating part of the flow field u^c in the Helmholtz resonator and its vicinity for two forcing amplitudes and four different phases at a momentum-flux ratio of $I = 0.75$	72
4.3	Time-averaged seeding particle concentration captured by the QLS measurement technique for two different momentum-flux ratios and two forcing amplitudes.	73
4.4	Analysis of neck-correction	75
4.5	Impact of grazing flow temperature on the resonance frequency.	77
4.6	Normalized resonance frequency for various temperature ratios of grazing and purging flow.	79
4.7	Modeled acoustic velocity and density in the resonator neck	80
4.8	time-averaged temperature in the resonator neck at different axial positions in the neck for various momentum-flux ratios and two forcing amplitudes at a frequency of 196 Hz.	81
4.9	Normalized acoustic energy flux for different momentum-flux ratios in the linear amplitude regime and two different grazing flow temperatures.	82
4.10	Normalized acoustic energy loss for two forcing amplitudes at constant $I = 0.15$ for two different temperature differences	84
4.11	Impact of grazing flow temperature on the normalized acoustic energy loss at the resonance frequency.	86
4.12	Normalized calculated effective jet diameter for various amplitudes and temperature differences.	87

4.13	(a) Calibration procedure for the detailed impedance model. (b) Solution procedure for the time-averaged mean spatial density.	88
4.14	Comparison of model and measurements for temperature difference between grazing and purging flow of $\Delta\vartheta = 0K$ and $\Delta\vartheta = 450K$	89
4.15	Comparison of model and measurements for temperature difference between grazing and purging flow of $\Delta\vartheta = 600K$ and $\Delta\vartheta = 900K$	90
4.16	Four burner transfer matrix elements at the investigated operation point. . . .	93
4.17	Real and imaginary part of the burner transfer matrix element B_{12} for various frequencies and amplitudes.	94
4.18	Open-end reflection coefficient for various frequencies and acoustic velocity amplitudes.	95
4.19	Upstream reflection coefficient for various frequencies at small acoustic velocity amplitudes.	96
5.1	Network model used in the present work to represent thermoacoustic oscillations observed in the experimental test-rig.	100
5.2	Linear flame transfer function measured with MMM and OH*-PMT.	102
5.3	Comparison of linear FTF model results to microphone measurements downstream of the flame for various combustion chamber lengths.	103
5.4	Pressure spectra of downstream and upstream microphone for different combustion chamber lengths.	105
5.5	Linear modeling results of the dominant instability frequency for various downstream temperatures and combustion chamber lengths.	106
5.6	Correlation of linear growth rate obtained by the system identification routine and measured limit cycle amplitude.	107
5.7	Flame describing function	108
5.8	Comparison of FDF obtained by MMM and PMT-OH* and modeled FDF at an amplitude level of $ \hat{u}/\bar{u} = 0.63$	109
5.9	Relative error of flame describing function approximation with $n-\tau$ model. .	110
5.10	Comparison of measured and calculated dominant limit cycle frequencies and amplitudes for various combustion chamber lengths.	111
5.11	Absolute deviation of model results and measurements in terms of frequency and limit cycle amplitude for various combustion chamber lengths.	113
5.12	Comparison of measured and calculated limit cycle amplitudes and frequencies for two unstable modes for various combustor lengths.	113
5.13	Frequency, growth rate and flame describing function at combustor length of 1.335 m	114
5.14	Frequency and growth rate (real and imaginary part) of eigenfrequency at combustor length of 0.93 m for various acoustic velocity amplitudes.	115
5.15	(a) Measured flame describing function gain and (b) phase at three frequencies. .	116
5.16	Network model used for the theoretical assessment of the nonlinear interaction between Helmholtz resonator and flame response.	117
5.17	Simulated Helmholtz resonator response	117
5.18	Normalized acoustic energy dissipation of damper at 85 Hz and respective flame describing	118
5.19	Growth rate of unstable mode at combustor length of 1.335 m with additional Helmholtz dampers installed.	119

List of Tables

2.1	Operation points used for the flame response measurements in the respective sections	17
4.1	Comparison of measured and modeled spatially-averaged density in the neck for forcing at 196 Hz for various amplitudes and a temperature of the grazing flow of $\vartheta_{\text{gf}} \approx 1273$ K. Measured density derived from five point temperature measurements in the neck at $I=0.75$	83
4.2	Comparison of measured and modeled spatially-averaged density in the neck for forcing at 196 Hz for various amplitudes and a temperature of the grazing flow of ≈ 1273 K. Measured density derived from five point temperature measurements in the neck at $I=0.05$	83

Nomenclature

Latin letters

Δh	Heat of reaction per unit mass of mixture
\dot{V}	Volume flow
S	System matrix
\mathbf{v}	Flow field velocity vector
He	Helmholtz number
M	Mach number
Pr	Prandtl number
Sh	Shear number
\vec{e}	Unit vector
A	Admittance
α	Equivalence ratio oscillation attenuation factor
b	Flow direction reversal point in time
b	Model constant
B_{ij}	Transfer matrix elements of the burner
C	Concentration
C	Model constant
c	Model constant
c	Speed of sound
c_1	Point in time when flow direction becomes negative
c_2	Point in time after all hot-gas has left neck
D	Diameter with respect to the combustor geometry
d	Effective diameter of Helmholtz resonator
d	Model constant
D_h	Hydraulic diameter with respect to the mixing tube
D_{cc}	Diameter of combustion chamber
d_n	Diameter of Helmholtz resonator neck
f	Downstream traveling acoustic wave
f	Frequency
f_c	Cut-on frequency
f_{olc}	Open loop control forcing frequency

F_{ij}	Transfer matrix elements of the flame
g	Scaling factor
g	Upstream traveling acoustic wave
$h(X)$	Fundamental harmonic of nonlinear Helmholtz resonator loss-term
I	Momentum-flux ratio
i	Imaginary unit
I_{OH^*}	OH^* chemiluminescence intensity
J	Raw images
K	Coherent fluctuation intensity
k	Model constant
k	Wavenumber
L	Length
l	Virtual length
n	Model constant
p	Pressure
q	Heat release
R	Reflection coefficient
r	Radial profile
r	Radius
R_s	Specific gas constant
S	Swirl number
S_A	Cross-sectional surface
S_f	Flame surface area
s_L	Laminar burning velocity
s_T	Turbulent burning velocity
T	Turbulent shear stress integrated over the flame and premixed zone
t	Time variable
T_{ij}	Transfer matrix element
u	Total axial velocity
V	Volume
W_J	Acoustic energy flux
x_c	Axial component of center of gravity
Y	Normalized acoustic energy flux/damping efficiency
y_c	Radial component of center of gravity
Z	Impedance

Z_{ij}	Transfer matrix elements of the impedance
----------	---

Calligraphic letters, operators, and other symbols

$\mathfrak{I}()$	Imaginary part
\mathcal{F}	Flame describing function
\mathcal{F}_u	Velocity describing function contribution
\mathcal{F}_ϕ	Equivalence ratio flame describing function contribution
\mathcal{G}	Equivalence ratio flame describing function
$\mathfrak{R}()$	Real part

Greek letters

Δ	Difference
δ	Virtual neck extension
γ	Ratio of specific heat
λ	Wavelength
Ω	Vorticity vector
∇	Nabla operator
ν	Kinematic viscosity
Ω	Turbulence Intensity integrated over the flame and premixed zone
ω	Angular frequency
ω_Ω	Local turbulence Intensity
ψ	Phase angle
ρ	Density
σ	Standard deviation of the time delay
τ	Time Delay
τ_Ω	Local turbulent shear stress
ε	Fuel-split ratio
φ	Equivalence ratio
ϑ	Temperature
ζ	Loss-coefficient
ζ_Ω	Loss-coefficient associated with vorticity
ζ_{vis}	Loss-coefficient associated with visco thermal losses
ζ_N	Loss-coefficient associated with asymmetrical flow profile
ζ_T	Loss-coefficient associated with density stratification

Subscripts

0	Reference value at isothermal conditions and small forcing amplitudes
δ	Virtual neck
Ω	Associated to vorticity/turbulence
cc	Combustion chamber
ds	Downstream
gf	Grazing flow
nc	Plane between neck and combustion
pf	Purging flow
res	Resonance
us	Upstream
vis	Visco-thermal
A	Area
i, j	Control variable 1,2,3...
L	Laminar
n	Neck (Helmholtz resonator)
T	Temperature
v	Volume of Helmholtz resonator
bulk	Bulk flow velocity
c	Cold
h	Homogeneous
h	Hot
lin	Linear regime
max	Maximum value
mt	Microphone tube
res	Value at resonance frequency
rms	Root mean square
x	Component in x direction
y	Component in y direction

Superscripts

$(\cdot)'$	Perturbation/Fluctuation in time
$(\cdot)^c$	Coherent part
$(\cdot)^s$	Stochastic part
$(\cdot)^+$	Positive direction

$(\cdot)^-$	Negative direction
$\bar{(\cdot)}$	Mean quantity
$\bar{\bar{(\cdot)}}$	Mean value (over one oscillation cycle)
$\hat{(\cdot)}$	Fourier Transform

Abbreviations

BTM	Burner transfer matrix
FDF	Flame describing function
FTF	Flame transfer function
LIF	Laser induced fluorescence
MMM	Multi-Microphone-Method
PIV	Particle image velocimetry
PMT	Photomultiplier-tube
ppm	Perfectly premixed
QLS	Quantitative light sheet
RMS	Root mean square
tpm	Technically premixed
TTM	Tube transfer matrix

Chapter 1

Introduction

sine ira et studio

Tacitus, Annales I,1

This chapter explains the general context of the current work. Overall, the problem of thermoacoustic instabilities in modern gas turbines is not only related to the shortage of natural resources and the greenhouse effect. From a general point of view, it is also associated with the desire of human kind to predict future events and control them. After a brief introduction to the motivation and the challenges of thermoacoustic instabilities the structure of this thesis and how it contributes to the solution of important problems is explained.

1.1 General Background and Motivation

Exponential growth can be observed in daily life. A popular example is the development of the world population, which exponentially grows since the 19th century, as shown in Figure 1.1. Consequently, more and more people have demands for water, food, medical care, electricity, and consumer goods, which drive the growth of the world economy. Other examples from the field of economics and biology are shown in Figure 1.2a and Figure 1.2b. The first one illustrates the normalized crude oil production in the Eurasia region and the second one the cumulated number of cars in Germany. The quantities are normalized with their respective maximum. Both curves show a strong growth at the beginning of the time line but saturate at a certain point. The growth of the oil production saturated the first time around 1990 and even declined due to political reasons like the collapse of the USSR. After a second period of growth, the production saturates again at a similar level, which suggests that the saturation is caused by the limitation of this natural resource. At the same time, the number of cars in Germany is limited by the number of inhabitants. Limitation of growth is an important observation, which is also present in natural systems that exhibit exponential growth. The normalized population density of bacteria, shown in Figure 1.2b, suggests that the exponential growth of human beings

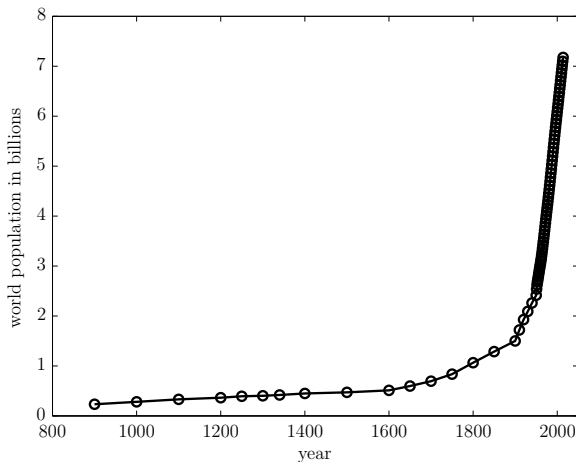


Figure 1.1: World population from the year 900 AD to 2014 AD [136].

may also be limited by finite resources. There are many other examples of strong growth that saturate eventually, like the processing power of computers, the citation of references, or the growth of tree roots. Naturally, these growth curves are limited at some point in time and saturate at a certain level generating s-shaped growth curves. The undeniable fascination of this conceptual scheme is the large array of topics it can be applied to [74]. Futurologists [2], social scientist [82], physicists [86], economists [41], and engineers [6], among others, try to describe and to explain the very different processes with uniting theories. Mostly, this is motivated by the desire of forecasting the future. In the 1970s, Meadows [84] predicted in such an attempt, in a very influential study financed by the Club of Rome, that the growth of the world economy is limited. The limited fossil energy resources and the limitation of the environmental pollution are the key arguments for this and similar hypotheses postulated by others. Additionally, in recent years the level of confidence has increased that human influence has been the dominant cause of the worldwide observed warming since 1950 [129].

As a consequence, the regulative authorities have increased the standards for pollutant emissions and energy conversion efficiencies in the last decades. Especially NO_x (Nitrogen Oxides) emissions have been limited because the responsibility for acid rain, the ozone depletion, and dangers for the human health are undeniable. Nitrogen Oxides are mostly produced during combustion processes at elevated temperatures [27]. Unfortunately, very high temperatures are needed for an efficient energy conversion of fossil fuels to electricity [15], which is of crucial importance for the reduction of green-house gases and emissions.

Currently, the stationary gas turbine is the core technology for the highest energy conversion rates available. Liquid and gaseous fuels are burnt at very high temperatures of approximately 1600°C and electricity is produced at a conversion efficiency of more than 60%. Additionally, gas turbines are very flexible and can complement the power production of wind turbines and solar power stations very well and they are widely used as propulsion engines in

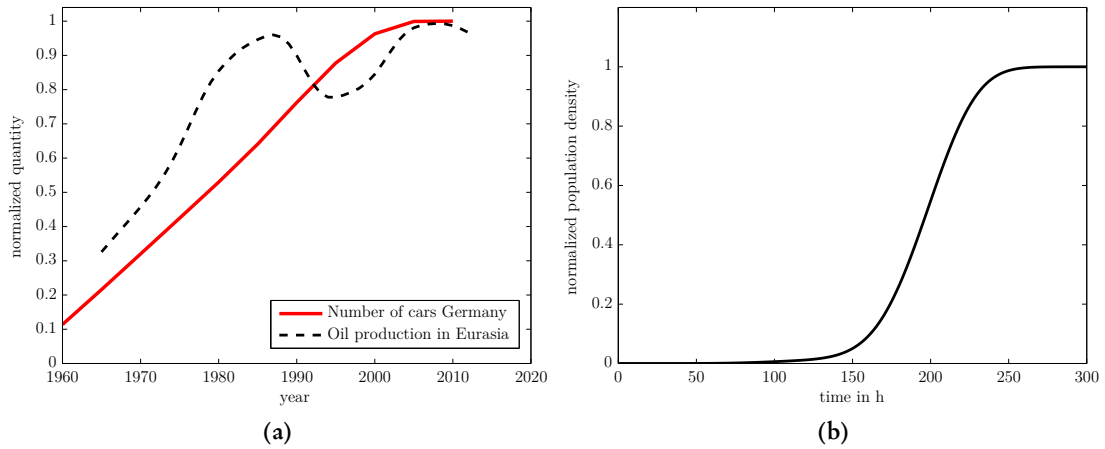


Figure 1.2: (a) Yearly oil production in the Eurasia region from the year 1965 AD till 2012 AD [23] and cumulated number of cars in Germany [44]. Values are normalized with its respective maximum. (b) Time dependency of normalized population density of a bacteria population [24].

the aviation industry. The strict emission regulations are satisfied with the help of the lean premixed combustion technology. Here, large amounts of air are mixed with the fuel prior to burning it. This limits the peak temperature in the flame and thereby reduces the NO_x emissions drastically. The major drawback of this technology is the susceptibility to thermoacoustic instabilities. These are coupled high amplitude heat release and pressure oscillations, which can significantly limit the operation range of engines [80]. The analysis of thermoacoustic instabilities started to be important in the 1950s because of their appearance in rocket engines [34]. With the introduction of the lean premixed combustion in gas turbines, thermoacoustic instabilities became one of the major obstacles of low emission combustion systems [18].

Already in the 19th century Rayleigh [109] has ascertained that it is a necessary condition for self-excited thermoacoustic instabilities that pressure and heat oscillation are oscillating in phase. This is mathematically expressed in the famous Rayleigh criterion:

$$\oint p' \dot{q}' dt > 0, \quad (1.1)$$

which means that the product of the acoustic pressure p' and the heat release fluctuation \dot{q} integrated over one oscillation cycle is positive and heat energy is transferred to the acoustic field. In this case a positive feedback cycle can be established, which causes stronger heat release fluctuations due to the acoustic fluctuations that amplify again the pressure oscillations. Nevertheless, the system will only turn unstable, if the amount of energy added by the heat source exceeds the acoustic energy dissipation. This principle is illustrated in Figure 1.3. At small amplitudes the energy gain is higher than the acoustic losses and the system becomes unstable. Energy is fed to

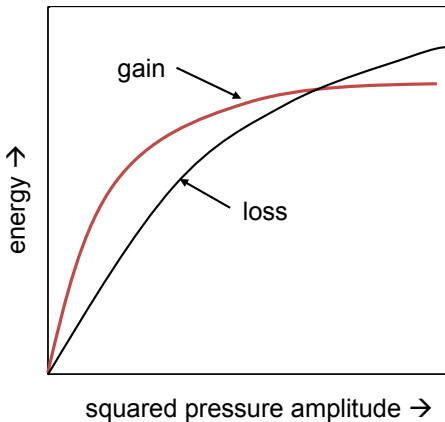


Figure 1.3: Evolution of a thermoacoustic instability. Limit cycle is established at equilibrium between energy gain and loss.

the acoustic field and the amplitude rises exponentially with time due to the positive feedback loop. Eventually, the energy gain saturates at higher amplitudes due to nonlinear processes. The acoustic losses can exhibit nonlinear effects, too. At the intersect of the two curves, a finite amplitude is established because a new equilibrium between energy gain and loss is found.

The concept of an initially linearly unstable system that establishes a finite limit-cycle due to nonlinear effects of the flame (source of energy) and the damper (energy loss) is the basis of this work. The principle is also illustrated in Figure 1.4 with a simulation of the acoustic pressure of a self-excited unstable system in the time domain. The acoustic pressure oscillation rises exponentially in amplitude when the system turns unstable. Very small perturbations are amplified by the transfer of heat energy to the acoustic field and the acoustic perturbations cause a stronger heat release fluctuation. A positive feedback cycle is established, which causes the increase of the pressure amplitude until it saturates. Finally, a s-shape saturation is observed, as it was described at the beginning of the chapter for totally different problems. The ultimate task of this thesis is to significantly improve the prediction of the frequency and the finite amplitude of thermoacoustic instabilities for low emission combustors.

1.2 Scope of this Thesis

Thermoacoustic instabilities are difficult to predict and can, in the worst case, destroy essential parts of the gas turbine. These combustion instabilities restrain the operational range of gas turbines and are a reason for increased emissions and decreased efficiency. Models and prediction tools are of high importance in the design process of combustion chambers. Moreover, the understanding of the physical effects causing nonlinear damping and the nonlinear flame response is of utmost importance.

The scope of this thesis is the prediction of limit cycle amplitudes of an industrially relevant combustion system with realistic acoustic boundary conditions and to further improve

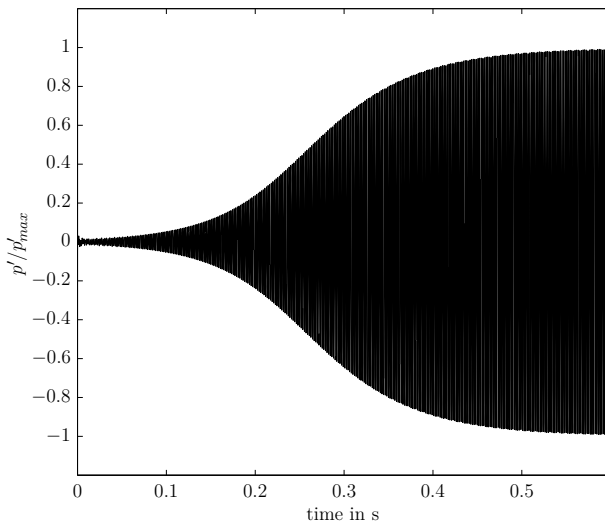


Figure 1.4: Time domain simulation of a thermoacoustic instability. Acoustic pressure time signal is normalized with its maximum.

the understanding of the relevant nonlinear effects. Firstly, the nonlinear flame response is investigated. Subsequently, the amplitude-dependent acoustic response of Helmholtz dampers and of the combustion chamber boundary conditions are analyzed. These dampers are used by all gas turbine manufacturers in gas turbines to control and attenuate thermoacoustic instabilities. Finally, the stability map of a premixed combustor is predicted and compared to stability experiments. The structure of this thesis is illustrated in Figure 1.5, which shows a sketch of a typical combustor system.

The present work significantly extends the state of the art in flame describing function based nonlinear network modeling in several ways. The nonlinear response of a premixed

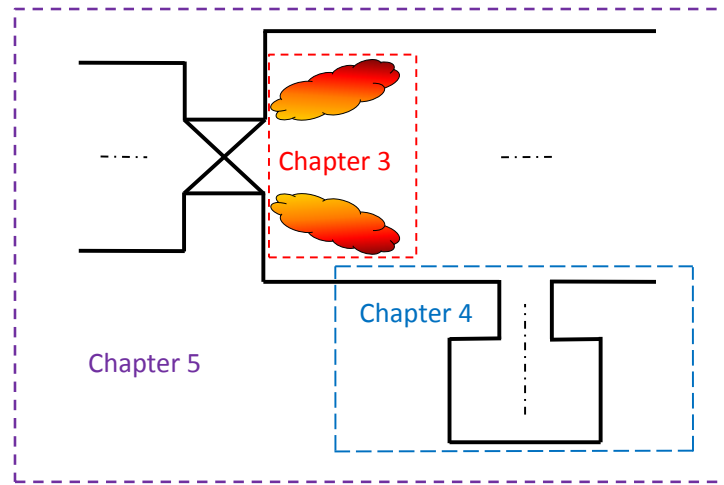


Figure 1.5: Structure of this work: Chapter 3 deals with the nonlinear flame dynamics, Chapter 4 with the damper response and the acoustic boundary conditions, and in Chapter 5 the whole system is analyzed.

and partially premixed flame is studied up to extremely high excitation amplitudes. Nonlinear mechanisms of the practically relevant flame are investigated in detail allowing for a better understanding and future modeling of the complex mechanisms. The correct assessment of the nonlinearity of the acoustic dampers is of crucial importance for the prediction of instabilities in a real engine. For the first time, the temperature differences between the grazing flow and the cross-flow emanating from a Helmholtz resonator are investigated in terms of the influence on the acoustic response of the resonator. As explained with the help of Figure 1.3, the nonlinear flame and damper response can be used in a nonlinear stability analysis to predict the frequency and amplitude of thermoacoustic instabilities. This is done for the first time for an industrially relevant combustor for a range of combustor lengths, thus allowing for a realistic assessment of the accuracy of the method. Additionally, a theoretical analysis of the interaction between damper and flame paves the way for encouraging investigations in the future.

Various experiments were conducted and the respective results are presented, analyzed and modeled in the following four chapters:

- The experimental set-ups and the applied measurement techniques as well as the underlying theory are briefly explained. Additionally, the results of a sensitivity analysis of the effect of the measurement uncertainties and other impacts on the flame transfer function are presented.
- The flame describing functions of perfectly and partially premixed flames are investigated in detail. Flow field and flame measurements are presented, as well as, acoustic measurements at different swirl numbers and degrees of unmixedness are used to get phenomenological explanations for the flame response saturation.
- The nonlinear acoustic response of Helmholtz resonators used in gas turbine chambers is investigated and the impact of the nonlinearities of the system acoustics are assessed. The influence of the hot grazing flow that is present in the combustor, is taken into consideration. The effects are incorporated in an impedance model, which accurately predicts the acoustic response of Helmholtz dampers that are applied at engine conditions.
- The nonlinear flame response and the nonlinear damper response are incorporated in a prediction tool for thermoacoustic instabilities. Measured limit cycle amplitudes at different operation points are used for the verification of the nonlinear instability analysis. Finally, the interaction of the nonlinear damper response and the flame describing function is theoretically investigated.

Chapter 2

Theory and Experimental Methods

Can one think that because we are engineers, beauty does not preoccupy us or that we do not try to build beautiful, as well as solid and long lasting structures? Aren't the genuine functions of strength always in keeping with unwritten conditions of harmony? ... Besides, there is an attraction, a special charm in the colossal to which ordinary theories of art do not apply.

Gustave Eiffel, in Henry Petroski, Remaking the World: Adventures in Engineering (1998), 173.

The fundamental theoretical background of the applied measurement techniques is briefly explained in this chapter. Additionally, the experimental set-ups used for the flame response measurements and damper investigations are described in detail as well as the burner and damper used. The operation points of the combustor used in the different sections are given and a repeatability and accuracy assessment of the flame response measurements is presented. Nonlinear flame describing functions obtained with photomultiplier and microphone measurements are compared.

2.1 Acoustic Fundamentals and the Multi-Microphone-Method

A comprehensive overview of the general relation between the fundamental acoustic state quantities acoustic pressure p' , the sound density, and the temperature can be found in the textbooks of Möser [90] and Munjal [91]. The analyses presented in this work are focused on the plane acoustic waves in ducts, where only the axisymmetric mode propagates. Higher modes can be neglected up to a frequency that is limited by the cut-on frequency f_c [110], which is defined for a cylindrical duct as:

$$f_c < \frac{1.84c}{\pi d} \quad (2.1)$$

with c and d denoting the speed of sound and the duct diameter, respectively. For the experiments presented in this work, the smallest cut-off frequency is $f_c \approx 1000$ Hz, which is much

higher than the frequencies investigated. The acoustic amplitudes considered in this work are in a range where nonlinearities of the acoustic field are negligible.

Considering only the one-dimensional propagation of waves in a pipe with a quiescent fluid and uniform cross section, additionally neglecting effects like friction and heat conduction, the wave equation [90] writes:

$$c^2 \frac{\partial^2 p'}{\partial x^2} = \frac{\partial^2 p'}{\partial t^2}, \quad (2.2)$$

where the total pressure $p = \bar{p} + p'$ is a function of the axial coordinate x and the time variable t . At this point turbulence is neglected. It will be shown later that the velocity perturbation can be decomposed in a turbulent part and a coherent part. The latter one is associated to the acoustic velocity. Considering the presence of a mean velocity it is convenient to introduce the axial velocity $u = \bar{u} + u'$ and to rewrite the wave equation into its convective form:

$$c^2 \frac{\partial^2 p'}{\partial x^2} = p' \left(\frac{\partial}{\partial t} + \bar{u} \frac{\partial}{\partial x} \right)^2, \quad (2.3)$$

Furthermore, the wave equation is transformed into the frequency domain by replacing the time derivative with the frequency domain equivalent $i\omega$ and denoting the Fourier transform of a variable with[^]:

$$(M^2 - 1) \frac{\partial^2 \hat{p}}{\partial x^2} + 2iMk \frac{\partial \hat{p}}{\partial x} - k^2 \hat{p} = 0. \quad (2.4)$$

here the Mach-number $M = \bar{u}/c$ and the wave number $k = \omega/c$ are introduced as dimensionless quantities. The angular frequency is denoted by ω and i is the imaginary unit. This second-order differential equation with constant coefficients can be solved by assuming a harmonic time dependence of $e^{i\omega t}$ [16, 87, 91]:

$$\hat{p} = \rho c (\hat{f} e^{-ik^+ x} + \hat{g} e^{ik^- x}) \quad (2.5)$$

where \hat{f} and \hat{g} are the complex amplitudes of the down- and upstream traveling waves and $k^\pm = \omega/(c \pm M)$ are the associated wave numbers of the plane mode.

Considering the convective acoustic momentum equation:

$$\frac{\partial p'}{\partial x} = -\bar{\rho} \left(\frac{\partial}{\partial t} + \bar{u} \frac{\partial}{\partial x} \right) u', \quad (2.6)$$

a respective expression to (2.5) can be derived for the acoustic velocity u' :

$$\hat{u} = (\hat{f} e^{-ik^+ x} - \hat{g} e^{ik^- x}). \quad (2.7)$$

The acoustic pressure \hat{p} and velocity \hat{u} or the upstream \hat{g} and downstream \hat{f} traveling waves

can be used to model an acoustic subsystem, which is part of a thermoacoustic framework. This is a well-known technique to represent thermoacoustic systems. In this network modeling approach, the actual system is divided into several subsystems, each of which is represented by acoustic response functions in the frequency domain. A subsystem is typically represented by a two-input–two-output system. The generic transfer matrix mapping the upstream acoustic state to that downstream has the form:

$$\begin{bmatrix} \hat{\rho}_{ds} \\ \hat{u}_{ds} \end{bmatrix} = \begin{bmatrix} T_{11} & T_{12} \\ T_{21} & T_{22} \end{bmatrix} \begin{bmatrix} \hat{\rho}_{us} \\ \hat{u}_{us} \end{bmatrix}, \quad (2.8)$$

where the elements of the transfer matrix, T_{11} etc., are complex functions of frequency, and $\hat{\rho}$ and \hat{u} are Fourier transforms of the acoustic pressure and the axial particle velocity, respectively.

It is assumed that only plane waves propagate between two elements. Boundary conditions are represented as single-input–single-output systems, in form of an impedance, admittance or a reflection coefficient. For instance, the impedance $Z_{us} = \hat{\rho}/\hat{u}$ is again a complex-valued function of frequency. The definition of the boundary condition does not have to coincide with the actual physical boundary of the set-up. It may be defined at a suitable reference location, at which only plane waves propagate.

All elements in the network model for the present set-up are measured with the Multi-Microphone-Method (MMM). This technique uses a decomposition of the plane acoustic field based on multiple microphone measurements in a duct, for frequencies sufficiently low so that only plane waves propagate [101]. Experimental characterization of transfer matrices of thermoacoustic elements for swirl stabilized flames using the Multi-Microphone-Method was first applied by Paschereit et al. [101]. Here, two microphone arrays with five water-cooled condenser microphones each are used for the plane wave decomposition of the acoustic field for the experimental results presented in this thesis. The microphones are mounted upstream and downstream of the burner. The MMM is used for the identification of the acoustic properties of the boundary conditions, the burner, the flame and the Helmholtz resonator. The latter one in conjunction with two flush mounted microphones in the resonator volume and two radially distributed at the exit plane of the resonator in the combustion chamber. To obtain the forcing amplitude upstream of the flame in terms of the acoustic velocity, the acoustic velocity is determined with the microphone array upstream of the burner in conjunction with the Burner Transfer Matrix (BTM). The upstream reflection coefficients are obtained from the microphone array upstream of the burner with acoustic excitation from the downstream end. Analogously, the acoustic boundary conditions at the combustor outlet are determined with the microphone downstream array and acoustic excitation from the upstream loudspeakers. Transfer matrices are obtained from two excitation states, employing the speakers on both sides. Mono-frequency

excitation is used with records of 16–32 seconds length for each frequency. This is necessary to obtain two acoustically independent states, to determine the four transfer matrix elements with the help of the resulting four linearly independent equations. By assuming or modeling single elements of the transfer matrix of flame or burner, it is possible to determine the transfer matrix elements with one measurement only.

Originally, the wave decomposition goes back to Seybert and Ross [125] as well as Chung and Blaser [26] who used only two microphones for the characterization of absorbing materials and mufflers. Poinsot et al. [105] extended the decomposition method by using multiple microphones for the measurement of the reflection coefficient of a premixed flame. This extension allows for a simple assessment of the measurement error by the comparison of the reconstructed acoustic field with the pressure measurements.

With the pseudoinverse \mathcal{M}^+ of the propagation matrix \mathcal{M} [16, 87]:

$$\mathcal{M} = \begin{bmatrix} e^{-ik^+x_1} & e^{ik^-x_N} \\ \vdots & \vdots \\ e^{-ik^+x_1} & e^{ik^-x_N} \end{bmatrix}, \quad (2.9)$$

the pressure measurements at N different locations x_N along the tube axis can be used to obtain the complex amplitudes of the upstream \hat{g} and downstream \hat{f} traveling waves. If at least two pressure measurements are known, they can be obtained by solving:

$$\begin{bmatrix} \hat{f} \\ \hat{g} \end{bmatrix} = \mathcal{M}^+ \hat{\mathbf{p}} \frac{1}{\rho c}. \quad (2.10)$$

If three or more pressure measurements are available, the residual of the wave decomposition can be estimated with the help of the normalized mean square deviation ς :

$$\varsigma = \frac{\|(\mathbf{I} - \mathcal{M}\mathcal{M}^+)\hat{\mathbf{p}}\|_2^2}{\|\hat{\mathbf{p}}\|_2^2}, \quad (2.11)$$

here \mathbf{I} is the identity matrix and $\|\cdot\|_2^2$ denotes the square of the Euclidean L2-norm. The residual can be considered as a measure of deviation of the MMM from the exact pressure measurements. The decomposition of the acoustic field is more robust to errors with a large number of axial measurement points. However, the spacing between the measurements points has to be reasonable with respect to the wavelength to achieve a reliable assessment of the error. To ensure good accuracy at low frequencies and avoid breakdown of the method at frequencies for which half a wavelength fits between two microphones, the axial sensor locations are distributed non-uniformly. The mean square deviation ς estimated for the Multi-Microphone-Method were for

both microphone sets for all measurements presented well below 2% for the frequency ranges investigated.

2.2 Flame Response and Stability Map Measurements

For laminar premixed flames, kinematic effects like wrinkling and the movement of the flame are the main reasons for acoustically induced oscillations of the heat release. The generated heat release perturbations are usually related to flame surface area variations [39, 122, 123]. The excitation mechanisms for industrially relevant premixed flames can be classified in two major groups, see e.g., [54, 139]: (i) velocity perturbations and (ii) equivalence ratio perturbations. Velocity perturbations are caused by coherent vortices [99] and swirl fluctuations [52, 70, 97]. Swirl fluctuations are generated by an acoustic wave impinging on the swirler. While longitudinal acoustic perturbations travel at the speed of sound, vorticity waves are advected by the mean flow. The heat release rate fluctuations generated by these two mechanisms may have a considerably phase difference and, thus, may interfere constructively or destructively. Coherent structures are especially important for the pronounced vortex-flame interactions of swirl stabilized flames. Schadow and Gutmark [116] interpreted the evolution of coherent flow structures in combustors, which lead to periodic heat release, as shear layer or hydrodynamic instabilities. The vortices are amplified if the shear layers are convectively unstable at the frequency of the thermoacoustic instability. The fluctuation of the heat release caused by the vortices provides the feedback loop between the flame, the acoustic and the hydrodynamic field [100]. The frequency of the vortex roll-up locks onto the frequency of the acoustic field, which acts as a pacemaker for the coherent structures [62].

In practical gas turbine burners, air and fuel are not perfectly mixed before reaching the flame. This would require a relatively long mixing distance, which cannot be realized for safety reasons due to possible flashback problems. Additionally, flames with a certain degree of unmixedness feature a broader operational range. This type of flame is often referred to as partially [104] or technically [121] premixed. For the sake of clarity of the abbreviations, the terms perfectly premixed (ppm) and technically premixed (tpm) are used in this study.

Only technically premixed flames are affected by equivalence ratio oscillations. Perturbations in the mixture fraction originate from pressure and velocity oscillations at the location of the fuel injection [55, 56, 81]. These perturbations are advected to the flame, subject to diffusion and dispersion [106, 112], and may generate large oscillations in the heat release rate. This is in particular the case for lean combustion, where flame properties such as the burning velocity become strongly susceptible to perturbations in the equivalence ratio [81]. Moreover, strong

temporal variations in the mixture fraction may lead to a dynamical displacement of the flame anchoring position, which then results in the generation of an unsteady heat release rate [11].

The above mentioned excitation mechanisms and their interaction lead to a frequency dependent response of the flame to flow disturbances commonly called Flame Transfer Function (FTF). The transfer function of the flame can be incorporated into a framework to calculate the linear stability limits of flame-combustor systems [114]. However, this type of network stability analysis is limited to the linear domain and cannot be used for the prediction of the limit-cycle oscillation amplitude. This remains one of the key-challenges in combustion dynamics related research. The limit-cycle amplitude is determined by equilibrium of energy addition and removal. As will be shown in this thesis, acoustic damping can decrease with the oscillation amplitude. However, even stronger nonlinearities are featured by the flame response. Only a saturation in the energy addition rate can lead to an equilibrium state or an increase of the acoustic losses, which is reported in the literature [111, 138]. The energy equilibrium state is a necessary condition for the limit cycle oscillation, which is always observed in practically relevant systems.

All previous studies that have used experimentally determined flame describing functions to estimate the limit cycle oscillation amplitude made use of chemiluminescence signals to assess the heat release rate oscillations of the flame. However, it is known that a quantitative link between the chemiluminescence of certain radicals, CH^* or OH^* for example, can be only established for perfectly premixed conditions [51]. Since practical combustion systems in gas turbines never meet this requirement, the applicability of the flame describing function method remains an issue. This is addressed in the present work through the application of the Multi-Microphone-Method for the determination of the heat release rate fluctuations. Since this method rests on a direct evaluation of the acoustic source and, thus, the heat release rate fluctuation, the degree of partial premixedness is irrelevant.

A flame transfer matrix formally treats the reaction zone as an acoustic quadrupole and incorporates the flame transfer function. The Rankine–Hugoniot relations are used to relate the flame transfer function [121] to the flame transfer matrix (or vice versa) by

$$\left(\frac{\hat{p}}{\rho c} \right)_{\text{ds}} = \left(\frac{\hat{p}}{\rho c} \right)_{\text{us}} \quad (2.12)$$

$$\hat{u}_{\text{ds}} = [1 + (\vartheta_{\text{ds}}/\vartheta_{\text{us}} - 1)\mathcal{F}(\omega)] \hat{u}_{\text{us}}, \quad (2.13)$$

where \hat{p} denotes the Fourier transform of the acoustic pressure and ϑ is the mean temperature, respectively. It is furthermore assumed that the extent of the domain of heat release is compact with respect to the acoustic wavelength (see, Equation (2.12); $T_{11} \approx 1$). $\mathcal{F}(\omega)$ is the flame transfer function relating normalized fluctuations in heat release rate (\hat{q}/\bar{q}) to normalized

fluctuations in velocity:

$$\mathcal{F}(\omega) = \frac{\hat{q}/\bar{q}}{\hat{u}/\bar{u}}.$$

In case of finite amplitude levels, the flame transfer function is replaced by the flame describing function (FDF), which has an additional dependence on the velocity fluctuation amplitude: $\mathcal{F}(\omega, |\hat{u}|)$. The off-diagonal flame matrix elements can be considered as zero because the pressure loss induced by the flame is negligible for the small Mach number regime ($T_{12} \approx 0$) and the fuel injector is insensitive to pressure fluctuations ($T_{21} \approx 0$). Consequently, the amplitude dependent flame transfer matrix becomes:

$$\begin{bmatrix} \left(\frac{\hat{p}}{\rho c}\right)_{ds} \\ \hat{u}_{ds} \end{bmatrix} = \begin{bmatrix} 1 & 0 \\ 0 & [1 + (\vartheta_{ds}/\vartheta_{us} - 1)\mathcal{F}(\omega, |\hat{u}|)] \end{bmatrix} \begin{bmatrix} \left(\frac{\hat{p}}{\rho c}\right)_{us} \\ \hat{u}_{us} \end{bmatrix}, \quad (2.14)$$

hence measurements of the acoustic variables for upstream forcing of the flame is sufficient for the determination of the T_{22} matrix element of the flame transfer matrix and the flame describing function \mathcal{F} , respectively.

The flame describing function element T_{22} is experimentally determined with the help of the burner transfer matrix, which is measured under cold flow conditions. Subsequently, the describing function of burner and flame together is obtained by measuring the acoustic field upstream of the burner and downstream of the flame. In a final step, the flame describing function is separated mathematically by calculating the acoustic field in front of the flame with the help of the cold-flow burner matrix. Now, with the help of Equation (2.14) the flame describing function can be calculated out of the measured downstream data and the post-processed upstream data. The latter ones are also used as input for the flame describing function obtained from optical measurements.

The experimental determination of the flame describing function and the associated optical measurements were conducted at an atmospheric combustion test rig shown in Figure 2.1. It is equipped with a radial swirl generator and is used for all combustion experiments presented in this thesis. This test-rig was also used for the assessment of the burner transfer matrix and the upstream and downstream impedances.

Fuel (natural gas) can be injected at two positions. In practical gas turbine burners, air and fuel are not perfectly mixed before reaching the flame. This would require a relatively long mixing distance, which cannot be realized for safety reasons due to possible flashback problems. Additionally, flames with a certain degree of unmixedness feature a broader operational range. This type of flame is often referred to as partially [104] or technically [121] premixed. For the sake of clarity of the abbreviations, the terms perfectly premixed (ppm) and technically premixed (tpm) are used in this study. For perfectly premixed conditions, the fuel is injected more

than $20 D_{us}$ upstream of the burner, where D_{us} is the diameter of the upstream manifold. To achieve technically premixed conditions, the fuel is injected into the burner. Inside the mixing tube, at the exit of the swirler and at a distance of $0.6 D_h$ are 16 circumferentially distributed fuel injection holes (1 mm diameter) on the upstream plate of the swirl generator. Here, D_h – hydraulic diameter of the mixing tube. The holes are visible in the 3D broke-out view shown in Figure 2.2. Small injection holes, the fuel supply line, and the attached gas filter generate high fuel supply pressure losses. For higher fuel mass flows, only fluctuations in the air mass flow (i.e., the acoustic velocity) at the injector generate equivalence ratio perturbations, while the fuel mass flow is not affected by acoustic pressures oscillations. For some of the experiments the ratio between technically premixed and perfectly premixed was varied stepwise. This ratio is characterized by ε . The fuel supply line is probably not stiff for small fuel split ratios.

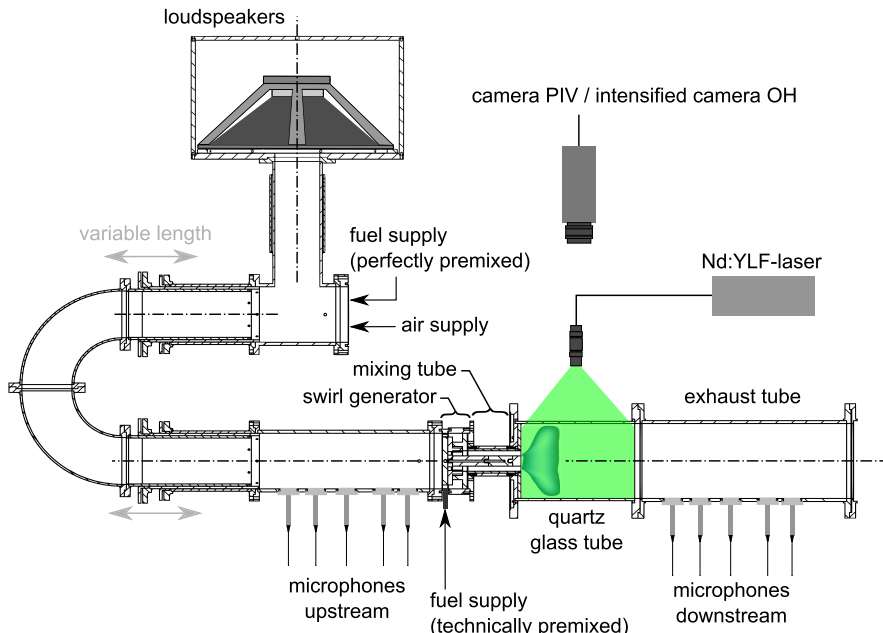


Figure 2.1: Schematic representation of the experimental set-up with measurement devices indicated.

The annular mixing duct is used to increase the mixing of air and fuel before it enters the combustion chamber. Despite the relatively good spatial mixing of the burner, temporal inhomogeneities are not effectively mixed, especially for lower frequencies [14]. For two of the presented experiments, the fuel, which was injected in the burner, was additionally modulated with an industrial automotive fast response on-off valve. The purpose of the fast response valve is to add equivalence ratio fluctuations interfering with the natural equivalence ratio oscillation in-phase or out-of-phase, without a change of the operation point or injection location.

A movable block swirl generator allows for a variation of the theoretical swirl number from $S = 0$ to $S = 2$ [76]. The swirl number is defined as the ratio of the axial flux of tangential momentum to the axial flux of axial momentum. The Reynolds number with respect to the hydraulic diameter of the mixing tube was approximately 35 000.

The Multi-Microphone-Method was used to measure the acoustic field upstream of the burner and inside the combustor with 5 condenser microphones on each side.

High-amplitude acoustic forcing is realized with four 18-inch 600 W subwoofers. To obtain sufficiently high excitation amplitudes, it is necessary to adjust the upstream tube length in order to generate resonant conditions. This is achieved by using a trombone-like plenum [117], which allows for an extension of about 2 m in length.

The natural gas, which was used as the fuel for all experiments, consists of 97–98% methane. Two Coriolis mass-flow meters are used to measure fuel and air mass flows.

An overview of the set-up used for the stability map experiments is shown in Figure 2.3. For the describing function measurements, the combustion system must be thermoacoustically stable. However, since the goal is to predict the limit cycle frequency and amplitude of combustion instabilities, these measurements have to be made at operating conditions, where the system is nominally unstable. This is achieved by placing an orifice downstream of the 0.7 m long microphone exhaust tube, which significantly decreases the magnitude of the reflection coefficient, and thus increases the acoustic losses, when the contraction ratio of the orifice is chosen in a specific manner depending on the flow velocity [5]. The orifice did not have an impact on the flow field of the flame because the reduced swirl number ($S \rho_{ds}/\rho_{us}$, S being the swirl number and ρ_{us} and ρ_{ds} the mean densities upstream and downstream of the flame, respectively) is well below 0.2, which is a critical value for the impact of outlet boundary conditions on swirl flames

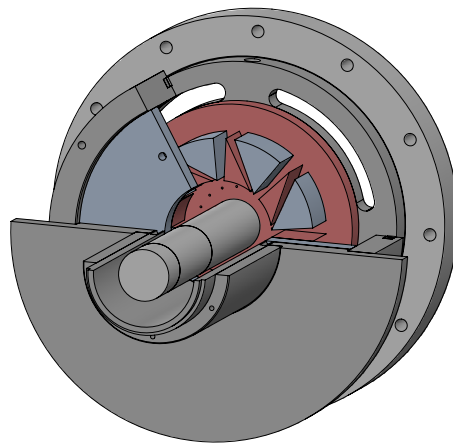


Figure 2.2: Broke-out view of the burner. Flow direction is perpendicular to the plane of the image towards the reader.

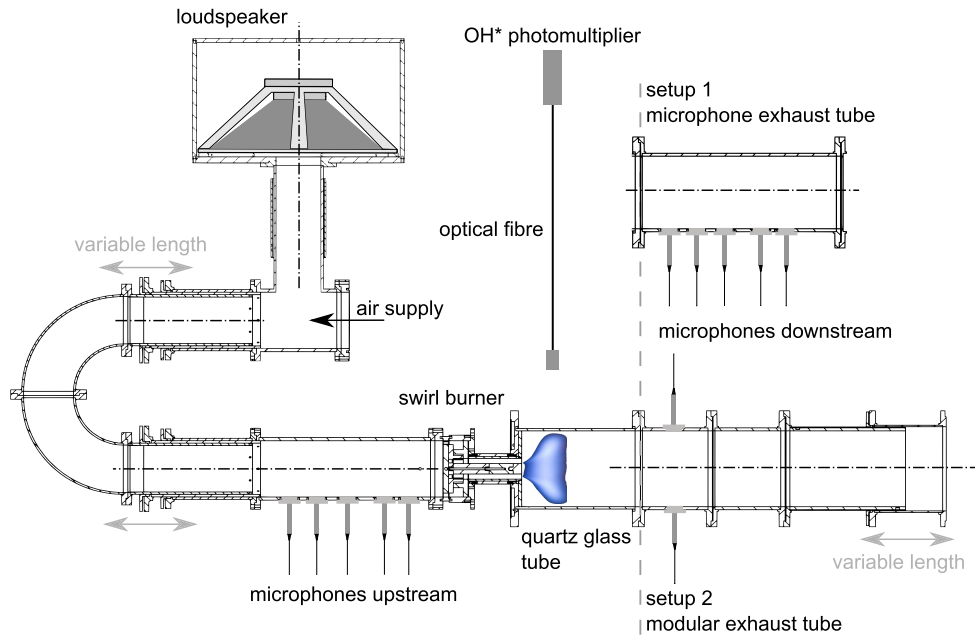


Figure 2.3: Overview of the test rig

[132]. For the measurement of self-excited instabilities, the downstream tube is replaced with an adjustable exhaust tube. The length of this exhaust tube can be varied continuously in the range of 0.18 m to 1.1 m, and it is equipped with two microphones at a position 0.3 m downstream of the flame.

Table 2.1 summarizes the operation conditions used for the flame response measurements presented in the respective chapters. The operation conditions are all not preheated and lean premixed featuring vortex breakdown.

2.3 Repeatability and Accuracy Assessment

¹A sensitivity analysis of the linear flame transfer function to several operational parameters was performed. A recent study of Kim and Santavicca [65] identified trends of several operation parameters on the flame transfer function for two different swirl stabilized turbulent burners. One of the major findings of this study is that the flame response is very sensitive to changes in mass-flow and thermal power. The sensitivity of the flame response of a laminar Bunsen flame was recently investigated by Duchaine et al. [38] with respect to various parameters, such as the

¹The work presented in this section is based on a journal publication [31]. Paragraphs and phrases of this chapter are very similar or identical to text paragraphs published in the article. These excerpts are written by me.

Table 2.1: Operation points used for the flame response measurements in the respective sections

Quantity	Section 3.3	Section 3.4.1-3.4.3	Section 5.2-5.3
\bar{m}_{air} in kg/h	165	150	165
$\bar{\varphi}$	0.65	0.7	0.65
tpm	x	x	x
ppm		x	
S	0.6/0.8/1	0.6	0.7
D_{cc} in m	0.2	0.2	0.2
D_h in mm	27.5	27.5	27.5
length mixing tube in m	0.17	0.17	0.17
Re	35,000	35,000	35,000
ϑ at combustor inlet in K	300	300	300

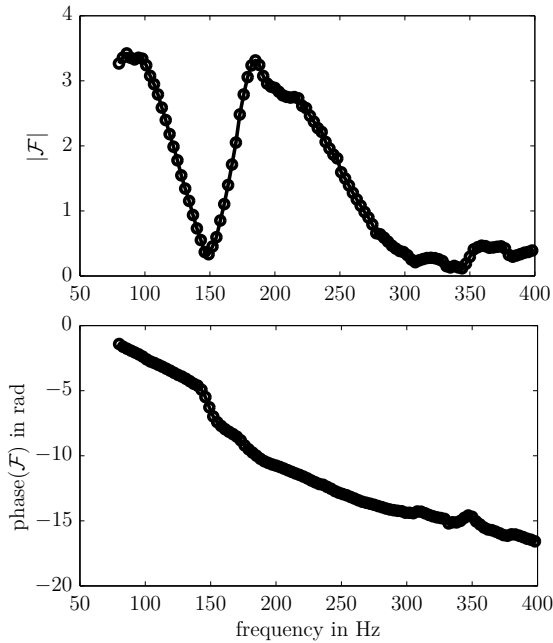


Figure 2.4: Gain and phase of the linear flame transfer function investigated and analyzed in Section 5.2. Markers indicate measurement points. Measurements are conducted at a constant amplitude of $|\hat{u}/\bar{u}|=0.1$. Sensitivity analysis is performed in this section with respect to this flame transfer function.

laminar burning velocity and the air inlet temperature. While from their results it can be seen that already a laminar flame is considerably sensitive to certain parameters, this aspect becomes even more severe in large scale turbulent industrial applications, where operational parameters cannot be controlled precisely as in a lab experiment; uncertain input parameters therefore will be common in real combustor configurations. The sensitivity analysis for a fully turbulent partially premixed swirl flame shown in this study allows for an assessment of the limits of the stability analysis approach for industrial configurations.

Consequently, it is interesting to assess the sensitivity of the flame transfer function to several operation parameters. The sensitivity investigations are made with respect to the flame transfer

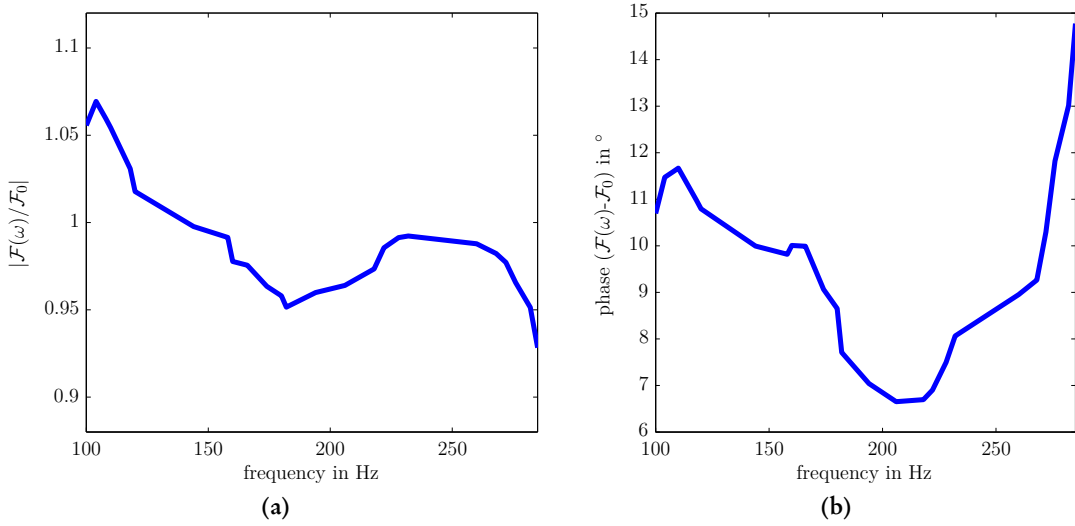


Figure 2.5: (a) Ratio of absolute transfer function values and (b) difference in phase of transfer function (right) measured on different days with an identical configuration but different ambient conditions.

function shown in Figure 2.4. This transfer function is later discussed and used in Section 5.2 for the stability analysis. However, the general results of the conducted sensitivity analysis are also valid for the other operation points investigated in this work. Trends are provided for similar burners. The transfer function was measured at a constant amplitude of $|\hat{u}/\bar{u}|=0.1$. In this amplitude regime the nonlinear effects are weak. The sensitivity analysis is conducted at these nominally linear conditions, which is indicated in the respective figures by using $\mathcal{F}(\omega)$ to emphasize that the effects are only frequency dependent in the investigated amplitude regime.

Gas turbine combustors operating in the field face differing fuel compositions, production tolerances and operation influences. Caused by limited measurement accuracy and variations in the ambient conditions from day to day, the prediction precision is limited, too. The susceptibility of the flame response to important operation parameters is especially critical for the comparison to numerical and to engine data. Additionally, the sensitivity of the flame transfer function can be used for an assessment of passive control strategies.

Figure 2.5a shows the ratio of the reference flame transfer function, depicted in Figure 5.2, and a transfer function measurement on a different day. Additionally, Figure 2.5b shows the corresponding phase difference of the flame transfer function. Both measurements were conducted with identical settings on different days. The repeatability of the flame transfer function gain is in the range of $\pm 5\%$ in the frequency range between 105 Hz and 280 Hz. The larger deviations for frequencies higher than 280 Hz are caused by the very small values of the gain in this frequency range. While the gain of the transfer function is overestimated for frequencies

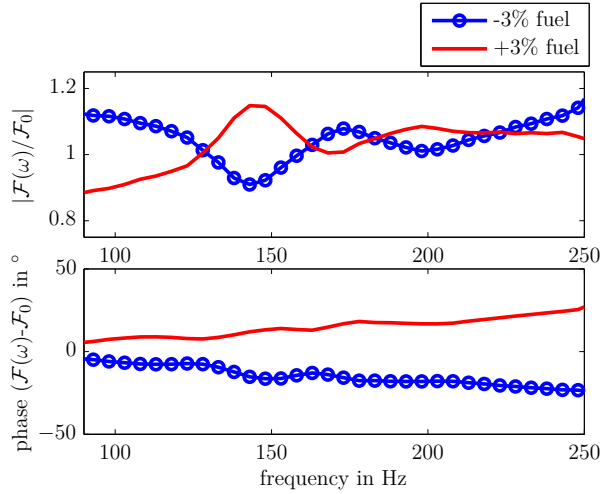


Figure 2.6: Flame transfer function with 3% increased and decreased fuel mass flow. Upper plot shows ratio of transfer function gain and lower plot difference in phase of the transfer functions with respect to the baseline condition.

lower than 150 Hz and underestimated for frequencies higher than 150 Hz, by one of the measurements, the phase difference is positive for all frequencies. The phase differences observed are in the range of 10 degree. The deviations may be caused by a number of changes in the ambient conditions, like changes in the fuel quality, the cooling efficiency, ambient pressure, sealing quality, temperature equilibrium of the test facility and the limited measurement precision. Since the instability measurements and the flame describing function measurements were not conducted consecutively but also, for some part, at different days, deviations observed in the range of at least $\pm 5\%$ have to be expected.

In order to assess the sensitivity of the flame transfer function to small perturbations in the operating parameters without effects of day-to-day variations described above, the following results were obtained from measurements immediately following each other in the range of the operation point.

It is especially important for partially premixed flames to determine the amount of fuel correctly. The amount of fuel has an impact not only on the mean thermal power but also on the amplitude of the equivalence ratio fluctuations and the mixing between injection point and flame front. Figure 2.6 illustrates the influence of a steady variation of $\pm 3\%$ of the fuel supply. Reducing the equivalence ratio by decreasing the amount of fuel leads to an increased gain for both frequency regions of strong amplification in the transfer function. Around 100 Hz the gain is increased by 10% and for frequencies around 180 Hz it is increased by 5%. Contrary to that, by adding 3% fuel, the gain is decreased in the range of 100 Hz for 10%. Both variations have a very strong impact around the frequency of 150 Hz, where the gain of the transfer function becomes small. This is to be expected since the slope of the transfer function is very high around

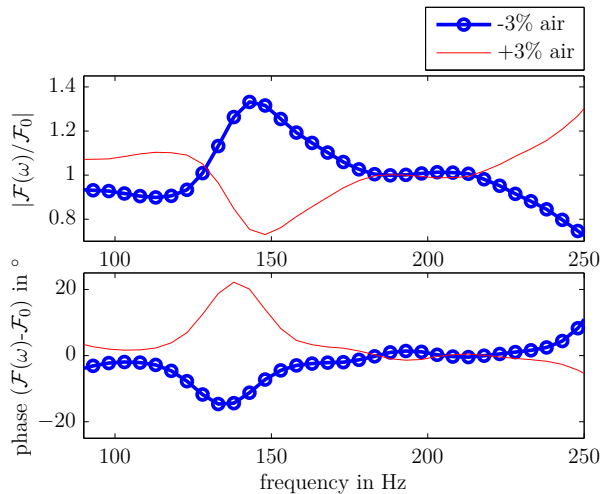


Figure 2.7: Flame transfer function with 3% increased and decreased air mass flow. Upper plot shows ratio of transfer function gain and lower plot difference in phase of the transfer functions with respect to the baseline condition.

the local minimum at 150 Hz. Small changes in the frequency position of the minimum lead to large deviations in gain. However, the effect on the phase response indicates an impact on the time lags associated with the flame response to acoustic perturbations. The time lags are affected because the mean flame position is very sensitive to the fuel mass flow. While the phase response is diverging for increasing frequencies, the gain is converging for the two perturbed operation conditions.

Relatively similar, however differently emphasized as shown in Figure 2.7, is the effect of changes in the air mass flow by 3%. Both, variations in the gas mass flow and the air mass flow, modify the equivalence ratio of the flame and thereby it is expected that the changes are similar. Nevertheless, some differences can be observed because changes in the air mass flow affect also the mean velocity, which additionally affects the time lags in the flame response. The deviations around 150 Hz are more pronounced in terms of the flame transfer function gain and phase. Neither the gain nor the phase is affected by the modified air mass flow in the frequency range around 200 Hz. For higher frequencies, at which the gain is very low, the effect is again higher. The variation of the phase response is, besides frequencies close to 150 Hz, of minor importance. Especially the gain in the region around 100 Hz is very sensitive to changes in the equivalence ratio.

The precision of the gas mass flow meter of $\pm 0.5\%$ and the air mass flow meter of $\pm 3\%$, introduces additional 5–24% of uncertainty for the flame transfer function gain. Moreover, the measured transfer matrices of the boundary conditions, the burner and the flame are subject to measurement uncertainties in the order of 1% caused by the Multi-Microphone-Method. A cumulative error in the range of 0–33% is thus expected for the flame transfer function gain. The

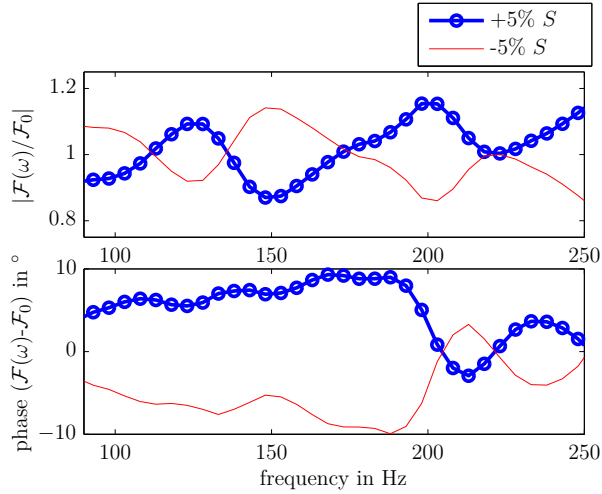


Figure 2.8: Flame transfer function with 5% increased and decreased Swirl number. Upper plot shows ratio of transfer function gain and lower plot difference in phase of the transfer functions with respect to the baseline condition.

error in the phase of the flame response is more pronounced for higher frequencies and is generally in the range between 10–30 degrees. These estimates are based on repeated measurements of the linear transfer function. Please note that the nonlinear flame response is responsible for the amplitude of the limit cycle oscillation and the associated deviations may be different from the one observed at small excitation amplitudes.

The sensitivity of the flame response to changes in the swirl number is important due to limited production precision for industrial combustors and for adjustable academic model combustors as well as for the comparison to CFD calculations. The swirl number has a pronounced effect on the flame transfer function and thus also on the stability characteristics, as recently shown by Durox et al. [40]. In the present study, increasing and decreasing the swirl number by 5% leads to a change in the order of 10% of the FTF (upper plot in Figure 2.8). The differences of the phase of the flame response are generally smaller than those associated with perturbations in fuel and air mass flows, and on average about ± 5 degrees but never exceeding ± 10 degrees.

Another source of uncertainty lies in using the chemiluminescent light emission from the flame as a measure for the heat release rate. Capturing the light emission with excited radicals using photomultipliers is sensitive to equivalence ratio fluctuations and is therefore not suitable for quantitative measurements of the flame response in partially premixed systems. However, this technique is widely used in industry and academia for the qualitative measurements of the flame response and for the quantitative measurement of the transfer function of perfectly premixed flames. Figure 2.9 shows the gain of the nonlinear flame response for 158 Hz for partially premixed combustion. Since the equivalence ratio fluctuations grow nonlinearly with

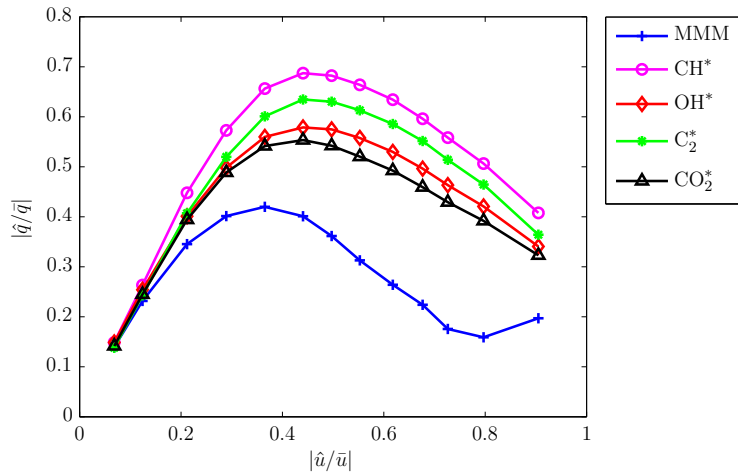


Figure 2.9: Gain of the nonlinear flame response at 158 Hz for various PMT signals compared to MMM measurement.

the velocity perturbation amplitude, the difference between the photomultiplier signals and the acoustic method increases, too. The differences between the individual chemiluminescence signals are caused by the differing sensitivity to equivalence ratio oscillations.

For the incorporation of the flame transfer function in a thermoacoustic modeling framework, the Rankine–Hugoniot relations must be applied (Equation (2.13)), if the transfer function is measured with a photomultiplier. The temperature needed for this relation is subject to measurement uncertainty. The ratio of the upstream and downstream temperature of the flame directly affects the gain of the acoustic flame transfer function. In the presented experiments, the temperature was measured 0.3 m downstream of the flame in the center of the exhaust tube.

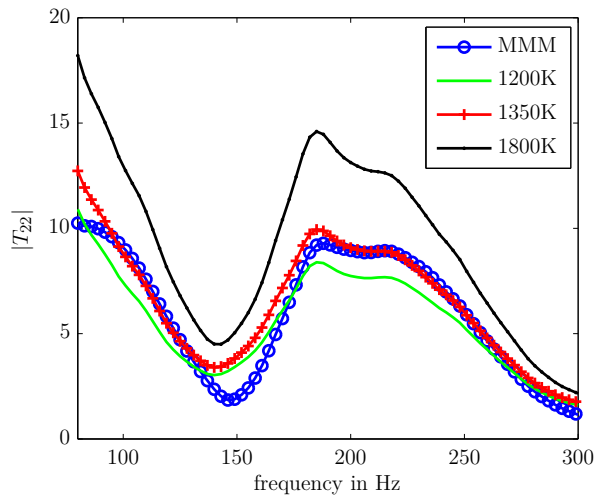


Figure 2.10: Comparison of linear acoustic flame transfer function obtained with MMM and PMT-OH* for three different downstream temperatures estimates.

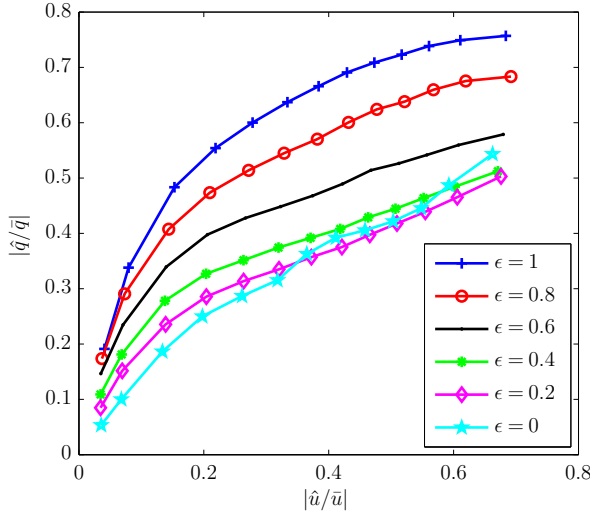


Figure 2.11: Flame response at 180 Hz obtained with the MMM for various degrees of partial premixedness.

As depicted in Figure 2.10, taking the temperature of 1200 K of the measurement point to calculate the acoustic transfer function T_{22} ($T_{22} = \hat{u}_{ds}/\hat{u}_{us}$) underestimates the gain. Taking heat radiation and convection into account [75], which yields a corrected temperature of 1350 K, leads to significantly more accurate results. The OH* photomultiplier results match the MMM obtained transfer function well, besides the ranges around 150 Hz and 95 Hz. The remaining differences can be attributed to the susceptibility to equivalence ratio fluctuations. However, using the adiabatic flame temperature of 1800 K overestimates the flame response significantly.

Especially important for the comparison of experimental and numerical results is the correct representation of the degree of partial premixedness at the flame. Figure 2.11 exemplary illustrates the magnitude of the flame response at 180 Hz for various splits of partial to perfect premixedness. The degree of partial premixedness was varied by injecting part of the fuel far upstream ($x/D > 20$) of the burner. With increasing amplitude, the flame response starts to saturate around an amplitude of $|\hat{u}/\bar{u}| = 0.2$ in all cases. However, with an increasing amount of partially premixed fuel, an increase in the flame response magnitude is observed. This indicates that heat release rate fluctuations associated with perturbations in the equivalence ratio are in phase with fluctuations resulting from perturbations in the flow field. In case of almost perfectly premixed conditions, the flame response is also qualitatively affected since the response of the perfectly premixed flame increases in magnitude for higher excitation levels. Hence, a comparison between numerical and experimental data becomes very difficult if the degree of temporal unmixedness is inaccurate

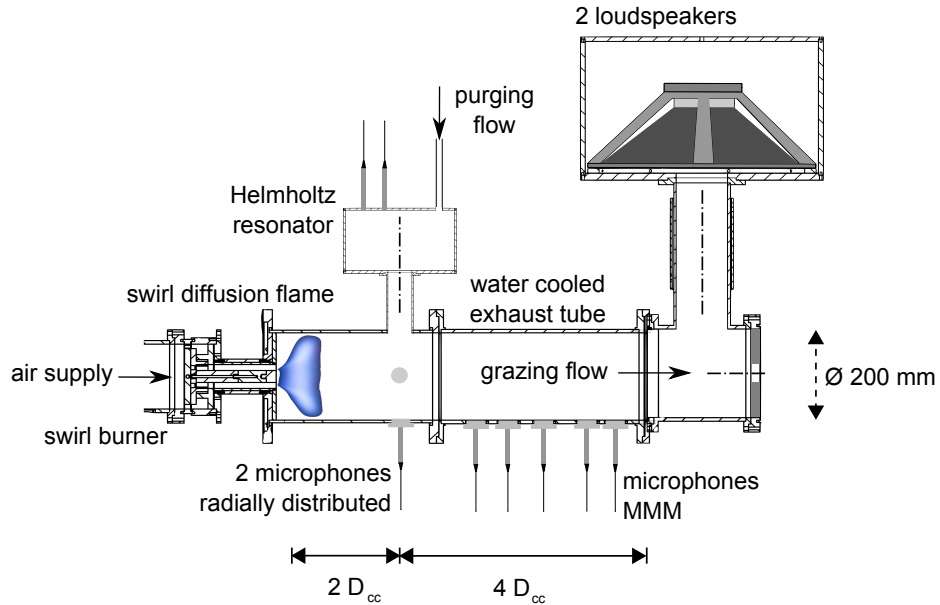


Figure 2.12: Experimental set-up for acoustic high temperature experiments.

2.4 Helmholtz Resonator Measurements

Two modifications of the same experimental set-up were used for the assessment of the realistic acoustic boundary conditions. The set-ups are depicted in Figure 2.12 and Figure 2.13, respectively. The first set-up, made completely of metal, was used for the investigation of the temperature impact of the grazing flow, while the second one, made of PMMA, provided optical access for the flow investigations inside and in the vicinity of the Helmholtz resonator. The temperature of the grazing flow was modified in the range between 750-1300 K with a swirl stabilized diffusion flame. The flame is stabilized in the wake of the center body of the burner with a total axial length of maximum $0.2 D_{cc}$ (denoting the diameter of the main tube of 0.2 m). Additional experiments were conducted with preheated air only, featuring temperatures up to 550 K. Three Coriolis mass-flow meters are used to measure the fuel mass flow and the air mass flows for purging and grazing flow. Downstream of the combustion chamber a water cooled exhaust tube is mounted. Two microphones are mounted radially distributed at the axial plane of the Helmholtz resonator to measure the acoustic pressure at the resonator entrance. Downstream of the resonator a microphone array is installed and two loudspeakers are mounted. The flame is again stabilized thermoacoustically by the application of an orifice at the downstream end.

The second set-up was used for the flow investigation. It is made of PMMA (Plexiglas) with

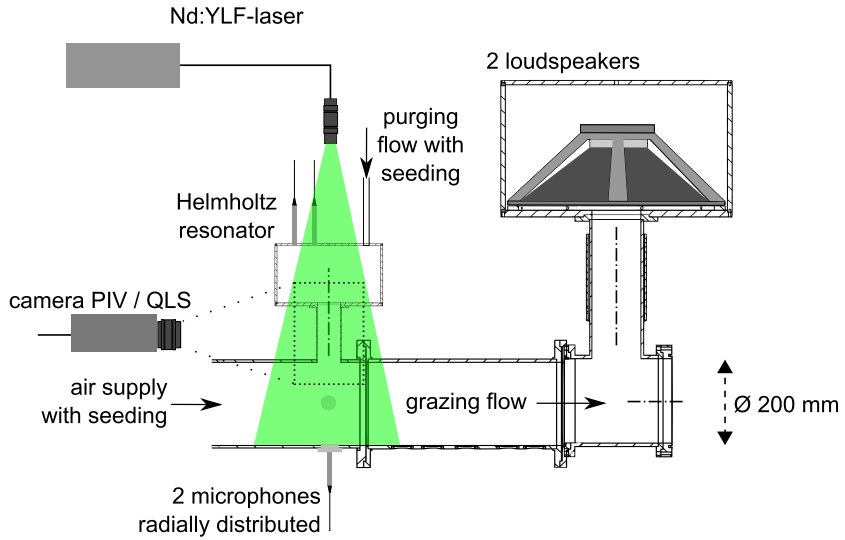


Figure 2.13: Experimental set-up for flow and concentration measurements.

the same geometrical dimensions as the metal set-up. However, the burner is not mounted to eliminate flow disturbances associated with swirling flow. PMMA allowed for the optical investigation of the flow at the entrance and in the resonator itself. The flow is seeded with silicon oil droplets (DEHS) of $1\mu\text{m}$ diameter and injected $3 D_{cc}$ upstream of the resonator using a lance, which distributed the seeding radially. Due to the joints between the single tubes (main tube, resonator neck and volume) optical access is obstructed in these regions.

The Multi-Microphone-Method was used to measure the acoustic field downstream of the resonator with five condenser microphones. Furthermore, the results of the MMM were used to verify the acoustic pressure measurements of the two radially distributed condenser microphones at the axial plane of the resonator. The deviation between the MMM and each of the two radial microphones is always well below 2%. Thus, it can be stated with respect to the limited measurement accuracy that the pressure field is steady in the plane of the resonator, despite the complex acoustic near field due to the interaction between grazing flow and oscillating cross-flow.

The acoustic velocity in the neck was calculated using Equation (4.7) and the pressure measurements at the resonator volume. Two microphones are flush mounted in the resonator volume at different positions, with a difference in pressure amplitude well below 0.5%.

Figure 2.14 illustrates the resonator set-up in detail. The cylindrical volume has a diameter of 81 mm and a connection to a secondary neck, which supplies the resonator with purging flow. This neck is very thin with a diameter of 2 mm and relatively long with a length of 50 mm, and

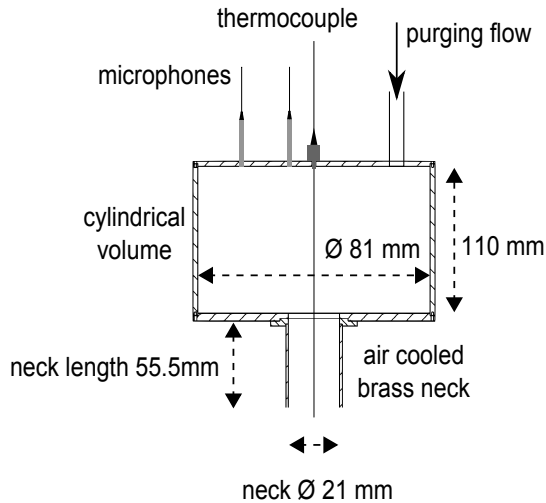


Figure 2.14: Detailed resonator geometry.

it is connected through an area jump to a long and flexible air supply pipe. Consequently, the pressure loss across the air supply tube is sufficiently high to neglect the acoustical effect of the air supply duct [63]. The resonator neck has a diameter of 21 mm and the physical length is 55.5 mm. To maintain a constant temperature of the neck wall, it is air cooled and made from brass to enhance the heat transfer.

2.5 Optical Measurement Techniques

In order to provide optical access for the combustion tests, the flame tube in the combustion zone is made of quartz glass with an inner diameter of 0.2 m. The PMMA set-up was used for the optical investigations of the resonator flow.

Time-resolved spatial distributions of the OH*-chemiluminescence light emission of the flame were obtained using an intensified high-speed camera with an optical bandpass filter centered at a wavelength of 308 nm. Optical access is also provided for the photomultiplier-tube measurements, which are used to measure chemiluminescent light emission of different radicals from the reaction zone, too. The light emissions are measured integrally by the photomultiplier. In contrast to that, the intensified camera measurements feature a spatially distribution in two dimensions with a line of sight integration. Consequently, Abel deconvolution was applied to the time-averaged and phase-averaged OH*-chemiluminescence images making use of the axisymmetric intensity distribution. The captured signal is proportionally associated to the heat release of a perfectly premixed flame. However, at partially premixed conditions the equivalence ratio fluctuations affect the light emission and consequently the measurements cannot be

used as a quantitative measure anymore. In order to select light emitted from excited radicals, the PMT is equipped with a multi channel optical fiber with several bandpass filters centered at 308 nm (OH^*), 407 nm (CO^*), 431 nm (CH^*) and 515 nm (C_2^*).

The two components of the velocity field in the stream wise plane aligned with the combustor axis was measured using high-speed Particle Image Velocimetry (PIV). The PIV system consists of a dual cavity diode pumped ND:YLF laser and a high-speed CMOS camera. The camera is able to operate in full frame mode ($1024 \text{ px} \times 1024 \text{ px}$) up to 5400 fps but the PIV system was used between 1000 and 1500 fps to increase the measurement time for each operation point. The OH^* -chemiluminescence imaging operated at a frequency between 1 and 1.5 kHz, too. A light sheet optic formed a laser sheet with a thickness of approximately 1 mm and the beam waist was located slightly beyond the measurement area. The time delay between the pulses was in the range of $30 \mu\text{s}$ and it was adjusted with respect to the maximum velocity in the measurement domain. The strong out-of-plane velocity component associated with swirling flows but also the very high acoustic velocity amplitudes at the Helmholtz resonator neck requires rather short pulse separations in order to minimize lost particle pairs. For the flame response measurements Zirconium Dioxide particles of a nominal diameter of $2 \mu\text{m}$ were seeded into the flow upstream of the swirl generator using a brush based powder disperser to ensure a homogeneous particle distribution without agglomerations. The Helmholtz resonator measurements were conducted with silicon oil droplets (DEHS) of $1 \mu\text{m}$ diameter. Reflections of the incoming laser light at the silica glass were minimized by using beam dumps for the sheet and primary reflections and by sandblasting parts of the silica glass. This procedure is not necessary for the PMMA (Plexiglas) tube used for the Helmholtz resonator investigations since the laser sheet entered the resonator through the back end of the resonator. Here, joints between the single tubes (main tube, resonator neck and volume) obstructed the optical access in these regions. The images were post-processed with a final interrogation area of $16 \text{ px} \times 16 \text{ px}$; with an interrogation window overlap of 50%, this resulted in a spatial resolution of 1.8 mm. The data were filtered for outliers and interpolated from adjacent interrogation areas. Based on the uncertainty of the correlation peak-finding algorithm of 0.1 px, the random uncertainty of the instantaneous velocities is estimated as 0.35 m/s to 1.14 m/s, depending on the pulse separation. This error, which is approximately 5% of the maximum velocity in the neck of the Helmholtz resonator ($|\hat{u} + \bar{u}|$), contributes mostly to the RMS error. The RMS error is for the flame response measurements of a similar amplitude.

During the measurements, over a time span of 15 s, the forcing amplitude was increased in 15 steps from very low to the maximum forcing amplitude. At every amplitude approximately 1000 instantaneous velocity and OH^* -chemiluminescence distributions were acquired.

Distributions of the density inside the Helmholtz resonator were estimated using the Quantitative Light Sheet (QLS) technique. The mixing between seeded air and air without particles is measured. In the next step, the density distribution is estimated based on these concentration measurements. The QLS technique is mainly used as an alternative to Laser Induced Fluorescence (LIF) measurements for mixing experiments [43]. The big advantage of the QLS technique is the simplicity of the set-up compared to Rayleigh or Raman scattering based techniques. Furthermore, the experimental set-up is almost identical to the PIV set-up, making it very convenient to be used simultaneously. In the present set-up only the grazing flow was seeded. Thus the amount of seeding particles can be taken as a surrogate measurement for the mixing of grazing and purging flow. As proposed by Findeisen et al. [43], the measured light intensity for the background light, the dark current, and the inhomogeneous light sheet intensity are corrected with a simplified mode. The correction consists of the subtraction of reference images J_0 at a known homogeneous particle concentration C_h from the raw images J . With the known homogeneous particle concentration C_h , the particle concentration distribution C can be calculated:

$$\frac{C}{C_h} = \frac{J - J_0}{J_h - J_0}. \quad (2.15)$$

Assuming that the mixing behaves qualitatively similar to the normalized temperature difference of the purging cross flow ϑ_{pf} to the grazing flow ϑ_{gf} , the temperature field is estimated from the particle density distribution:

$$\frac{\vartheta - \vartheta_{pf}}{\vartheta_{gf} - \vartheta_{pf}} = \frac{C}{C_h}. \quad (2.16)$$

This correlation allows for a qualitative assessment of the density field at the resonator entrance and in the resonator using the QLS measurement technique.

Chapter 3

Flame Response Saturation

Nicht die Wahrheit, in deren Besitz irgendein Mensch ist oder zu sein vermeinet, sondern die aufrichtige Mühe, die er angewandt hat, hinter die Wahrheit zu kommen, macht den Wert des Menschen. Denn nicht durch den Besitz, sondern durch die Nachforschung der Wahrheit erweitern sich seine Kräfte, worin allein seine immer wachsende Vollkommenheit besteht.

Gotthold Ephraim Lessing, Suche nach der Wahrheit

¹ The nonlinear flame response to equivalence ratio fluctuations and velocity perturbations, which accounts for the dependence of gain and phase on the acoustic velocity amplitude level was first of all investigated experimentally by Lieuwen and Neumeier [79]. It was found that the flame describing function decreases at large amplitudes of acoustic forcing. The gain saturation plays an important role in the establishment of a limit cycle amplitude of a linearly unstable flame-combustor system. Contrary to that, the role of the phase response is less clear. Generally, a change of the phase response may saturate the energy transfer to the acoustic field or even increase it.

Recent studies [21, 71, 93, 98] have proven that flame describing functions can be used to accurately predict the limit-cycle amplitude for various practical combustion systems and up to now, there are several approaches to model specific nonlinearities.

Dowling [37] was one of the first, who accounted for the amplitude dependency of the flame response analytically, by incorporating a flame describing function into an analytical model to determine the limit-cycle amplitude. She postulated that the total heat release rate oscillation obviously cannot become negative, and thus, saturates at oscillation amplitudes of 100% in a symmetric manner. However, the measurements conducted within this thesis have shown that heat release rate oscillations with a fundamental amplitude of more than 100% of the mean can

¹The work presented in this chapter is based on two journal publications [133] and [32]. The PIV measurements and the post processing were conducted together with Steffen Terhaar. He mainly contributed to the final presentation of the PIV and OH*-chemiluminescence camera results shown in the figures of this chapter. Jonas Moeck mainly contributed to the idea of an increased mixing of temporal mixture inhomogeneities at large acoustic pressure amplitudes. Paragraphs and phrases of this chapter are very similar or identical to text paragraphs published in [32]. These excerpts are written by me.

be observed. The corresponding flame describing function gain and time signal measurements are illustrated in Figure 3.1. This is possible because the heat release rate oscillation waveform is highly asymmetric.

Similarly to Dowling, Peracchio and Proscia [102] modeled a nonlinearity based on the consideration of the lower limit of the global equivalence ratio oscillation amplitude. They assumed that the integral equivalence ratio perturbations can never be lower than the lean extinction level of the steady flame. Both studies compared the empirical based analytical approaches to measurement results and achieved reasonable accuracy. In contrast to that, Keller [62] hypothesized that the dominant nonlinearity for technically premixed flames is the saturation of the heat of reaction oscillation amplitude at strong fuel-air ratio perturbations.

The three assumed saturation mechanisms were investigated and partly confirmed for laminar flames by Shreekrishna et al. [126] in a theoretical study of a laminar flame subject to massive fuel-air ratio variations. In this study, the nonlinear relation of the burning velocity and equivalence ratio as well as the heat of reaction dependence is coupled with a G -equation description, representing the flame surface dynamics. The findings of this theoretical study suggest that the flame response saturates due to stoichiometric and flammability crossover, kinematic restoration, and the nonlinear relationship between burning velocity and equivalence ratio. Kinematic restoration is the property of the flame kinematics to smooth locally and thereby saturate the flame surface growth [50, 104]. Probably, this mechanism was also observed in a numerical LES study of a turbulent technically premixed swirl flame, where Krediet et al. [72]

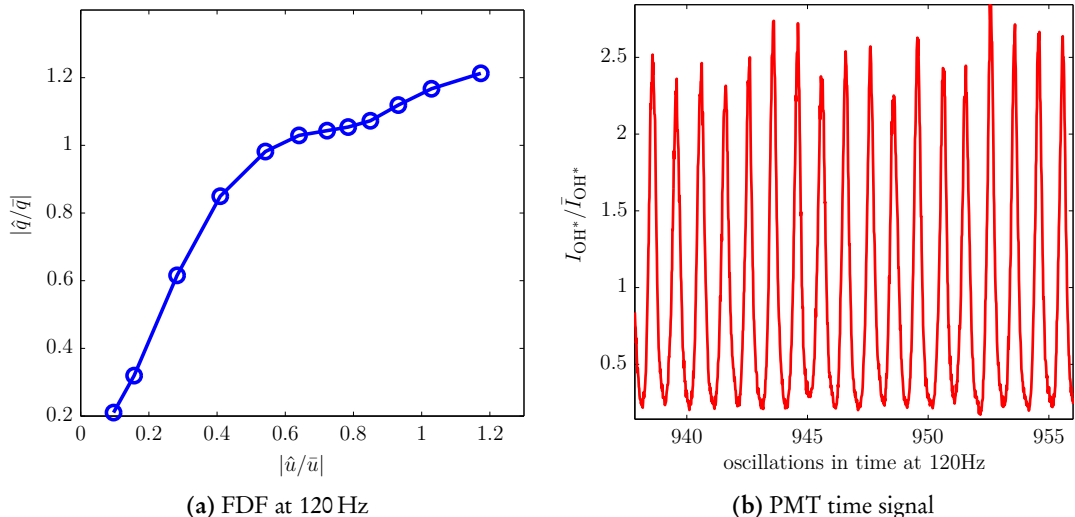


Figure 3.1: (a) Flame describing function measurement with MMM at 120 Hz for a technically premixed flame. (b) Corresponding OH^* chemiluminescence time signal for an amplitude of $|\hat{u}/\bar{u}| = 1.2$.

compared their numerically obtained flame describing function to experiments conducted by Schimek et al. [117]. From the experimentalist's point of view, Schimek et al. concluded that partial extinction of the technically premixed swirl flame at high oscillation amplitudes is the dominant saturation mechanism. It was observed with phase-averaged Abel-inverted chemiluminescence images that the flame locally extinguishes and the mean flame position varies significantly during one cycle of the high-amplitude acoustic pressure oscillations. Kim and coworkers experimentally investigated in a series of works [64, 66, 67] the amplitude-dependent flame response of turbulent technically premixed flames. The importance of the vortex-flame interaction and the degree of premixedness is underlined and the flame response is characterized for different flame shapes. Local extinction at high forcing amplitudes was observed. Additionally, periodic flame flash back was identified as a possible saturation mechanism. They also utilized the two-input-single-output approach of Huber and Polifke [55, 56] to emphasize the importance of the phase between equivalence ratio fluctuations and velocity oscillations.

Although saturation mechanisms associated with equivalence ratio fluctuations are often assumed to be dominant in practical combustors, velocity perturbations are an important excitation mechanism and, hence, also nonlinearities associated with them have to be considered. Besides the kinematic restoration of the flame surface, the flame response saturation can also be caused by a saturation of the energy transfer between hydrodynamic field and the velocity perturbations. For instance, Keller [62] assumed that if the flame is excited by coherent vortex shedding, the limitation of the vortex growth [96] is the main saturation effect. Oberleithner et al. [94, 95] investigated experimentally and analytically the connection between the amplification of vortices by shear layers and the flame describing function of a perfectly premixed swirl flame. Very good qualitative agreement was found between frequency dependent growth rates of coherent structures, obtained by a hydrodynamic stability analysis, and flame response measurements. This saturation can be understood in terms of the mean field theory, where the growth of hydrodynamic modes is limited by strong changes in the mean flow field [92], which are induced by the dynamic modes itself. This behavior is also observed by Oberleithner et al. [95]. Observations reported by Bellows et al. [7, 8], Balachandran et al. [4] and especially Thumuluru and Lieuwen [135] can also be interpreted in line with this concept. All three studies reported a full or intermittent saturation of the flame response associated with strong changes in the flame shape. Whereby, the smooth changes of the mean flame shape may likely be caused by mean flow changes and the drastic changes of the flame shape, like detachment of the flame, will always introduce a mean flow field change, too.

Besides the saturation of the vortical structures, strong changes of the flame shape and structure affect the flame response. Thumuluru and Lieuwen [135] emphasized that not only changes of the time-averaged flame shape at high forcing amplitudes but also the evolution of the flame

shape over one oscillation cycle is important. Since flames with differences in the flame shape show strongly differing flame responses even in the linear regime [3], it seems evident that strong changes in the flame shape and flame position are an important saturation mechanism. Nevertheless, Balachandran et al. [4] offer a different explanation for their observations. Local annihilation of the flame was observed with the help of OH-PLIF snap-shots. They argued that the vortical structures cause the flame annihilation, which saturates the flame surface growth.

Swirl fluctuations [52, 70, 97] may also introduce saturation effects to the flame response. The type of interference between the longitudinal acoustic waves and the perturbations in the azimuthal velocity can change with the acoustic amplitude because the advection velocity of the vorticity waves is affected by the forcing.

Generally, a burner-flame arrangement may exhibit all of the effects described above and additional not yet discovered saturation mechanisms. The specific occurrence and interaction between the mechanisms depend on the particular setup and the operating conditions. Despite the enormous work on phenomena related to the nonlinear flame response, no holistic investigation of the interaction between equivalence ratio perturbations and velocity oscillations is known to the author. The focus of this chapter lies therefore on the linear and nonlinear interaction between velocity perturbations and equivalence ratio fluctuations and their respective saturation processes. For the first time, the nonlinear response of practically relevant swirl flames is investigated by well-defined variations of the degree of unmixedness. Additionally, the connection between vortical structures and the nonlinear flame response is examined with well controlled changes of the swirl number. High-speed particle image velocimetry was used to measure the flow field of the perfectly and technically premixed flame. A fast-response valve was used to manipulate the amplitude of the equivalence ratio fluctuations specifically, without a change in the fuel split and the associated changes of the unforced flame and flow field. Open-loop control is applied to illustrate the nonlinear interaction between different frequencies. For the first time, an amplitude-dependent decomposition of the impact of velocity perturbations and equivalence ratio oscillations is performed for a turbulent swirl flame. Based on the experimental observations an explanation is presented for the presence of saturation mechanisms, which were previously not reported and are revealed by the analysis of the resulting transfer functions.

The remainder of this chapter is structured as follows. First, the theoretical background is explained. The concept of the flame describing function decomposition is briefly introduced and new saturation mechanisms are explained. Subsequently, the connection between the coherent velocity fluctuation intensity and the flame response nonlinearity is illuminated. The similarity of the time-averaged and phase-averaged flow fields between technically premixed and perfectly premixed flames is discussed and based on this discussion the decomposition of the

flame describing function is applied. Finally, the role of the equivalence ratio oscillations for the saturation of the flame response is discussed and the impact of artificially increased equivalence ratio fluctuations is presented.

3.1 Decomposition of Excitation Mechanisms

The concept of a multi-input-single-output flame transfer function was first introduced by Huber and Polifke [55, 56]. They applied the concept to RANS simulation data of a technically premixed flame. Reducing the approach to two inputs, the equivalence ratio perturbations and the velocity oscillations, a heat release rate relation for small amplitudes can be formulated in frequency domain as follows:

$$\frac{\hat{q}}{\bar{q}} = \mathcal{F}_u(\omega) \frac{\hat{u}}{\bar{u}} + \mathcal{G}_\varphi(\omega) \frac{\hat{\varphi}}{\bar{\varphi}}, \quad (3.1)$$

where hats and overbars denote Fourier transformed and mean quantities, respectively, and ω is the Fourier transform variable (angular frequency). In this relation all excitation mechanisms present in the system without equivalence ratio perturbations are represented by \mathcal{F}_u . All mechanisms generating unsteady heat release rate at the flame associated with equivalence ratio fluctuations $\hat{\varphi}$ at the fuel injector are represented by \mathcal{G}_φ .

By assuming a stiff injector and that the distance between fuel injector and burner nozzle can be considered compact (i.e., it is much shorter than the acoustic wavelength), the transfer function \mathcal{G}_φ and the transfer function between velocity and equivalence ratio fluctuations can be lumped in a single transfer function \mathcal{F}_φ . Both assumptions are justified for the investigated set-up. Hereby, the model is reduced to a single-input-single-output model, where the heat release rate relation is written with only the velocity oscillation as input. At finite oscillation levels, the linear transfer function concept is extended to a describing function that parametrically takes into account the variation of gain and phase response with input oscillation amplitude $|\hat{u}/\bar{u}|$:

$$\frac{\hat{q}}{\bar{q}} = \left[\mathcal{F}_u(\omega, |\hat{u}/\bar{u}|) + \mathcal{F}_\varphi(\omega, |\hat{u}/\bar{u}|) \right] \frac{\hat{u}}{\bar{u}} \quad (3.2)$$

The amplitude dependence of the individual mechanisms originating from velocity and equivalence ratio fluctuations is taken into account in the two describing functions \mathcal{F}_u and \mathcal{F}_φ . Here, it is assumed that these mechanisms do not interact at finite oscillation amplitudes so that the total unsteady heat release rate response can still be written as a superposition of the two. This is a strong assumption that will be critically assessed in Section 3.4 based on the experimental results.

Thus, given the total describing function for unsteady heat release rate

$$\mathcal{F}(\omega, |\hat{u}/\bar{u}|) = \frac{\hat{q}/\bar{q}}{\hat{u}/\bar{u}}, \quad (3.3)$$

and the describing function for the velocity oscillation induced response \mathcal{F}_u , the equivalence ratio describing function can be obtained from

$$\mathcal{F}_\varphi = \mathcal{F} - \mathcal{F}_u. \quad (3.4)$$

In the proper meaning of this relation, the contribution of the equivalence ratio fluctuations to the flame response can be decomposed by the subtraction of the premixed and the technically premixed flame transfer function. However, as pointed out above, this decomposition is only valid if the two contributions do not interact nonlinearly. Especially at higher perturbation levels, this effect may generally be present in the system, which means that the two describing function contributions are functions of both equivalence ratio perturbations and velocity oscillations. For instance, Birbaud et al. [13] and later Hemchandra [49] showed in numerical studies of elementary geometries that pure equivalence ratio fluctuations cause flame surface area fluctuations. Birbaud et al. have also shown that velocity perturbations upstream of the flame can result from this effect. Hence, adding fuel-air ratio perturbations to a perfectly premixed flame may change the flame surface kinematics and also the mean flow field and mean flame shape. Consequently, the decomposition approach is only admissible at finite amplitude if these effects are negligible.

In the present study, the degree of unmixedness is increased gradually from perfectly premixed to 100% technically premixed, which is reached when all of the fuel is injected inside the burner. To distinguish between the different combustion modes, the fuel-split ratio parameter ε is introduced, which is defined as

$$\varepsilon = \frac{\text{fuel mass flow injected in the burner}}{\text{total fuel mass flow}}. \quad (3.5)$$

In addition to the above mentioned assumptions, it is assumed that the impact of mixture inhomogeneities scales linearly with the fuel split. Consequently, Eqn. (3.4) can be rewritten as $\mathcal{F} = \mathcal{F}_u + \varepsilon \mathcal{F}_\varphi$, and the equivalence ratio contribution is obtained from

$$\mathcal{F}_\varphi = \frac{\mathcal{F} - \mathcal{F}_u}{\varepsilon}. \quad (3.6)$$

3.2 Assessment of Hydrodynamic Similarity and Vortical Growth

High speed PIV and OH*-chemiluminescence measurements were conducted to assess the possible impact of the equivalence ratio oscillations on the flow field and flame dynamics as well as on the mean flow field and on the flame shape. Additionally, the effects of a change of the swirl number on the perfectly premixed flame were assessed. The measurements were carried out for perfectly and technically premixed conditions for several frequencies and the full range of the investigated forcing amplitudes.

The similarity of the turbulence level, the position and strength of the coherent vorticity, and the mean flow field, were assessed with the triple decomposition ansatz [57]. The time and space dependent flow field $\mathbf{v}(\mathbf{x}, t)$ is decomposed into a time-averaged part $\bar{\mathbf{v}}(\mathbf{x})$, coherent fluctuations $\mathbf{v}^c(\mathbf{x}, t)$, and stochastic fluctuations $\mathbf{v}^s(\mathbf{x}, t)$:

$$\mathbf{v}(\mathbf{x}, t) = \bar{\mathbf{v}}(\mathbf{x}) + \mathbf{v}^c(\mathbf{x}, t) + \mathbf{v}^s(\mathbf{x}, t). \quad (3.7)$$

The coherent fluctuations are obtained from the measured velocity fields by applying a phase average with respect to the oscillation cycle. This removes the stochastic fluctuations, which are uncorrelated with the forcing signal. Subsequent subtraction of the temporal mean yields the coherent fluctuation field.

Acoustic fluctuations cause velocity fluctuations, for instance, at the area jump of the combustor inlet. Consequently, vortical structures are generated in the shear layers and can be further amplified or attenuated. In the case of the formation of large scale vortical structures, the flame response of perfectly premixed flames is often dominated by the interaction with these structures. Hence, depending on the receptivity of the shear layers, velocity perturbations induced by acoustic velocity oscillations are amplified in the shear layers. The vortical structures are advected downstream and interact with the flame, which fluctuates due to the modulation of the local flame surface area and the mass flow through the flame surface. From a general point of view, this mechanism can saturate due to the saturation of the vortical growth rate or due to a decreased receptivity of the flame to local vorticity fluctuations, for instance caused by a different flame anchoring point or a change of the flame shape.

To assess the strength of the vortices quantitatively the coherent fluctuation intensity is calculated for every point in the measured flow field plane. It can be integrated along the radial profiles r for all axial positions x and normalized with the respective volume flow at the combustor inlet \dot{V} :

$$K(x) = \frac{1}{\dot{V}_{\text{bulk}}} \int_0^{D_{cc}/2} \sqrt{0.5(v_x^c(x, r)^2 + v_y^c(x, r)^2)} 2\pi r \partial r, \quad (3.8)$$

where D_{cc} , v_x^c , and v_y^c denote the diameter of the combustion chamber, the local velocity coherent oscillation amplitudes of the axial and transverse velocity components in the streamwise plane as captured by the PIV measurements, respectively.

For high Reynolds number flows, such as investigated in this thesis, the main source of momentum exchange are the turbulent shear stresses. Thus, the molecular transport of scalars in the field is driven by the off-diagonal Reynolds-stresses. An increase of the normalized shear stresses, like $\tau_\Omega = \rho(\overline{v_x^s v_y^s})/\bar{u}_{\text{bulk}}^2$, is a clear indicator for an increased turbulent diffusion of fuel and air in the premixed zone. Hence, to assess the general influence of acoustic forcing on the mixing the integral quantity T is used:

$$T = \frac{\rho}{V_{cc} \bar{u}_{\text{bulk}}^2} \int \overline{v_x^s(x, r) v_y^s(x, r)} 2\pi r dA, \quad (3.9)$$

where the integration is performed over one half of the measurement domain in the flame area and the premixed zone, as indicated by the OH* field measurements. Another indicator for increased mixing is the turbulence intensity $\omega_\Omega = \sqrt{(v_x^s)_{\text{rms}}^2 + (v_y^s)_{\text{rms}}^2}/\bar{u}_{\text{bulk}}$ because it indicates the level of turbulence in the flow. A flow with an increased turbulence level will generally feature also a better mixing. It is assessed by integration over the measurement domain:

$$\Omega = \frac{1}{D_{cc} \dot{V}_{\text{bulk}}} \int \sqrt{(v_x^s(x, r)_{\text{rms}}^2 + v_y^s(x, r)_{\text{rms}}^2)} 2\pi r dA \quad (3.10)$$

where summation is performed over one half of the measurement domain in the flame area and the premixed zone, as indicated by the OH* field measurements. \dot{V}_{bulk} is the bulk volume flow in the mixing tube.

3.3 Velocity Fluctuation Based Saturation Mechanisms

In the absence of mixing inhomogeneities, velocity fluctuations induced by coherent structures or swirl number perturbations are besides the kinematic movement of the flame the most important mechanisms which convert acoustic fluctuations into heat release fluctuations. Generally, the kinematic movement of the flame plays an important role for laminar flame but is less important for swirl stabilized turbulent flames.

The role of coherent structures is important for the investigated burner–flame arrangement. Oberleithner et al. [94] have shown that the amplification of coherent structures in the shear layers and the respective saturation of this amplification process due to mean field changes is connected to the nonlinear flame response of the perfectly premixed flame. This general concept is investigated further in this section.

Three perfectly premixed operation points are investigated, which can be differentiated by the swirl number only. The flame is acoustically forced at 196 Hz for all three swirl numbers and the flame response shows three different characteristic saturation behaviors. First of all, the time-averaged flow field of the flame and the corresponding heat release is discussed for all three swirl numbers and four acoustic velocity amplitudes. Additionally, an isothermal flow field is shown at a swirl number of 0.8, to emphasize that the observed changes of the mean fields are caused by a complex flame–flow-field interaction.

Figure 3.2 depicts the corresponding measurement results, obtained with high-speed PIV and OH*-chemiluminescence cameras. The rows correspond to the investigated swirl numbers and the columns correspond to acoustic forcing amplitudes, increasing from left to right. The attributes of a typical swirl stabilized flame [134] are present in all flow fields. Firstly, a stable vortex breakdown featuring shear layers between the large inner recirculation zone and the jet can be observed for all investigated operation conditions. Especially the shear layers are of great interest, since they play an important role for the stream wise growth of vortical structures. In the absence of strong acoustic velocity fluctuations the flame stabilizes for all swirl numbers along the inner shear layer between the jet and the inner recirculation zone, showing a typical V-shape [134]. However, combustion leads to a broader inner recirculation zone and very uniform backflow velocities and consequently the isothermal flow field is significantly different to the reacting flow fields. Evidently, the effect of acoustic perturbations is relatively small on the mean flow field without the interaction of the flame and the flow field, underlining the importance of investigations at reacting conditions.

All three reacting cases show a similar trend with increasing forcing amplitude. However, due to the difference in the swirl number the steady jet opening angle without forcing is different. Accordingly, very similar changes of the mean flow field were observed between, e.g., the operation point with the highest and lowest swirl number. However, the case with the higher swirl number has an offset in terms of the jet opening angle and reaches similar states at higher forcing amplitudes than the low swirl number case.

The opening angle of the jet is decreased with increasing acoustic velocity amplitude. The heat release starts to concentrate behind the center body, forming a trumpet-like flame [134]. Higher acoustic velocity amplitudes lead even to detachment of the flame for the lowest swirl

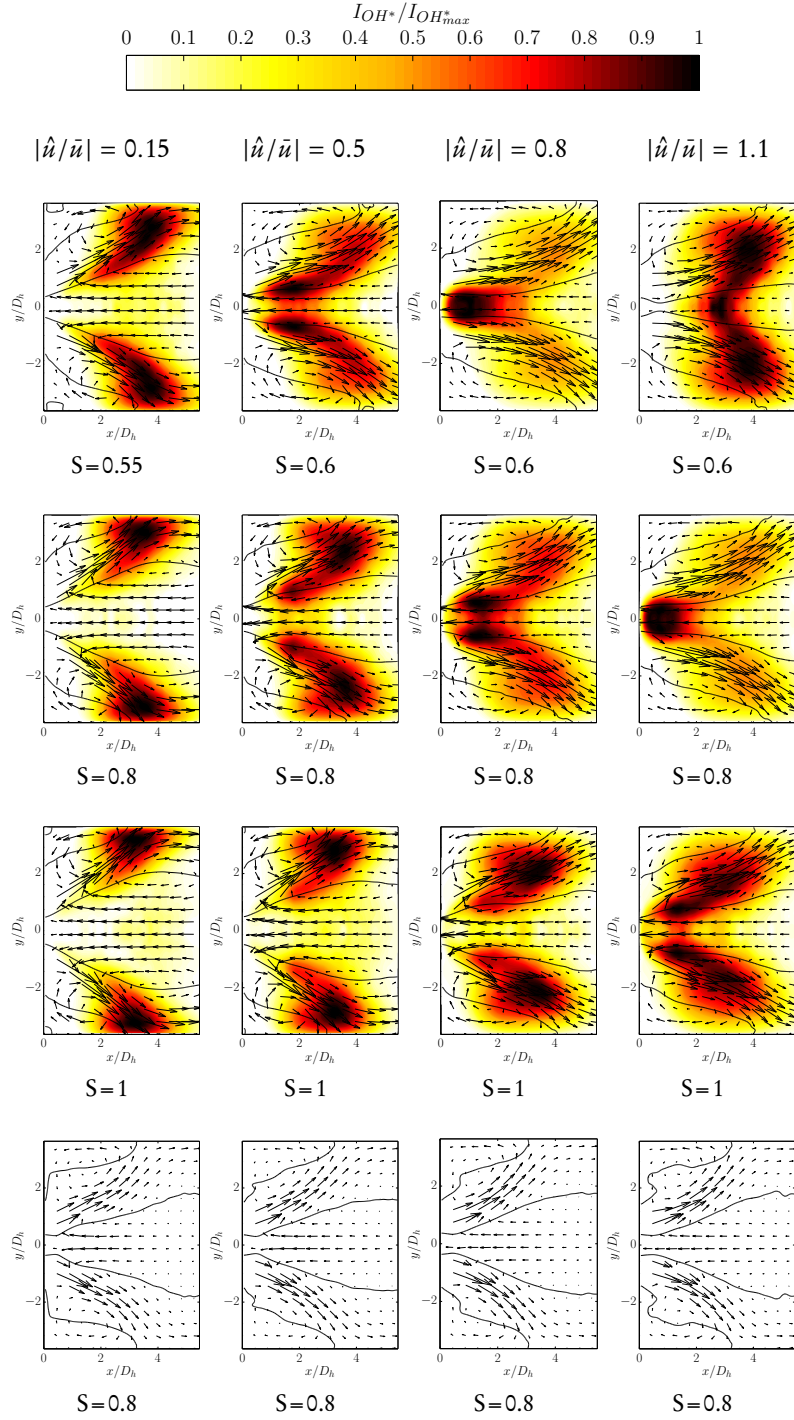


Figure 3.2: Mean flow field and mean chemiluminescence distribution for various amplitudes for the perfectly premixed flame and three swirl numbers. Forcing amplitude at 196 Hz is increasing from left to right. Color denotes chemiluminescence intensity and solid lines depict zero velocity. Arrows illustrate flow direction and relative velocity magnitude. Last line illustrates cold flow.

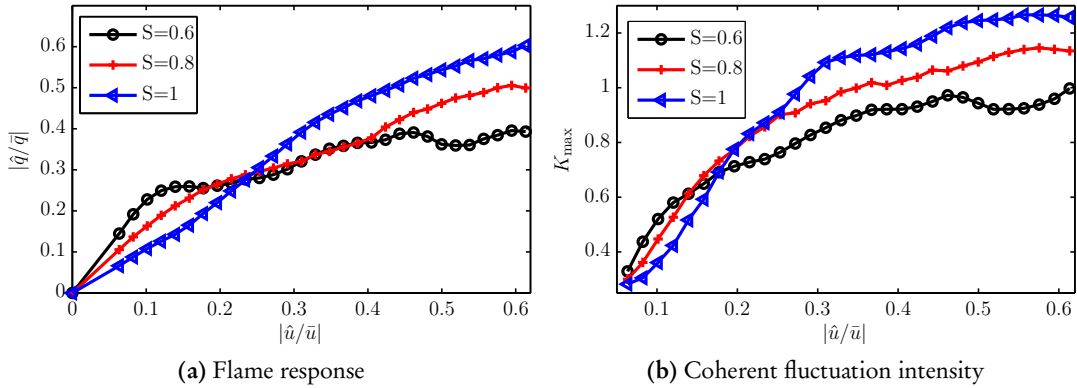


Figure 3.3: Flame response and coherent fluctuation intensity at 196 Hz for various amplitudes and three swirl numbers.

number. This detachment alters the flame response significantly, which is an important nonlinear saturation mechanism of the flame response. It is very likely, that a detachment will also happen to the other flames, if the forcing amplitude is further increased. This assumption is supported by the resemblance of the mean flame shape as well as the flow field for the different swirl numbers at different amplitudes. For instance, the measurement at a swirl number of 0.6 and a forcing amplitude of $|\hat{u}/\bar{u}| = 0.8$ shows very similar results to the measurement at $S = 0.8$ and a amplitude of $|\hat{u}/\bar{u}| = 1.1$.

In contrast to the averaged flow field and flame measurements, which are analyzed here, the flow field dynamics are analyzed at a similar operation point later in Section 3.4.1. There the dynamics between perfectly premixed and technically premixed conditions are compared, too.

The normalized heat release fluctuations associated with the discussed flow field measurements are depicted in Figure 3.3a. The three responses show noticeable nonlinearities at higher forcing amplitudes. However, the three swirl numbers are differentiated by the qualitative trend of the amplitude dependency. The lowest swirl number ($S = 0.6$) features the highest linear gain but saturates relatively early at an acoustic velocity amplitude of $|\hat{u}/\bar{u}| = 0.1$. In contrast to that, the highest swirl number case ($S = 1$) has the lowest linear flame transfer function gain but responds with the strongest heat release fluctuations at high amplitudes. The flame response of the $S = 0.8$ operation point features an intermediate saturation and a trend of the flame response, which is always in between the other two swirl number cases.

The associated maximum coherent fluctuation intensity K_{\max} measured in the flame and premixed area is depicted in Figure 3.3b. It is a measure for the strength of the vortices, which are amplified by the shear layers and interact with the flame. This interaction is later discussed and visualized in detail in the Figures 3.7 and 3.6. Evidently, this quantity features the same qualitative trends that are captured by the heat release oscillation measurements for all three swirl

numbers. Moreover, the proportions between the different cases are captured, too. Although being no strict evidence or proof for the causal connection between saturating growth of the coherent structure and the saturation of the flame response, the resemblance of the quantities indicates a strong connection. The connection between hydrodynamic coherent structures and the flame response, established in previous works, is emphasized and validated by the presented results.

3.4 Equivalence Ratio Fluctuation Based Saturation Mechanisms

The two excitation mechanisms mixing inhomogeneities and velocity oscillations can interfere constructively and destructively, and the interaction depends on the phase relation between the two mechanisms. This affects already the linear gain of the flame describing function and consequently the onset of the self-excited linear instability. If the initiation of the saturation is at a constant amplitude, a decreased linear gain affects the limit-cycle amplitude, too. Kim et al. [68] and Krebs et al. [71] have shown this to some extend experimentally and numerically, respectively. Here, these findings are extended to specific nonlinear aspects not considered previously. For example, changes in the mean flame shape and strong movements of the flame over the oscillation cycle will obviously affect the time delay distribution in the flame and thereby influence the phase relation at higher amplitudes between the heat release fluctuation caused by vortex shedding and equivalence ratio perturbations. Consequently, the flame describing function gain will saturate if the interference turns from constructive to destructive. In principle, the gain may also increase at higher amplitudes through this effect, promoting nonlinear instabilities.

The second new saturation mechanism, which is based on temporal changes of the equivalence ratio, is the increased mixing of fuel and air and the associated damping of equivalence ratio fluctuations at high acoustic velocity amplitudes. Potentially, certain mechanisms improve the temporal mixing of fuel and air at elevated forcing amplitudes. First of all, acoustic energy is converted into coherent and stochastic vortices in the burner and at the area jump from the mixing tube to the combustor, resulting in mean pressure losses and the attenuation of acoustic waves [120]. The generated coherent vortices can be amplified by the shear layers over a finite axial extent and their respective contribution to an enhanced mixing is very combustor and flame specific ; but, eventually the energy is transferred to the smaller scales, which are always associated with turbulent mixing. Ginevsky et al. [45] showed that acoustic excitation can intensify mixing in non-swirled, non-reacting conditions due to the elevated level of turbulence and it is likely that this effect is even more pronounced in a swirling flow field. It is also well known that coherent structures can directly affect the mixing of fuel and air in the

combustor [99]. Also findings by Eroglu and Breidenthal [42], who investigated the interaction of coherent structures of a pulsed jet in cross flow, indicate an enhanced mixing caused by coherent vortex shedding. They revealed that the interaction of neighboring vortex rings strongly increases mixing. It is to be expected that these mechanisms are more pronounced at higher frequencies due to shorter wavelengths and thus higher concentrations gradients. Additionally, the large periodic displacement of the flame and the corresponding changes in mean flame shape and flow field in the nonlinear regime will always have an impact on the mixing properties of the flow field.

In the following, the general principle of the saturation effect caused by increased mixing, is illustrated with the help of simple flame model. The heat release rate is written as

$$q = \rho s_\Omega \Delta h S_f, \quad (3.11)$$

where ρ , s_Ω , Δh and S_f denote density, turbulent burning velocity, the heat release per unit mass of mixture, and the flame surface area, respectively. Additionally, it is assumed that the quantities are constant over the flame surface. The turbulent flame speed s_Ω is modeled by a simple relation between turbulence intensity and laminar flame speed:

$$s_\Omega = s_L [1 + C(u_{\text{rms}}/s_L)^n]. \quad (3.12)$$

The variables C and n are model constants and u_{rms} represents the turbulent velocity fluctuation upstream of the flame. The values [83] $C = 1.25$ and $n = 0.7$ were used and a velocity fluctuation of $u_{\text{rms}} = 0.2 \text{ m/s}$ was chosen. Increasing turbulence intensity causes a saturation of the flame response due to this nonlinear relation between the turbulent burning velocity and the velocity fluctuation. However, the effect is relatively weak and is not suitable to explain the experimental observations of this study. Hence, a constant value is chosen for u_{rms} . The laminar flame speed s_L is calculated from the equivalence ratio with the relation given by Abu-Orf and Cant [1]:

$$s_L = k \varphi^b \exp(-c(\varphi - d)^2). \quad (3.13)$$

Here, k , b , c , and d are empirical constants determined to match the available experimental data. The dependence of the heat of reaction Δh on the equivalence ratio is given by [78]:

$$\Delta h = \frac{2.9125 \times 10^6 \min(\varphi, 1)}{1 + 0.05825\varphi} \left(\frac{J}{kg} \right). \quad (3.14)$$

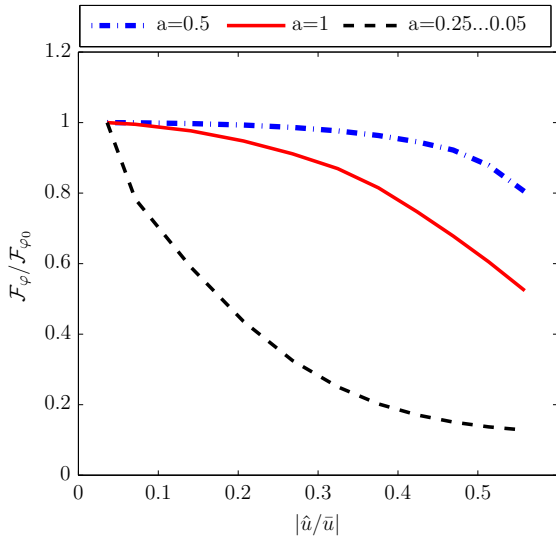


Figure 3.4: Normalized flame describing function model results for three different equivalence ratio oscillation attenuation factors. Two constant attenuation factors (1 and 0.5) and one decaying exponentially from 0.25 to 0.05. Flame describing function gain normalized with linear gain.

For a stiff fuel injector, the following relation between equivalence ratio fluctuations and velocity oscillations is valid in time domain:

$$\frac{\varphi}{\bar{\varphi}} = \frac{\alpha}{\left(1 + \frac{u'}{\bar{u}}\right)}, \quad (3.15)$$

which is obtained from the assumption that the fuel mass flow is constant. Dashes denote perturbations in time domain, which are not necessarily assumed to be small. A very similar version of this relation, was introduced by Peracchio and Proscia [102] and further investigated by Lieuwen et al. [81]. It is based on the assumption that fuel and air are instantaneously mixed at the fuel injector.

The formation of equivalence ratio perturbations is modeled by Equation (3.15). Turbulent and diffusive mixing attenuates the amplitude of the equivalence ratio oscillations before they reach the flame. This effect is taken into account by the attenuation factor α used in Equation (3.15). The governing variables of this turbulent mixing process are the turbulent diffusion coefficient and the individual mixing distance of the fluid particle. Especially the turbulent diffusion coefficient should be understood as a conceptional variable, which helps to handle the turbulent mixing similar to the diffusional mixing. It is connected to the turbulent shear stresses [107]. The damping of temporal equivalence ratio perturbations was recently investigated in a related study at operating conditions similar to the currently investigated ones [14]. It was found that the attenuation between fuel injector and flame of the amplitude of the equivalence ratio oscillations varies between 60% and 70% of the amplitude, increasing monotonically between 100 Hz and 200 Hz.

Figure 3.4 depicts the flame describing function of the presented analytical model. The

transfer function gain normalized with the linear gain is shown for various acoustic forcing amplitudes. Three cases are considered: one without mixing effects ($a=1$), one with a constant attenuation coefficient of 50% ($a=0.5$) and the last case illustrates the newly proposed saturation mechanism with a variable attenuation factor decreasing exponentially from $a=0.25$ to 0.05, defined by $a = 0.027(|\hat{u}/\bar{u}|)^{-0.7}$ for $|\hat{u}/\bar{u}| > 0.04$. The flame describing function obtained from the simple model with a constant attenuation coefficient of 50% starts to saturate for amplitudes higher than $|\hat{u}/\bar{u}| = 0.3$, while the case with increasing damping of equivalence ratio fluctuations saturates immediately and much stronger. The third scenario without turbulent mixing ($a=1$) is qualitatively similar to the case with a constant attenuation of 50% of the equivalence ratio oscillation amplitude but starts to saturate earlier; however, the saturation is much weaker compared to the simulation with an increasing attenuation coefficient. Neglecting turbulent temporal mixing of equivalence ratio perturbations is unrealistic for technical turbulent flames. Consequently, the case with a constant attenuation factor of $a=0.5$ represents the current understanding of saturation effects introduced by equivalence ratio fluctuations. It suggests that chemical effects will saturate the flame response at higher amplitudes. In contrast to that, the experiments conducted on this study suggest that the saturation of technically premixed flames sets in at low amplitudes. As shown with the results in Figure 3.4, this observation can be explained with an increased mixing of equivalence ratio fluctuations at higher acoustic amplitudes.

3.4.1 Flow-Field–Flame Interaction Technically Premixed Flame

In order to justify the decomposition ansatz and to further investigate the mechanisms causing the saturation of the technically premixed flame response, the flow field and flame dynamics shown in Figures 3.5, 3.6 and 3.7 are analyzed. Here, only the results for one frequency are presented, but they are representative for other forcing frequencies at these operating conditions.

Figure 3.5 depicts the time-averaged flow field and the mean chemiluminescence distribution at 110 Hz for the perfectly premixed and technically premixed flame with a fuel split ratio of $\varepsilon = 1$. The color intensity represents the Abel-inverted OH*-chemiluminescence intensity of the flame. The arrows denote the mean flow field, and the solid black lines indicate zero axial velocity. The center of gravity of the heat release rate distribution is indicated by a small cross. The coordinates of the center of gravity, (x_c, y_c) , are calculated as

$$x_c = \frac{\sum_{i,j} x_{ij} y_{ij} I_{OH,ij}}{\sum_{i,j} y_{ij} I_{OH,ij}} \quad (3.16)$$

$$y_c = \frac{\sum_{i,j} y_{ij} y_{ij} I_{OH,ij}}{\sum_{i,j} y_{ij} I_{OH,ij}}, \quad (3.17)$$

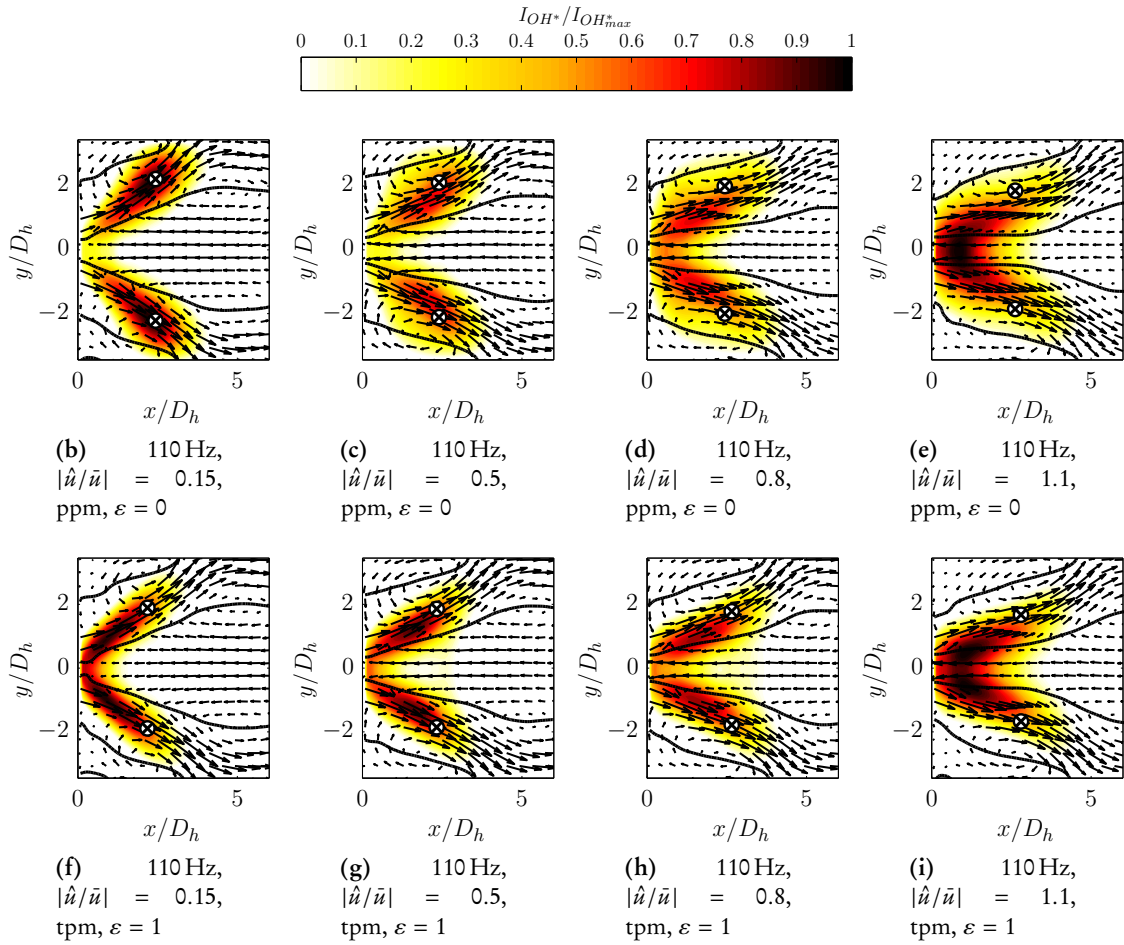


Figure 3.5: Mean flow field and mean chemiluminescence distribution for various amplitudes for perfectly (upper row) and technically premixed flame (lower row). Forcing amplitude at 110 Hz is increasing from left to right. Color denotes chemiluminescence intensity and solid lines depict zero velocity. Arrows illustrate flow direction and relative velocity magnitude based on axial and radial velocities.

where i and j are pixel indices, x_{ij} and y_{ij} the pixel coordinates, $I_{OH,ij}$ the measured OH^* intensity, and summation is performed over one half of the measurement domain.

Generally, in terms of the velocity field and in particular regarding the location of the shear layers, no significant differences between the two combustion modes were identified. However, downstream of the flame the recirculation bubble is slightly narrower for the perfectly premixed flame in case of high amplitude forcing.

High acoustic velocity amplitudes cause a significant decrease of the divergence of the jet at 110 Hz for the perfectly and technically premixed flame. Consequently, the flame opening angle changes with increasing amplitude, too, and becomes narrower. The flame shape and the flow field alter with increasing forcing amplitude significantly. The time-averaged flame shape is modified from the well-known V-shaped flame at small amplitudes in the way that combustion takes

3.4. Equivalence Ratio Fluctuation Based Saturation Mechanisms

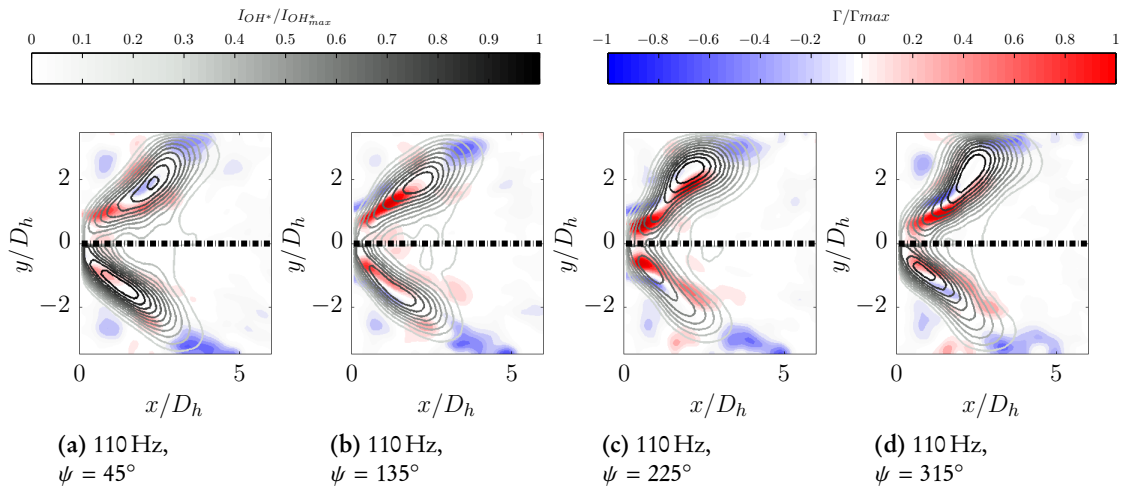


Figure 3.6: Normalized phase-averaged vorticity fluctuations and chemiluminescence distribution at 110 Hz for an amplitude of $|\hat{u}/\bar{u}| = 0.15$ for premixed (upper half, $\varepsilon = 0$) and technically premixed flame (lower half, $\varepsilon = 1$) compared in one figure for different oscillation phases. Color map of vorticity indicates rotation direction and brightness of contour lines represents Abel inverted chemiluminescence intensity. Symmetry line indicates border between the different flame types. The normalization values are the same for all four phase angles shown.

place directly behind the center body. The changes in the mean flow field are gradually increasing with increasing acoustic forcing amplitudes. This observation is consistent with the slow but continuous saturation observed for the perfectly premixed flame describing function. Comparing the mean flow field and the flame shape of the technically and perfectly premixed flame, it is evident that the changes are very similar. Please note that the OH*-chemiluminescence intensity is normalized with the respective maximum at perfectly and technically premixed conditions. Consequently, the increased intensity caused by the equivalence ratio fluctuations is not shown. However, the center of gravity of heat release rate moves a little bit upstream due to the increased local burning velocity at technically premixed conditions and the flame is less distributed, too.

The local through-plane vorticity ($\Gamma = \partial(\bar{v}_x + v_x^c)/\partial y - \partial(\bar{v}_y + v_y^c)/\partial x$) is depicted in Figure 3.6 in the linear forcing regime and the corresponding OH*-chemiluminescence distribution for four different phases of the oscillation at a forcing frequency of 110 Hz. Phase-averaged fields were computed for 16 equally distributed phases. Figure 3.6 only shows results for four equidistant phase angles to illustrate specific aspects within the oscillation cycle. Red and blue color indicate the rotation direction of the vortices in this illustration. The upper part of each image shows the premixed results and the lower one the technically premixed measurements. The contour lines indicate the intensity of the heat release.

The heat release of the flame fluctuates around the center of gravity without strong changes

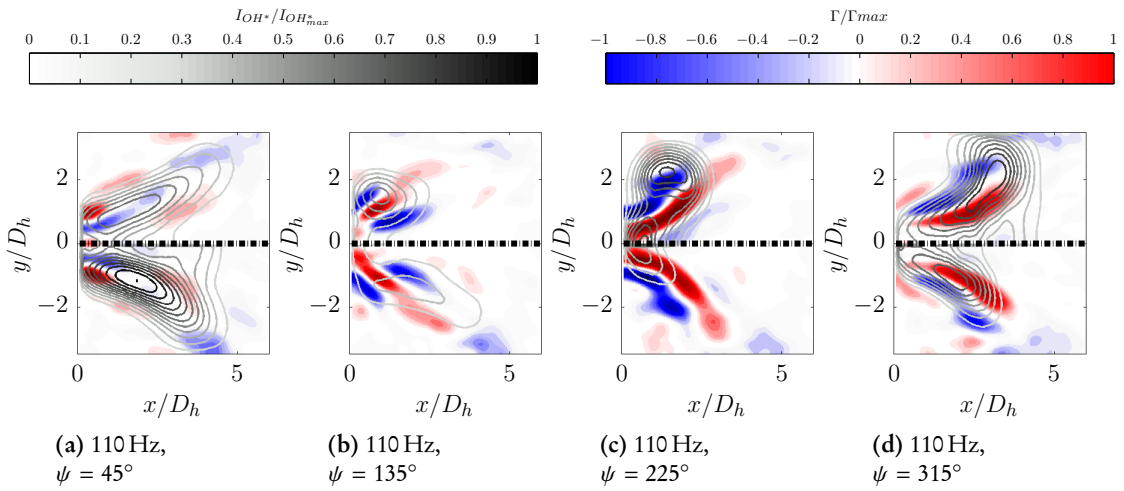


Figure 3.7: Normalized phase-averaged vorticity fluctuations and chemiluminescence distribution at 110 Hz for an amplitude of $|\hat{u}/\bar{u}| = 0.8$ for premixed (upper half, $\varepsilon = 0$) and technically premixed flame (lower half, $\varepsilon = 1$) compared in one figure for different oscillation phases. Color map of vorticity indicates rotation direction and brightness of contour lines represents Abel-inverted chemiluminescence intensity. Symmetry line indicates border between the different flame types. The normalization values are the same for all four phase angles shown.

of the flame shape. The convection of the vortical structures can be observed following the visualizations from left to right in the upper and lower row for the perfectly and technically premixed case, respectively. Large-scale vortical structures are generated in the inner and outer shear layer close to the combustor inlet. These coherent structures are amplified up to $3.5 D_h$ downstream of the inlet. Further downstream the structures are attenuated. No major differences in the structure or strength of the vortices between the two combustion modes are evident. The area of significant heat release rate is also very similar between the two modes of combustion across all phases of the oscillation.

Increasing forcing amplitudes are associated with larger wave lengths of the vortical structures and an increased zone of their extent, as can be seen in Figure 3.7, which shows the corresponding visualizations for a higher amplitude. The vortices are clearly interacting with the flame, which is evident from the corresponding position of the maximum of the chemiluminescence intensity and the vorticity for each phase. In contrast to the low-amplitude forcing, the flame and the flow field are subject to large displacement. The strong decrease in velocity causes the flame almost to extinguish as illustrated by the first three phases. Nearly no difference concerning the flow field dynamics can be identified between the two combustion modes. However, some differences of the spatial chemiluminescence distribution are observed. For instance, the phase relation between heat release and the flow field is different, which is in line with the flame response measurements shown later. These observations support the assumption that the

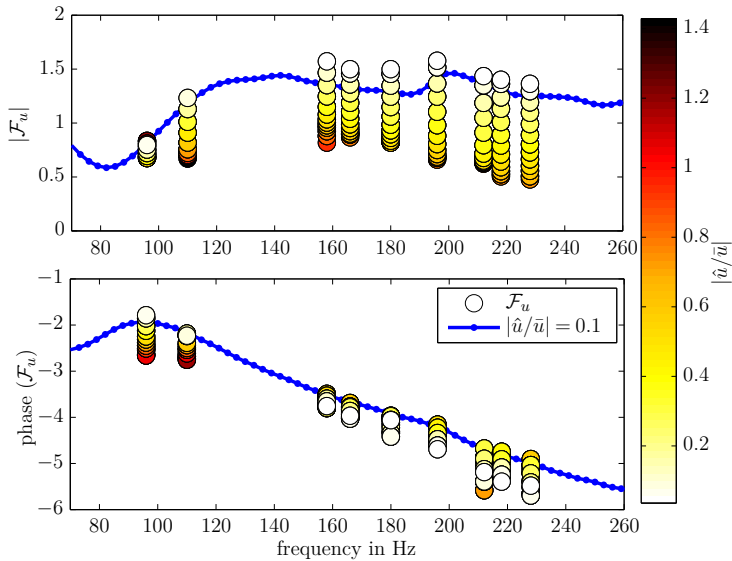


Figure 3.8: Flame describing function at perfectly premixed conditions. Flame describing functions for various amplitudes and frequencies. The color of the circles indicates the forcing amplitude at the flame. Solid line represents linear flame response.

contribution of the coherent structures to the heat release rate fluctuations remains unaltered regardless of the additional mixing inhomogeneities.

3.4.2 Flame Describing Function Analysis

The flame response of the perfectly premixed flame in terms of transfer function gain and phase is shown in Figure 3.8 for various frequencies. Each measurement point is associated with a color, which indicates the acoustic forcing amplitude. The line, which connects 90 flame response measurement points at an amplitude of $|\hat{u}/\bar{u}| = 0.1$, depicts the linear transfer function, which is commonly measured at this acoustic forcing level. The upper plot shows the gain of the flame describing function, and the lower one illustrates the phase response for various frequencies. For some frequencies a forcing amplitudes of up to $|\hat{u}/\bar{u}| = 1.2$ was achieved.

The flame has a gain of around 1.5 at 120 Hz, and is almost constant in the investigated frequency regime. Coherent hydrodynamic structures and possibly swirl number fluctuations are responsible for the perfectly premixed flame response as discussed in section 3.3. Since the time lag calculated from the phase response corresponds well to the convective time lag of the coherent structures, this mechanism is believed to be the dominant one. For all investigated frequencies, strong nonlinear effects are observed for the transfer function gain, as it is the case for 196 Hz, which was discussed in detail previously. Interestingly, an increased susceptibility of the flame response to nonlinearities at low amplitudes is observed at higher frequencies. Some nonlinear effects are present in the phase response, especially at higher frequencies. Since the

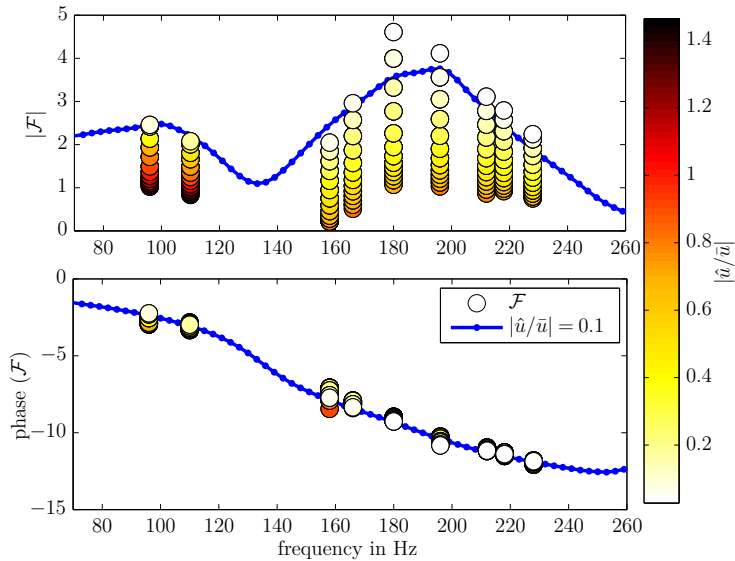


Figure 3.9: Flame describing function at technically premixed conditions ($\varepsilon = 1$). Flame describing functions for various amplitudes and frequencies. The color of the circles indicates the forcing amplitude at the flame. Solid line represents linear flame response.

phase relation between heat release rate and velocity oscillations is of crucial importance for the transfer of energy and the resulting feedback between the acoustic field and the flame, small changes in the phase response can already affect linear stability and the limit-cycle amplitude.

For technically premixed conditions, the flame response is a combination of the perfectly premixed flame response and the effects caused by the equivalence ratio fluctuations. The respective gain and phase response of the technically premixed flame to velocity perturbations is shown in Figure 3.9. The gain of the transfer function exhibits two frequency intervals of high amplification and two frequency ranges with weak or no amplification. Around 140 Hz the two mechanisms interfere destructively and consequently a local minimum is situated in this frequency region. For frequencies higher than 230 Hz, the flame transfer function gain is very small. Nonlinear effects are observed already for small amplitudes in the frequency range around 200 Hz, which is characterized by a large linear transfer function gain. In contrast to that, at relatively high forcing amplitudes of $|\hat{u}/\bar{u}| \approx 0.2$, the flame responds still without strong nonlinear effects at frequencies around 100 Hz.

Figures 3.10a to 3.11b depict the amplitude dependence of the normalized heat release fluctuation for different forcing frequencies and fuel split ratios. The degree of technical premixedness was increased gradually in $\Delta\varepsilon = 0.2$ steps from 0 to 1. The top part of each figure illustrates the gain of the amplitude-dependent flame response in terms of the normalized heat release rate. The lower plot shows the respective phase response. Each marker represents a measurement point. The frequencies were chosen to represent certain expected interactions between

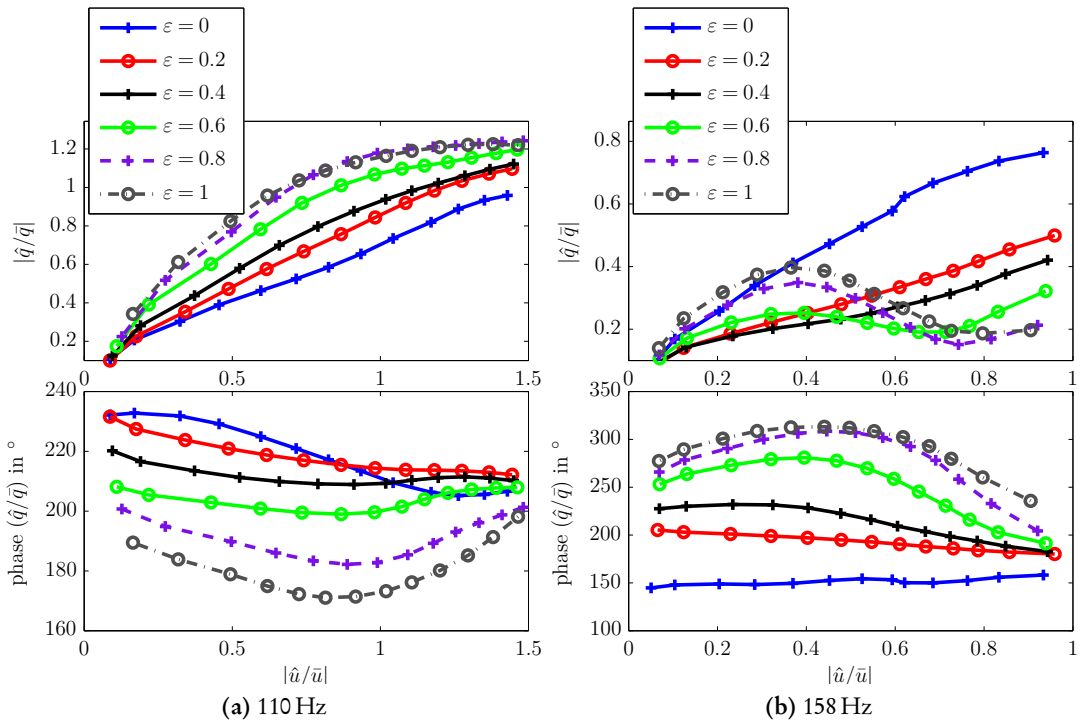


Figure 3.10: Flame response at 110 Hz and 158 Hz for various amplitudes and fuel splits.

equivalence ratio fluctuations and velocity fluctuations.

Figure 3.10a depicts the normalized heat release fluctuation at 110 Hz. At perfectly premixed conditions ($\varepsilon = 0$), the gain of the flame response features only very weak nonlinear effects. The lower plot indicates a slightly decreasing phase response with increasing amplitude. As the unmixedness of fuel and air increases, so does the linear normalized heat release fluctuation, and a constant offset is added to the phase. Since the gain is seen to increase with ε , fuel flow perturbations and velocity fluctuations interfere constructively at this frequency. The phase response is not strongly affected by the forcing amplitude and the degree of unmixedness plays only a role in case of strong changes in the degree of unmixedness. However, at $\varepsilon = 0.4$ the gain of the flame response starts to saturate significantly. The higher the unmixedness, the lower is the amplitude where saturation effects appear first. This connection between the degree of unmixedness and the onset of the saturation of the flame response has to be expected if the equivalence ratio fluctuations cause the saturation through the nonlinear relation of the burning velocity and the heat of reaction dependence. It is worth noting that no significant difference between 80% and 100% technical premixedness is observed for the gain, while the phase response is different.

As expected from the comparison between flame transfer functions for perfectly and technically premixed conditions, equivalence ratio and velocity oscillations interfere destructively

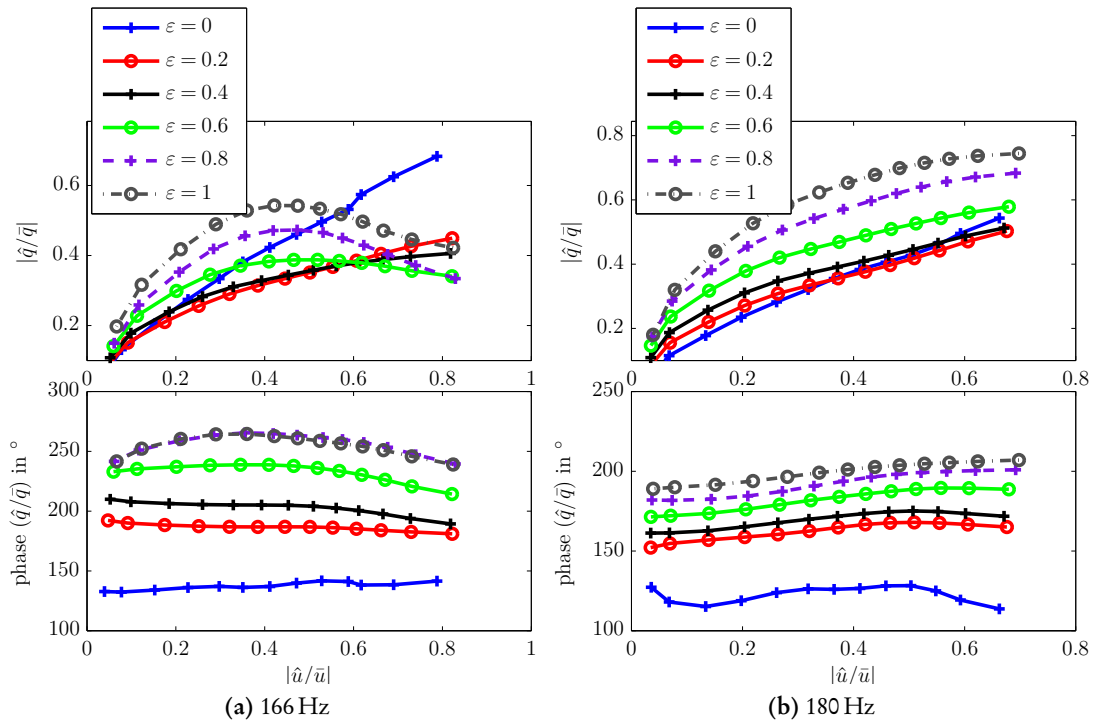


Figure 3.11: Flame response at 166 Hz and 180 Hz for various amplitudes and fuel splits.

for 158 Hz, as shown in Figure 3.10b. Again, the flame response is almost linear for the perfectly premixed flame. However, with increasing injection of fuel in the mixing tube, the linear gain first decreases and then increases again for values of $\varepsilon > 0.4$. The linear gain of the 100% technically premixed case is even higher compared to the perfectly premixed flame, despite the destructive interference. The investigated fuel split ratios have in common that the gain of the heat release fluctuation decreases at high velocity perturbation levels and major saturation effects are observed. In addition, the phase response is affected for very high forcing amplitudes and high degrees of unmixedness and hence strong equivalence ratio perturbations.

Similarly to the 158 Hz case, at 166 Hz the equivalence ratio fluctuations and the velocity oscillations interfere destructively. The perfectly premixed flame response, as depicted in Figure 3.11a, shows an almost linear trend, indicating only relatively weak nonlinearities. However, with increasing unmixedness the linear gain first decreases and then for values of $\varepsilon > 0.4$ increases compared to the perfectly premixed case. In contrast to the 158 Hz case, the heat release amplitude of the 166 Hz flame response is already higher for very small fuel split ratios $\varepsilon > 0.2$. Again, for very high forcing amplitudes the heat release gain of the technically premixed flames is decreased below the gain of the perfectly premixed, although the initial gain is higher. Saturation is observed for all technically premixed flame responses. The phase response for all degrees of premixedness is essentially independent of the forcing level at 166 Hz.

The phase response is shifted towards shorter time delays with increasing unmixedness. This is probably due to a shift of the center of gravity of the flame that may result from locally higher burning velocities caused by the spatial unmixedness with increasing ε .

Similar to forcing at 166 Hz, the 180 Hz case is characterized by an almost immediate saturation of all technically premixed flames (Figure 3.11b). Nevertheless, with increasing mixing inhomogeneities, the gain of the flame response is increased as well as the phase response, which is shifted by an forcing amplitude independent offset. The flame response of the perfectly premixed flame is for very high amplitudes higher than for the technically premixed flame with fuel split ratios smaller than $\varepsilon < 0.4$. In contrast to the 110 Hz case, where equivalence ratio fluctuations and velocity oscillations also interfere constructively, the flame response at 180 Hz saturates already at very low forcing amplitudes without an obvious relation between the degree of unmixedness and amplitude of first saturation.

3.4.3 Flame Describing Function Decomposition

Applying Equation (3.6) to the discussed flame describing functions, reveals the scaled difference between the perfectly and technically premixed flame, which is attributed to the contribution of the equivalence ratio fluctuations to the flame response. Figures 3.12 to 3.15 show on the respective left side the φ' contribution for each technically premixed flame, as indicated by the different markers, resulting from the decomposition of the respective flame describing function. The right side depicts the transfer function gain and phase of the perfectly premixed and fully technically premixed flame ($\varepsilon = 1$) as well as the contribution of the mixing inhomogeneities to the technically premixed flame describing function. The purpose of the left figures is to emphasize the strong resemblance of the scaled equivalence ratio contribution to the flame describing function for each technically premixed flame forced at the same frequency. Collapsing markers indicate that the assumptions made and the decomposition ansatz are correct. Please note that the repeatability of a single flame describing function measurement is in the range of 5% and the accuracy of each of the three mass flow meters is in the range of 2%. Both measurement deviations directly affect the accuracy of the decomposition approach. The right-hand side of the figures reveals the role of the mixing inhomogeneities for the transfer function saturation as well as the phase relation between velocity oscillations and equivalence ratio perturbations.

The small sudden discontinuities at $|\hat{u}/\bar{u}| \approx 0.6$ and $|\hat{u}/\bar{u}| \approx 1.2$ in the measurements of the premixed flame response (see, Fig. 3.10a), which are also present at other frequencies, were smoothed before the decomposition ansatz was applied.

All $\varepsilon=0.2$ cases show a qualitatively similar trend for all investigated frequencies. They feature an additional significant offset for all amplitudes. It is assumed that the transition between

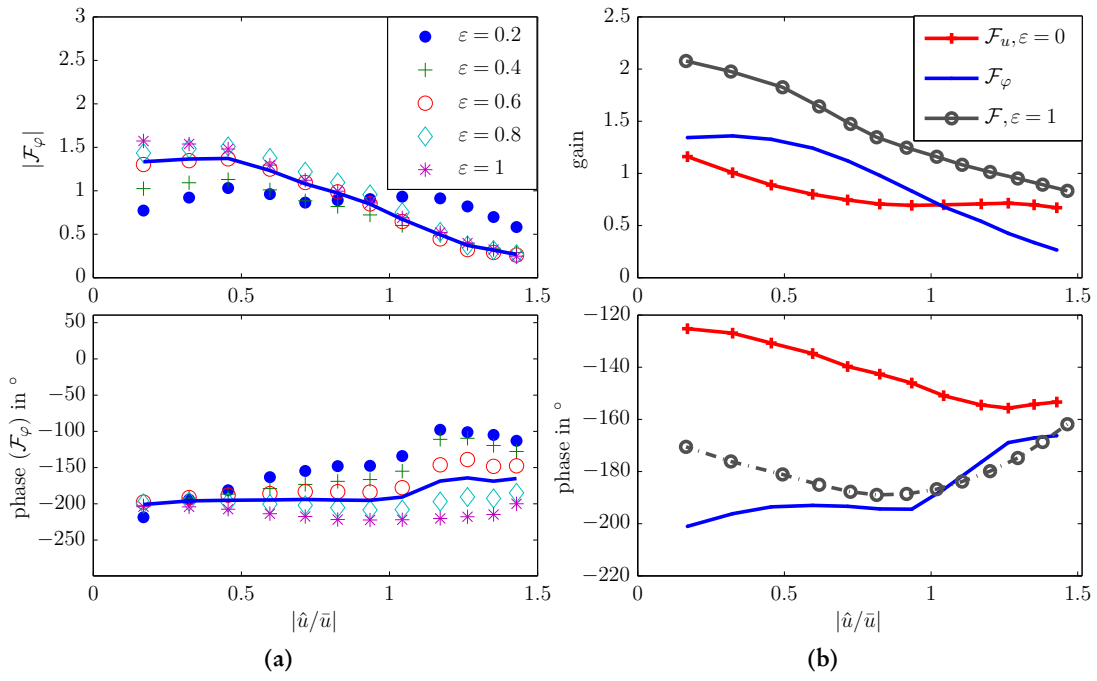


Figure 3.12: Flame describing function decomposition at 110 Hz. (a) Equivalence ratio contribution for the different premixed flames; solid line represents the average over all values of ε . (b) Comparison of the contributions to fully technically premixed flame.

premixed and fully technically premixed flame response is linear and scales with the fuel ratio. Although this seems to be the case for higher fuel split ratios, it is evidently not correct for $\varepsilon=0.2$. The initial transition between perfectly premixed and technically premixed is not smooth for the investigated burner. Adding only a small amount of fuel inside the burner affects the flame response stronger than a fuel-split factor of 20% suggests. Since the decomposition results revealed for $\varepsilon = 0.2$ poor results, this data is not included in the averaging. The poor agreement probably stems from problems with the fuel supply stiffness, which vanishes for very small fuel flows.

The gain of the equivalence ratio contribution shows the same trend for all degrees of partial premixedness for forcing at 110 Hz except for the $\varepsilon = 0.2$ case. This is illustrated in Fig. 3.12a. Especially for low amplitudes, the scattering of the gain data is relatively high. At higher amplitudes, the results collapse fairly well for the gain but show some significant differences in the phase response. Without the $\varepsilon = 0.2$ case, the standard deviation between the single decomposition results and the average over all fuel split ratios of the gain features values of approximately 8% for higher amplitudes. For small amplitudes the standard deviation is around 18%. The phase response features significant differences, up to 60° between the single measurements at different fuel splits and the average phase response at higher forcing amplitudes.

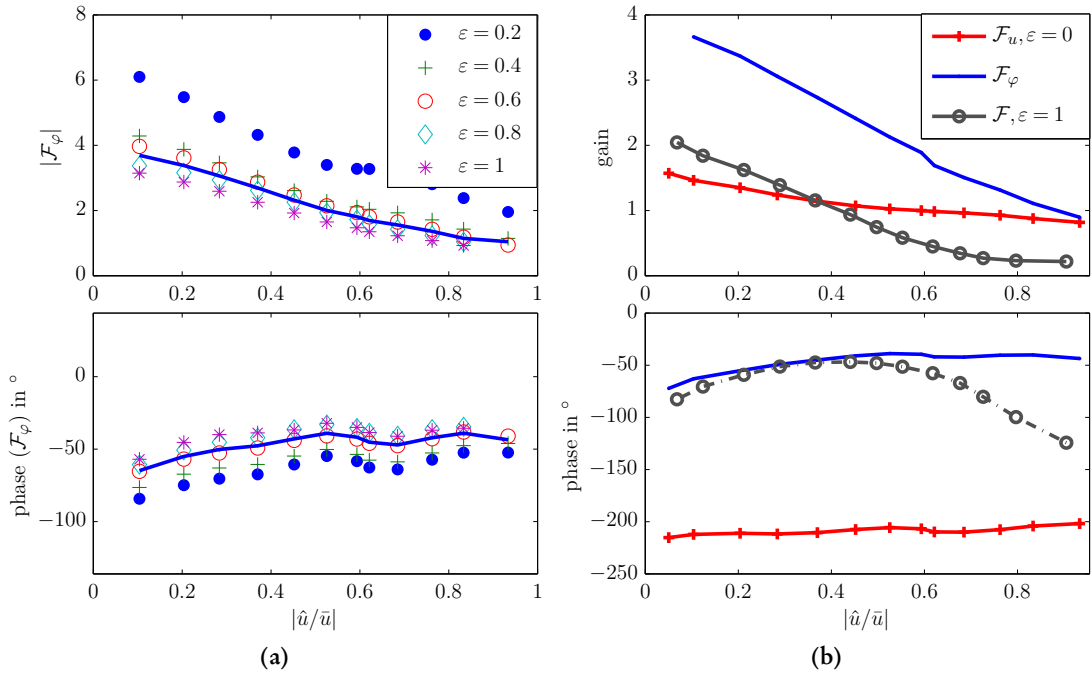


Figure 3.13: Flame describing function decomposition at 158 Hz. (a) Equivalence ratio contribution for the different premixed flames; solid line represents the average over all values of ε . (b) Comparison of the contributions to fully technically premixed flame.

Overall the gain of the decomposition at 110 Hz indicates trends, which suggest that saturation at high amplitudes occurs. It is shown in Fig. 3.12b. The saturation is similar to the model results discussed in section 3.4 for a constant mixing factor. However, the agreement of the F_ϕ phase is poor, revealing nonlinear interaction. The mean phase difference between the equivalence ratio perturbations and velocity oscillations changes by more than 40°. Since the scattering of the phase decomposition features higher differences, no conclusions can be drawn from the phase relation. A possible explanation for the poor agreement at 110 Hz is the break down of the MMM at small frequencies due to the increased wavelength. The decomposition approach is sensitive to inaccuracies of the flame describing function measurements.

As shown in Fig. 3.13a, the various technically premixed flames with varying unmixedness show all a qualitatively very similar contribution of the equivalence ratio perturbations for the 158 Hz forcing case. The scattering is for all amplitudes relatively small. Again, especially for $\varepsilon = 0.2$ strong quantitative differences are present. Nevertheless, without the $\varepsilon = 0.2$ case, the standard deviation between the single gain results and the average is in the range of 8–15%. Taking into account the measurement uncertainty, the resulting agreement is good. The maximum difference between the single phase response measurements and the average response is 10°.

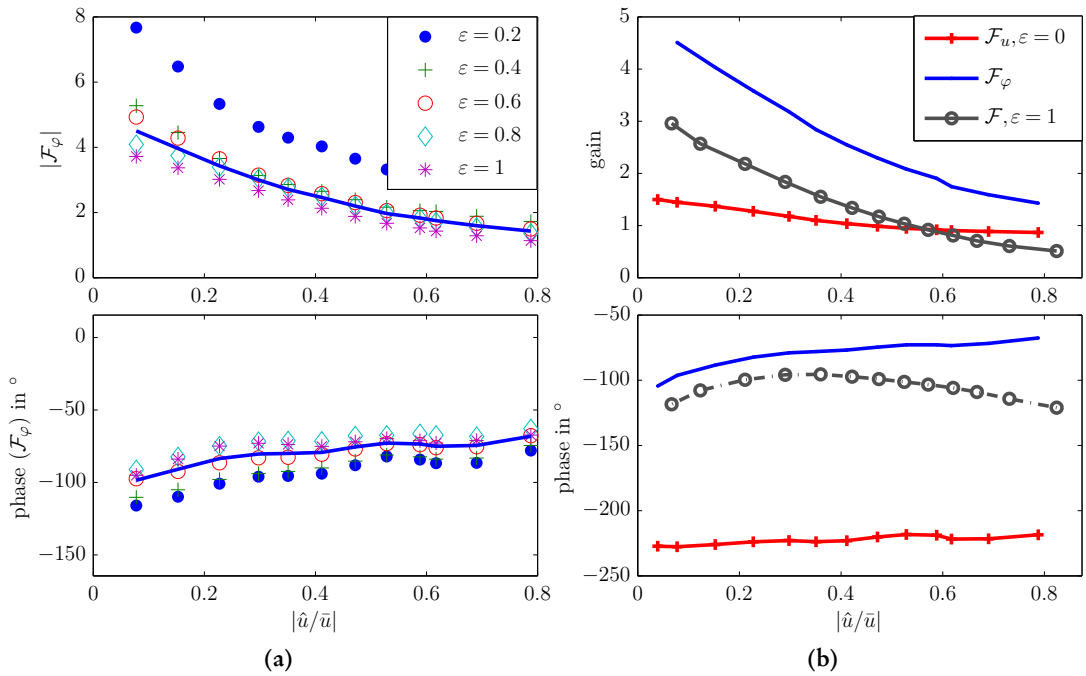


Figure 3.14: Flame describing function decomposition at 166 Hz. (a) Equivalence ratio contribution for the different premixed flames; solid line represents the average over all values of ε . (b) Comparison of the contributions to fully technically premixed flame response.

The transfer functions depicted in Fig. 3.13b give insight into the responsible interaction mechanisms. As expected from the discussion of the flame response shown in Figure 3.10b and from the flame describing functions shown in Figures 3.9 and 3.8, the mixing inhomogeneities and the velocity oscillations interfere destructively at 158 Hz. The phase responses of both contributions slightly increase with the forcing amplitude. Starting from a phase difference of $\Delta\psi = 147^\circ$, the difference increases to $\Delta\psi = 164^\circ$ for the highest amplitude, meaning that the two mechanisms are even more out of phase at higher amplitudes. The contribution of the equivalence ratio fluctuations to the gain of the flame describing function is quite high for small amplitudes and monotonically decreases with a much higher rate than the contribution of the velocity oscillations. At the highest forcing amplitude, both contributions have the same gain, explaining why the heat release reaches almost zero for high amplitudes.

Figure 3.14a depicts the decomposition for the 166 Hz forcing case. The phase features again only small difference and the gain contribution shows some minor differences, too. Similar to the other results, the technically premixed flame with $\varepsilon = 0.2$ shows the largest deviation from the mean gain. Without the $\varepsilon = 0.2$ case, the standard deviation of the measurements and the mean gain is in the range of 6–15%.

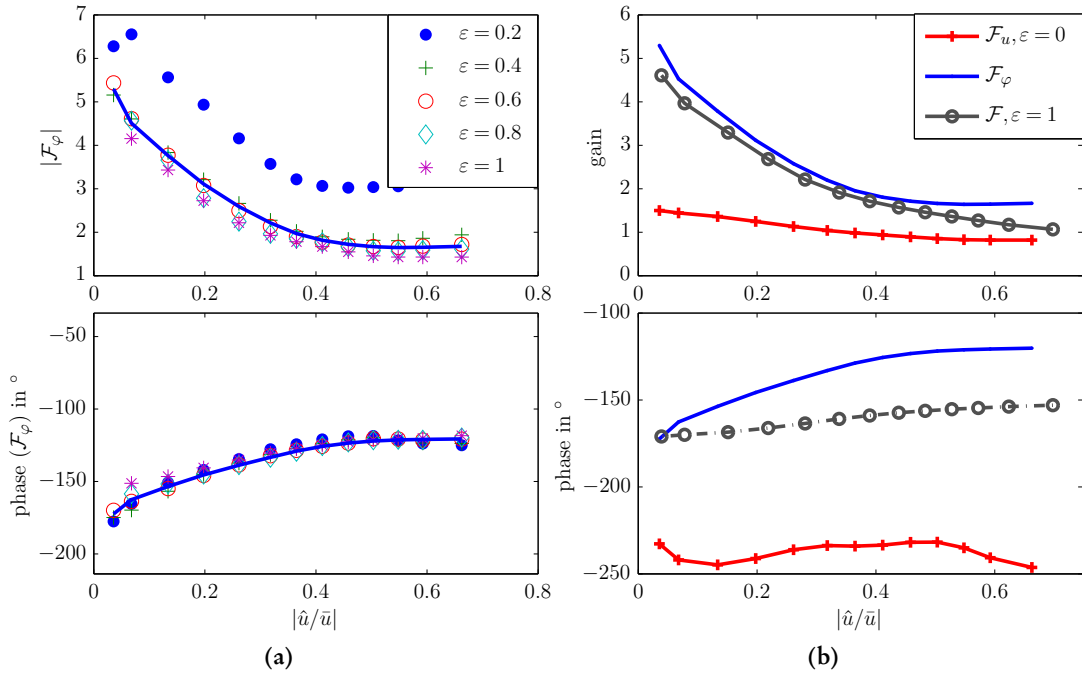


Figure 3.15: Flame describing function decomposition at 180 Hz. (a) Equivalence ratio contribution for the different premixed flames; solid line represents the average over all values of ε . (b) Comparison of the contributions to fully technically premixed flame.

Forcing at 166 Hz is also a case with destructive interference of the two mechanisms, as indicated in Fig. 3.14b. The gain of both contributions saturates, but the gain of the equivalence ratio fluctuations contribution does so much stronger and already at smaller forcing amplitudes. Consequently, the resulting phase response of the technically premixed flame changes with increasing amplitude, although the phase responses of the two contributions are almost constant. The destructive interference and the strong saturation of the equivalence ratio contribution explains the observed behavior of the associated flame response (see Fig. 3.11a). For a certain degree of unmixedness, the linear flame response is higher than that of the perfectly premixed flame response, despite the destructive interaction, due to the large gain of the equivalence ratio contribution. However, this contribution saturates fast and consequently the resulting flame response of the technically premixed flame can be smaller at higher amplitudes than that of the perfectly premixed flame.

The proposed flame describing function decomposition method works almost perfectly for the case of 180 Hz, as illustrated in Figure 3.15a. Both gain and phase are very similar for all flames, except for the case with $\varepsilon = 0.2$, where again the gain deviates with a constant offset. Without the $\varepsilon = 0.2$ case, the standard deviation between the single measurements and the mean gain is in the range of 5–10%, which is in the range of the measurement accuracy.

As can be seen from Fig. 3.15b, relatively strong changes can be observed in the phase response of the equivalence ratio contribution. The phase response changes by 46° between the small amplitude forcing and the higher amplitudes. The contribution of the velocity fluctuations is almost constant in terms of the phase response. Consequently, the interaction between the two mechanisms changes. At small amplitudes a phase difference of $\Delta\psi = 68^\circ$ is observed, which suggests a constructive interference. In contrast to that, at higher amplitudes a phase difference of $\Delta\psi = 127^\circ$ is observed, which suggests a destructive interference. This change of interaction contributes to the saturation of the technically premixed flame response. The equivalence ratio contribution decays immediately in terms of gain, while the perfectly premixed flame describing function is almost constant for all forcing amplitudes.

The flame describing function analysis is summarized with the help of Figure 3.16a that compares the flame transfer function contribution of the equivalence ratio perturbation for three cases. The gain is normalized with the respective linear gain to emphasize the nonlinear effects. With increasing forcing frequency, the saturation sets in at a smaller acoustic velocity amplitude. Nonlinear effects are evident at small amplitudes in contrast to the late saturation level, which can be expected by the two mechanisms: heat of reaction saturation and burning velocity nonlinearity. The presented flow field and flame shape analysis have shown that the mean flow field and flame shape are strongly modified. Significant flow field dynamics and a strong movement of the reaction zone were observed, too. Comparing the perfectly and technically premixed flame describing functions suggests that the saturation of the flame transfer function is caused by a decreased receptivity of the flame to equivalence ratio perturbations. The excessive movement of the flame at high amplitudes, the modified mean flow field and the altered reaction zone decrease the effect of the equivalence ratio perturbations due to changes in the time delays and mixing quality. The proposed new saturation mechanism, which suggests that the increased turbulence intensity and the changes in the flame shape and flow field increase the mixing significantly, fits qualitatively well to the observed results. For higher frequencies, mixing increases due to shorter wavelengths and thus higher spatial concentration gradients. This increased damping of fuel-air ratio fluctuations can cause a significant saturation of the flame response to equivalence ratio perturbations, especially for higher frequencies. The saturation of the 110 Hz forcing case, however, appears to be mainly caused by the heat of reaction and burning velocity nonlinearity.

The corresponding perfectly premixed flame describing functions are depicted in Figure 3.16b. A weak trend of stronger nonlinearities at higher frequencies can be observed. The saturation starts already at low amplitudes and shows an almost constant rate of decay. However, the saturation seems to be limited to 60% of the linear flame describing function gain.

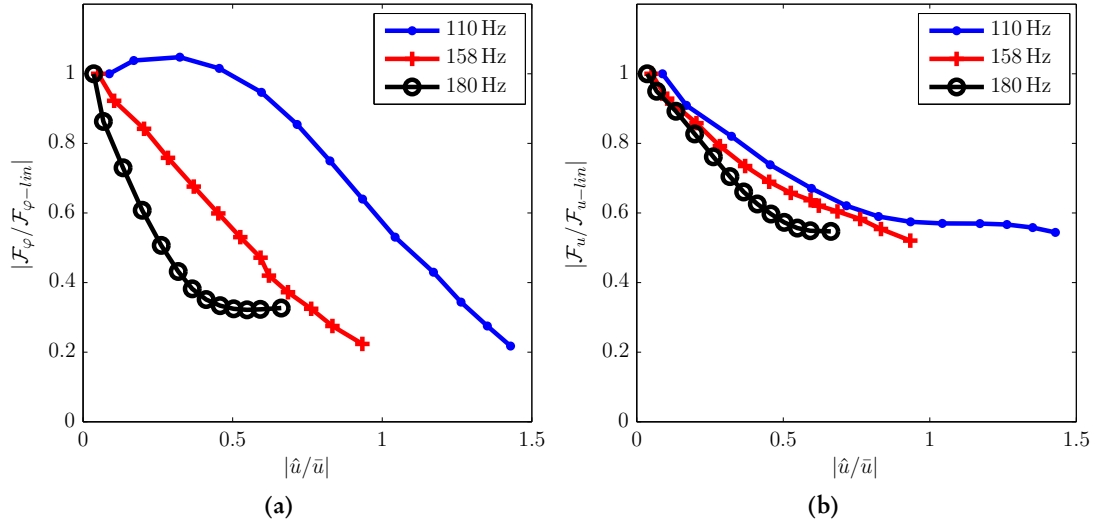


Figure 3.16: (a) Normalized equivalence ratio oscillation contribution to the flame describing function for three different frequencies and various amplitudes. The gain is normalized with the respective linear gain. (b) Normalized velocity oscillation contribution to the flame describing function for three different frequencies and various amplitudes. The gain is normalized with the respective linear gain.

The hypothesis of saturation due to increased mixing is supported by the results presented in Figure 3.17. Here, normalized turbulence intensity Ω and the turbulent shear stress T , which are integrated quantities over the flame and premixed zone in the combustor, are shown for various frequencies at different forcing amplitudes. Both quantities feature qualitatively very similar trends. 158 Hz and 212 Hz show a similar behavior in the linear regime, in contrast to the results at 110 Hz. Forcing amplitudes smaller than $|\hat{u}/\bar{u}| < 0.1$ do not affect the turbulence level or the turbulent shear stresses. However, both quantities significantly increase with higher forcing amplitudes. This is also the case for forcing at 110 Hz but they initially drop to reach again the initial level at a acoustic forcing amplitude of $|\hat{u}/\bar{u}| \approx 0.55$. This decrease in turbulence intensity and turbulent shear stress explains the initial increase of the equivalence ratio fluctuation contribution since it leads to decreased mixing, which also increases the impact of the equivalence ratio perturbations. The shear stresses are almost quadrupled and keeping in mind that the shear stresses are responsible for turbulent diffusion, this supports the scenario presented in Section 3.4, where the attenuation factor a is decreased by a factor of five. Additionally, the coherent structures enhance the mixing most likely, too. However, a direct correlation between simple model constants and the complicated flow field of a turbulent swirl flame is very probably impossible to find.

For thermoacoustically stable flames, most of the turbulent mixing is generated in the shear layers. This is, for instance, indicated in Figures 3.18a and 3.19a, which show the local turbulent

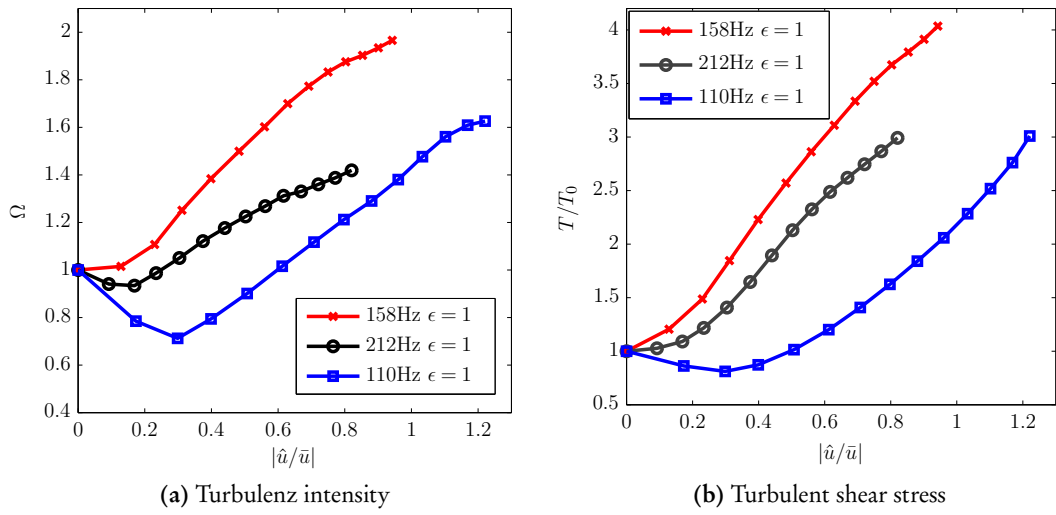


Figure 3.17: (a) Normalized turbulence intensity integrated over the flame and premixed zone in the combustor for three frequencies and various amplitudes. (b) Normalized turbulent shear stress integrated over the flame and premixed zone in the combustor for three frequencies and various amplitudes.

shear stresses and the turbulence intensity without acoustic excitation, respectively. The local maxima are located in both cases in the shear layers. However, this is clearer for the turbulent shear stresses. The shear layers amplify not only the naturally occurring eddies but also the coherent structures generated by the acoustic forcing. As indicated by Figure 3.18b, which shows the local turbulent shear stresses for strong acoustic excitation at 110 Hz, the coherent forcing generates stochastic velocity fluctuations, too. These generate strong turbulent shear stresses especially in the shear layers. Additionally, due to the more distributed mean flame shape, the area of mixing is significantly broader. At the same time, the turbulence intensity, shown in Figure 3.19b, is significantly increased, too. However, the turbulence intensity is distributed more uniformly compared to the turbulent shear stresses. This Figure clearly indicates that the turbulence level is increased in the flame and premixed zone due to the acoustic forcing. From the turbulent shear stresses and the turbulence intensity plots it can be concluded that the turbulent mixing is significantly increased by the acoustic forcing. However, it is not clear how strong the increased mixing affects the attenuation of equivalence ratio fluctuations.

It can be argued that a change of the fuel split ratio affects the flame describing function since the mean quantities of the flame, like the flame position or shape, alter with the mode of injection. Consequently, despite the very good agreement for the decomposition of the different technically premixed flames, the results need some further justification. Thus, the equivalence ratio fluctuations were increased artificially without changing the point of fuel injection or changes in the fuel split ratio and the associated combustion mode. An injector was installed,

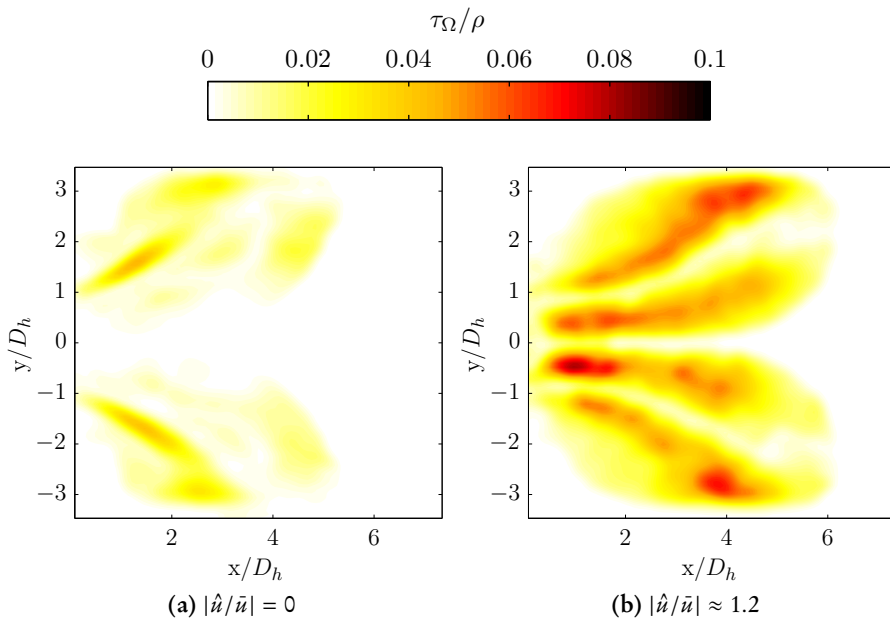


Figure 3.18: (a) Turbulent shear stress in the flame and premixed zone without forcing. (b) Turbulent shear stress in the flame and premixed zone with acoustic forcing at 110 Hz at an forcing amplitude of $|\hat{u}/\bar{u}| \approx 1.2$.

which modulates the technically premixed part of the fuel injected in the mixing tube.

The injector causes an additional increase or decrease of the equivalence ratio fluctuations depending on the phase relation between the forced equivalence ratio perturbation and the one caused by the acoustic velocity according to Equation (3.15). The flame was operated at technically premixed conditions with 40% of the gas injected through the injector in the mixing tube and 60% far upstream of the burner at the same operating conditions and set-up as used previously. The flame was forced with the loudspeakers to generate the air mass flow fluctuations. The injector was simultaneously forcing in phase at the same frequency of 196 Hz.

Figure 3.20 illustrates the decomposition in terms of the perfectly premixed flame and the contributions of the equivalence ratio fluctuations to the technically premixed describing functions. Four curves are shown, one representing the flame describing function at 40% technically premixed fuel and one at 55%, both without additional injector forcing. The third curve represents the 40% technically premixed fuel case with in-phase injector forcing and the last curve depicts the perfectly premixed transfer function. The upper plot shows the gain of the respective describing function and the lower plot illustrates the respective phase response. It is important to note that the different F_φ shown in Figure 3.20 have not been normalized with the specific ε , in order to make them comparable.

All three technically premixed cases respond immediately nonlinearly, while the perfectly premixed contribution to the describing function is only weakly nonlinear. The gain of the

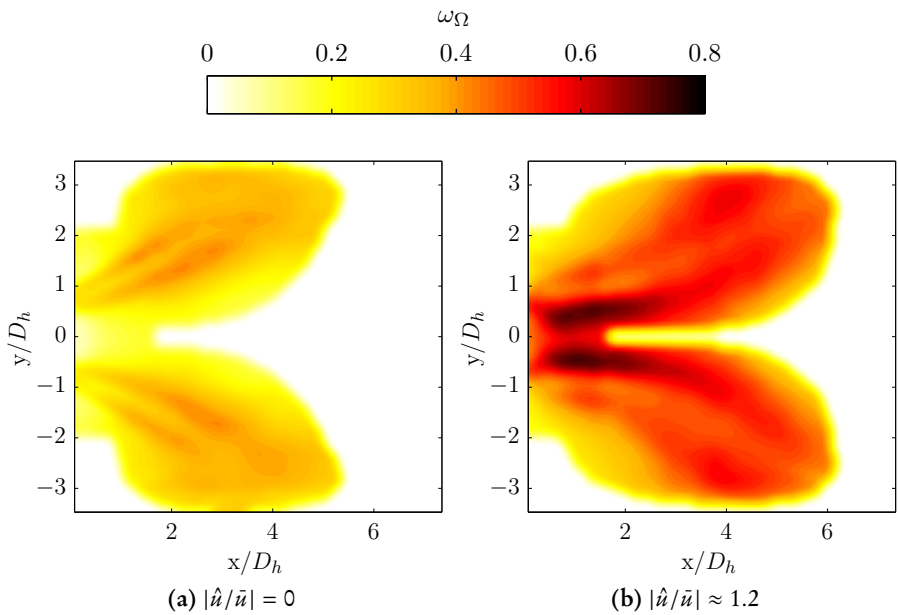


Figure 3.19: (a) Turbulence intensity in the flame and premixed zone without forcing. (b) Turbulence intensity in the flame and premixed zone with acoustic forcing at 110 Hz at an forcing amplitude of $|\hat{u}/\bar{u}| \approx 1.2$.

equivalence ratio contribution decreases almost to zero for very high acoustic velocity amplitudes. The equivalence ratio contribution of the 40% technically premixed case with additional injector forcing is very similar to the 55% case. This underlines that the gradual change of fuel split mainly increases the unmixedness and affects the amplitude of the equivalence ratio fluctuations, with less relevant secondary effects. The flame response of the injector forcing case is in line with the findings of the decomposition approach applied at the different fuel split flame response measurements.

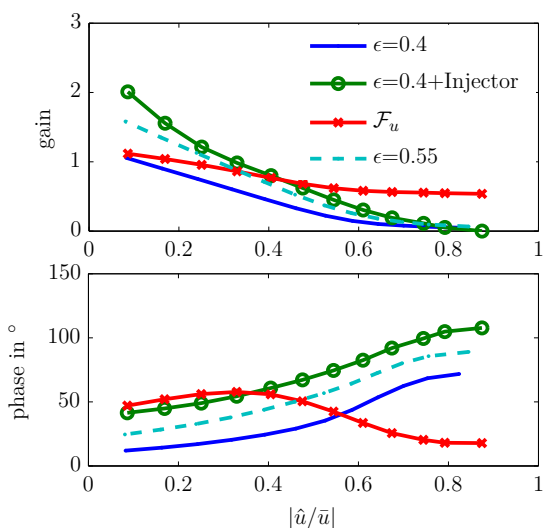


Figure 3.20: Gain and phase of flame describing function contributions at 196 Hz for three different fuel splits and artificially increased equivalence ratio fluctuations. The different F_φ are not normalized with the specific ε .

The phase responses of the technically premixed flames show a growing offset with increasing initial equivalence ratio perturbations. The behavior of the phase response with increasing acoustic velocity amplitude illustrates well the saturation mechanism associated with the change in interference type between velocity and equivalence ratio oscillations. This is very clear especially for the case with additional injector forcing. The two contributions start with almost the same phase delay (“ \mathcal{F} ” and “0.4+Injector” curves), beginning to drift apart at $|\hat{u}/\bar{u}| = 0.4$, to be almost 90° out of phase at an amplitude of $|\hat{u}/\bar{u}| = 0.85$. However, the gain of the equivalence ratio contribution is relatively small at high amplitudes and consequently the effect of the change in interference type is relatively small. Similarly to the 180 Hz case, the type of interference between the two mechanisms does not entirely change with increasing forcing amplitude. Nevertheless, this can be an important saturation mechanism, which has not been considered previously.

Neither the amplitude of the equivalence ratio oscillations nor the mixing process could be measured, which could potentially provide direct verification of the assumption that strong acoustic velocity perturbations affect the amplitude of temporal mixing inhomogeneities. However, other measurements fit very well to the presented hypothesis. For instance, the measurements conducted at a very similar set-up, with the same burner at different operation conditions, which deal with the nonlinear response to two-frequency forcing [28], show some indications; the linear flame transfer function was measured for a technically premixed flame at a frequency of 155 Hz, while simultaneously forcing acoustically at a different frequency. The results for additional acoustic forcing at 50 Hz, 130 Hz, and 190 Hz are shown in Figure 3.21.

The linear flame transfer function gain at 155 Hz decreases monotonically with increasing

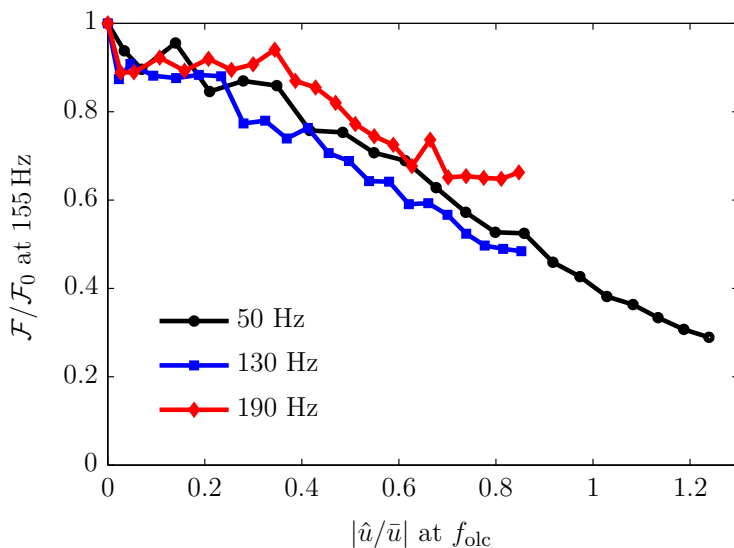


Figure 3.21: Linear flame transfer function gain at 155 Hz for three open loop forcing frequencies and various acoustic velocity amplitudes at the respective open loop frequency

forcing amplitude of the secondary frequency for all frequencies. Interpreting the results according to the discussed hypothesis, leads to the explanation that the additional forcing creates turbulence, which increases the mixing of the temporal inhomogeneities and accordingly attenuates the equivalence ratio fluctuations at 155 Hz, leading to a decreased flame transfer function gain.

The flame describing function of perfectly and technically premixed flames were phenomenologically investigated in this chapter. Justified hypotheses were presented to explain the observed saturation processes of the practically relevant flames. While the perfectly premixed flame response is driven by the amplification of coherent structures by the shear layers, the technically premixed flame is influenced by an increased mixing at higher forcing amplitudes. The presented investigations pave the way for a better understanding of the complex mechanisms featuring the nonlinear flame response of partially premixed flames. However, for the prediction of instabilities the nonlinear response of the acoustic dampers is needed, too. The next chapter deals with the nonlinear effects that influence the acoustic response of dampers.

Chapter 4

Acoustic Boundary Conditions

Though I speak with the tongues of men and of angels, and have not charity, I am become as sounding brass¹, or a tinkling cymbal. And though I have the gift of prophecy, and understand all mysteries, and all knowledge; and though I have all faith, so that I could remove mountains, and have not charity, I am nothing.

1. Corinthians 13, 1-2

² The fundamental improvements in gas turbine combustion design of the last thirty years lead to an increased susceptibility to thermoacoustic instabilities. Following the transition of diffusion type jet flames to premixed swirl stabilized combustion was the transition from silo-type combustors to very compact annular or can-annular type combustors [36]. These designs increase the compactness, which is advantageous from an overall efficiency point of view because less cooling air is needed and the pressure drop is smaller. Additionally, the annular design provides the most uniform temperature distribution. While the premixed swirl-stabilized combustion reduces the NO_x and CO emissions, it is more prone to thermoacoustic instabilities. At the same time, the compact annular and can-annular type combustors feature a ratio of damping surface to combustor volume, which is inferior to the silo-type combustor design. Hence, additional acoustic attenuators are necessary.

The employment of passive acoustic dampers is restricted due to space limitations in the combustion chamber and the demand of high-pressure cooling air. Evidently, since acoustic damping is either associated with pressure loss or with the utilization of cooling air, acoustic dampers must be designed carefully to avoid either negative effects on the engine efficiency or thermoacoustic instabilities.

¹According to Harris [47], *sounding brass* refers to a device used in Greek theaters to cancel echoes. Today, this device is called Helmholtz resonator.

²The work presented in this chapter is based on two journal publications [29] and [33]. The PIV measurements and the post processing were conducted together with Steffen Terhaar. He mainly contributed to the final presentation of the PIV and QLS results shown in the figures of this chapter. Dominik Waßmer mainly contributed to the determination of the virtual neck extension and the damping coefficients presented later in this chapter. Paragraphs and phrases of this chapter are very similar or identical to text paragraphs published in the two articles. These excerpts are written by me.

A typical gas turbine combustor features an area jump at the exit of the circumferential arranged burners. The area jump increases the flame stability and prevents flame flashback. Vortices are generated at the area jump, which are one of the reasons for heat release fluctuations but also for acoustic damping. The amount of acoustic damping generated by these vortices depends on the mean flow velocity [5], the acoustic amplitude [25] and the geometry of the edges [63]. The burner itself represents an acoustically compact body, which generates acoustic losses due to eddy zones, area jumps and flow redirection within the burner. For stability analyses these losses and the other acoustic characteristics of the burner are taken into account by the acoustic burner transfer matrix. However, burners are generally optimized towards small pressure losses to increase the overall engine efficiency, and burner with small pressure drops tend to provide only limited acoustic damping.

Thermal barrier coating and ceramic shields protect the gas turbine housing from the combustion heat and reduce heat losses, but they do not provide any acoustic damping. The first turbine stages are also almost fully reflective to acoustic waves because the combustion chamber exhaust flow is accelerated up to $M \approx 1$.

Most of the damping needed for the attenuation of thermoacoustic instabilities is provided by cooled liners and Helmholtz dampers. Compared to active control, dampers have the striking advantage of their passive principle of work and, hence, high lifetime and reliability. Acoustic liners can be adjusted to mitigate a broad frequency range or very effectively a narrow frequency range [115]. They are used to cool the combustion chamber walls and to provide damping. Helmholtz dampers, in contrast to that, are installed usually in the vicinity of the burners [10, 18] but are also cooled with air from the last compressor stages. A single Helmholtz damper can attenuate a narrow frequency range around the resonance frequency of the device. Depending on the burner arrangement and external factors like the range of the fuel quality and the load flexibility of the machine a combustion chamber can exhibit various types of instabilities. They can differ in the mode shape, frequency, and amplitude. Considering that, Helmholtz resonators, optimized for different frequency ranges, can be connected via one neck and thereby provide broad-band damping [19].

Instabilities occur mainly at favorable operation points with low emissions. Consequently, as pointed out by Bothien et al. [18], stationary gas turbine manufacturers tolerate a certain acoustic pressure amplitude in the combustion chamber as long as the materials in the combustion chamber are not overburdened. To push the envelope in terms of operational flexibility, low emissions and minimum usage of cooling air, the prediction of the acoustic dissipation is of crucial importance. Based on isothermal data, this part of the thesis significantly extends the current knowledge in terms of the reliable prediction of the acoustic dissipation of industrial gas turbine combustors.

First, a detailed Helmholtz damper model is introduced and the impact of the density field is analyzed with the help of PIV, QLS, and microphone measurements. Subsequently, the application of the model at various temperature differences is verified. Finally, an assessment of the nonlinearities of the burner transfer matrix and the acoustic boundary conditions of the flame is presented.

4.1 Helmholtz Resonator

A Helmholtz resonator consists of a cavity filled with compressible gas (resonator volume) and a small tube (resonator neck), which connects the cavity to its surroundings (see, 2.14). This acoustic oscillation system is in everyday life referred to as a “bottle” and acts similar to a mechanical mass-spring-damper oscillator. Depending on the size of the volume, which is comparable to the spring-stiffness, acoustic pressure fluctuations in the enclosure might excite the air-mass in the neck to oscillate. The damper corresponds to the acoustic dissipation generated by vorticity and viscous forces, which limit the oscillation amplitude.

The mathematical approximation of the resonance frequency of the Helmholtz resonator was found more than 100 years ago by its eponym Helmholtz [48]:

$$\omega_{\text{res}} = c \sqrt{\frac{S_n}{V(L_n + \delta)}}. \quad (4.1)$$

where c , S_n , V , L_n denote the speed of sound, the cross-sectional area of the neck, the volume of the cavity and the geometrical length of the neck, respectively. The virtual neck correction δ represents the extension of the neck length due to the inertia of the air in the neck vicinity. As will be shown later, this correlation is only valid for the theoretical limit of an isothermal loss-free resonator at low amplitudes. It is especially difficult to predict the virtual neck correction because it is very sensitive to the geometry of the neck, the acoustic amplitude, the mean flow velocity in the neck, and the grazing flow velocity. Additionally, will be shown later in this chapter, the cooling flow through the damper and the hot flows in the combustor affect not only the resonance frequency but also the magnitude of the acoustic response.

The reminder of this section is structured as follows: first a detailed impedance model of the Helmholtz resonator will be derived, which includes all relevant effects for the acoustic response of Helmholtz dampers in combustion chambers. Subsequently, the amplitude-dependent flow field in the resonator and its vicinity as well as concentration measurements in the resonator are discussed. The influence of hot grazing flow and the acoustic amplitude on the virtual neck extension is investigated, and an analytical model of the mean density in the neck at

higher amplitudes is presented. Finally, measurements of the damping efficiency at elevated temperatures are examined and properly incorporated into the model.

4.1.1 Prediction of Acoustic Response

The theoretical considerations are based upon the impedance model first of all published by Keller and Zauner [63], which was later extended by Bellucci et al. [9, 10]. The original model accounts for mean flow effects of the purging flow as well as effects of the secondary neck needed for the purging flow supply and includes the nonlinear dissipation with a describing function ansatz. For the sake of clarity, the effects of the secondary neck are neglected here. However, it can be easily incorporated. The model is extended within this work to include the following effects: hot-gas penetration, additional losses due to density stratification, and the respective shift of the resonance frequency.

Assuming that the acoustic wavelengths are much larger than the dimensions of the neck, the equation of motion of the neck can be written as:

$$\bar{\rho}_n (L_n + \delta) \frac{\partial u}{\partial t} + p_{cc} - p_v + \bar{\rho}_j u \left(\zeta_{vis} + \zeta_n + \zeta_T(\Delta\vartheta) + \sum^i \zeta_{\Omega_i} \frac{|u|}{2} \right) = 0, \quad (4.2)$$

where u , p , and δ denote the total axial velocity ($u = \bar{u} + u'$), the total pressure ($p = \bar{p} + p'$), and the virtual neck extension, respectively. The mean spatial density of the neck averaged over one oscillation cycle $\bar{\rho}_n$ and the respective (index $j = vis, n, T, \Omega_i$) densities for every loss-coefficient $\bar{\rho}_j$ are calculated as a function of the velocity. The function is derived in Section 4.1.4. The loss-coefficients denoted by ζ include several loss mechanisms into the model. ζ_{vis} represents the visco-thermal losses, which can be calculated a-priori and were already determined quite accurately by Kirchhoff [69] in the late 19th century. For high shear numbers ($Sh = r \sqrt{\omega/v} \gg 1$) and very low Helmholtz numbers ($He = kr \ll 1$) the damping coefficient ζ_{vis} for visco-thermal losses at the walls in a quiescent fluid can be defined as [63, 103]:

$$\zeta_{vis} = L_n \omega \left(\frac{1}{\sqrt{2} Sh} \left(1 + \frac{\gamma - 1}{\sqrt{Pr}} \right) + \frac{1}{Sh^2} \left(1 + \frac{\gamma - 1}{\sqrt{Pr}} - \frac{1}{2} \gamma \frac{\gamma - 1}{Pr} \right) \right). \quad (4.3)$$

In this equation γ represents the ratio of the specific heats and Pr is the Prandtl number. The Sh^{-2} term in Eqn. (4.3) can in some cases attain values of 2% of the first term [103]. However, here it is neglected since it is assumed that visco-thermal dissipation at the walls is much stronger than the influence of the visco-thermal losses in the bulk of the flow. Following Peters et al. [103] this assumption is reasonable because losses in the bulk of the flow are of lower order compared to the losses at the walls.

The coefficient ζ_n accounts for the losses created by an asymmetrical flow profile and small recirculation zones of the purging flow in the neck. It is obtained from cold measurements at small amplitudes and was kept constant for all investigations with the same geometry. Non-linear losses created by the vorticity produced at the area jumps are represented by ζ_{Ω_i} . The coefficients are modeled with the help of correlations obtained for a steady contraction or expansion [58], which yield in case of the area jump between neck and combustion chamber:

$$\zeta_{\Omega}^+ = \left(1 - \frac{S_N}{S_{cc}}\right)^2 \quad (4.4)$$

$$\zeta_{\Omega}^- = \frac{1}{2} \left(1 - \frac{S_N}{S_{cc}}\right), \quad (4.5)$$

where S_n and S_{cc} are the cross sectional surfaces of the neck and the combustion chamber, respectively. The correlations for ζ_{Ω}^+ and ζ_{Ω}^- are opposed for the area jump between resonator volume and neck. The effective area jump changes with increasing acoustic velocity amplitude, as will be shown later.

The loss-coefficient ζ_T is a coefficient to account for the losses created by the temperature gradients present at the entrance of the resonator neck. The physical background and the magnitude of the losses caused by density stratification are discussed in Section 4.1.5.

The equation of motion of the resonator volume is used for the impedance model and for the experimental determination of the acoustic velocity in the neck:

$$\frac{d\rho_v}{dt} V = -u' \rho_v S_n \quad , \quad (4.6)$$

assuming the isentropic relation $\frac{dp_v}{dt} = c^2 \frac{d\rho_v}{dt}$, with u' denoting the acoustic velocity fluctuation, performing a transformation into the frequency domain the equation can be rewritten as:

$$\hat{p}_v = \frac{\hat{u} \rho_v S_n c^2}{V \omega} i \quad . \quad (4.7)$$

The acoustic pressure, which is measured with flush mounted microphones in the resonator volume, is transformed into the acoustic velocity using this relation. Keller and Zauner [63] modeled the nonlinear part of the pressure loss terms that accounts for the vortex shedding in Equation (4.2) by only considering the fundamental harmonic. The validity of this assumption can be confirmed by the results of Ingård's and Ising's hot-wire measurements [60]. Hence, a Fourier analysis simplifies the nonlinear pressure losses to:

$$\zeta \rho \omega \hat{u} |\hat{u}| h(X) i \omega \quad (4.8)$$

with $X = |\bar{u}_{\text{pf}}/\hat{u}|$ and \bar{u}_{pf} being the mean purging flow velocity

$$h(X) = \begin{cases} \frac{1}{\pi} \left(2X \arcsin(X) + \frac{2}{3} \sqrt{1-X^2} (2+X^2) \right) & \text{if } 0 \leq X \leq 1 \\ X & \text{if } 1 < X \end{cases}. \quad (4.9)$$

With the differentiation of Equation (4.2) with respect to time and the relations from Equations (4.7) and (4.9) the following equation is obtained for the impedance ($Z = \hat{p}/\hat{u}$) in the frequency domain:

$$Z(\omega, \hat{u}, \vartheta) = -\bar{\rho}_n (L_n + \delta) \omega i + \frac{\rho_v S_n c^2}{V \omega} i - \bar{\rho}_j \left(\zeta_{\text{vis}} + \zeta_N + \zeta_T(\Delta\vartheta) + |\hat{u}| h(X) \sum_i \zeta_{\Omega_i} \right) \quad (4.10)$$

where the first term represents the oscillating mass in the neck and in its vicinity, the second term the potential energy of the compressible gas in the volume and the third term the dissipation of energy, respectively. Here, $\bar{\rho}_j$ are functions of ω, \hat{u}, L_n and ϑ . This detailed impedance model can predict the acoustic response of Helmholtz dampers in the combustion chamber based on a few isothermal measurements and one measurement at elevated temperatures, which are needed for the determination of the pressure loss-coefficients.

Assessing the damper efficiency is done by means of the acoustic energy flux $W_J = p \hat{u} S_A$ through the control area S_A . This quantity is usually used with a normalization factor for an assessment of the efficiency of liners (e.g., [73, 111]) and Helmholtz resonators (e.g., [10, 63, 138]). Here, it is employed normalized with the squared pressure amplitude:

$$Y = \frac{W_J}{\hat{p}^2} = \frac{\Re(A)}{2} S_A \quad , \quad (4.11)$$

where Y is proportional to the real part of the admittance ($A = \hat{u}/\hat{p}$), which is a measure of the damping efficiency. It correlates the amount of acoustic energy flux to the acoustic pressure amplitude, illustrating, for instance, that a resonator dissipates more energy at the resonance frequency than at other frequencies for the same acoustic pressure amplitude. Furthermore, it reproduces the characteristic narrow frequency response of the Helmholtz resonator very well and is directly proportional to the damping efficiency. The net acoustic energy flux is equivalent to the amount of energy converted from acoustic into hydrodynamic energy by means of vortices and eventually is transferred to the smaller scales and dissipated into heat. Here, it is referred to as normalized acoustic energy flux or damping efficiency and is usually normalized to a linear isothermal reference state since the focus is on relative effects caused by different impact factors. All frequency response data shown in the various figures were carefully interpolated between two closely adjacent measured points to assure that the curves

always represent the same forcing amplitude.

4.1.2 Helmholtz Resonator Flow and Density Field

The governing parameter for the interaction between a steady jet in cross-flow was identified by Smith and Mungal [127] as the momentum-flux ratio, which controls the trajectory of the emanating jet and is defined as:

$$I = \frac{\rho_{\text{gf}}}{\rho_{\text{pf}}} \cdot \frac{\bar{u}_{\text{gf}}^2}{\bar{u}_{\text{pf}}^2}. \quad (4.12)$$

Here, the momentum-flux-ratio I is defined as the ratio between the momentum-flux of the grazing flow and the nominal momentum-flux of the purging flow. This momentum-flux ratio of the steady flow components is used as the control parameter to correctly assess the impact of the grazing flow at isothermal and hot conditions.

The optical access was limited due to laser reflections caused by joints between the single tubes (main tube, resonator neck and volume). These areas are left in white color without streamlines in Figure 4.1 and all other figures.

For two different forcing amplitudes time-averaged flow fields of the emanating jet are depicted for the momentum-flux ratios of $I=0.15$ and $I=0.75$ in the Figures 4.1a to 4.1d. The neck axis coordinates are for all figures normalized with the neck diameter. In the left column the flow field for an acoustic velocity of $|\hat{u}/\bar{u}_{\text{pf}}|=0.5$ is illustrated, while the right column depicts the flow field at a higher amplitude of $|\hat{u}/\bar{u}_{\text{pf}}|=5$. The upper row shows the results for a momentum-flux ratio of $I=0.75$ and the lower one for a momentum-flux ratio of $I=0.15$. The acoustic excitation was forcing at 168 Hz, which is near the nominal resonance frequency. The color represents the local time-averaged axial flow velocity normalized with the nominal purging flow velocity \bar{u}_{pf} in the neck of 4 m/s. Superimposed are arrows, indicating the flow orientation in both directions.

For a momentum-flux-ratio of $I=0.75$ and a low forcing amplitude, the jet is deviating in the grazing flow direction forming a curved trajectory and decaying within two hydraulic diameters downstream of the resonator entrance to approximately $0.25|\bar{u}_{\text{pf}}|$. The jet velocity is close to 4 m/s, which is the nominal cooling flow velocity expected in the resonator neck. A smooth transition between the axial jet and the crossing grazing flow is featured without strong velocity gradients in the grazing flow direction. No significant axial component is observed in the resonator cavity at low amplitudes. High amplitude forcing has a strong impact on the flow field at both area jumps of the resonator neck. The jet emanating into the combustor is not curved anymore and the jet axis does not deviate significantly from the neck axis within three

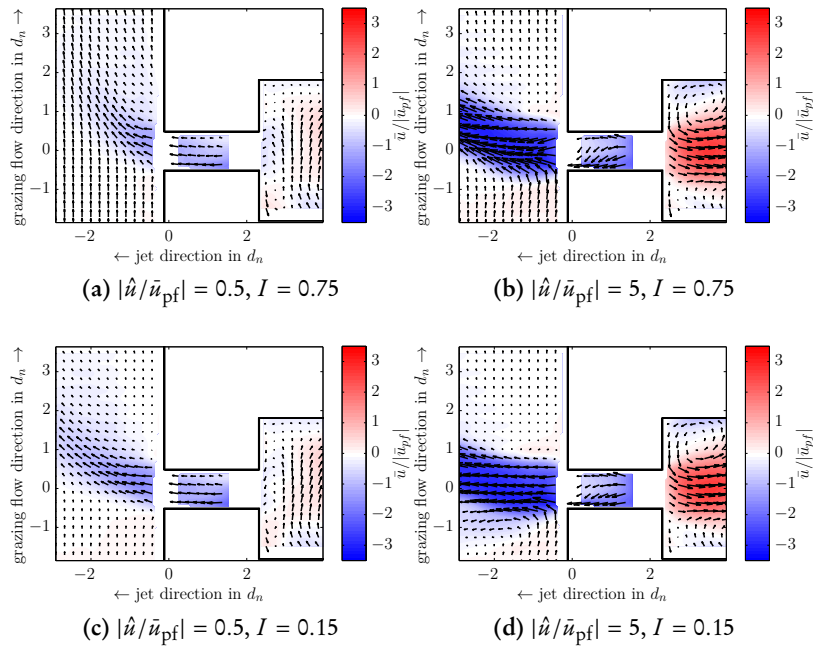


Figure 4.1: time-averaged flow fields of the emanating jet in the resonator and its vicinity for two momentum-flux ratios and forcing amplitudes.

diameters away from the neck exit. The local time-averaged flow velocity of the emanating jet exceeds three times the nominal mean flow velocity in the neck and is constant across the whole jet diameter. Additionally, the jet diameter significantly increases. The increase of the local mean flow velocity and the associated thickening of the jet is caused by the transition from a static cross-flow to a pulsating (synthetic) jet behavior. The transition in the grazing flow direction between the high axial velocities in the cross-flow jet and the grazing flow is very rapid. At these high amplitudes a strong steady back-flow emanating from the vicinity of the neck into the resonator volume is detected. This reverse flow is caused by the pulsating jet in the resonator volume. The flow in the neck shows some asymmetries in the flow profile, which may be caused by the recirculation zones at the resonator exit. Compared to the low amplitude case, the mean flow velocity in the neck is slightly increased.

For a different momentum-flux ratio of $I=0.15$ the time-averaged flow field is depicted in Figures 4.1c and 4.1d. The lowered velocity of the isothermal grazing flow has less impact on the trajectory of the steady cross-flow emanating from the resonator compared to the case with $I=0.75$. Within the measured range downstream of the resonator the jet velocity does not decay. Again, the local time-averaged velocity is in the range of the nominal purging flow velocity. Forcing at an amplitude of $|u_hat/u_pf|=5$ results in a very similar flow field in the resonator and in the vicinity of the neck as in the case with the higher momentum-flux ratio. The only

difference is observable around 2.5 hydraulic diameters downstream of the resonator entrance, where the jet is not bended in contrast to the higher momentum-flux ratio case.

A higher grazing flow momentum-flux has a significant impact on the jet trajectory at low forcing amplitudes while the influence at high forcing amplitudes is negligible.

To further analyze the interaction between grazing and oscillating cross flow, the time dependent flow fields are decomposed in the framework of a triple decomposition according of Equation (3.7) into the mean flow field $\bar{v}(x)$, the coherent fluctuations $v^c(x, t)$ and the turbulent fluctuations $v^s(x, t)$. The axial component of the coherent fluctuation u^c , obtained from a phase-averaging, is depicted for two amplitudes and a momentum-flux ratio of $I = 0.75$ in Figures 4.2a to 4.2h for different phases ψ of the oscillation. The superimposed streamlines depict u^c and v^c normalized with the nominal mean flow velocity in the neck. The thick solid line at the exit of the resonator represents the mean jet contour defined as the area where the mean jet velocity is higher than $0.25 |\bar{u}_{pf}|$ and for the higher amplitude case where the mean jet velocity is higher than $|\bar{u}_{pf}|$.

The formation of vortical structures is indicated by the streamlines for the low amplitude case. They are formed and convected downstream along the bended jet. Since the acoustic velocity fluctuation leads to a periodic change in the momentum-flux ratio, the jet trajectory is oscillating. The emanating jet straightens at high axial velocities and bends at low acoustic velocities, whereas the axial component is modulated by the acoustic velocity oscillation. As indicated by the curved stream lines, this process generates vorticity that manifest in a periodic perturbation of both velocity components.

The fluctuating flow field in the resonator neck indicates that it is not fully parallel, which is probably caused by asymmetries of the purging flow. These secondary flow phenomena are also responsible for acoustic energy losses in the linear regime. The same trend can be observed in the resonator volume.

High amplitude forcing alters the flow field in the resonator cavity as well as in the neck vicinity. Air from the vicinity of the neck is sucked into the resonator due to the high acoustic velocity amplitude neck. This would cause hot-gas penetration at engine conditions. Two large coherent structures are formed at the exit of the resonator neck. These are convected downstream along the emanating jet, creating a pulsating (synthetic) jet behavior, which explains the steady flow in the resonator volume. Evidently, the vortices entrain a constant volume flow from the vicinity of the area jumps into the jet, which is responsible for the increased mean velocities illustrated in Figure 4.1b. This higher mean velocity shifts also the static momentum-flux ratio and, consequently, straightens the jet trajectory. The steady jet, which is generated by the two large vortical structures in the resonator volume, significantly decreases the effective area jump and creates a steady back-flow.

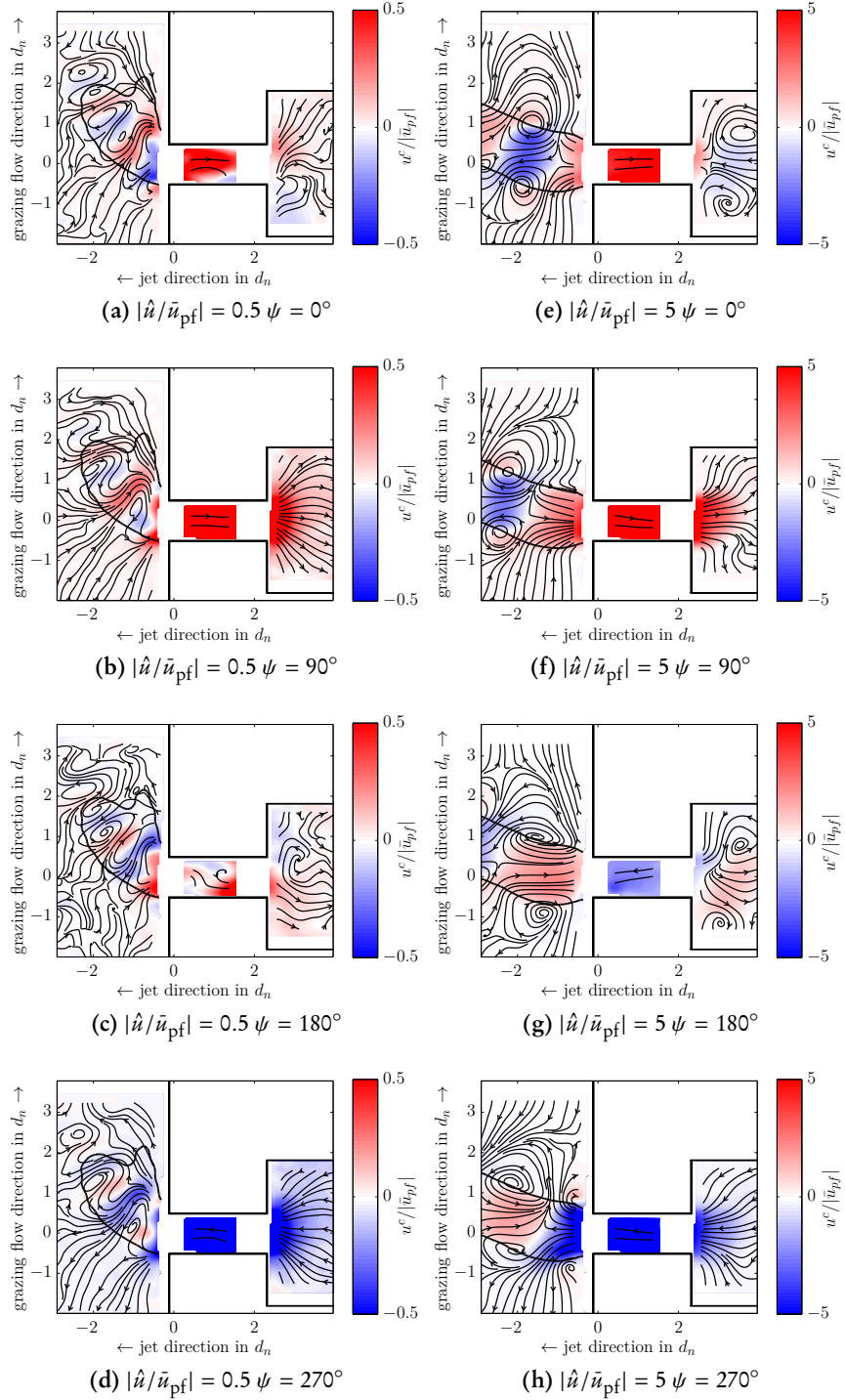


Figure 4.2: Phase-averaged fluctuating part of the flow field u^c in the Helmholtz resonator and its vicinity for two forcing amplitudes and four different phases at a momentum-flux ratio of $I = 0.75$.

Figures 4.3c and 4.3d depict the time-averaged seeding particle density captured by the QLS measurement technique for two forcing amplitudes at a momentum-flux ratio of $I=0.15$ at isothermal conditions. The grazing flow was seeded, while the purging flow was free of seeding particles. Although physical properties of the high temperature grazing flow set-up like thermal losses and other differences like the diffusion between the flows cannot be reproduced by the seeded isothermal flow, some valuable conclusions can be drawn from these measurements. Qualitatively, a high seeding concentration corresponds virtually to high temperature in the high-temperature resonator experiments.

In the linear regime, at an amplitude of $|\hat{u}/\bar{u}_{\text{pf}}|=0.5$, hot-gas does not enter the resonator neck. However, the virtual neck is subject to turbulent and molecular diffusion and the emanating jet influences the density field in the vicinity of the neck. The particle density is decreased downstream of the resonator entrance because the crossing purging-flow dilutes the grazing flow. At a higher momentum-flux ratio of $I=0.75$, which is shown in Figures 4.3a and 4.3b, the dilution of the grazing flow is much weaker. Besides the stronger deviation of the jet, which was already evident in the PIV results, the upstream concentration profile of the grazing flow is slightly different due to the higher inflow velocity at the increased momentum-flux ratio. The non-zero values in the resonator volume and neck indicate measurement errors that are probably caused by reflections and seeding deposition due to molecular diffusion during the

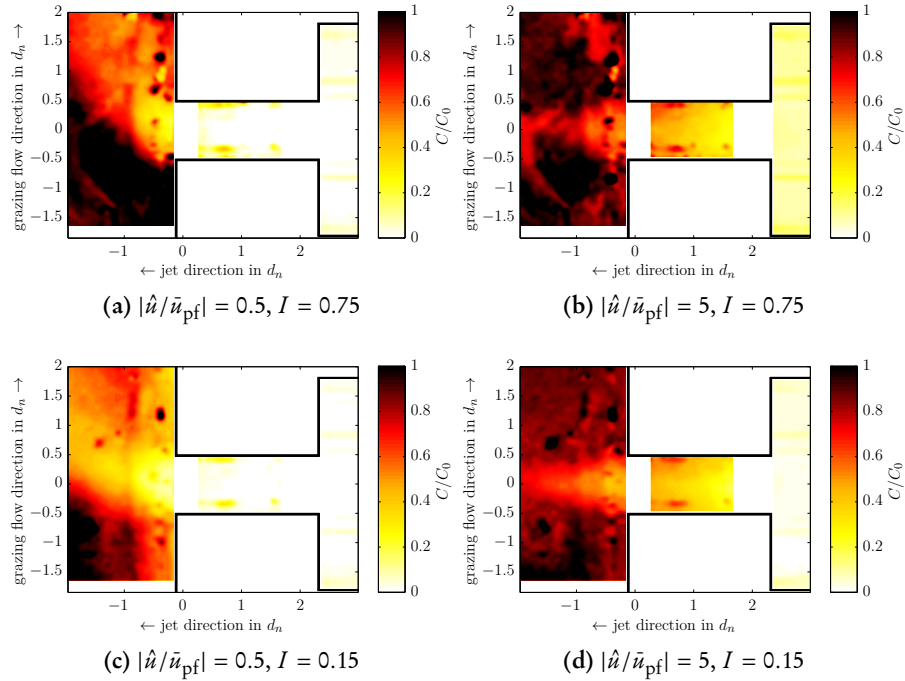


Figure 4.3: Time-averaged seeding particle concentration captured by the QLS measurement technique for two different momentum-flux ratios and two forcing amplitudes.

measurement time as well as seeding transport by recirculation flows in the neck.

At higher amplitudes, which are depicted in Figures 4.3b and 4.3d, weaker density gradients can be observed in the time-averaged grazing flow and the mean density in the neck is increased. The concentration field is significantly changed compared to the low amplitude case. Contrary to the low amplitude case, the density field is relatively homogeneous in the vicinity of the neck and is not significantly influenced by the emanating cross flow. For the higher momentum-flux ratio even a small ingestion of particles in the resonator volume is observed. Reverse flow in the neck causes severe ingestion of particles into the resonator neck and influences the time-averaged density in the neck.

The observed changes in the flow and density field have a substantial effect on the acoustic response of the Helmholtz resonator. In the consecutive subsection the effect of density gradient on the virtual neck extension will be discussed. Subsequently, the impact of density changes in the neck at higher amplitudes is modeled and the effects of flow field changes and density gradients on the energy dissipation are examined.

4.1.3 Neck-Correction

It is still not fully understood, how the virtual neck extension is influenced by the mean flow velocity, the acoustic amplitude, and temperature differences. Addressing the problems of the virtual neck extension and dissipation mechanisms, Ingård [59] suggested design guidelines for acoustic resonators for various geometries. For several geometries, correlations as a function of the neck diameter and similar geometrical dimensions are given. Like Ingård, Bies and Wilson [12] experimentally confirmed that the neck-correction is decreased by strong acoustic velocity oscillations. An overview over the influence of the Mach number and the Strouhal number is given by Peters [103]. However, a significant impact is only seen for higher Mach numbers and low wave numbers. High Mach number grazing flows affect the virtual neck extension because the trajectory of the emanating jet is influenced [131].

Highly relevant for gas turbine applications is the influence of temperature differences between the damper volume, purged with cooling air, and the plenum the resonator is flanged to. The temperature difference between the grazing flow in a combustor and the purging flow through the neck can be higher than 1000 K. The latter flow is taken from the last compressor stages and can feature temperatures of 700 K [128].

To analyze the behavior of the virtual neck extension for different temperatures and amplitudes, the measured temperatures at different axial positions in the neck were used to calculate the virtual neck extension with the help of Equation (4.10). Figure 4.4a depicts the virtual neck

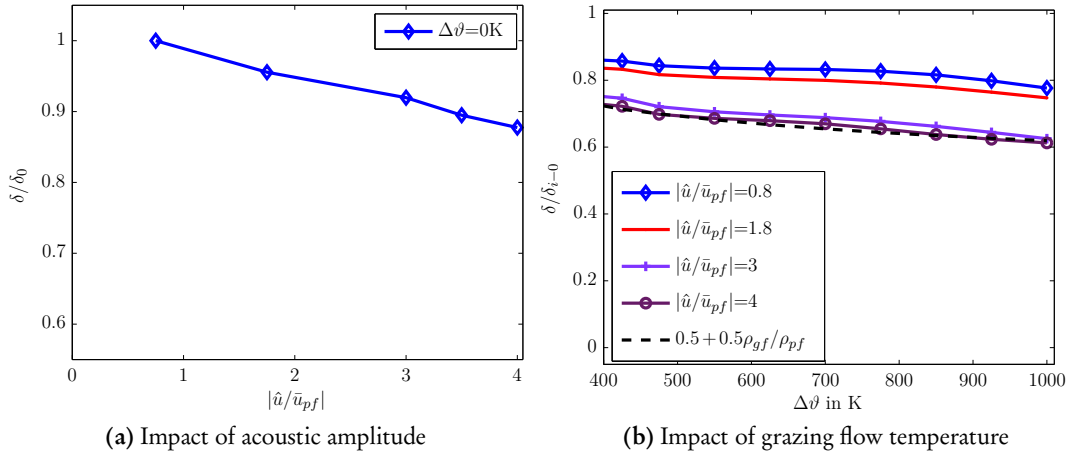


Figure 4.4: (a) Behavior of neck correction for increasing acoustic velocity amplitudes and (b) various temperature differences between grazing and purging flow. Values in (a) are normalized with the end-correction at isothermal conditions and small forcing amplitudes. Values in (b) are normalized with the end-correction at isothermal conditions and the respective forcing amplitudes.

extension for different forcing amplitudes normalized with the virtual neck extension at isothermal conditions and small forcing amplitudes δ_0 . In line with the findings of Ingård [59] as well as Bies and Wilson [12], the neck extension decreases with increasing acoustic amplitude due to the increasing acoustic displacement. As shown by means of the flow field measurements, at low amplitudes the flow field is characterized by small particle displacement and turbulent mixing is of lower importance. At higher amplitudes turbulent mixing due to vortical structures causes a nonlinear displacement of the mass in the vicinity of the neck preventing the neck extension due to inertial forces.

Figure 4.4b illustrates the total virtual neck extension δ for various temperature differences between grazing and purging flow, normalized with $\delta_{i=0}$, which denotes the end correction at isothermal conditions at the respective amplitude. The trend of a decreasing neck-correction with increasing amplitude is preserved at higher temperatures. However, a weak temperature dependence is observed. This probably stems from the inaccuracy of the temperature measurements. Consequently, the frequency shift caused by hot-gas ingestion may not be correctly reproduced by the fitted model. Nevertheless, a clear trend is identified for all amplitudes.

The mass end-correction is decreased anti proportionally to the temperature difference between purging and grazing flow. Furthermore, these results are consistent with the observation made by Jörg et al. [61]. They numerically investigated the reflection coefficient of an open-end pipe at different jet temperatures in a cold environment and compared the results to experiments conducted by Rämmal and Lavrentjev [108]. It was found that the mass end-correction

decreases with increasing temperature difference between the hot jet and the cold surrounding. This observation and the current finding of a decrease of the mass end-correction with a cold jet in a hot environment, support the note made by Bothien et al. [19], who suggested that the mass end-correction has to be scaled with the density ratio. Howe also mentioned that the mass end-correction is a function of the density ratio [53]. Following the findings of Bothien et al. [17], who investigated the effects of density gradients with the help of Krypton as purging gas, and assuming that the neck extensions on both sides are equal, one obtains:

$$\frac{\delta(\Delta\vartheta)}{\delta_0} = 0.5 + 0.5 \frac{\rho_{pf}}{\rho_c} . \quad (4.13)$$

Scaling the cold flow neck-correction with the density ratio and using the mean purging flow temperature as the cold gas density ρ_c is not in good agreement with the measured small amplitude results, as illustrated in Figure 4.4b. The model fits well to higher amplitude results. Applying the correlation with the mean density present in the virtual neck extension ($\rho_c = \rho_\delta$) results in a better agreement between theory and measurement. It must be noted that it is unclear which density must be used as the effective grazing flow density. It is evident with respect to the QLS measurement results shown in Figure 4.3 that the temperature field in the vicinity of the neck is diluted at small amplitude conditions. Hence, applying a lower grazing flow temperature to the correlation would further improve the agreement. However, further experiments are needed to justify this approach. At the highest temperature difference investigated, the total virtual neck length is decreased by 40% for linear forcing and by 100% at very high amplitudes with respect to linear forcing at isothermal conditions. The main limitation of the presented extraction of the mass end-correction out of the impedance model is the limited accuracy of the temperature measurements (deviation up to 5% of the measured value) in the neck. They are used to account for the effect of hot-gas ingestion into the neck, hence, any measurement errors result in a higher or lower neck-correction and, thus, a shorter or longer virtual neck-extension predicted by the model-fit. Especially at higher amplitudes and temperatures with large amounts of hot gas in the neck this leads probably to some smaller deviations.

Figure 4.5 depicts the normalized measured resonance frequency for various temperatures and acoustic velocity amplitudes. The temperature difference was increased between 400 K and 1000 K at a fixed momentum-flux ratio of $I = 0.15$. This was achieved by adjusting the grazing flow velocity and temperature. A damper with a nominal resonance frequency of 168 Hz was investigated.

Increasing the temperature leads to an increase in resonance frequency at very low forcing amplitudes, which is linearly connected to the change in temperature of the grazing flow. In

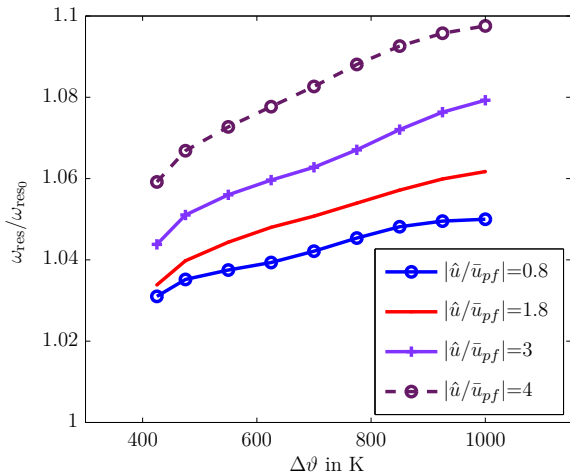


Figure 4.5: Impact of grazing flow temperature on the resonance frequency. Values are normalized with the respective resonance frequency at isothermal conditions and small forcing amplitudes. Fixed momentum-flux ratio of $I = 0.15$.

the linear regime at a temperature difference of 1000 K, the resonance frequency is increased by 5% compared to the isothermal case. At higher amplitudes the change is significantly stronger and the frequency deviates for more than 9%. At small amplitudes, the shift of the resonance frequency is caused by a modification of the virtual neck extension. At higher amplitude, the resonance frequency is strongly shifted to higher frequencies, which is caused by additional hot-gas penetration, which will be discussed in the next section.

4.1.4 Hot-Gas Penetration

The resonance frequency is not only affected by the end-correction but also by hot-gas ingestion into the neck. Since the amount of cooling flow negatively influences the engine efficiency, the design purging flow velocity in the neck is in the range of 1 m/s to 10 m/s, while the acoustic velocities in the neck can be much higher. Additionally, the damping efficiency is also adversely influenced by higher purging flow velocities. Instability amplitudes and frequencies can significantly change in the operational range of stationary gas turbines and are very dependent on the fuel composition and quality. Consequently, reverse flow cannot be always avoided or the problems associated to hot-gas penetration are even accepted to safe cooling air. While the safety distance in terms of maximum material temperature is clear, the effects on the acoustic response and, thus, the instability amplitude are more difficult to assess. Here, the effects of hot-gas penetration are modeled in Equation (4.10) with the stationary component of the spatially averaged density $\bar{\rho}_j$ in the neck (index j) and at both area jumps.

The impact of hot-gas intrusion can be nicely illustrated by analyzing the influence of the neck density on the resonance frequency. Neglecting dissipation in Equation (4.2) and differentiating with respect to time leads with the help of Equation (4.7) to the following homogeneous

differential equation:

$$\frac{\partial^2 u}{\partial t^2} + \frac{S_n \rho_v c_v^2}{VL \rho_n} u = 0. \quad (4.14)$$

This equation represents the differential equation of a harmonic oscillator and the according resonance frequency can be calculated by assuming ideal gas behavior ($c = \sqrt{\gamma R_s \vartheta}$, with R_s denoting the specific gas constant):

$$\omega_{\text{res}} = c \sqrt{\frac{S_n}{VL} \frac{\rho_v}{\rho_n}} = \sqrt{\frac{\gamma R_s S_n}{VL}} \sqrt{\frac{1}{\rho_n}}. \quad (4.15)$$

At isopycnic and isothermal conditions this equation simplifies to the well-known Helmholtz resonator resonance frequency relation reproduced in Equation (4.1) at the beginning of this chapter. It is evident that hot-gas penetration affects the density of the air in the neck and consequently the density becomes smaller for regions of the neck, with hot-gas ingestion, which causes a decreased time-averaged density. Hence, the resonance frequency is shifted towards higher frequencies. If the purging flow velocity is small compared to the acoustic velocity amplitude, it becomes possible that the neck is exposed, in a worst-case scenario, to hot gas for half of every oscillation period or it can even enter the cavity. The later case would lead to a further decreased neck density, since it would affect the purging flow temperature.

Using the ideal gas law $\rho = p/(RT)$ and using a time-averaged density of the neck, the relationship between the resonance frequency without (index c = "cold") and with hot-gas penetration (index h = "hot") becomes a sole function of the temperatures of the volume and the combustion chamber:

$$\frac{\omega_h}{\omega_c} = \sqrt{\frac{\rho_v}{\bar{\rho}_n}} = \sqrt{\frac{2\rho_c}{\rho_c + \rho_h}} = \sqrt{\frac{2}{1 + \vartheta_v/\vartheta_{cc}}}. \quad (4.16)$$

Figure 4.6 illustrates the normalized resonance frequency deviation for hot-gas penetration of the whole neck. The resonance frequency can be shifted by more than 20% for realistic engine temperatures of, for instance, $\vartheta_{gf} \approx 1800\text{ K}$ and $\vartheta_v \approx 700\text{ K}$ [128] and high velocity amplitudes in the neck or short necks, which are common due to the strict space limitations in combustion chambers.

Assuming that the flow in the region of the neck extension behaves similarly to the flow in the neck, the time dependent spatially averaged density of the air during reverse flow is modeled

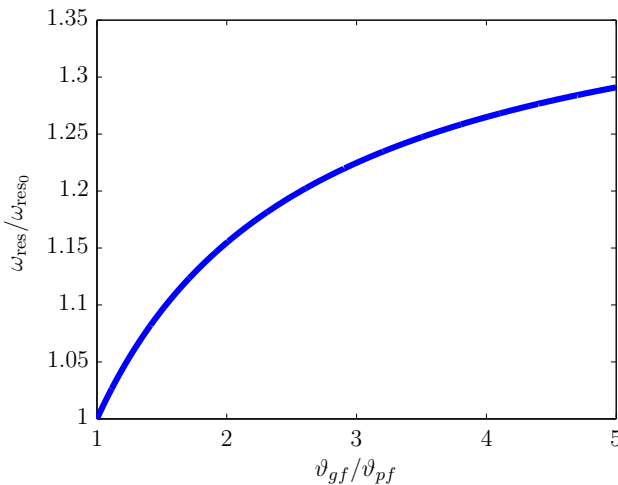


Figure 4.6: Normalized resonance frequency for various temperature ratios of grazing and purging flow. Full penetration of neck assumed.

as:

$$\bar{\rho}_n(t) = \rho_v + \frac{\rho_v - \rho_{gf}}{L} \left| \int_{c_1}^t (\bar{u} + u') dt \right| \quad \text{for } c_1 < t \leq c_2. \quad (4.17)$$

This equation implicitly neglects the effect of thermal diffusion in the neck. From a practical point of view this is reasonable for most of the Helmholtz Resonator applications. The integration interval $[c_1, c_2]$ is defined by the moments of total flow direction reversal in the neck and exit of all hot gas out of the neck. These points in time are marked in the sketch shown in Figure 4.7 together with the reverse point b , which marks the moment when the total flow is again positive and moving towards the neck exit. The sketch illustrates the air velocity in the neck and the assumed corresponding behavior of the spatially averaged density. The point c_1 is derived by solving $\bar{u} + u = 0$ and becomes $c_1 = (\pi + \arcsin X)/\omega$. Whereas the upper integration limit c_2 is derived by solving the following condition, which implies that the distance covered between the points $c_1 - b$ is the same as $b - c_2$, where b is the second zero-crossing of the velocity ($b = (2\pi - \arcsin X)/\omega$):

$$\int_{c_1}^b X + \sin \omega t dt = - \int_b^{c_2} X + \sin \omega t dt. \quad (4.18)$$

It can be rewritten as:

$$X(\pi + \arcsin X) + \cos(\arcsin X) = (X\omega)c_2 - \cos(\omega c_2), \quad (4.19)$$

and it can only be solved iteratively. Finally, using the presented integration limits and Equation (4.17), an expression for the air density in the neck, which corresponds to Figure 4.7,

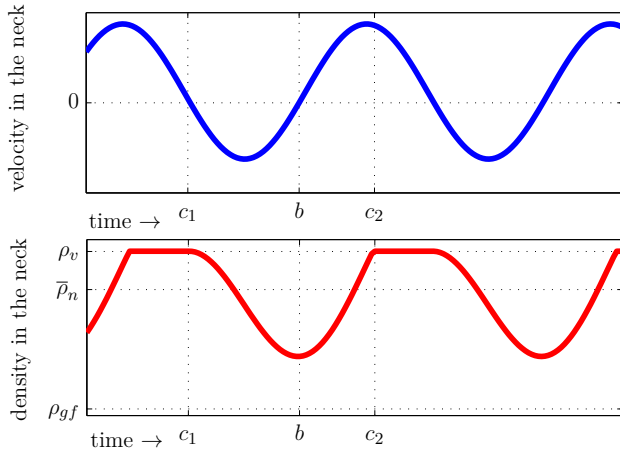


Figure 4.7: Acoustic velocity in the neck at very high amplitudes (top), and corresponding assumed spatially-averaged density of the neck (bottom). Time-averaged density ($\bar{\rho}_n$), density of the cavity (ρ_v), density of grazing flow (ρ_{gf}), and integration limits of Equation (4.18) indicated.

can be found:

$$\bar{\rho}_n = \begin{cases} \rho_v + t X \frac{-\cos(\omega t) + \sqrt{1-X^2} - X(\pi + \arcsin X)}{\omega} \hat{u} \frac{\rho_v - \rho_{gf}}{L} & \text{if } c_1 \leq t \leq c_2 \\ \rho_v & \text{if } c_2 \leq t \leq c_1 + 2\pi. \end{cases} \quad (4.20)$$

Consequently, the density at the plane between neck and combustion chamber, which is needed for the impedance model can be written as:

$$\rho_{nc} = \begin{cases} \rho_{gf} & \text{if } c_1 \leq t \leq c_2 \\ \rho_v & \text{if } c_2 \leq t \leq c_1 + 2\pi. \end{cases} \quad (4.21)$$

These unsteady expressions for the different densities of neck and area jump can be included into the proposed frequency space impedance model by performing a Fourier series decomposition and considering the steady component only, which leads to:

$$\begin{aligned} \bar{\rho}_n = & -\frac{\omega}{2\pi} \left(\frac{-2\pi\rho_{pf}}{\omega} + \frac{c_2^2 \bar{u}_{pf} (\rho_{gf} - \rho_{pf})}{2L} \right. \\ & + \frac{c_2 u \sqrt{(1-X^2)(-\rho_{gf} + \rho_{pf})}}{L\omega} + \frac{c_2 \bar{u}_{pf} (\pi + \arcsin(X))(-\rho_{gf} + \rho_{pf})}{L\omega} \\ & + \frac{u(X + \sin(c_2\omega))(-\rho_{gf} + \rho_{pf})}{L\omega^2} + \frac{u \sqrt{(1-(X)^2)(\pi + \arcsin(X))(\rho_{gf} - \rho_{pf})}}{L\omega^2} \\ & \left. + \frac{\bar{u}_{pf}(\pi + \arcsin(X))^2(\rho_{gf} - \rho_{pf})}{2L\omega^2} \right) \end{aligned} \quad (4.22)$$

and for the density at the neck entrance:

$$\bar{\rho}_{nc} = \frac{\omega}{2\pi} \left(c_2(\rho_{gf} - \rho_{pf}) - \frac{\rho_{gf}(\pi + \arcsin(X))}{\omega} + \frac{\rho_{pf}(3\pi + \arcsin(X))}{\omega} \right) . \quad (4.23)$$

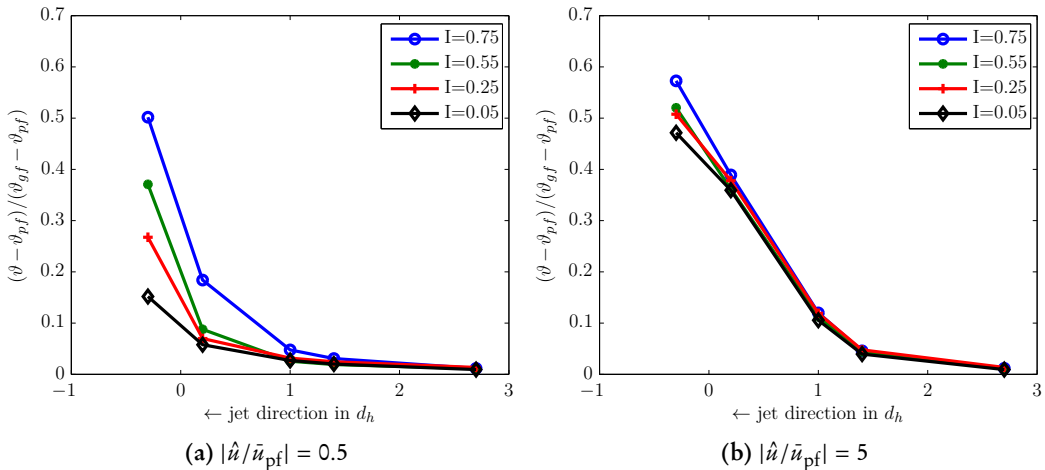


Figure 4.8: time-averaged temperature in the resonator neck at different axial positions in the neck for various momentum-flux ratios and two forcing amplitudes at a frequency of 196 Hz.

Limiting the model to the steady component of the density function is advantageous in terms of calculation time and still very accurate. The model can be used in the frequency domain and the stability of the iterative solution procedure is improved. The model remains reliable because the impact of the varying components is small compared to the other terms of the differential equation.

Temperature measurements are used to verify the density model results. The temperature in the resonator neck can be used to assess the time-averaged density in the neck. These were measured with an ultra-thin thermocouple in the resonator neck for different amplitudes and grazing flow velocities. The spatial temperature distribution in the neck was obtained by adjusting the thermocouple at different positions along the longitudinal axis of the neck and measuring for at least eight seconds for every forcing amplitude and frequency. The influence of heat radiation and convective effects on the detected temperature were not considered. Especially for higher temperatures in the range of approximately 1500 K, for which heat radiation plays an important role, this may introduce an error of roughly 80 K [75]. It is difficult to correct the measured temperatures in the investigated unsteady temperature field. For the highest temperatures observed, the error can be up to 5% of the measured value.

The normalized temperature difference along the neck axis is shown in Figures 4.8a and 4.8b. Please note that the total length of the investigated resonator neck was $L_n \approx 2.6 d_n$. The temperature profile for four different momentum-flux ratios at a linear amplitude of $|u_hat/u_bar_pf| = 0.75$ is depicted in Figure 4.8a. The same momentum-flux ratios are shown in Figure 4.8b at a nonlinear forcing amplitude of $|u_hat/u_bar_pf| = 5$, which features strong reverse flow in the neck.

In the linear regime, strong differences between the different momentum-flux ratios were

observed for the temperature of the virtual neck extension and the vicinity of the neck, respectively. The differences are caused by the increased turbulent mixing between grazing and purging flow emanating out of the resonator neck. Although no reverse flow is caused by the acoustic velocity at this amplitude level, the mean temperature in the neck is increased up to a length of $1 d_n$ in the neck. This increase of mean temperature in the physical neck is caused by a recirculation zone created by the grazing flow [127]. Consequently, the temperature is increasing with rising momentum-flux ratio. This effect is not captured by the presented time-averaged spatial density approach. However, as shown in Figure 4.9, the effect on the acoustic response is relatively small for a very similar geometry. These measurements were carried out as limited preliminary investigations in the low amplitude and low Mach number regime. However, at an increased difference between grazing and purging flow temperatures of 900 K, a shift of 2 Hz of the resonance frequency is observed due to the increased temperature at the neck entrance. Nevertheless, for configurations with very short necks and large cross sectional areas of the neck this effect can become important. The strong temperature differences at the entrance of the resonator are also an import information for the design of Helmholtz resonators and the resulting component lifetime.

At very high amplitudes, the differences between various momentum-flux ratios in terms of temperatures in the neck vanish. These measurement results are depicted in Figure 4.8b. Hot-gas penetration significantly increases the mean temperature in the neck up to $x/d_n = 1.5$. As shown in the phase-averaged fluctuating flow field for high amplitudes (Figures 4.2e – 4.2h), the flow field is dominated by the unsteady jet emanating from the Helmholtz resonator. In line

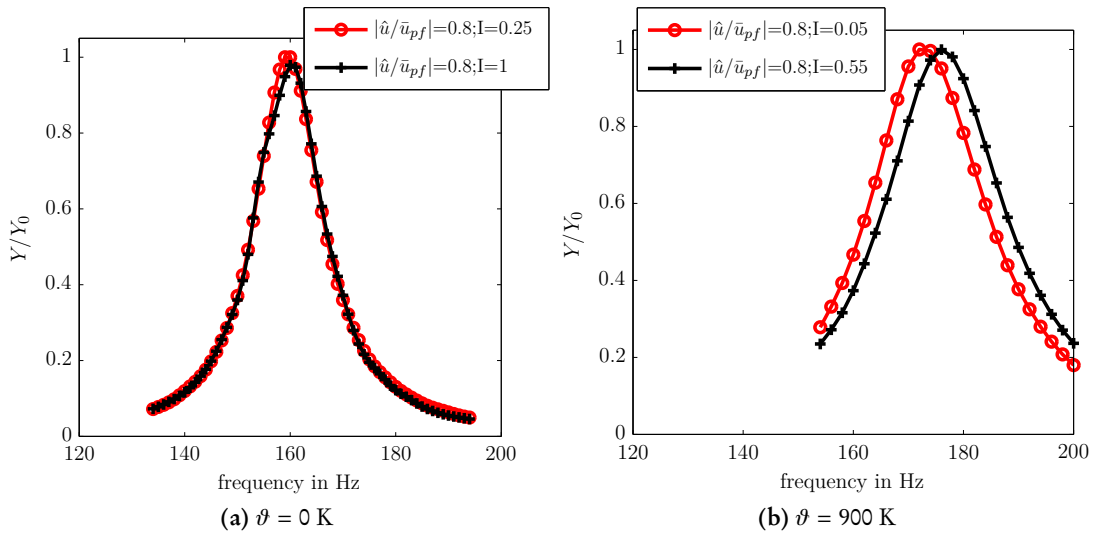


Figure 4.9: Normalized acoustic energy flux for different momentum-flux ratios in the linear amplitude regime and two different grazing flow temperatures.

Table 4.1: Comparison of measured and modeled spatially-averaged density in the neck for forcing at 196 Hz for various amplitudes and a temperature of the grazing flow of $\vartheta_{gf} \approx 1273$ K. Measured density derived from five point temperature measurements in the neck at $I=0.75$.

Velocity amplitude in $ \hat{u}/\bar{u} $	Measured $\bar{\rho}_n$ in kg/m^3	Modeled $\bar{\rho}_n$ in kg/m^3	Deviation in %
0.75	0.96	1.13	15
3	0.91	1.02	11
5	0.83	0.87	5
6	0.77	0.78	1

Table 4.2: Comparison of measured and modeled spatially-averaged density in the neck for forcing at 196 Hz for various amplitudes and a temperature of the grazing flow of ≈ 1273 K. Measured density derived from five point temperature measurements in the neck at $I=0.05$.

Velocity amplitude in $ \hat{u}/\bar{u} $	Measured $\bar{\rho}_n$ in kg/m^3	Modeled $\bar{\rho}_n$ in kg/m^3	Deviation in %
0.75	1.05	1.13	7
3	0.99	1.02	3
5	0.85	0.87	2
6	0.78	0.78	0

with this observation, at high amplitudes very little temperature differences in the neck can be observed for different grazing flow velocities. The similarity of the flow fields at high amplitudes for different static momentum-flux ratios is the reason for the vanishing differences between the temperature profiles. The QLS-results, shown in Figure 4.3, are qualitatively similar to the trend provided by the temperature profiles, although the concentration of hot-gas in the resonator was overestimated up to 10% compared to the temperature measurement results.

To compare the model results to the measurements, the mean density in the neck is calculated using the thermocouple measurements in the neck. In Table 4.1 the results are compared in a worst-case scenario to the measurements with a high momentum-flux ratio at $\Delta\vartheta = 900$ K, which feature relatively high temperatures already for small amplitudes due to the strong recirculation zone at the neck entrance.

The temperature in the resonator volume at the neck plane is assumed to be known, which is from a practical point of view reasonable. Due to heat conduction and radiation the air temperature at this plane is increased by 7 K at a temperature difference of 1000 K. An idealized theoretical consideration of the heat conduction and radiation from the exhaust tube to the air in the neck leads to an increase of 10 K.

As expected, the deviation between model and measurement is relatively high at low amplitudes, tending to small deviations for very strong forcing. The flow field in the neck and in the vicinity of the neck features at high amplitudes obviously much more the model assumptions of a clear separation between cold and hot flow streams. Since the model does not account for hot-gas ingestion into the cavity, it is only valid for amplitudes smaller than $|\hat{u}/\bar{u}| < 6$ for the investigated geometry. The agreement seems reasonable, taking into account that the calculation of the mean density of the neck out of five measurement points in the neck features only a limited accuracy.

Comparing the model results to measurements taken for a very small momentum-flux ratio of $I=0.04$ at the same grazing flow temperature in Table 4.2, shows a better agreement for low amplitudes. Evidently, the deviation at very low amplitudes stems from the hot-gas recirculation zone at the neck entrance. Due to the square route correlation between resonance frequency and mean density of the neck (see, Equation (4.15)), even the relatively high deviations at small amplitudes in the range of 7% to 15% cause only single digit deviations in terms of the resonance frequency.

The acoustic response of the Helmholtz resonator and the effect of temperature gradients between grazing and purging flow on the damping performance and the resonance frequency is illustrated in Figure 4.10. Four curves are shown, reproducing the normalized acoustic energy loss Y/Y_0 for two amplitudes and two different grazing flow temperatures at the same momentum-flux ratio of $I=0.15$. For low amplitude forcing, the resonance frequency is shifted by 10 Hz with respect to the isothermal reference case due to the change of the virtual neck length. At higher amplitudes the resonance frequency is shifted due to hot-gas penetration by

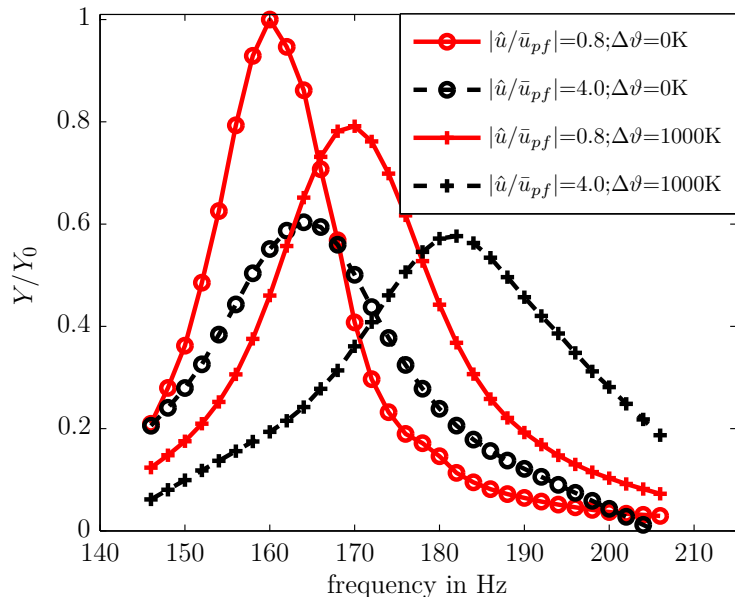


Figure 4.10: Normalized acoustic energy loss, additionally normalized with the maximum value at isothermal small amplitude conditions, for two forcing amplitudes at constant $I=0.15$ for two different temperature differences between grazing and purging flow.

additional 12 Hz with respect to the linear acoustic response at elevated temperatures. It is worth noting that the resonance frequency is shifted between the linear and nonlinear response by 2 Hz already in the isothermal case. This shift is apparently caused by a change of the virtual neck extension at high amplitudes. Evidently, all three introduced effects, the amplitude and temperature dependence of the length correction as well as the change of the resonance frequency due to hot-gas penetration important, as shown with the presented hot-gas experiments.

However, increasing the temperature of the grazing flow by 1000 K leads to a decreased normalized acoustic energy loss for the linear amplitude regime, which is about 25% lower with respect to the isothermal case. For the nonlinear forcing amplitude, almost no difference is observed in terms of the damping efficiency between the isothermal case and the measurement results with hot grazing flow. Nevertheless, as expected, the normalized acoustic energy loss is decreased at higher forcing amplitudes compared to the linear amplitude regime. The next sub-section is focused on explaining the observed effects on the damping efficiency in the linear and nonlinear regime.

4.1.5 Acoustic Dissipation at High Amplitudes and Density Stratification

High acoustic pressure oscillations cause very strong acoustic velocity oscillations in the neck of the damper, especially at the resonance frequency. These fluctuations cause vortices, which are responsible for the conversion of acoustic energy into vorticity and finally into heat. Although it seems to be contradictory, the increased generation of vorticity and the associated dissipation of acoustic energy decreases the damping efficiency of the Helmholtz resonator around the resonance frequency because the quality factor of the oscillator is decreased. At the same time, the damping can be increased at off-design frequencies [138]. Hence, additional dissipation will always tend to decrease the normalized acoustic energy dissipation at the resonance frequency while off-design frequencies can feature an increasing or decreasing damping efficiency, with an optimum at a certain ratio of amplitude and dissipation.

For low amplitude forcing, the illustration of the ratio of the normalized acoustic energy loss in Figure 4.11a reveals that the damping efficiency at the resonance frequency is decreased linearly with increasing temperature compared to the isothermal case. However, at higher amplitudes the effect becomes less pronounced and almost vanishes at a forcing amplitude of $|\hat{u}/\bar{u}_{pf}|=4$. Hence, for industry relevant temperature differences between purging and grazing flow the normalized acoustic energy loss can be up to 20% smaller for the investigated geometry compared to isothermal conditions.

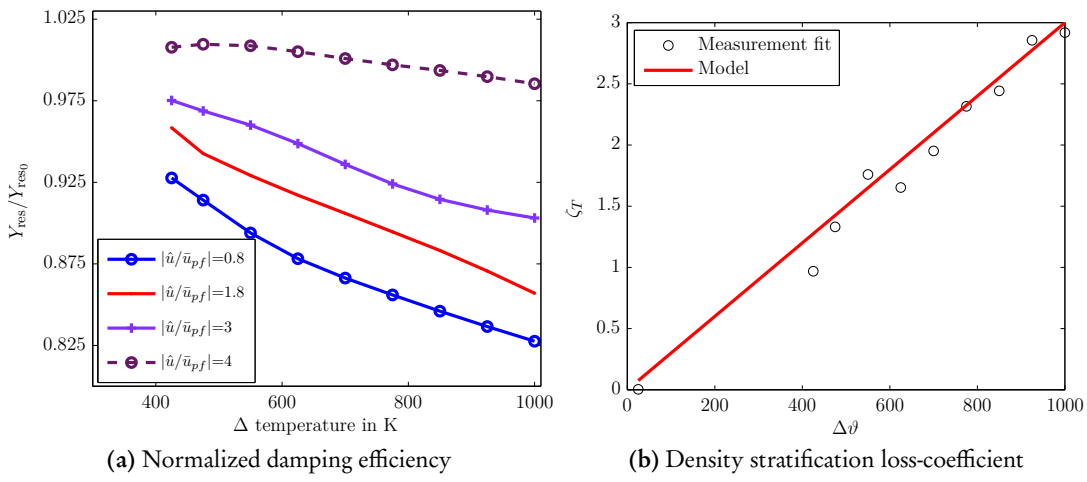


Figure 4.11: (a) Impact of grazing flow temperature on the normalized acoustic energy loss at the resonance frequency; additionally normalized with the respective values at the isothermal resonance frequency at small forcing amplitudes. (b) Comparison of fitted data and empirical modeling approach ζ_T .

To account for the losses created by the density stratification at the entrance of the resonator the neck loss-coefficient ζ_T is introduced in the impedance model (see, Equation (4.10)). Although not discussing the effect further, the additional losses were mathematically distinguished already by Howe [53], who identified the acoustic energy flux as:

$$W_J = \int \mathbf{v}' \rho_{pf} \left((\boldsymbol{\Omega} \times \mathbf{v}) + p' \nabla \frac{1}{\rho_i} \right) dx_i \quad , \quad (4.24)$$

with the cross product of the vorticity vector $\boldsymbol{\Omega}$ and the velocity vector \mathbf{v} representing the dissipation created by vorticity and the term $p' \nabla \frac{1}{\rho_i}$ denoting the losses generated by acceleration in a stratified density field. The latter effect is taken into account by means of the proposed loss-coefficient ζ_T , which is a linear function of the temperature difference between grazing and purging flow $\Delta \vartheta$. For the investigated geometry and a momentum-flux ratio of $I = 0.15$ the loss-coefficient becomes $\zeta_T \approx 0.003 \Delta \vartheta$ as depicted in Figure 4.11b. The fit of the impedance model for small amplitudes and various temperatures of the grazing flow is shown, clearly revealing a linear trend of the additional loss-coefficient. However, this is an empirical correlation strictly valid for the investigated geometry, which requires further investigation. Nevertheless, with respect to Equation (4.24) the proposed concept of a linear loss-coefficient should be generally valid in the presence of density stratification.

The decreased damping efficiency is caused by the density gradients between grazing and purging flow and the associated additional dissipation. Since this mechanism is linearly connected to the acoustic velocity amplitude, it becomes less important for higher amplitudes,

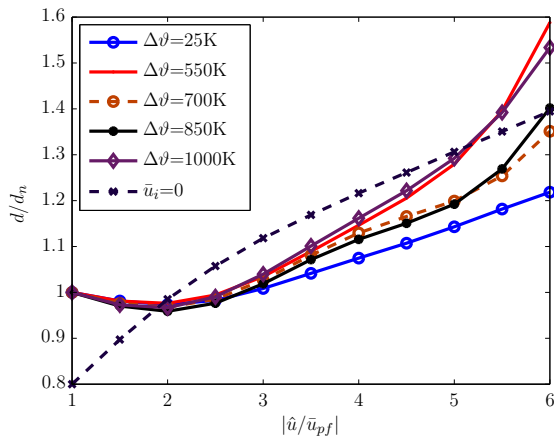


Figure 4.12: Normalized calculated effective jet diameter for various amplitudes and temperature differences at $I = 0.15$, beside one curve ($\bar{u}_i = 0$) that denotes the case without any mean flow, which is normalized with the nominal purging flow velocity.

where the nonlinear vortex shedding mechanisms dominate the dissipation of acoustic energy. At the same time, the density at the area jump between resonator and combustor decays due to hot-gas penetration. This decreases the momentum-flux of the emanating jet and causes less dissipation caused by the nonlinear vortex shedding at the edges of the neck exit. Consequently, at extremely high amplitudes, the losses at the resonance frequency can also be smaller than at isothermal conditions, leading to an increased normalized acoustic energy loss at the resonance frequency compared to the isothermal acoustic response.

The nonlinear pressure loss-coefficients are functions of the effective area change (see, Equations (4.4) and (4.5)). As shown with the phase-averaged flow field measurements in Figures. 4.1c and 4.1d, the jet diameter increases with rising acoustic velocity amplitude. This trend is also reflected in Figure 4.12, which illustrates the effective diameter as a function of the normalized acoustic amplitude for different temperatures and for an isothermal case without purging and grazing flow. The curves are obtained from a fitting between the impedance model and the experimental data for various grazing flow temperatures at a constant momentum-flux ratio of $I = 0.15$. The effective diameter of the neck remains almost constant up to $|\hat{u}/\bar{u}_{pf}| = 2$. At this amplitude the curves for the different temperatures intersect the curve that represents the virtual diameter for the response without purging and grazing flow. Without any mean flow influence the response is immediately nonlinear, showing a change of the effective jet diameter also for small amplitudes. At high amplitudes, the data show some scattering between the experiments performed with different temperatures. This indicates that the losses produced by the density gradient have also a nonlinear component, which is not covered in the current modeling approach and affects the fitting of the model and the measurements. It probably stems from the strong changes in the density field caused by the changed flow field in the vicinity of the neck and the hot-gas penetration, as it is also shown qualitatively by the QLS results (see, Figures 4.3).

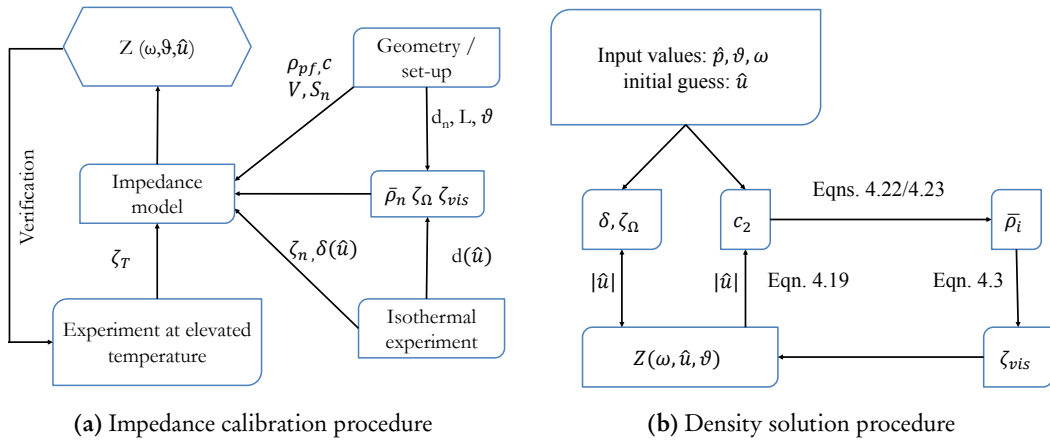


Figure 4.13: (a) Calibration procedure for the detailed impedance model. (b) Solution procedure for the time-averaged mean spatial density.

Summarizing and reorganizing the presented findings, the subsequent sub-section gives guidance for the application of the detailed impedance model and the associated derivation of the hot-gas response of the Helmholtz resonator from isothermal experiments.

4.1.6 Application of the Detailed Impedance Model

The proposed detailed impedance model accounts for all effects observed in the hot-gas experiments. Nevertheless, it depends on the experimental calibration of the loss-coefficients, the amplitude dependency of the end-correction and the effective jet diameter. Additionally, at least one measurement at elevated temperatures of the grazing flow is needed to incorporate the impact of the density stratification at the vicinity of the neck. In the typically effective frequency range of Helmholtz resonators, the frequency dependence of these quantities can be neglected. Hence, isothermal single frequency measurements at several amplitudes levels and one measurement at elevated temperature in the linear amplitude regime is sufficient for the model calibration. Then, the model is applicable to resonators with different geometrical dimensions of the volume, grazing flow temperatures, instability amplitudes and operation points of the combustor without further experiments.

Figure 4.13a illustrates the calibration procedure for the detailed impedance model. The damper dimensions and purging flow properties can be taken from the geometry and installation set-up. Isothermal experiments at various amplitude levels are needed for the empirical determination of the end-correction and the virtual jet diameter dependency on the acoustic velocity amplitude. The losses due to flow asymmetries and so forth can only be incorporated by experimental calibration. Additional acoustic response measurements at elevated temperatures

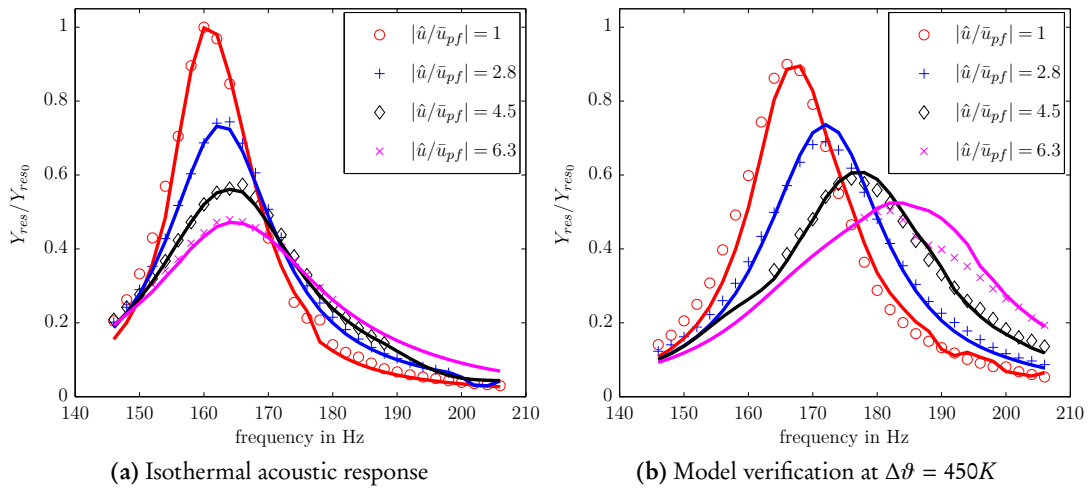


Figure 4.14: Normalized acoustic energy dissipation. Additionally normalized with isothermal linear response at the resonance frequency. Comparison of model and measurements for temperature differences between grazing and purging flow of (a) $\Delta\vartheta = 0K$ and (b) $\Delta\vartheta = 450K$. Markers represent measurement points and lines depict model results.

can be used for the determination of the loss-coefficient ζ_T that accounts for the density stratification. Furthermore, the measurements at elevated temperature can also be used for the model verification step. The time-averaged flow temperature in the neck is of crucial importance for the viscous loss-coefficient ζ_{vis} (see, Equation (4.3)). It depends on the angular frequency and the Prandtl number, which is temperature dependent. The mean temperature in the neck can be calculated from the time-averaged mean density in the neck $\bar{\rho}_n$. This quantity and the acoustic velocity amplitude, which determines the actual end-correction and nonlinear loss-coefficients, have to be found iteratively, as illustrated in Figure 4.13b.

The solution procedure for the determination of the time-averaged density in the neck for a given pressure amplitude p_{cc} generating reverse flow can be described as follows: In a first step, \hat{u} has to be estimated. The value is used in a second step for the solution of Equation (4.19) and for obtaining the end-correction and nonlinear pressure loss-coefficient. In the next step, the steady components of ρ_n and ρ_{nc} are obtained with the help of Equations 4.22 and 4.23. Using the steady component of the density function and the ideal gas law ($\vartheta = p/(R_s \rho)$), the time-averaged temperature in the neck can be calculated. This leads with the help of Equation (4.3) to the viscous pressure loss-coefficient. By solving of Equation (4.10), a new guess for \hat{u} can be obtained. The procedure must be repeated, until the desired level of deviation is reached. It was observed that the solution procedure is independent of the start values, as long as the start value is physically meaningful, and the computational time is negligible for a strict convergence criterion of 10^{-5} .

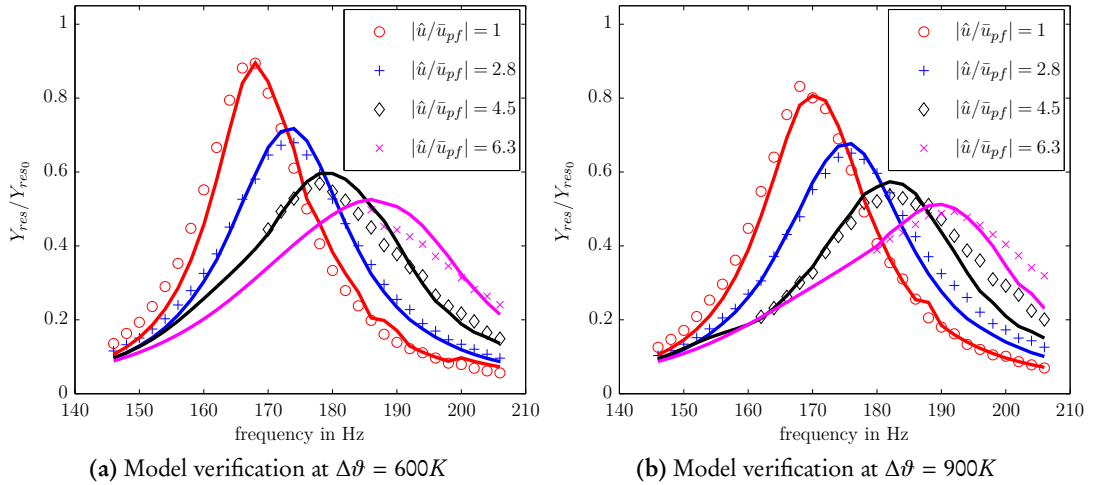


Figure 4.15: Normalized acoustic energy dissipation. Additionally normalized with isothermal linear response at the resonance frequency. Comparison of model and measurements for temperature differences between grazing and purging flow of (a) $\Delta\vartheta = 600K$ and (b) $\Delta\vartheta = 900K$. Markers represent measurement points and lines depict model results.

The results of the isothermal model calibration for the investigated Helmholtz resonator are depicted in Figure 4.14a. The markers depict the measurement results for various amplitudes of the acoustic velocity in the resonator neck. An outstanding agreement between model and measurements is achieved for all amplitudes. The damping efficiency decays rapidly at the resonance frequency and the resonance frequency is slightly shifted to higher frequencies due to the reduction of the virtual neck length. Off-design frequencies show an increasing damping efficiency, while frequencies in between the resonance frequency and off-design frequencies have an optimum damping efficiency at intermediate amplitudes. The very good agreement was achieved with empirical correlations for the amplitude dependence of the virtual neck extension and the virtual neck diameter that were discussed in the previous sections of this chapter.

As discussed in Section 4.1.3, the end-correction is a function of the acoustic amplitude and the density ratio between grazing and purging flow. In the investigated amplitude range, the end-correction is linearly decaying with increasing amplitude. Here, the value of $\delta = 8/(3\pi)0.84d_n$ is applied for small amplitudes up to $|\hat{u}/\bar{u}_{pf}| < 1$. It was found with the help of the isothermal calibration measurements. For higher forcing amplitudes, the value decays linearly to a value of $\delta = 8/(3\pi)0.64d_n$ at an amplitude of $|\hat{u}/\bar{u}_{pf}| = 8$. At elevated grazing flow temperatures the relation of Equation (4.13) is used.

The correlations given in Equations (4.4)-(4.5) are used for the determination of the nonlinear loss-coefficients ζ_Ω . At small amplitudes, a total value of $\zeta_{\Omega-1} = 0.98$ and $\zeta_{\Omega-2} = 0.47$ can be found for the two area jumps. Incorporating the findings presented in Figure 4.12, these values are set to be constant for amplitudes up to $|\hat{u}/\bar{u}_{pf}| = 2$. At very high amplitudes, the increased

effective jet diameter and the reverse flow have a strong impact on the loss-coefficient. These effects are modeled by decreasing the loss-coefficients linearly to $\zeta_{\Omega-1} = 0.73$ and $\zeta_{\Omega-2} = 0.36$ at a normalized amplitude of $|\hat{u}/\bar{u}_{pf}| = 10$. This correlation is obtained by considering the effect of the reverse flow by using again the correlations in Equations (4.4)-(4.5) and taking into account the different flow direction. Additionally, it is assumed that ζ_{Ω} can be averaged at $|\hat{u}/\bar{u}_{pf}| = 10$ between the respective values for backward and forward flow. The change of the effective jet diameter was obtained from the isothermal measurements.

Additionally, the loss-coefficient ζ_T which accounts for the additional dissipation generated by the density stratification is set to $0.003\Delta\vartheta$. Basically, a single frequency measurement at moderately increased temperatures is sufficient to obtain this variable.

At an elevated temperature difference between grazing and purging flow of $\Delta\vartheta = 450K$, which is depicted in Figure 4.14b, a very good agreement between model and measurement is obtained. The initial change in resonance frequency and damping efficiency as well as the differences with increasing velocity amplitude are very good reproduced. At extremely high amplitudes of $|\hat{u}/\bar{u}_{pf}| > 6$, the model overestimates the normalized acoustic energy loss towards higher frequencies. This deviation is mainly caused by the temperature dependent spread of the virtual neck diameter depicted in Figure 4.12 for very high amplitudes. Nevertheless, the agreement is still acceptable.

Furthermore, Figures 4.15a and 4.15b illustrate the comparison of model and measurements for various amplitudes at temperature differences of $\Delta\vartheta = 600K$ and $\Delta\vartheta = 900K$. The agreement is very good without significant deviations in terms of frequency or normalized damping efficiency. It is interesting to compare the isothermal acoustic response to the response at an elevated temperature of $\Delta\vartheta = 900K$. From a practical point of view it is worth noting that neglecting the effects of density stratification and hot-gas penetration leads to an overestimation of the normalized acoustic energy loss at the design resonance frequency by 40% at small amplitudes and by 50% at very high amplitudes. Hence, taking the hot-gas effects into account, which were found in this work, significantly improves the passive control of combustion instabilities. However, damping is also provided by other elements of the gas turbine combustor. These are discussed in the next section.

4.2 System Damping

All elements of the acoustic network model of the investigated set-up provide acoustic damping: ducts, burner, and the terminations. However, the damping of the ducts is of lower order compared to the other contributions and is consequently neglected. The other elements providing damping in the investigated combustor are discussed subsequently.

Assessing the acoustic damping accurately is challenging because it depends on the temperature, flow field, and several other influence factors. For instance, Palies et al. [98] measured the system response to acoustic excitation at reacting conditions and reconstructed a quality factor of the measured oscillation. However, this approach is very vulnerable because it is difficult to filter the contribution of the flame and the system boundary conditions. In contrast to that, Krebs et al. [71] applied numerical Siemens in-house tools to incorporate the system damping. However, the results of the limit-cycle analysis were very inaccurate.

Here, the Multi-Microphone-Method was employed. The upstream reflection coefficient is obtained from the microphone array upstream of the burner with acoustic excitation from the downstream end. Analogously, the acoustic boundary condition at the combustor outlet is determined from the microphone signals on the downstream side when using excitation from the upstream end. The burner transfer matrix is obtained from two excitation states, employing the speakers on both sides. Mono-frequency excitation is used with records of 16–32 seconds length for each frequency. A significant advantage of using these experimental response functions for the network elements is that the damping effect is accurately incorporated into the model.

However, as pointed out by, e.g., Schuller et al. [124] the damping of the acoustic boundary conditions can vary with the acoustic velocity amplitude. To assess the influence of this effect measurements for various amplitudes and frequencies were conducted for the burner and open-end reflections coefficient. Due to the limitations of the experimental set-up, the upstream boundary conditions could be only measured in the linear regime.

4.2.1 Acoustic Burner Transfer Matrix

The burner transfer matrix connects the acoustic pressure and velocity at the inlet plane to the quantities at the outlet. The burner can be treated as acoustically compact, which leads to an analytical expression of the transfer matrix [9, 119]. The so-called $l - \zeta$ model treats the burner as a compact acoustic discontinuity and is applicable if the wavelength is large compared to the geometrical length. Similarly to the Helmholtz resonator neck, the burner features then a virtual length l and acoustic dissipation incorporated by the pressure loss variable ζ . However, the model has some weaknesses. For instance, the virtual length is not identical to the geometrical length augmented with the end-correction at the inlet and outlet of the burner as it is the case with the Helmholtz resonator. Due to the complex stream lines of each particle through the burner, the model input and output reference positions have to be adjusted to fit to the model behavior. The loss-coefficient ζ is an additive combination of the nonlinear pressure loss-coefficient ζ_Ω and the various losses created in the burner. In this modeling approach, the losses are linearized. Hence, the analytical transfer matrix for an acoustically compact burner

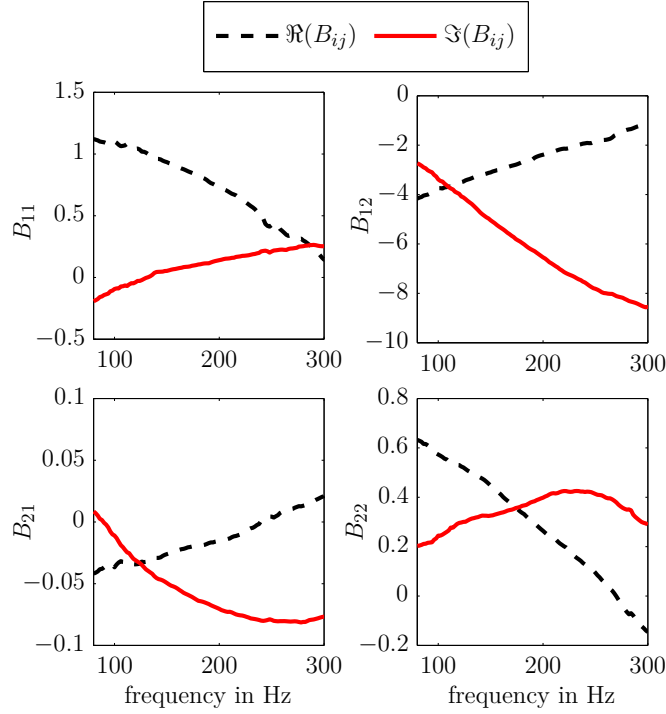


Figure 4.16: Four burner transfer matrix elements at the investigated operation point.

writes:

$$\text{BTM}(\omega) = \begin{pmatrix} 1 & i\omega\bar{\rho}l + \bar{\zeta}\bar{\rho}\bar{u} \\ 0 & \frac{S_1}{S_2} \end{pmatrix}, \quad (4.25)$$

where the element B_{11} is one due to the assumption of acoustical compactness and B_{21} is zero because the acoustic velocity is insensitive to the pressure as long as the assumption of mass continuity holds, which means that no significant acoustic sources or sinks are present in the burner. The continuity assumption is also the basis for the modeling of B_{22} , which accounts for the effective area jump between the inlet and outlet of the burner. Element B_{12} incorporates the effective length and the acoustic dissipation, where $\bar{\zeta}$ and $\bar{\rho}$ are averages between inlet and outlet conditions and \bar{u} represents the mean flow component.

Figure 4.16 depicts the burner transfer matrix elements in terms of the real and the imaginary part of the four transfer matrix elements of the investigated burner. Evidently, the agreement between the $l - \zeta$ model and the measurement results is limited. Nevertheless, with respect to the measurement accuracy the element B_{21} can be treated as zero and is in very good agreement. On the other hand, the real part of B_{22} should be approximately 0.64, however, this value is only in good agreement at very low frequencies. The same holds for the element B_{11} , which approaches unity for low frequencies. Adjusting the acoustic input- and output-planes would improve the results for higher frequencies but would deteriorate the agreement at low

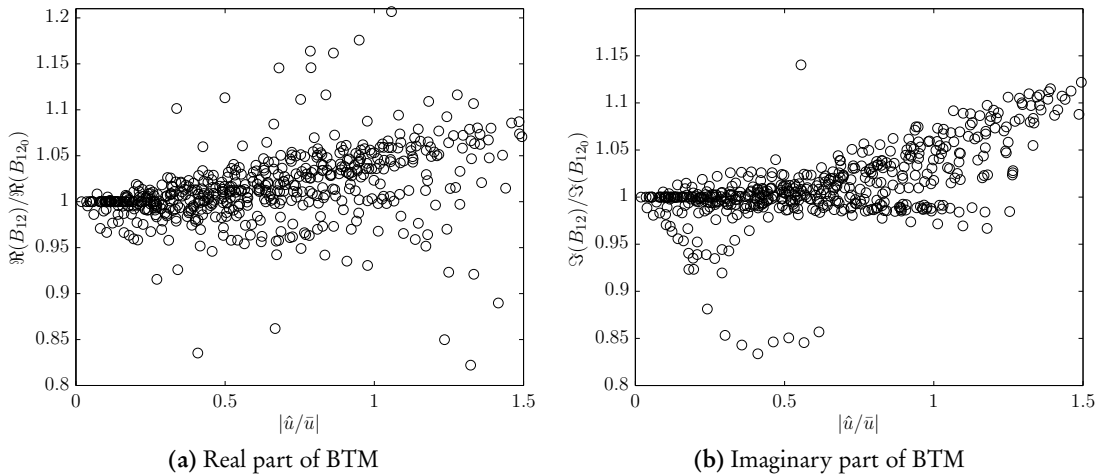


Figure 4.17: (a) Real and (b) imaginary part of the burner transfer matrix element B_{12} for various frequencies and amplitudes. The vertical axis shows the ratio between higher amplitude values and the linear regime. The horizontal axis depicts the amplitude ratio at the burner entrance. Frequencies are not distinguished

frequencies. Although the $l - \zeta$ model does not reproduce the characteristics of the investigated burner for the whole frequency range at constant acoustic planes, some conclusion can be drawn from the comparison. The losses due to the interaction of the hydrodynamic and the acoustic field and the phase-shift due to the end-correction is mainly represented by the transfer matrix element B_{12} . For the exact assessment of the effect of higher velocity amplitudes, high amplitude excitation with two linearly independent acoustic configurations is needed, which is difficult to realize from a practical point of view. Assuming that B_{21} is still negligible at higher amplitudes and that B_{22} is approximately constant, a single excitation setup is sufficient to assess the development of B_{12} at higher amplitudes.

Figure 4.17a depicts the normalized real part of the burner transfer matrix element B_{12} , which represents the damping of the burner. Measurements are shown for various amplitudes and frequencies, altogether 605 different measurement points for 55 frequencies between 50 Hz and 300 Hz. The horizontal axis represents the normalized forcing amplitude and the vertical axis the normalized real part of the burner transfer matrix element B_{12} . Figure 4.17b shows the normalized imaginary part of B_{12} , which is responsible for the length correction. Both values were normalized with the corresponding value of the respective frequency in the linear regime ($|\hat{u}/\bar{u}| < 0.1$). The different frequencies are not distinguished because no frequency dependent trend was identified. The ratio between the values measured at higher amplitudes and in the linear regime is for both cases only weakly dependent on the excitation amplitude. For self-excited instabilities, amplitudes of up to $|\hat{u}/\bar{u}| = 1$ are expected. In this range a standard deviation of $\pm 2\%$ from the linear value has to be expected for the real and imaginary part of

B_{12} . A deviation of 5% in the real and imaginary part of the B_{12} -element affects the limit cycle amplitude in the presented study by only approximately 1%. Hence, this effect is negligible for the investigated set-up.

4.2.2 Upstream and Downstream Reflection Coefficients

The nonlinearity of the open-end reflection coefficient was examined since in case of a $\lambda/4$ -mode a velocity anti-node is situated at the open end of the combustion chamber causing acoustic velocity amplitudes of up to $|\hat{u}/\bar{u}| \approx 6$.

As shown in Figure 4.18 the cold flow open end reflection coefficient of the combustion chamber decreases with increasing frequency as expected by assuming a typical Levine and Schwinger [77] correction of the open end termination. The Figure shows the isothermal reflection coefficient in the frequency range of 50–300 Hz for various amplitudes of the acoustic velocity. However, around 90 Hz, 102 Hz, 180 Hz and 204 Hz the acoustic response deviates from the typical open-end reflection coefficient. These deviations are related to an interaction of the room acoustics and the combustion chamber exhaust tube. The change in the reflection coefficient absolute value is relatively small. Consequently, the amplitude dependence can be neglected. The same holds for the phase response, which features, as expected from an open-end, a constant decay with increasing frequency.

As shown by Rämmal & Lavrentjev [108] and further investigated and modeled by Jörg et al. [61], the damping may be significantly affected at the open end termination for the case of a hot jet expanding into a cold environment. Consequently, the reflection coefficient used for the stability analysis was measured in the linear regime at hot conditions. However, the results are qualitatively very similar to the reflection coefficient shown in Figure 4.18.

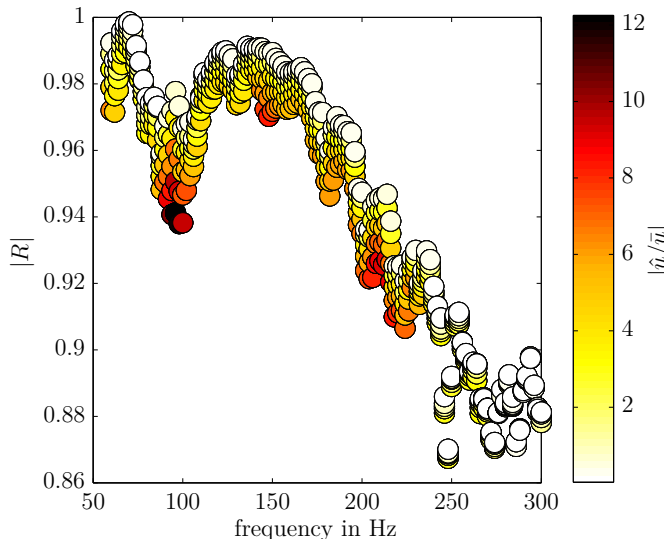


Figure 4.18: Open-end reflection coefficient for various frequencies and acoustic velocity amplitudes.

The reflection coefficient upstream of the burner, which characterizes the acoustic response of the upstream tubing and the attached loudspeakers, is depicted in Figure 4.19. Since the test-rig is not equipped with a high amplitude forcing device downstream of the burner, it is only possible to measure the linear acoustic response. It was measured at cold flow conditions with the burner installed.

The reflection coefficient features three nodes around 140 Hz, 160 Hz, and 240 Hz, respectively. In these frequency regions, the reflection coefficient decreases almost to zero. The anti-nodes feature a magnitude of the reflection coefficient between 1 and 0.5. The reflection coefficient depends on the length of the variable upstream trombone, which is used to create the high acoustic velocity amplitude forcing. For the stability measurement results in Chapter 5 the trombone was set to the shortest possible length, featuring the reflection coefficient as it is shown in Figure 4.19. The length of the trombone basically affects the exact positions of the nodes and, thus, is used to adjust the amplitude for the flame describing function measurements.

After the phenomenological investigation of the flame nonlinearities in Chapter 3 and the detailed investigations of the nonlinear damping effects in this chapter, the next chapter of this work will utilize the findings of the previous chapters in a nonlinear stability analysis of the investigated combustor.

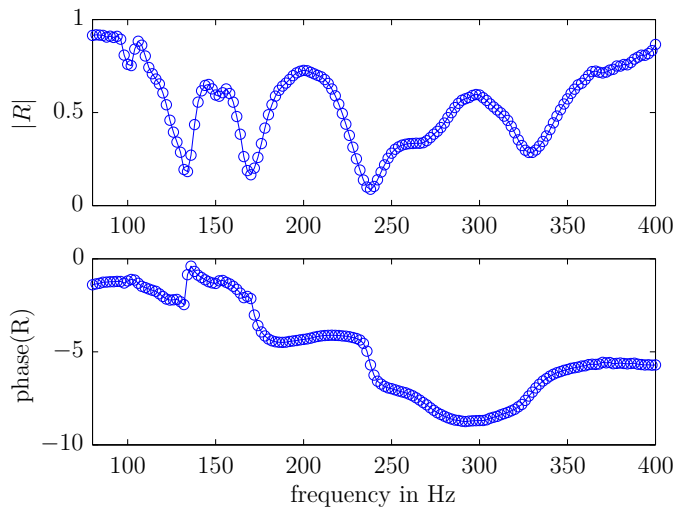


Figure 4.19: Upstream reflection coefficient for various frequencies at small acoustic velocity amplitudes. The trombone position was set to the shortest possible length.

Chapter 5

Nonlinear Stability Analysis

Prediction is difficult, especially when dealing with the future

Danish Proverb

¹ In the 1950s, Merk [85] was one of the first, who applied a frequency-domain type analysis to determine the stability of thermoacoustic systems. By now, two approaches can be distinguished for the determination of linear stability. Either the open-loop gain can be used to assess the system stability via a generalized Nyquist stability criterion [114], or the dispersion relation of the system can be solved as an eigenvalue problem, which yields the unstable frequencies [113]. Formally, the latter approach requires all sub elements in the model to be evaluated at complex frequencies for the calculation of linear stability. But, if the transfer matrix was obtained experimentally or numerically, it can be only evaluated at real frequencies. The effect of the imaginary part of the frequency can be taken into account by using a physics-based or a parametric model [118].

Linear instability is featured by an energy addition rate, which exceeds the damping. Subsequently, the initially small perturbations grow exponentially until the limit cycle amplitude is reached. It is defined by an equilibrium of oscillation energy gain and acoustic losses. Depending on the source of acoustic damping the dissipation can be increased or decreased at higher amplitudes. Since the acoustic pressure amplitude typically does not exceed 5% of the static pressure in the combustion chamber, the acoustic field responds linearly and, hence, does not change its behavior at higher amplitudes. However, due to various effects, already discussed in chapter 3, the energy addition caused by the fluctuating flame saturates at higher amplitudes. The nonlinear response of the flame can be modeled by an amplitude-dependent transfer function, here introduced as flame describing function. Incorporating the relevant nonlinearities in the stability analysis, introduces an amplitude dependency, which allows for the determination of the limit cycle amplitude.

¹The work presented in this chapter is based on two publications [30] and [31]. Jonas Moeck mainly contributed to the linear stability analysis presented later in this chapter. Paragraphs and phrases of this chapter are very similar or identical to text paragraphs published in the two articles. These excerpts are written by me.

The applicability of this approach was demonstrated with reasonable accuracy in recent studies [21, 71, 93, 98]. Noiray et al. [93] observed the development of a linear instability and investigated the established limit cycle amplitude. Different dynamic phenomena such as triggering or mode switching were observed in a unconfined laminar Bunsen flame test rig. These effects were successfully predicted by incorporating the nonlinear flame response in a describing function framework. The approach was extended by the same research group to confined laminar flames [21] and to turbulent perfectly premixed swirl flames at relatively low Reynolds number [98].

Krebs et al. [71] investigated the limit cycle oscillations of a turbulent, technically premixed and perfectly premixed swirl flame that were very similar to the one used in the present work. They used experimental flame describing functions to validate numerical simulations. For the technically premixed case, the flame describing function, which was measured on the basis of OH*-chemiluminescence, was rescaled using the data from numerical simulations. The relatively high deviation of the modeled limit cycle amplitude from the measured one was partly attributed to the damping in the model, which was obtained numerically with an in-house code. Additionally, only one geometrical configuration is discussed, which makes it generally difficult to evaluate the accuracy of the method.

Due to the circumferential design of modern gas turbine combustion chambers azimuthal modes are often dominant. However, numerical and experimental analyses of combustion instabilities, manifested in azimuthal modes, indicate that the dominant heat release rate fluctuations occur as a response to mass flow fluctuations through the burner, induced by the circumferential pressure field [22, 130, 137]. The annular combustion chamber and plenum design can be considered by using the flame transfer function to longitudinal perturbations and incorporating this information in an acoustic model, which accounts for the three-dimensional acoustic field. For instance, Schuermans et al. [121] accurately predicted the instability spectrum in a gas turbine by applying a flame transfer function, which was measured in a single-burner test-rig at engine conditions.

Extending the works that were conducted on scientific burners, in this chapter the flame describing function is used for the prediction of various limit cycle amplitudes experimentally observed on an industrially relevant set-up. Additionally, the nonlinear Helmholtz resonator response is coupled with the nonlinear flame response in a theoretical investigation.

The remainder of this chapter is structured as follows. First, the theoretical background of the nonlinear stability analysis is explained. Consequently, the experimentally obtained flame describing function is incorporated together with the acoustic boundary conditions, discussed in the previous chapter 4, into a thermoacoustic modeling framework to calculate the stability limits of the flame-combustor system. Although the operation point is slightly different than

the one discussed in chapter 3, the dominant saturation mechanisms are the same. The measurement results are then compared to the linear and nonlinear model predictions. An assessment of the accuracy of the presented modeling methods and experimental approaches is made. Finally, the nonlinear Helmholtz resonator model is coupled with the flame describing function. The interaction of both nonlinearities is investigated.

5.1 Theory and Modeling

Acoustic network models can adequately represent the features of Thermoacoustic systems. Such a network consists of several subsystems of acoustic transfer functions. Figure 5.1 illustrates the network model that is used to model the experimental combustor set-up.

Boundary conditions are included as single-input-single-output systems (see, Figures 4.18 and 4.19). The additional difficulty that the measured acoustic impedances of the system boundary conditions are only real valued have been overcome through the analytic continuation of the measured data based on models obtained from a system identification routine [46]. The models are in the form of rational transfer functions with orders sufficiently high to provide a good match with the measurements. It is suitable to define the acoustic boundary condition at a reference location, at which only plane waves propagate. To account for the variable length tube downstream of the flame (see, Figure 2.3), an analytical tube transfer matrix TTM of a loss free tube with low Mach number flow is included in the network model. The tube transfer matrix can be easily derived from Eqn. (2.5) and (2.7) by applying the approach $\hat{p}_4 = \hat{p}_3(x + L)$:

$$\begin{bmatrix} \left(\frac{\hat{p}}{\rho c}\right)_4 \\ \hat{u}_4 \end{bmatrix} = \begin{bmatrix} \cos(kL) & -i \sin(kL) \\ -i \sin(kL) & \cos(kL) \end{bmatrix} \begin{bmatrix} \left(\frac{\hat{p}}{\rho c}\right)_3 \\ \hat{u}_3 \end{bmatrix}, \quad (5.1)$$

with the wavenumber $k = \omega/c$ and length of the downstream tube segment L .

To model the flame, the transfer function model introduced by Schuermans et al. [120] for technically premixed flames is used. It fits the experimental flame response data from the set-up used in the present work reasonably well. The modified model writes:

$$\mathcal{F} = g(e^{-i\omega\tau_1} e^{-\omega^2\sigma_1^2/2} - e^{-i\omega\tau_2} e^{-\omega^2\sigma_2^2/2}), \quad (5.2)$$

where τ_1 and τ_2 correspond to two time delays, associated with different response mechanisms, and σ_1 and σ_2 are the corresponding standard deviations of the time delays. The complexity of the model can be increased by introducing additional variables; however, it was not found that the more complex models fit significantly better to the flame describing function measurements.

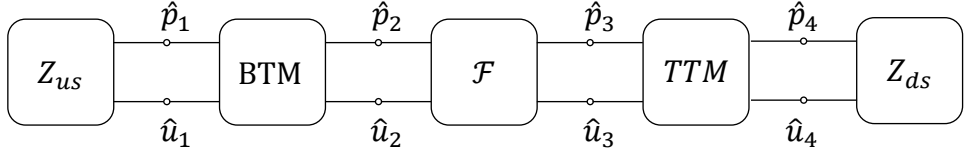


Figure 5.1: Network model used in the present work to represent thermoacoustic oscillations observed in the experimental test-rig.

The gain of the original model yields a maximum gain of unity, which is not observed in the experiments. Hence, Equation (5.2) is complemented with a scaling factor ϱ to match the experimental data. The application of the model enables the evaluation of the flame transfer function at complex frequencies, allowing for the determination of correct growth rates at non-limit cycle amplitudes and simplifying the numerical solution procedure. Equation (5.2) is extended to the nonlinear regime of the flame response by modeling all parameters of the equation as functions of the amplitude, which results basically in a decay of the empirical coefficient ϱ with increasing amplitude. Consequently, although the model is not capable of modeling physically correctly the underlying mechanisms of the flame response saturation it is still used for the nonlinear stability analysis to analyze the growth rate of the eigenfrequencies better. Hence, the flame describing function is modeled as a amplitude-dependent flame transfer function, which is composed of two feedback mechanisms, where the flame response saturation is mainly reproduced by scaling the transfer function gain with increasing amplitude. The approach fits very well up to excitation amplitudes of $|\hat{u}/\bar{u}| = 0.85$. Due to the physics based approach, the measurement data is reasonably smoothed and filtered. This is especially at high acoustic amplitude conditions useful since the flame response is relatively sensitive to external influences and changes of the boundary conditions at high amplitudes.

Linking all subsystems and considering only the homogeneous part of the system matrix S yields for the network depicted in Figure 5.1 the form

$$\underbrace{\begin{bmatrix} -1 & Z_{us} & 0 & 0 & 0 & 0 & 0 \\ B_{11} & B_{12} & -1 & 0 & 0 & 0 & 0 \\ B_{21} & B_{22} & 0 & -1 & 0 & 0 & 0 \\ 0 & 0 & 1 & 0 & -1 & 0 & 0 \\ 0 & 0 & 0 & [1 + (\vartheta_{ds}/\vartheta_{us} - 1)\mathcal{F}(\omega, |\hat{u}|)] & 0 & -1 & 0 \\ 0 & 0 & 0 & \cos(kL) & -i \sin(kL) & 0 & -1 \\ 0 & 0 & 0 & -i \sin(kL) & \cos(kL) & 0 & 0 \\ 0 & 0 & 0 & 0 & 0 & 0 & -1 \\ 0 & 0 & 0 & 0 & 0 & -1 & Z_{ds} \end{bmatrix}}_S \begin{bmatrix} \frac{\hat{p}_1}{\rho_1 c_1} \\ \hat{u}_1 \\ \frac{\hat{p}_2}{\rho_1 c_2} \\ \hat{u}_2 \\ \frac{\hat{p}_3}{\rho_3 c_3} \\ \hat{u}_3 \\ \frac{\hat{p}_4}{\rho_4 c_4} \\ \hat{u}_4 \end{bmatrix} = 0, \quad (5.3)$$

where B_{ij} and Z_{ij} are the transfer matrix elements of the burner and the impedance of the

upstream as well as downstream boundary conditions, respectively. The form of the flame transfer matrix is taken from Equation (2.14). A solution of the system matrix exists only if the determinant vanishes. This is the so-called dispersion relation:

$$\det \mathbf{S}(\omega) = 0. \quad (5.4)$$

The solutions of this relation are the eigenvalues of the system matrix, which can be interpreted as the eigenfrequencies of the thermoacoustic system. Since a harmonic time dependence of $e^{i\omega t}$ was assumed (see, Section 2.1) the real part of ω yields the frequency and the growth rate of the eigenmode is represented by the imaginary part of ω , where $\Im(\omega) < 0$ indicates an unstable eigenfrequency. An initially small pressure perturbation at the linearly unstable eigenfrequency will grow exponentially until finally a limit cycle amplitude is reached at which the growth rate is zero. Hence, a thermoacoustic instability is characterized by a literally stable equilibrium of acoustic dissipation and energy addition by the flame.

Employing the flame transfer function obtained at small forcing amplitudes gives information about the initial mode stability. Nonlinear acoustic effects are not generated by gasdynamic nonlinearities, as it is inherent in the Euler equations because the limit cycle amplitude is usually not high enough to produce significant wave steepening effects in the acoustic field. Thus, the final pressure oscillation level, can only be calculated by taking into account the acoustic response of the flame and dampers at higher amplitudes. The phenomenological explanation and an appropriate modeling approach for the amplitude dependence of the acoustic response functions of flame and damper were given in the previous chapters 3 and 4, respectively. Incorporating these describing functions, which are essentially transfer functions linearized at finite amplitude levels, in the network model yields a dispersion relation that also depends on the fluctuation amplitude [21, 93, 98]:

$$\det \mathbf{S}(\omega, |\hat{u}|) = 0. \quad (5.5)$$

This corresponds to oscillations with zero growth, thus the limit cycle. The stability of the limit cycle furthermore requires $\partial(\text{Im}(\omega))/\partial|\hat{u}| > 0$.

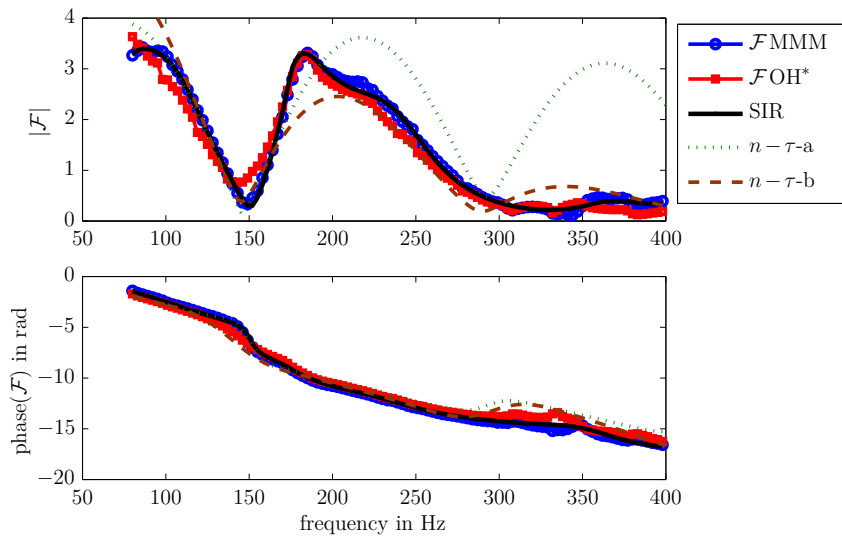


Figure 5.2: Linear flame transfer function measured with MMM and OH*-PMT. Models obtained with $n\text{-}\tau$ model and system identification routine shown in addition, where $n\text{-}\tau\text{-}a$ and $n\text{-}\tau\text{-}b$ illustrate two different fits of the same model.

5.2 Linear Stability Analysis

The gain and phase of the flame transfer function at a constant and small amplitude of the investigated operation point is illustrated in Figure 5.2. It was measured with the Multi-Microphone-Method and the OH*-photomultiplier. For these measurements, the flame was forced acoustically with the upstream loudspeakers at various frequencies with a normalized velocity amplitude of $|\hat{u}/\bar{u}| = 0.1$ approximately. Usually, the nonlinear effects are small at such low acoustic amplitudes. Additionally, the results of the system identification routine, a rational model of order 8, and two fits of the $n\text{-}\tau$ model (see, Equation (5.2)) are shown.

The transfer function gain indicates a strong amplification of velocity disturbances by the flame around 100 Hz and in the range around 200 Hz. Although equivalence ratio fluctuations tend to distort the transfer functions obtained with the photomultiplier, the results are in good quantitative agreement to the microphone based results. However, especially at frequencies around 100 Hz and in the range between 150 and 180 Hz some differences are present. Nevertheless, the phase response is almost identically acquired by both measurement techniques for the whole frequency range. The three modeling approaches also show a very good agreement in terms of the phase response. In contrast, only the system identification routine (SIR) reveals a perfect agreement in terms of the transfer function gain. It reproduces the gain of the flame transfer function almost exactly, while the gain of the $n\text{-}\tau$ model either overestimates or underestimates the response in some frequency ranges. Two fits are depicted in Figure 5.2.

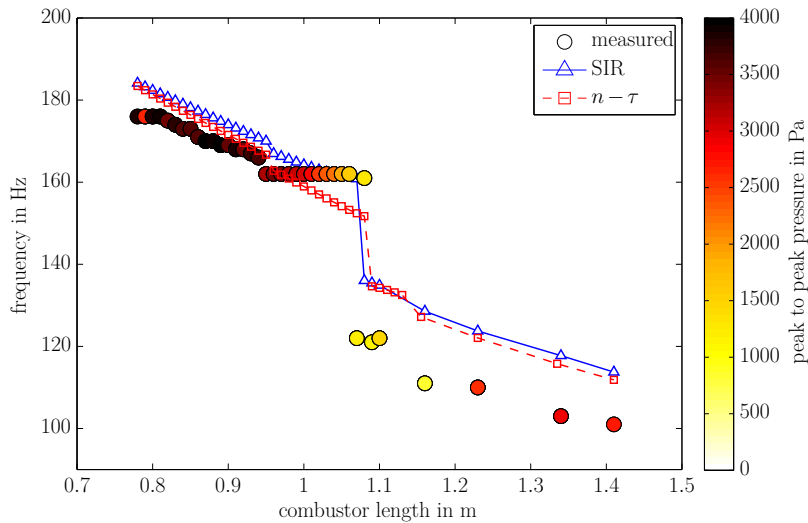


Figure 5.3: Comparison of linear FTF model results to microphone measurements downstream of the flame for various combustion chamber lengths. Only the dominant frequency from the measurements and the frequency with the highest growth rate from the model are shown.

The first one, labeled $n-\tau$ -a, fits good in the frequency range between 100 Hz and 200 Hz but overestimates the response for higher frequencies very strongly. At the same time the second fit, labeled $n-\tau$ -b, shows some deviations in the frequency range of 170 to 200 Hz and overestimates the response for very low frequencies, which are not in the focus of the investigation. However, the accuracy of the model can be increased by introducing additional free model parameters. The current level of model complexity assumes two dominant mechanisms. The averaged time delays identified by the phase response of $\tau_1 = 0.01$ s and $\tau_2 = 0.003$ s match to the convective time needed from the injector to the flame and to the distance of the area expansion at the combustor inlet to the center of gravity of the flame, respectively. Hence, the mean time delays indicate that the two governing instability mechanisms are equivalence ratio fluctuations and coherent flow structures generated at the area expansion. Although increasing the model complexity improves the quality of the fit, it is omitted here. The third excitation mechanism could be associated with the presence of swirl-number fluctuations[52]. However, this approach is not pursued in this study because the improved agreement is mainly caused by additional non-physics based scaling parameters and the agreement is at higher amplitudes again worse. Consequently, the two-mechanisms based model, presented in Equation (5.2), is used to smooth the measured transfer function and to allow for an correct assessment of the dispersion relation at non-limit-cycle amplitudes. The model is only used in frequency ranges with a very good agreement.

For the assessment of the self-excited instabilities frequency and limit-cycle amplitude of

different combustor volumina, the length of the variable downstream tube was gradually increased from 0.6 m to 1.41 m. Two microphones were mounted in the combustion chamber 0.3 m downstream of the flame measuring the acoustic frequency spectrum and the limit cycle amplitude at this position. The measurement and model results are depicted in Figure 5.3. Here, the dominant frequency is defined as the frequency with the highest limit cycle amplitude. Additionally, the frequencies with the highest growth rates obtained with the linear stability analysis using the system identification routine and the $n-\tau$ model are depicted. This implies that the instability with the highest growth rate will always be the dominant instability. This assumption holds for the measurements and analyses conducted in this work. The combustor is thermoacoustically unstable for lengths higher than 0.78 m. The instability oscillates at this combustor length with 176 Hz and decreases down to 105 Hz at the maximum length of 1.41 m. A constant decay of frequency with an almost constant amplitude in the range of 3500–4000 Pa was measured for lengths between 0.78 m and 0.94 m, associated with a $\lambda/4$ -mode downstream. For combustor lengths larger than 0.94 m, the instability frequency of 162 Hz is constant. However, the limit-cycle amplitude decays and the mode becomes almost stable. As will be discussed later, these operation points feature two unstable modes. At 1.1 m, the dominant mode changes from a frequency of 162 Hz to 120 Hz. This mode again increases in amplitude and decays in frequency for higher exhaust tube lengths.

The prediction quality of both modeling approaches is good. The models capture the dominant self-excited instability frequency very accurately for smaller exhaust tube lengths. Especially the flame transfer function obtained by the $n-\tau$ model reveals some inaccuracies between 0.96 m and 1.07 m, where the frequency leveling at 162 Hz is not predicted. However, the model correctly implies a change in the mode shape around 0.96 m, which is indicated by a jump in frequency and is also present in the measurements. In contrast to that, the system identification routine predicts for the same lengths a much smaller decay in frequency, with less deviation from the measurements. This can be attributed to the accurate fit of the flame transfer function gain. The low frequency range between 100 Hz and 120 Hz was predicted by both models with an accuracy in terms of frequency deviation of approximately 10%.

Between 1.06 m and 1.1 m a double peak in the frequency spectrum was observed in the experiments. The corresponding spectra are depicted in Figure 5.4. The pressure spectrum of one of the upstream and one of the downstream microphones is depicted for various lengths. Around a length of 1.07 m a hysteresis in the strength of the two modes was observed. Depending on the direction of the change in tube length, one or the other mode is dominant. As shown in Figure 5.4a, at 1.06 m, the 162 Hz mode is dominant in the upstream and downstream plenum. Increasing the length in one step to 1.08 m results in an increased amplitude of the 120 Hz mode (see, Figure 5.4b), which becomes the dominant frequency in the upstream

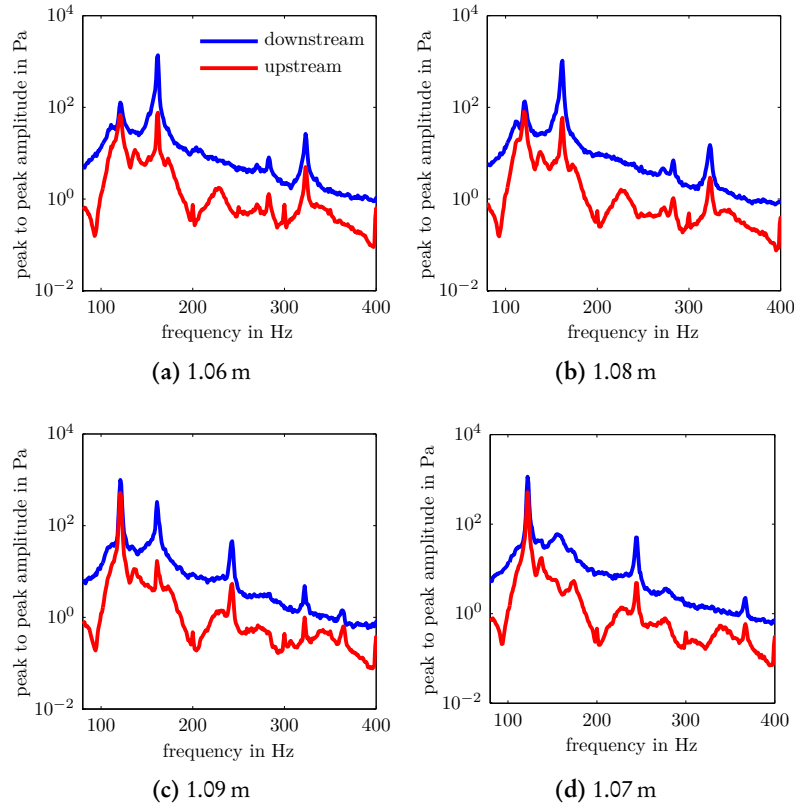


Figure 5.4: Pressure spectra of downstream (blue) and upstream (red) microphone for different combustion chamber lengths. The exhaust tube length was changed subsequently from (a) to (d).

plenum but is still weaker downstream of the flame than the other mode. Finally, as depicted in Figure 5.4c, at 1.09 m the 120 Hz mode is dominant upstream and downstream of the flame. Once the 120 Hz mode is fully stabilized at larger lengths, the length can be decreased without any evidence of the 160 Hz mode. For instance, the pressure spectrum illustrated in Figure 5.4d shows no sign of a second mode at a length of 1.07 m in the upstream spectrum and only a small bump in the downstream pressure signal at the frequency of 162 Hz.

Hysteresis in the oscillation mode is a natural phenomenon arising from two modes being simultaneously linearly unstable [88]. Here, the hysteresis in the pressure spectrum is probably caused by a temperature effect. The change of the exhaust tube length marginally affects the downstream temperature field. If the growth rates of both instabilities are similar, the limit cycle amplitude of the respective modes is highly susceptible to the temperature field. However, small changes can affect the growth of the natural modes at initially small amplitudes. Eventually, the temperature field varies the wavenumber in the downstream tube and this effect can be reproduced by a linear stability analysis as shown in Figure 5.5. Based on the assumption that

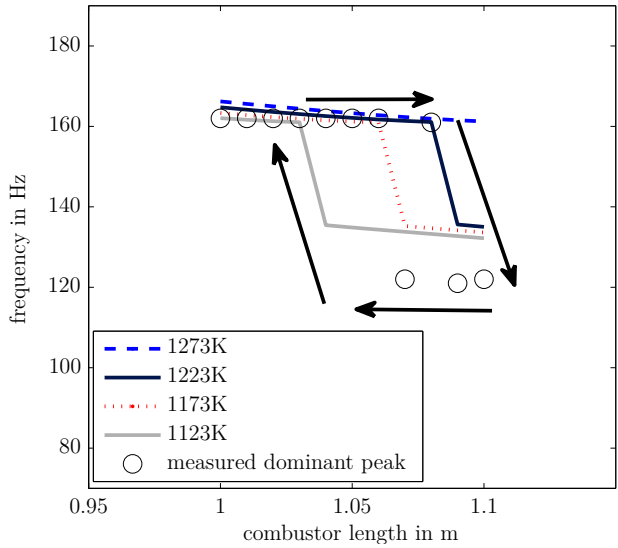


Figure 5.5: Linear modeling results of the dominant instability frequency for various downstream temperatures and combustion chamber lengths. Markers depict measurement points.

the mode with the initially higher growth rate will establish a higher limit cycle amplitude, the dominant mode can be predicted. Figure 5.5 illustrates the jump in the dominant frequency between the upstream and downstream mode for various downstream temperatures. The pure downstream mode at 120 Hz becomes dominant already at shorter combustor lengths for lower downstream temperatures. The upstream mode, on the other hand, remains dominant for larger combustion chamber lengths if the downstream temperature is relatively high. In real engines, such temperature changes can be induced by variations in the equivalence ratio φ or thermal power and by frequency dependent nonlinear effects of the flame, such as the creation of rich pockets. This induces additional difficulties for the prediction of the limit cycle amplitude if two modes are linearly unstable.

To draw some more conclusions from the linear stability analysis on the limit cycle amplitude, an empirical correlation between the growth rate and the limit cycle amplitude is needed. For instance, Krebs et al. [71] suggest considering a relation between linear growth rates and the limit-cycle amplitude. Figure 5.6 illustrates a similar correlation from the current investigations. The linear growth rate is taken from the solution of the dispersion relation using the flame transfer function modeled with the system identification routine. The ordinate shows the measured acoustic velocity amplitude at the flame position. Evidently, high growth rates are related to strong limit cycle amplitudes, obtained with the Multi-Microphone-Method upstream of the burner in conjunction with the burner transfer matrix. The correlation has a square-root type trend up to growth rates of -11 s^{-1} . For very high growth rates, the correlation is scattered around a normalized amplitude of $|\hat{u}/\bar{u}| \approx 0.6$. Using such an empirical relation between linear growth rates and nonlinear oscillation amplitudes allows the estimation of the limit-cycle from the linear stability analysis. This is advantageous in many ways and in the first place it is much

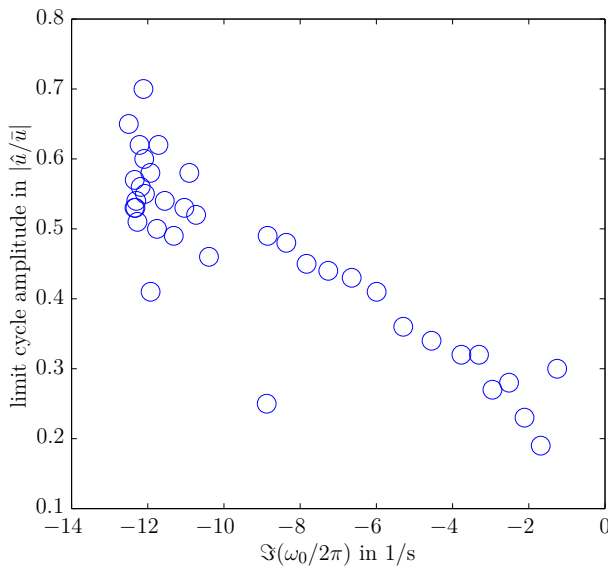


Figure 5.6: Correlation of linear growth rate obtained by the system identification routine and measured limit cycle amplitude.

easier to obtain the linear flame transfer function needed for the stability analysis. Additionally, if engine data is available the limit cycle amplitude can be estimated for different operation points. However, the relation is system specific, it cannot be predicted *a priori*, and depending on the correlation a lot of limit-cycle amplitudes are needed to estimate the correct trend and shape of the correlation. In contrast, the flame describing function, which is needed for the nonlinear stability analysis, can be measured at atmospheric conditions and can be used for reliable prediction of instability modes, as discussed in the next section.

5.3 Amplitude Prediction

The response of the flame and the system boundary conditions at higher amplitudes is needed to perform a linear stability analysis at a higher acoustic amplitude level. This correspondingly called nonlinear stability analysis, yields the limit-cycle amplitude of the instability when zero growth rate of the unstable mode is reached. The flame describing function is of crucial importance for the prediction of the limit cycle amplitude. Additionally, the experiments were not conducted with a Helmholtz damper and, thus, no significant nonlinear damping was present in the experimentally investigated system (see, Section 4.2). Consequently, the flame response is the dominant system nonlinearity. The flame describing function applied in the nonlinear stability analysis is presented in Figure 5.7. The gain is depicted in the upper part of the figure and the corresponding phase response is illustrated in the lower part. The gain and phase response are shown on the abscissa and the frequency on the ordinate. The normalized acoustic velocity amplitude level at which the flame response was obtained is indicated by the color of the respective markers. Commonly, an amplitude level of 10% is considered to be the limit

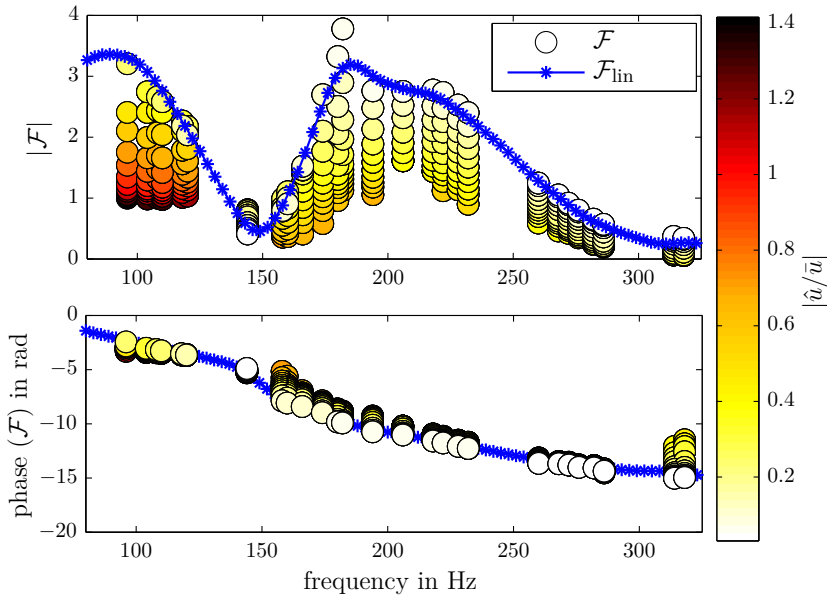


Figure 5.7: Measured linear flame transfer function (blue stars) and flame describing function for various amplitudes (circles). The color of the circles indicates the forcing amplitude at the flame.

of linearity. This is accordingly represented by the blue line, measured at a frequency spacing of 3 Hz. However, for frequencies around 200 Hz, nonlinear effects are observed at smaller amplitudes already.

An amplitude dependence of the phase response is observed for frequencies around 160 Hz and 340 Hz. Since equivalence ratio fluctuations and velocity perturbations are not in phase around a frequency of 150 Hz, it is likely that the change in the phase response is caused by the increasing equivalence ratio fluctuations. The change in the phase response around 340 Hz is caused by a detachment of the flame at high forcing amplitudes.

Around 100 Hz and 200 Hz velocity perturbations are strongly amplified but these frequency ranges show also major changes in the gain of the flame response. Due to the specific acoustic response of the upstream rig segment, the achievable forcing amplitudes are frequency dependent. Around 100 Hz, the flame was forced with acoustic velocity amplitudes up to $|\hat{u}/\bar{u}| = 1.4$, while the realizable amplitudes for frequencies around 200 Hz were significantly lower, at approximately $|\hat{u}/\bar{u}| = 0.75$ and for some frequencies amplitudes higher than $|\hat{u}/\bar{u}| \approx 0.1$ were impossible to realize.

At low amplitudes the transfer function gain is approximately three for the two ranges of high amplification. It decreases down to approximately unity for high amplitudes. The flame responds linearly to forcing around 100 Hz up to an amplitude of $|\hat{u}/\bar{u}| = 0.2$. In contrast to

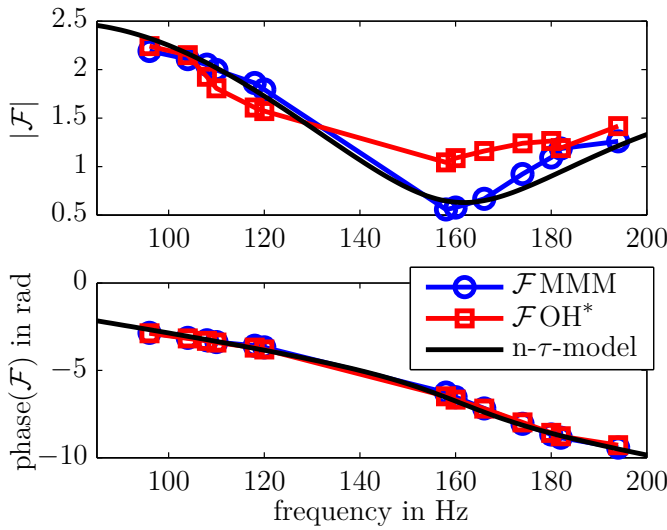


Figure 5.8: Comparison of FDF obtained by MMM and PMT-OH* and modeled FDF at an amplitude level of $|\hat{u}/\bar{u}| = 0.63$.

that, the response becomes nonlinear almost immediately for frequencies around 200 Hz and small acoustic velocity amplitudes cause a significant reduction of the gain in this frequency region. It is interesting to note that the transfer function gain is increased with the forcing amplitude for frequencies around 145 Hz, which is likely caused by changes in the flame shape and the mean flow field. Although the presented flame describing function was obtained at slightly different operation condition than the ones discussed in Chapter 3, the describing functions are similar and the dominant saturation mechanism presented there are expected to be the same. The excitation by the coherent structures saturates due to the limited amplification of the shear layers. At the same time, increased attenuation of the equivalence ratio fluctuations at higher amplitudes for higher frequencies and a decreased heat of reaction at lower frequencies lead to a reduction of the transfer function gain.

As already explained, the parameters of the $n-\tau$ flame describing function model (see, Equation (5.2)) were determined to match the results of the Multi-Microphone-Method in the frequency range between 100 Hz and 200 Hz for all investigated amplitudes. This is the range where the instabilities in the combustor test rig were observed. Figure 5.8 illustrates a comparison between the flame describing function measured with the Multi-Microphone-Method, the OH*-photomultiplier results, and the $n-\tau$ model for a normalized acoustic velocity amplitude of $|\hat{u}/\bar{u}| = 0.63$. The modeling of the flame describing function is applied because there is only a very limited number of measurement points for amplitudes higher than $|\hat{u}/\bar{u}| = 0.5$ available. The $n-\tau$ model smoothes the data, and it is ensured that the flame describing function preserves a physically meaningful shape, which is lost when applying interpolation between widely scattered measurement points. Additionally, it allows for a correct assessment of the growth rates at all levels of amplitudes.

The deviation of the chemiluminescence light emissions from the actual heat release rate at technically premixed conditions is the supposed reason for the significant deviation of the OH*-photomultiplier obtained describing function for some frequencies. While the accurate microphone measurements indicate a node of the transfer function gain at approximately 160 Hz, the OH*-photomultiplier results suggest a flat response at this amplitude level. Depending on the phase relation between fluctuations in equivalence ratio and velocity, the flame response can either be overestimated or underestimated by the photomultiplier measurements due to the exponential dependency [51] on the equivalence ratio and the linear dependency on the mass flow. A constructive phase relation of the two contributions to the chemiluminescence intensity leads to an overestimated flame response while a destructive phase relation causes an underestimation.

The $n-\tau$ model fits very well to the measurements. To quantify the quality of the chosen model, the deviation to the measurements is depicted in the Figures 5.9a and 5.9b in terms of gain and phase difference, respectively. The relative error of the $n-\tau$ model in terms of the normalized difference between measurement and model ($\Delta\mathcal{F}/\mathcal{F}_0$), is except for frequency between 120 Hz and 160 Hz well below 20%. For most of the points even well below 10%. The absolute deviation in terms of the phase response is below 50°, except for the frequency of 160 Hz. The poor agreement in the range between 120 Hz and 160 Hz is technically caused by the relatively low values of the gain in this region. Hence, small absolute deviations in terms of the gain cause a relatively strong mismatch. Additionally, only two measurement points are available in this frequency range for higher forcing amplitudes. As pointed out in section 2.3, the day to day variations of flame transfer function measurements can exceed $\pm 5\%$

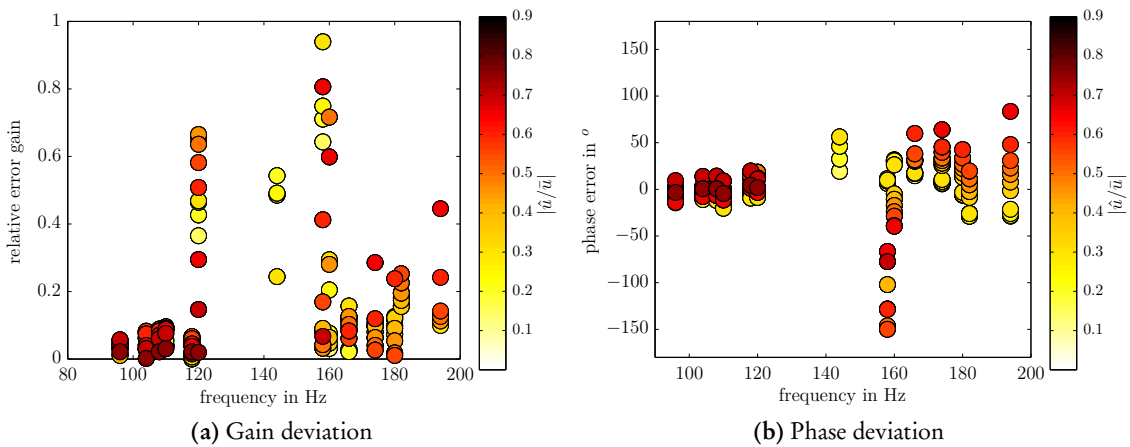


Figure 5.9: (a) Relative error of flame describing function approximation with $n-\tau$ model. Here, relative error is defined as the normalized difference between the measurement results and the model: $\Delta\mathcal{F}/\mathcal{F}_0$. (b) Depicts the absolute deviation of the $n-\tau$ model in terms of phase response.

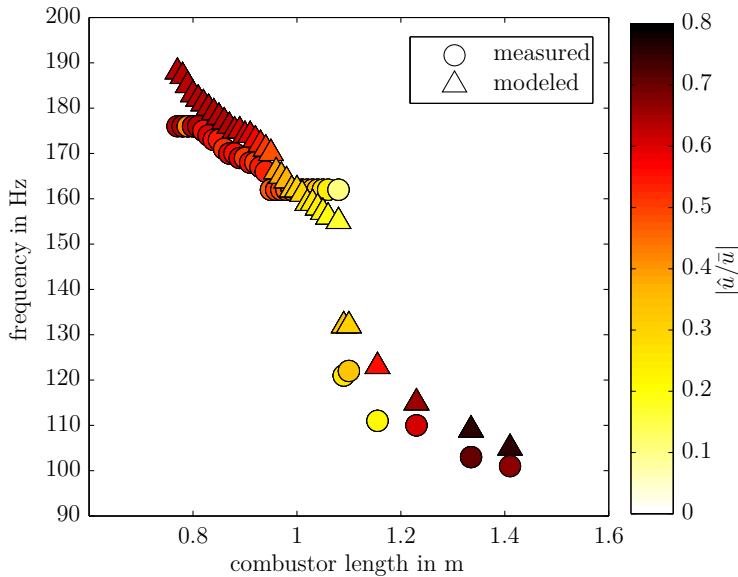


Figure 5.10: Comparison of measured and calculated dominant limit cycle frequencies and amplitudes for various combustion chamber lengths.

and additional variations introduced by the mass flow meters can also significantly affect the flame response measurement results. Hence, deviations between 10-20% are in the range of the effective measurement accuracy. Nevertheless, despite the punctually relatively high deviations between measurements and nonlinear $n-\tau$ model, the modeling has some important advantages. It simplifies the numerical solution of the dispersion relation and smooths and interpolates the transfer function with a physics based approach. Especially the measurement of the nonlinear transfer function is very sensitive to many operation parameters and susceptible to measurement inaccuracies, hence a physics based interpolation and filtering is justified.

The comparison of the dominant limit cycle amplitudes at the flame, obtained with the nonlinear stability analysis using the amplitude-dependent $n-\tau$ model, and the experimentally measured dominant instability amplitudes is shown in Fig. 5.10. The dominant mode is here again defined as the mode with the highest limit-cycle amplitude. For the cases with two modes present in the combustor, it is important to note, that the modes were not simultaneously oscillating but rather alternating in time. Hence, the system was not in limit-cycle state by definition, when two modes were present. However, the time signals measured have a length of 32 to 64 seconds and were digitally filtered with a bandpass-filter centered around the respective instability frequency. The resulting separation of the pressure signal of each mode was used to obtain a representative amplitude. For both, simulation and experimental results, the color of the markers indicate the limit cycle amplitude of the dominant instability frequency in terms of normalized acoustic velocity at the flame.

For the measurement of the self-excited instabilities, the length of the variable downstream tube was gradually increased from 0.6 m to 1.41 m. The combustor becomes unstable at a length of approximately 0.76 m with a frequency of 176 Hz and remains unstable up to the maximum combustor length of 1.41 m. As expected from the discussion of the downstream acoustic pressure measurements, the instability frequency decays with increasing combustor length and the relative amplitude behaves similar to the pressure amplitudes shown in Figure 5.3. Nevertheless, the relation between acoustic pressure and velocity is frequency dependent, which means that some differences in the relative amplitude between the Figures 5.3 and 5.10 are present. The acoustic velocity amplitude at the flame, which was obtained with the microphones upstream of the burner in conjunction with the burner transfer matrix, is generally very high and in the range of $0.5 < |\hat{u}/\bar{u}| < 0.75$. Around the combustor length of 1 m, where two modes were observed, the amplitude decays to small amplitudes in the range of $|\hat{u}/\bar{u}| \approx 0.1$, which is close to a thermoacoustically stable system. However, as pointed out with the spectra shown in the Figure 5.4, clear instability peaks are still present in the pressure spectrum.

A very good quantitative agreement in terms of frequency and amplitude for the whole range of investigated combustor lengths is obtained with the nonlinear stability analysis. Decaying frequencies as well as the two mode jumps around 0.95 m and 1.1 m are predicted in good agreement with the experimental results. In contrast to the measurements, the model predicts a decaying frequency for combustor lengths between 0.97 m and 1.08 m. At 0.8 m and at 1.15 m the model overestimates substantially the limit cycle amplitude compared to the measurements. Especially the discontinuity in terms of amplitude at 0.8 m, where the amplitude level drops from a $|\hat{u}/\bar{u}| \approx 0.65$ level to an amplitude of 0.4, seems to be a measurement outlier.

A systematic assessment of the modeling error is presented in Figure 5.11. The absolute deviation of frequency and amplitude for the whole range of investigated combustor lengths is shown. The absolute deviation in terms of frequency is generally in the range of -10 Hz to +10 Hz with a peak deviation of 12 Hz. The median of the relative error $\Delta f/f_0$ for all measurement points is 3.5%. Generally, the absolute deviation in terms of velocity oscillation amplitude is in the range of $-0.1 < \Delta|\hat{u}/\bar{u}| < 0.1$, with a peak deviation of $\Delta|\hat{u}/\bar{u}| = 0.33$. The corresponding median of the relative error is 14.6% for all data points. Especially around the mode jump at 1.1 m, the prediction deviates relatively strong from the measurement in terms of frequency as well as amplitude.

The amplitudes of the secondary frequencies, which were observed around a combustion chamber length of 1.06 m to 1.1 m are depicted in Figure 5.12. The amplitudes and the frequencies were accurately predicted by the describing function analysis. However, an anticipated secondary peak at 1.07 m, was not observed in the measurements due to the temperature hysteresis effects discussed in the previous chapter.

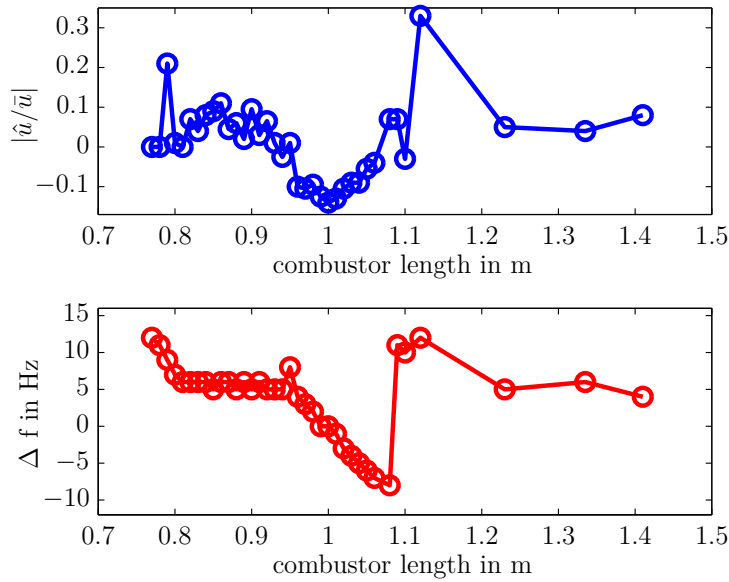


Figure 5.11: Absolute deviation of model results and measurements in terms of frequency and limit cycle amplitude for various combustion chamber lengths.

Figure 5.13a depicts the growth rate and instability frequency at a combustor length of 1.335 m for various acoustic velocity amplitudes at the flame. The nonlinear stability analysis predicts a limit cycle instability at a frequency of approximately 110 Hz. The frequency slightly deviates from 111 Hz at very low amplitudes to 113 Hz at higher amplitudes and again back to

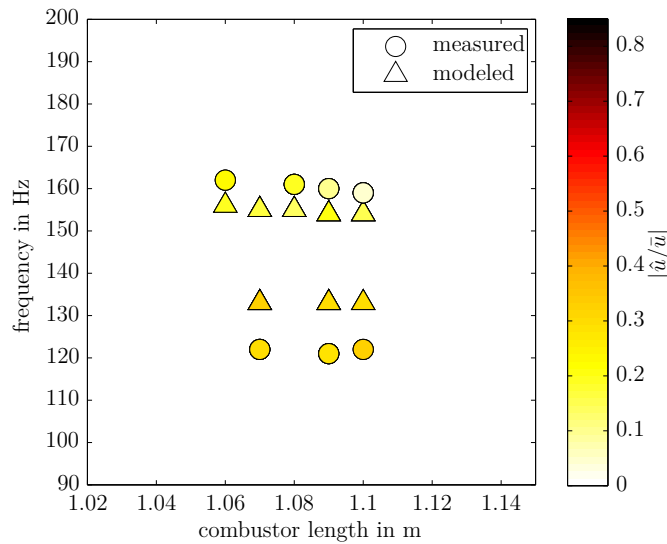


Figure 5.12: Comparison of measured and calculated limit cycle amplitudes and frequencies for two unstable modes for various combustor lengths.

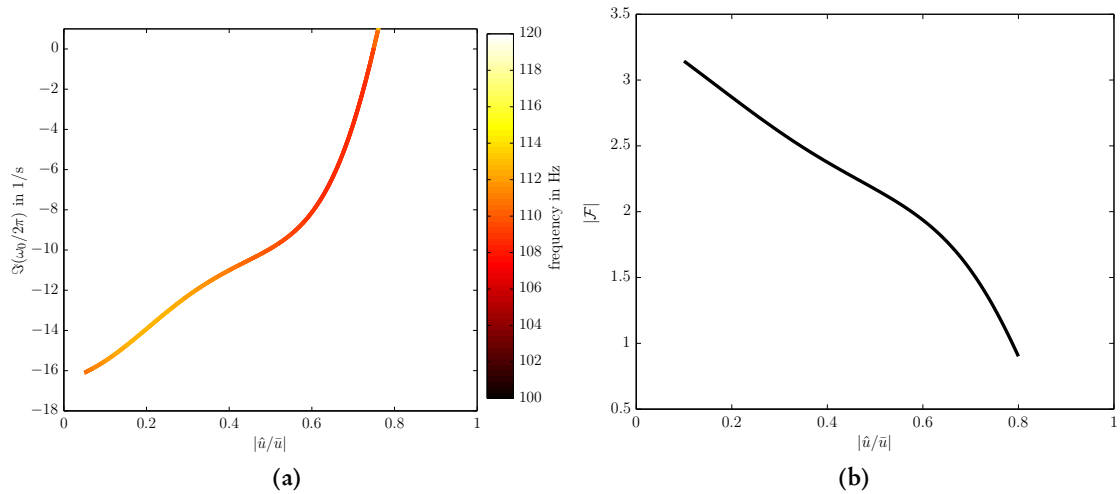


Figure 5.13: (a) Frequency and growth rate (real and imaginary part) of eigenfrequency at combustor length of 1.335 m for various acoustic velocity amplitudes. (b) depicts the flame describing function gain at 110 Hz.

110 Hz at limit cycle conditions, as indicated by the color painting. Hence, it is almost constant. At low amplitudes, the linearly unstable system features a relatively high growth rate of $\Im(\omega_0/2\pi) \approx -161/s$. The growth rate decreases linearly with the increasing amplitude up to $|\hat{u}/\bar{u}| \approx 0.6$, and it decreases stronger for higher amplitudes. A comparison between the flame describing function gain at 110 Hz, which is depicted in Figure 5.13b, and the amplitude dependency of the growth rate reveals the strong connection between the flame response saturation and the establishment of the limit cycle amplitude. The trend of both curves is exactly opposing to each other. This is to be expected, since the phase response of the flame describing function changes only by less than 10° at this frequency. Additionally, linear damping was assumed, consequently, only the transfer function gain can affect the growth rate of the unstable mode. A reduced amplification of the perturbations affecting the flame, causes a decreased energy addition rate to the acoustic field and hence a reduced growth rate of the instability.

At a combustor length of 0.93 m a different evolution of the linearly unstable mode, which is initially small in terms of amplitude, can be observed until the limit cycle is reached. The corresponding illustration of the frequency and growth rate for various acoustic amplitudes is shown in Figure 5.14. Here, initially very small perturbations at 161 Hz will cause a self-excited instability, which eventually oscillates at a frequency of 173 Hz. This change of 12 Hz is caused by the change of the acoustic response of the flame at higher amplitudes, which affects the system acoustics and thereby the resonance frequencies of combustor. The growth rate decays initially very fast up to an amplitude of $|\hat{u}/\bar{u}| \approx 0.2$ but eventually approaches the limit cycle just before $|\hat{u}/\bar{u}| \approx 0.6$. At this operation point, the connection between the flame describing

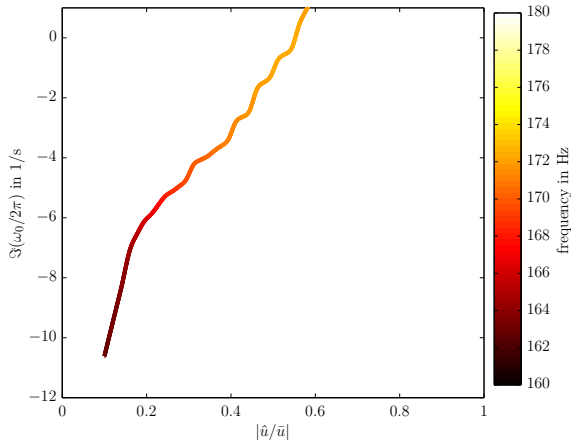


Figure 5.14: Frequency and growth rate (real and imaginary part) of eigenfrequency at combustor length of 0.93 m for various acoustic velocity amplitudes.

function and the growth rate, determined by the nonlinear stability analysis, is not clear due to the relatively strong shift in terms of frequency and because of the gradient of the flame describing function in this frequency range (see also, Figure 5.7).

The magnitudes of the flame describing functions at the three measured frequencies in the range of the discussed instability frequency are depicted in Figure 5.15a. Evidently, the linear gain at the three frequencies is qualitatively and quantitatively very different. At 174 Hz a monotonic decay of the initially relatively high gain is observed. At the same time, at 166 Hz the gain is constant up to an amplitude of $|\hat{u}/\bar{u}| \approx 0.3$, while the gain at 160 Hz is even increasing slightly. For higher amplitudes, the three curves become relatively similar. The corresponding phase responses, shown in Figure 5.15b, reveal comparatively strong gradients with increasing amplitude and between the three frequencies. A clear correlation between the flame response and the growth rate of the unstable mode is difficult, since the discussed instability evolves from a perturbation at 160 Hz and eventually oscillates at 172 Hz. Accordingly, the phase response relative to the acoustic velocity is almost constant during the evolution of the instability. Although the gain increases initially due to the change in frequency, the growth rate decays very strongly, especially at low amplitudes. However, the phase relation between the heat release and the pressure field changes. While the initial oscillation at 160 Hz fits very good to a quarter wave mode, higher frequencies feature an unfavorable eigenmode and will cause a decrease of the acoustic pressure amplitude at the flame. Not only that the damping is higher at higher frequencies, the energy addition rate is also determined by the amplitude-dependent phase relation between the pressure field and the flame, both effects decrease the growth rate of the unstable mode in this case and are responsible for the decay of the growth rate at small amplitudes. Eventually, the limit cycle is established due to the decrease of the flame describing function gain at 172 Hz at higher amplitudes.

The flame describing function gain at 160 Hz can potentially give rise to subcritical instabilities [87, 89] because the gain slightly increases at lower amplitudes. Subcritical instabilities

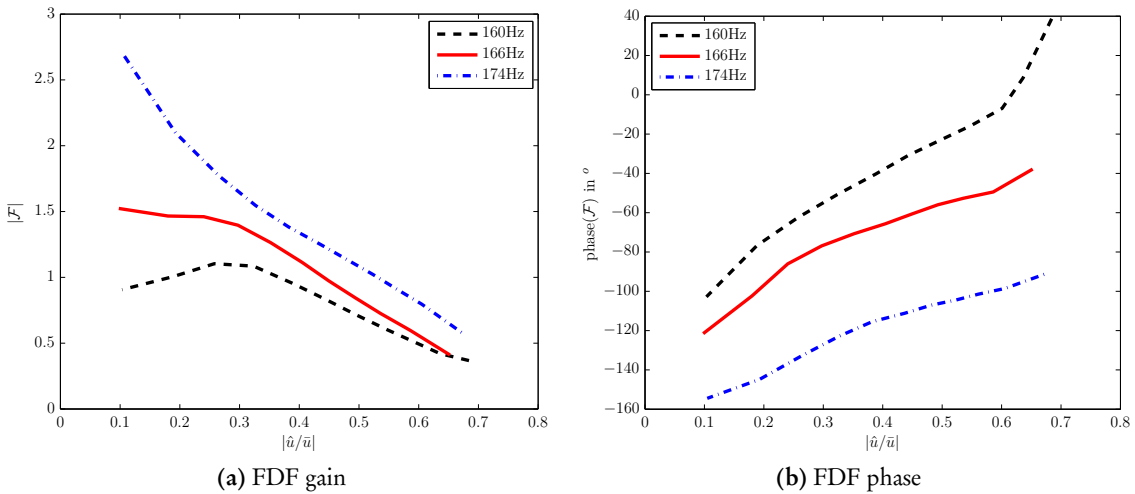


Figure 5.15: (a) Measured flame describing function gain and (b) phase at three frequencies.

or nonlinear instabilities, as they are called sometimes, are instabilities that do not evolve from small perturbations but are rather manifested at higher amplitudes due to an increased gain or decreases damping. However, small increases of the gain as in this case will cause subcritical instabilities at special circumstances, only. As will be discussed in the next subsection, strong nonlinear damping effects promote these kind of instabilities considerably.

5.4 Coupling of Nonlinear Damping and Flame response

As discussed, instabilities can be predicted in terms of frequency and amplitude quite accurately, if all relevant acoustic responses are known as functions of frequency and amplitude. Consequently, corrective measures can be taken to stabilize the system or to reduce the pulsation amplitude. Increasing the system damping sufficiently leads to a linearly stable system. However, if the flame describing function gain increases with increasing amplitude, which is very unusually, or if the damping decreases at the same time, the system can turn unstable at a higher amplitude, although the system is linearly stable. This behavior was, for instance, discussed by Culick et al. [35] for rocket combustors. It is often referred to as triggering [20], subcritical instability [87, 89], or nonlinear instability [139]. In a gas turbine, pressure shocks can be induced by the ignition or extraordinary events occurring in the compressor or turbine. These shocks or high amplitude pressure waves can trigger subcritical thermoacoustic instability.

The effect of hot gas penetration (see, Section 4.1.4) into the damper causes a strong amplitude dependency of the damping efficiency, additionally to the nonlinearity caused by the vorticity at the neck at higher acoustic velocity amplitudes. To investigate the interaction between this strong nonlinearity and the flame describing function theoretically, the acoustic

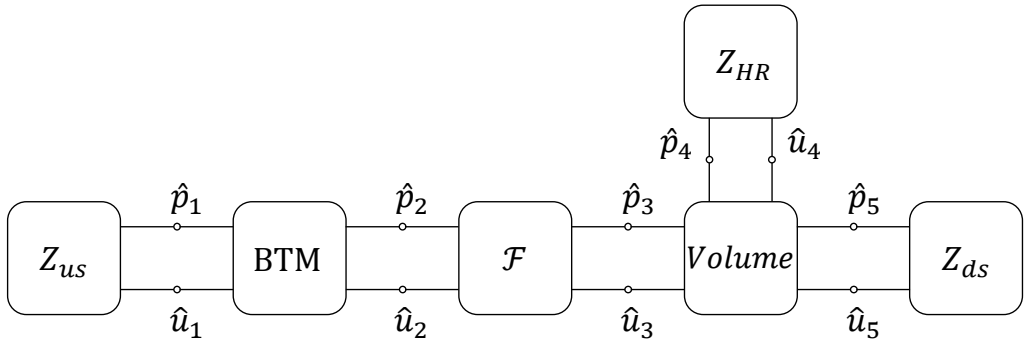


Figure 5.16: Network model used for the theoretical assessment of the nonlinear interaction between Helmholtz resonator and flame response.

network model used in the previous sub section is modified. It is illustrated in Figure 5.16. The combustor is linearly stabilized at a combustion chamber length of 1.335 m with the help of Helmholtz dampers attached virtually to the chamber at the location of the flame. The flame describing function and the nonlinear Helmholtz resonator impedance are acoustically connected by an infinitesimal small volume. This means that the acoustic pressures at this node are equal ($\hat{p}_3 = \hat{p}_4 = \hat{p}_5$) and the acoustic velocities are connected by the continuity equation ($\hat{u}_3 A_3 = \hat{u}_4 A_4 + \hat{u}_5 A_5$). Due to the coupling of the heat release rate and the acoustic pressure field, it is suitable to install the resonator near the flame. Hereby it is ensured that the resonator is situated at a pressure anti node in case of a constructive feedback cycle between heat release and the acoustic field, which is a necessity for a self-excited thermoacoustic instability. Placing the resonator in a worst case at a pressure node would minimize the acoustic dissipation because the resonator response is driven by the acoustic pressure. The exhaust tube transfer matrix is lumped into the downstream impedance since only one combustor length is investigated.

The original instability frequency was experimentally observed at 105 Hz, at an instability amplitude of $|\hat{u}/\bar{u}| \approx 0.7$. The respective simulation results were discussed with the help of the

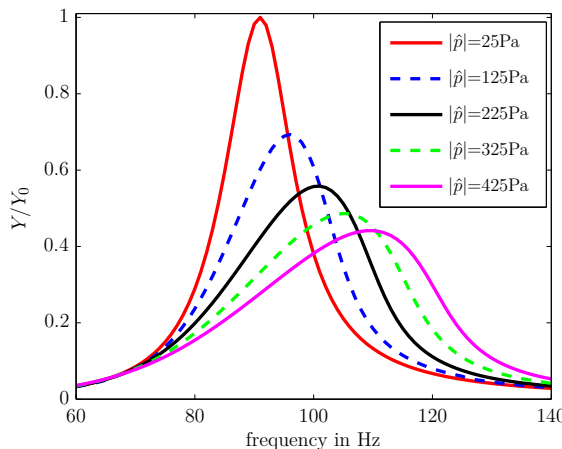


Figure 5.17: Normalized acoustic energy flux of simulated Helmholtz resonator for various pressure amplitudes and a temperature difference between grazing and purging flow of 1000 K.

Figures 5.10 and 5.13. Both, frequency and amplitude were slightly overestimated by the model, leading to a frequency of 110 Hz and an amplitude $|\hat{u}/\bar{u}| \approx 0.78$.

Increasing the acoustic dissipation with acoustic resonators alters the system acoustics and can cause additional instabilities at other frequencies. Consequently, dampers were applied in the frequency range of approximately 135 Hz and 100 Hz. Figure 5.17 illustrates the normalized damper efficiency for the latter one. The amount of acoustic energy dissipation was carefully adjusted to ensure linear stability at all frequencies. The frequency shift caused by the hot gas penetration at higher amplitudes increases the damping at the former unstable frequency of 110 Hz. However, at lower frequencies around 85 Hz the modified combustor system can become unstable, which is the reason for centering the Helmholtz damper response between 85 Hz and 110 Hz. Please note that the presented resonator response is only valid for real frequencies and thus limit-cycle conditions. The dissipation is decreased for linear unstable systems and the associated negative imaginary values of the oscillation frequency.

The normalized acoustic energy dissipation at a constant frequency of 85 Hz is depicted in Figure 5.18a as a function of the acoustic pressure amplitude in the combustion chamber at the flame. The damping efficiency decays exponentially and approaches 30% of the linear damping efficiency at an acoustic pressure amplitude of 450 Pa. In contrast to that, the flame describing function gain, which is associated to the energy addition rate, is relatively constant at low amplitudes. It is shown in Figure 5.18b as a function of the acoustic velocity amplitude upstream of the flame. The flame response is taken from the amplitude-dependent $n-\tau$ model and it starts to saturate slowly for amplitudes $|\hat{u}/\bar{u}| > 0.1$. The nonlinear stability analysis

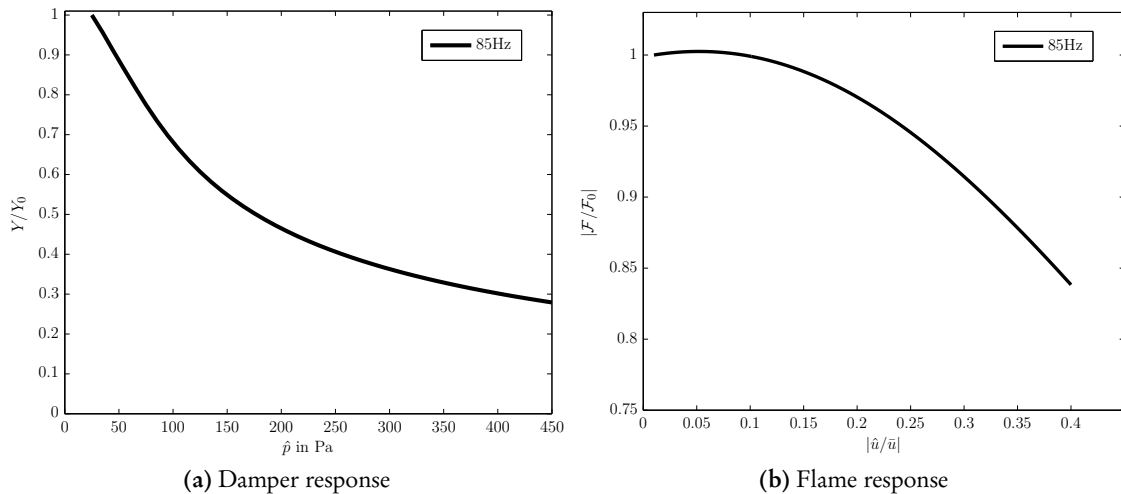


Figure 5.18: (a) Normalized acoustic energy dissipation of damper at 85 Hz for various pressure amplitudes and (b) normalized flame describing function gain at 85 Hz for different acoustic velocity amplitudes at the flame.

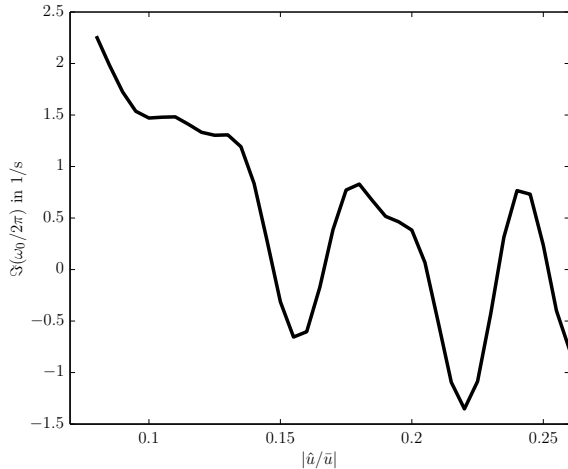


Figure 5.19: Growth rate of unstable mode at combustor length of 1.335 m with additional Helmholtz dampers installed.

of this artificial system is especially challenging due to the dependence of the flame describing function on the acoustic velocity and the corresponding dependency of the resonator to the acoustic pressure. The connection of both quantities depends on the system acoustics, which are again amplitude-dependent due to dependency on the flame describing function and the Helmholtz resonator impedance.

The growth rate of the initially stable eigenfrequency with the smallest growth rate is depicted in Figure 5.19 as a function of the acoustic velocity amplitude at the flame. The system is linearly stable and becomes unstable at an amplitude of $|\hat{u}/\bar{u}| \approx 0.14$ with a frequency of 85 Hz, which slightly increases with increasing amplitude. At an acoustic velocity amplitude of $|\hat{u}/\bar{u}| \approx 0.17$ a limit cycle is established with an acoustic pressure amplitude of $|\hat{p}| \approx 300$ Pa. Increasing the forcing amplitude even further leads to a second nonlinear instability at $|\hat{u}/\bar{u}| \approx 0.21$, which is associated to a limit cycle at an amplitude of $|\hat{u}/\bar{u}| \approx 0.24$ and $|\hat{p}| \approx 350$ Pa. For higher acoustic velocity amplitudes at the flame the system becomes again unstable. However, the application of the damper model is limited to amplitudes, which do not cause hot gas ingestion into the volume. Increasing the amplitude further would inquire a resonator with an extremely long neck, which is from a practical point of view irrelevant.

The nonlinear instabilities are caused by the different decay rates of the damping efficiency and the flame describing gain. A reduction of the normalized acoustic dissipation has a destabilizing effect, while a reduced flame describing function gain stabilizes the thermoacoustic system. Hence, single high amplitude pressure waves or temperature fluctuations in the resonator neck can trigger a subcritical instability of a linearly stable system.

Chapter 6

Summary and Outlook

Writing, at its best, is a lonely life. Organizations for writers palliate the writer's loneliness but I doubt if they improve his writing. He grows in public stature as he sheds his loneliness and often his work deteriorates. For he does his work alone and if he is a good enough writer he must face eternity, or the lack of it, each day. For a true writer each book should be a new beginning where he tries again for something that is beyond attainment. He should always try for something that has never been done or that others have tried and failed. Then sometimes, with great luck, he will succeed.

Ernest Hemingway, Nobel Banquet at the City Hall in Stockholm, December 10, 1954,
the speech was read by John C. Cabot

Emissions of nitrogen oxides, which are harmful to the human health and the environment, are strictly regulated. To satisfy these regulations, modern gas turbine manufacturers mostly rely on the implementation of lean premixed combustion in their high efficiency gas turbines. Unfortunately, lean premixed combustion is prone to thermoacoustic instabilities. These self-excited high-amplitude pressure oscillations arise from the coupling of heat release fluctuations in the flame and the acoustic field. Thermoacoustic instabilities negatively affect the emissions of pollutants and restrict the operation regime of gas turbines, which ultimately has negative effects on the engine efficiency and flexibility. They can reduce the lifetime of the engine or even destroy parts of it. Improvement and further development of the understanding and the modeling tools for premixed flames are needed to reduce the emissions and further increase the gas turbine efficiency. This work contributed to this task in the following ways.

The design of the investigated generic burner is similar to the design applied in real engines. The flame response investigations of the swirl stabilized turbulent flame were conducted for perfectly and technically premixed conditions.

An extensive sensitivity analysis of the flame transfer function revealed that significant deviations and errors are introduced in the measurements even by very accurate mass flow meter systems. It was also shown that nonlinearities at the acoustic boundary conditions introduce

additional errors in the single digit range. More over, the comparison between the photomultiplier and microphone measurements confirmed that the former is quantitatively wrong and even may be qualitatively misleading in the case of a technically premixed flame. Unfortunately, photomultiplier tubes are often used for flame response measurements because of the compactness of this technique. It was also shown that inaccuracies caused by production tolerances of the burner limit the prediction capabilities further. Unavoidable differences, between analytical models and CFD on the one side and the experiment on the other side, in the degree of partial premixedness and the temperature in the combustion chamber, limit the accuracy of prediction tools, too.

It was empirically shown in this work that the flame response of the perfectly premixed swirl flame is connected to the amplification of vortices in the shear layers of the flame. The maximum coherent fluctuation intensity measured in the flame area and the heat release fluctuation feature the same trends with respect to different forcing amplitudes and the swirl numbers. The flame response and the corresponding flow fields for three different swirl numbers indicate that acoustic forcing causes significant changes in the time-averaged reacting flow fields and flame shapes. A triple decomposition is applied to the time-resolved data, which reveals that coherent velocity fluctuations at the forcing frequency are considerably stronger amplified in the shear layers at low forcing amplitudes than at high amplitudes. This is an indicator for a nonlinear saturation process. The strongest saturation is found for the lowest swirl number, where the forcing additionally detached the flame. This is in line with the characteristics of the flame describing function at the investigated frequency for the different swirl numbers. Consequently, the hypothesis of an interaction between the shear layer amplification of the vortical structures and the perfectly premixed flame response is presented. The saturation of the growth of the vortical structures causes a saturation of the heat release fluctuation of the perfectly premixed flame. Hence, future investigations of the transfer function between vortical structures and the flame response by means of numerical calculations could significantly improve the modeling of flame transfer functions.

The influence of equivalence ratio fluctuations on the dynamic response of a swirl flame was investigated, too. To separate the influences from the equivalence ratio perturbations and the velocity fluctuations, the flame describing function was decomposed for several frequencies. In this approach the difference between the perfectly premixed flame describing function and the flame describing function for various degrees of technical premixedness is analyzed and attributed to the influence of the mixture inhomogeneities. Detailed investigations of the flow field and the flame dynamics of perfectly and technically premixed flames have justified this approach because the mean flame shape and the flame and flow field dynamics are very similar. The degree of unmixedness was gradually varied, and equivalence ratio fluctuations

were artificially increased. The decomposition approach delivered consistent results for most of the investigated frequencies for this combustor–flame arrangement. Applying this technique at other combustors could significantly improve the development of these systems since it allows for a simple assessment of the thermoacoustic impact of variations in the degree of unmixedness. The time consuming experiments and numerical calculations, which are needed for the development of a combustor, can be significantly reduced . However, the decomposition approach still needs further validation at different burner types.

Two previously not considered saturation mechanisms were identified for the technically premixed flame. Firstly, caused by the strong movement of the flame and due to significant effects in the mean flow field and the flame shape, the phase of the equivalence ratio contribution to the flame response changes with increasing pulsation amplitude. The strong modifications of the mean flow field and mean flame shape affect the respective time delays of velocity oscillations and equivalence ratio fluctuations. This can have an impact on the interference between velocity and air–fuel mixture oscillations; in case of an initially constructive interference, this leads to saturation. Secondly, because of the increase of turbulent shear stresses and the turbulence intensity with growing oscillation level, the interaction of coherent structures and the changes in the mean flow field and the flame shape, the mixing of fuel and air varies with increasing fluctuation amplitude. The increased attenuation of equivalence ratio fluctuations at higher acoustic forcing amplitudes in the premixed section causes a significant saturation of the flame response to equivalence ratio fluctuations and explains the saturation of the technically premixed flame response at relatively small amplitudes. However, the mixing inhomogeneities were not measured. An investigation addressing the verification of an increased damping of equivalence ratio oscillations should be conducted in the future.

Helmholtz resonators are used in the gas turbine industry as acoustic dampers in the combustion chamber. The precise knowledge of the acoustic damper response is as important as the flame describing function for the correct prediction of thermoacoustic instabilities. The dampers are subject to hot-grazing flow from the combustor and high amplitude pressure oscillations. They are cooled by a constant purging flow taken from the compressor. Due to the negative effect of cooling flows on the overall engine efficiency, the amount of purging flow is limited. As a consequence, the ingestion of hot-gas cannot be avoided for every operation point.

The effect of hot grazing flow on the damping efficiency and resonance frequency was investigated in detail. Two different set-ups were subject to the investigation. High-speed PIV measurements were conducted on the isothermal set-up to measure the flow field in the Helmholtz resonator and in the vicinity of the resonator entrance for various amplitudes and momentum-flux ratios between purging and grazing flow. Additionally, seeding was used as a tracer to visualize the ingestion of the grazing flow into the resonator neck and volume. The second

experimental set-up featured the possibility of investigating the effects of a hot grazing flow acoustically. Comprehensive acoustic measurements were conducted for a variety of amplitudes and temperature differences between grazing and purging flow of up to 1000 K. Furthermore, the temperature in the neck was measured at different axial positions. The acoustic data were also used in conjunction with a detailed impedance model for the calculation of the virtual neck extension and the effective area jump.

Limited investigations in the very low Mach-number regime at momentum-flux ratios up to unity revealed that the grazing flow has no significant influence on the acoustic response of the Helmholtz resonator. Nevertheless, it was observed that the momentum-flux ratio influences the temperature at the Helmholtz resonator neck entrance for small amplitudes. The PIV measurements revealed that a complex interaction between grazing flow and purging flow is present at low amplitudes. Moreover, at high amplitudes the flow field is dominated by the jet emanating out of the resonator. Independent of the momentum-flux ratio of the static purging and grazing flow, a pulsating jet is generated at both area jumps of the resonator neck. Consequently, the entrainment of the surrounding fluid increases the time averaged volume flow of the purging flow strongly, similar to a synthetic jet. The mixing experiments illustrated very well the change in the density field at high amplitudes in the resonator neck, which is in line with the temperature measurements at reacting conditions. They also revealed that relatively small changes in the momentum-flux ratio have an impact on the density field in the vicinity of the resonator entrance.

It was shown for the first time that density gradients have a significant impact on the resonance frequency and the damping performance. For a correct assessment of the acoustic energy flux at reacting conditions, the density gradients in the vicinity of the resonator entrance have to be taken into account. The reduction of the neck length correction, which is proportional to the temperature difference between grazing and purging flow, has a strong impact regardless of the amplitude. It influences the resonance frequency significantly. The impedance model of the Helmholtz resonator is extended with an additional loss-coefficient, which takes the losses generated by density gradients into account. Furthermore, the trend of the effective area change is analyzed with the help of the impedance model in the linear and nonlinear regime and fits qualitatively very well to the flow field analysis. Due to the synthetic jet, which is observed at high amplitudes, the area jump ratios are decreased at higher velocity amplitudes due to the thickening of the emanating jet. The effects on the air density in the neck caused by hot-gas penetration were modeled analytically. The time-averaged value of the spatially-averaged density of the air in the neck is incorporated into the detailed impedance model. It predicts a significant shift of the resonance frequency already for small and moderate pressure amplitudes due to hot-gas intrusion. The penetration depth depends on the purging flow velocity and the pressure

oscillation amplitude in the combustion chamber at the entrance of the Helmholtz resonator. It was found that a rough knowledge of the mean flow temperature in the exhaust tube is sufficient to achieve accurate results with the nonlinear impedance model. The model is in very good agreement with the obtained experimental data for all investigated cases. Additionally, a very simple rule of thumb was introduced to assess the worst-case impact of hot-gas penetration on the damper resonance frequency in a first step.

The presented results suggest that taking temperature gradients between purging and grazing flow into account, significantly improves state of the art impedance models and allows for an accurate prediction of the impedance with very few experiments at isothermal conditions and at least one experiment at elevated temperature. A reliable a-priori impedance prediction of new designs without any experiments remains a challenge and should be in the focus of future work.

The investigated flame describing functions can be used in conjunction with the newly developed damper model to predict thermoacoustic instabilities in the engine. Until now, the accurate prediction of limit cycle amplitudes has not been demonstrated for industry relevant combustion systems. The flame response, the acoustic burner transfer matrix and the impedance upstream and downstream of the burner were obtained with the Multi-Microphone-Method. The acoustic responses of all subsystems were incorporated into a nonlinear thermoacoustic modeling framework to determine frequency and amplitude of the self-excited limit cycle oscillation. In order to verify the simulation results without the damper influence, measurements were made for various lengths of the exhaust gas tube.

The results of the acoustic network model are in very good agreement for the entire range of combustor lengths investigated. Frequencies and acoustic amplitudes of the instabilities were accurately predicted. The flame describing function was also able to reproduce secondary peaks in amplitude and frequency with good accuracy. For the first time, a detailed stability map for a range of instabilities was predicted for an industry type burner including dynamic nonlinear features such as the change of oscillation frequency or a temperature hysteresis. Additionally, an empirical correlation between the linear growth rates and limit cycle amplitudes was found, which should be investigated further.

The presented methodology is proven to be reliable for gas turbine relevant combustion systems with a verified high degree of accuracy. At least for natural gas fired combustors, the results can be scaled to high pressure conditions. However, the correct assessment of the system damping for realistic geometries and engine conditions remains challenging. Additionally, the interaction of the flame describing function and the enhanced nonlinear Helmholtz resonator impedance model was investigated theoretically. It was found that the interaction promotes subcritical instabilities. These need to be investigated experimentally in future work.

Bibliography

- [1] ABU-ORF, G. M. & CANT, R. S. (1996). "Reaction rate modelling for premixed turbulent methane-air flames." In: *Proceedings of the Joint Meeting of the Portuguese, British and Swedish Sections of the Combustion Institute*.
- [2] AYRES, R. U. (1969). *Technological forecasting and long-range planning*. McGraw-Hill, New York.
- [3] BADE, B., WAGNER, M., HIRSCH, C., SATTELMAYER, T., & SCHUERMANS, B. (2013). "Design for Thermo-Acoustic Stability: Procedure and Database." *Journal of Engineering for Gas Turbines and Power*, **135**(12):121507. doi:[10.1115/1.4025131](https://doi.org/10.1115/1.4025131).
- [4] BALACHANDRAN, R., AYOOLA, B. O., KAMINSKI, C. F., DOWLING, A. P., & MASTORAKOS, E. (2005). "Experimental investigation of the nonlinear response of turbulent premixed flames to imposed inlet velocity oscillations." *Combustion and Flame*, **143**(1-2):37–55. doi:[10.1016/j.combustflame.2005.04.009](https://doi.org/10.1016/j.combustflame.2005.04.009).
- [5] BECHERT, D. W. (1980). "Sound absorption caused by vorticity shedding, demonstrated with a jet flow." *Journal of Sound and Vibration*, **70**(3):389–405. doi:[10.1016/0022-460x\(80\)90307-7](https://doi.org/10.1016/0022-460x(80)90307-7).
- [6] BEJAN, A. & LORENTE, S. (2011). "The constructal law origin of the logistics S curve." *Journal of Applied Physics*, **110**(2):024901. doi:[10.1063/1.3606555](https://doi.org/10.1063/1.3606555).
- [7] BELLOWS, B. D., BOBBA, M. K., SEITZMAN, J. M., & LIEUWEN, T. (2007). "Nonlinear Flame Transfer Function Characteristics in a Swirl-Stabilized Combustor." *Journal of Engineering for Gas Turbines and Power*, **129**(4):954–961. doi:[10.1115/1.2720545](https://doi.org/10.1115/1.2720545).
- [8] BELLOWS, B. D., HREIZ, A., & LIEUWEN, T. (2008). "Nonlinear Interactions Between Forced and Self-Excited Acoustic Oscillations in Premixed Combustor." *Journal of Propulsion and Power*, **24**(3):628–631. doi:[10.2514/1.33228](https://doi.org/10.2514/1.33228).
- [9] BELLUCCI, V. (2009). *Modeling and Control of Gas Turbine Thermoacoustic Pulsations*. Ph.D. thesis, Technische Universität Berlin, Berlin.
- [10] BELLUCCI, V., FLOHR, P., PASCHEREIT, C. O., & MAGNI, F. (2004). "On the Use of Helmholtz Resonators for Damping Acoustic Pulsations in Industrial Gas Turbines." *Journal of Engineering for Gas Turbines and Power*, **126**(2):271–275. doi:[10.1115/1.1473152](https://doi.org/10.1115/1.1473152).
- [11] BIAGIOLI, F., GÜTHER, F., & SCHUERMANS, B. (2008). "Combustion dynamics linked to flame behaviour in a partially premixed swirled industrial burner." *Experimental Thermal and Fluid Science*, **32**(7):1344–1353. doi:[10.1016/j.expthermflusci.2007.11.007](https://doi.org/10.1016/j.expthermflusci.2007.11.007).

- [12] BIES, D. A. & WILSON, O. B. J. (1957). "Acoustic Impedance of a Helmholtz Resonator at Very High Amplitude." *The Journal of the Acoustical Society of America*, **29**(6):711–714. doi:[10.1121/1.1909021](https://doi.org/10.1121/1.1909021).
- [13] BIRBAUD, A., DUCRUIX, S., DUROX, D., & CANDEL, S. M. (2008). "The nonlinear response of inverted "V" flames to equivalence ratio nonuniformities." *Combustion and Flame*, **154**(3):356–367. doi:[10.1016/j.combustflame.2008.05.017](https://doi.org/10.1016/j.combustflame.2008.05.017).
- [14] BOBUSCH, B. C., ĆOSIĆ, B., MOECK, J. P., & PASCHEREIT, C. O. (2014). "Optical Measurement of Local and Global Transfer Functions for Equivalence Ratio Fluctuations in a Turbulent Swirl Flame." *Journal of Engineering for Gas Turbines and Power*, **136**(2):021506. doi:[10.1115/1.4025375](https://doi.org/10.1115/1.4025375).
- [15] Bošnjaković, F. (1998). *Technische Thermodynamik*. Steinkopff, Darmstadt, 8th edn.
- [16] BOTHIEN, M. R. (2008). *Impedance Tuning: A Method for Active Control of the Acoustic Boundary Conditions of Combustion Test Rigs*. Ph.D. thesis, Technische Universität Berlin, Berlin.
- [17] BOTHIEN, M. R. & WASSMER, D. (2014). "On the Impact of Density Discontinuities on the Resonance Frequency of Helmholtz Resonators." *AIAA Journal*. doi:[10.2514/1-J053227](https://doi.org/10.2514/1-J053227), (just accepted).
- [18] BOTHIEN, M. R., PENNELL, D. A., ZAJADATZ, M., & DÖBBELING, K. (2013). "On key features of the AEV burner engine implementation for operational flexibility." In: *Proceedings of ASME Turbo Expo 2013*. doi:[10.1115/GT2013-95693](https://doi.org/10.1115/GT2013-95693).
- [19] BOTHIEN, M. R., NOIRAY, N., & SCHUERMANS, B. (2014). "A Novel Damping Device for Broadband Attenuation of Low-Frequency Combustion Pulsations in Gas Turbines." *Journal of Engineering for Gas Turbines and Power*, **136**(4):041504. doi:[10.1115/1.4025761](https://doi.org/10.1115/1.4025761).
- [20] BOUDY, F., DUROX, D., SCHULLER, T., & CANDEL, S. M. (2011). "Nonlinear mode triggering in a multiple flame combustor." *Proceedings of the Combustion Institute*, **33**(1):1121–1128. doi:[10.1016/j.proci.2010.05.079](https://doi.org/10.1016/j.proci.2010.05.079).
- [21] BOUDY, F., DUROX, D., SCHULLER, T., JOMAAS, G., & CANDEL, S. M. (2011). "Describing Function Analysis of Limit Cycles in a Multiple Flame Combustor." *Journal of Engineering for Gas Turbines and Power*, **133**(6):061502. doi:[10.1115/1.4002275](https://doi.org/10.1115/1.4002275).
- [22] BOURGOUIN, J.-F., DUROX, D., MOECK, J. P., SCHULLER, T., & CANDEL, S. M. (2013). "Self-Sustained Instabilities in an Annular Combustor Coupled by Azimuthal and Longitudinal Acoustic Modes." In: *Proceedings of ASME Turbo Expo 2013*. doi:[10.1115/GT2013-95010](https://doi.org/10.1115/GT2013-95010).
- [23] BP (2013). "BP Statistical Review of World Energy June 2013." URL: www.bp.com/content/dam/bp/pdf/statistical-review/statistical_review_of_world_energy_2013.pdf, retrieved August 12, 2014.
- [24] BUCHANAN, R., WHITING, R., & DAMERT, W. (1997). "When is simple good enough: a comparison of the Gompertz, Baranyi, and three-phase linear models for fitting bacterial growth curves." *Food Microbiology*, **14**(4):313–326. doi:[10.1006/fmic.1997.0125](https://doi.org/10.1006/fmic.1997.0125).

- [25] BUICK, J. M., ATIG, M., SKULINA, D. J., CAMPBELL, D. M., DALMONT, J. P., & GILBERT, J. (2011). "Investigation of non-linear acoustic losses at the open end of a tube." *The Journal of the Acoustical Society of America*, **129**(3):1261. doi:[10.1121/1.3543987](https://doi.org/10.1121/1.3543987).
- [26] CHUNG, J. Y. & BLASER, D. A. (1980). "Transfer function method of measuring induct acoustic properties." *The Journal of the Acoustical Society of America*, **68**(3):907–913. doi:[10.1121/1.384779](https://doi.org/10.1121/1.384779).
- [27] CORREA, S. M. (1993). "A Review of NO x Formation Under Gas-Turbine Combustion Conditions." *Combustion Science and Technology*, **87**(1-6):329–362. doi:[10.1080/00102209208947221](https://doi.org/10.1080/00102209208947221).
- [28] Ćosić, B., BOBUSCH, B. C., MOECK, J. P., & PASCHEREIT, C. O. (2012). "Open-Loop Control of Combustion Instabilities and the Role of the Flame Response to Two-Frequency Forcing." *Journal of Engineering for Gas Turbines and Power*, **134**(6):061502. doi:[10.1115/1.4005986](https://doi.org/10.1115/1.4005986).
- [29] Ćosić, B., REICHEL, T. G., & PASCHEREIT, C. O. (2012). "Acoustic Response of a Helmholtz Resonator Exposed to Hot-Gas Penetration and High Amplitude Oscillations." *Journal of Engineering for Gas Turbines and Power*, **134**(10):101503. doi:[10.1115/1.4007024](https://doi.org/10.1115/1.4007024).
- [30] Ćosić, B., MOECK, J. P., & PASCHEREIT, C. O. (2013). "Prediction of pressure amplitudes of self-excited thermoacoustic instabilities for a partially premixed swirl-flame." In: *Proceedings of ASME Turbo Expo 2013*. doi:[10.1115/GT2012-69774](https://doi.org/10.1115/GT2012-69774).
- [31] Ćosić, B., MOECK, J. P., & PASCHEREIT, C. O. (2014). "Nonlinear Instability Analysis for Partially Premixed Swirl Flames." *Combustion Science and Technology*, **186**(6):713–736. doi:[10.1080/00102202.2013.876420](https://doi.org/10.1080/00102202.2013.876420).
- [32] Ćosić, B., TERHAAR, S., MOECK, J. P., & PASCHEREIT, C. O. (2014). "Response of a swirl-stabilized flame to simultaneous perturbations in equivalence ratio and velocity at high oscillation amplitudes." *Combustion and Flame*, **-(-):-**. doi:[10.1016/j.combustflame.2014.09.025](https://doi.org/10.1016/j.combustflame.2014.09.025), in press.
- [33] Ćosić, B., WASSMER, D., TERHAAR, S., & PASCHEREIT, C. O. (2015). "Acoustic response of helmholtz dampers in the presence of hot grazing flow." *Journal of Sound and Vibration*, **335**(0):1 – 18. doi:[10.1016/j.jsv.2014.08.025](https://doi.org/10.1016/j.jsv.2014.08.025).
- [34] CROCCO, L. (1965). "Theoretical studies on liquid-propellant rocket instability." *Symposium (International) on Combustion*, **10**(1):1101–1128. doi:[10.1016/S0082-0784\(65\)80249-1](https://doi.org/10.1016/S0082-0784(65)80249-1).
- [35] CULICK, F. E. C., BURNLEY, V., & SWENSON, G. (1995). "Pulsed instabilities in solid-propellant rockets." *Journal of Propulsion and Power*, **11**(4):657–665. doi:[10.2514/3.23891](https://doi.org/10.2514/3.23891).
- [36] DÖBBELING, K., HELLAT, J., & KOCH, H. (2007). "25 Years of BBC/ABB/Alstom Lean Premix Combustion Technologies." *Journal of Engineering for Gas Turbines and Power*, **129**(1):2. doi:[10.1115/1.2181183](https://doi.org/10.1115/1.2181183).

- [37] DOWLING, A. P. (1997). "Nonlinear self-excited oscillations of a ducted flame." *Journal of Fluid Mechanics*, **346**:271–290. doi:[10.1017/s0022112097006484](https://doi.org/10.1017/s0022112097006484).
- [38] DUCHAINE, F., BOUDY, F., DUROX, D., & POINSOT, T. (2011). "Sensitivity analysis of transfer functions of laminar flames." *Combustion and Flame*, **158**(12):2384–2394. doi:[10.1016/j.combustflame.2011.05.013](https://doi.org/10.1016/j.combustflame.2011.05.013).
- [39] DUROX, D., SCHULLER, T., NOIRAY, N., & CANDEL, S. M. (2009). "Experimental analysis of nonlinear flame transfer functions for different flame geometries." *Proceedings of the Combustion Institute*, **32**(1):1391–1398. doi:[10.1016/j.proci.2008.06.204](https://doi.org/10.1016/j.proci.2008.06.204).
- [40] DUROX, D., MOECK, J. P., BOURGOUIN, J.-F., MORENTON, P., VIALLON, M., SCHULLER, T., & CANDEL, S. M. (2013). "Flame dynamics of a variable swirl number system and instability control." *Combustion and Flame*, **160**(9):1729–1742. doi:[10.1016/j.combustflame.2013.03.004](https://doi.org/10.1016/j.combustflame.2013.03.004).
- [41] ENZ, R. (2000). "The S-curve relation between per-capita income and insurance penetration." *Geneva Papers on Risk and Insurance. Issues and Practice*, pp. 396–406.
- [42] EROGLU, A. & BREIDENTHAL, R. E. (2001). "Structure, Penetration, and Mixing of Pulsed Jets in Crossflow." *AIAA Journal*, **39**(3):417–423. doi:[10.2514/2.1351](https://doi.org/10.2514/2.1351).
- [43] FINDEISEN, J., GNIRSS, M., DAMASCHKE, N., SCHIFFER, H.-P., & TROPEA, C. (2005). "2D - Concentration Measurements Based on Mie Scattering using a Commercial PIV system." In: *6th International Symposium on Particle Image Velocimetry*, PIV05 Paper.
- [44] FRAUNHOFER-ISI (2010). "Entwicklung der PKW-Flotte in Deutschland." URL: http://www.fraunhofer-isи-cms.de/elektromobilitаet/Media/forschungsergebnisse/13062438635288-10.92.21.153-Forschungsergebnisse_Verkehrszenarien_Fahrzeugflossen.pdf, retrieved August 12, 2014.
- [45] GINEVSKY, A. S., VLASOV, E. V., & KARAVOSOV, R. K. (2004). *Acoustic control of turbulent jets*. Foundations of engineering mechanics. Springer, New York.
- [46] GUSTAVSEN, B. & SEMLYEN, A. (1999). "Rational Approximation of Frequency Domain Responses by Vector Fitting." *IEEE Transactions on Power Delivery*, **14**(3):1052–1061. doi:[10.1109/61.772353](https://doi.org/10.1109/61.772353).
- [47] HARRIS, W. (1982). ""Sounding Brass" and Hellenistic Technology." *Biblical Archaeology Review (BAR)*, **8**:38–41.
- [48] HELMHOLTZ, H. (1896). "Theorie der Luftschwingungen in Röhren mit offenen Enden." *Journal für die reine und angewandte Mathematik*, **57**(1):1–72. doi:[10.1515/crll.1860.57.1](https://doi.org/10.1515/crll.1860.57.1).
- [49] HEMCHANDRA, S. (2012). "Premixed flame response to equivalence ratio fluctuations: Comparison between reduced order modeling and detailed computations." *Combustion and Flame*, **159**(12):3530–3543. doi:[10.1016/j.combustflame.2012.08.003](https://doi.org/10.1016/j.combustflame.2012.08.003).
- [50] HEMCHANDRA, S., PETERS, N., & LIEUWEN, T. (2011). "Heat release response of acoustically forced turbulent premixed flames—role of kinematic restoration." *Proceedings of the Combustion Institute*, **33**(1):1609–1617. doi:[10.1016/j.proci.2010.06.115](https://doi.org/10.1016/j.proci.2010.06.115).

- [51] HIGGINS, B., MCQUAY, M., LACAS, F., ROLON, J., DARABIHA, N., & CANDEL, S. M. (2001). "Systematic measurements of OH chemiluminescence for fuel-lean, high-pressure, pre-mixed, laminar flames." *Fuel*, **80**(1):67–74. doi:[10.1016/S0016-2361\(00\)00069-7](https://doi.org/10.1016/S0016-2361(00)00069-7).
- [52] HIRSCH, C., FANACA, D., REDDY, P., POLIFKE, W., & SATTELMAYER, T. (2005). "Influence of the swirler design on the flame transfer function of premixed flames." In: *Proceedings of ASME Turbo Expo 2005*. doi:[10.1115/GT2005-68195](https://doi.org/10.1115/GT2005-68195).
- [53] HOWE, M. S. (1979). "Attenuation of sound in a low Mach Number nozzle flow." *Journal of Fluid Mechanics*, **91**(02):209. doi:[10.1017/S0022112079000124](https://doi.org/10.1017/S0022112079000124).
- [54] HUANG, Y. & YANG, V. (2009). "Dynamics and stability of lean-premixed swirl-stabilized combustion." *Progress in Energy and Combustion Science*, **35**(4):293–364. doi:[10.1016/j.pecs.2009.01.002](https://doi.org/10.1016/j.pecs.2009.01.002).
- [55] HUBER, A. & POLIFKE, W. (2008). "Impact of fuel supply impedance on combustion stability of gas turbines." In: *Proceedings of ASME Turbo Expo 2008*. doi:[10.1115/GT2008-51193](https://doi.org/10.1115/GT2008-51193).
- [56] HUBER, A. & POLIFKE, W. (2009). "Dynamics of practical premixed flames, part I: model structure and identification." *International Journal of Spray and Combustion Dynamics*, **1**(2):199–228. doi:[10.1260/175682709788707431](https://doi.org/10.1260/175682709788707431).
- [57] HUSSAIN, A. K. M. F. & REYNOLDS, W. C. (1970). "The mechanics of an organized wave in turbulent shear flow." *Journal of Fluid Mechanics*, **41**(02):241. doi:[10.1017/S0022112070000605](https://doi.org/10.1017/S0022112070000605).
- [58] IDELCHIK, I. E. & FRIED, E. (1986). *Handbook of hydraulic resistance*. Hemisphere Pub. Corp., Washington, second edn.
- [59] INGÅRD, U. (1953). "On the Theory and Design of Acoustic Resonators." *The Journal of the Acoustical Society of America*, **25**(6). doi:[10.1121/1.1907235](https://doi.org/10.1121/1.1907235).
- [60] INGÅRD, U. & ISING, H. (1967). "Acoustic Nonlinearity of an Orifice." *The Journal of the Acoustical Society of America*, **42**(1):6–17. doi:[10.1121/1.1910576](https://doi.org/10.1121/1.1910576).
- [61] JÖRG, C., GIKADI, J., & SATTELMAYER, T. (2013). "Numerical investigation of the plane-wave reflection coefficient of an exhaust pipe at elevated temperatures using linearized Navier-Stokes equations." In: *Proceedings of ASME Turbo Expo 2013*. doi:[10.1115/GT2013-94843](https://doi.org/10.1115/GT2013-94843).
- [62] KELLER, J. J. (1995). "Thermoacoustic oscillations in combustion chambers of gas turbines." *AIAA Journal*, **33**(12):2280–2287. doi:[10.2514/3.12980](https://doi.org/10.2514/3.12980).
- [63] KELLER, J. J. & ZAUNER, E. (1995). "On the use of Helmholtz resonators as sound attenuators." *Zeitschrift für angewandte Mathematik und Physik*, **46**(3):297–327. doi:[10.1007/BF01003552](https://doi.org/10.1007/BF01003552).
- [64] KIM, K. T. & HOCHGREB, S. (2011). "The nonlinear heat release response of stratified lean-premixed flames to acoustic velocity oscillations." *Combustion and Flame*, **158**(12):2482–2499. doi:[10.1016/j.combustflame.2011.05.016](https://doi.org/10.1016/j.combustflame.2011.05.016).

- [65] KIM, K. T. & SANTAVICCA, D. A. (2013). "Generalization of Turbulent Swirl Flame Transfer Functions in Gas Turbine Combustors." *Combustion Science and Technology*, **185**(7):999–1015. doi:[10.1080/00102202.2012.752734](https://doi.org/10.1080/00102202.2012.752734).
- [66] KIM, K. T. & SANTAVICCA, D. A. (2013). "Interference mechanisms of acoustic/convective disturbances in a swirl-stabilized lean-premixed combustor." *Combustion and Flame*, **160**(8):1441–1457. doi:[10.1016/j.combustflame.2013.02.022](https://doi.org/10.1016/j.combustflame.2013.02.022).
- [67] KIM, K. T., LEE, J. G., QUAY, B. D., & SANTAVICCA, D. A. (2010). "Response of partially premixed flames to acoustic velocity and equivalence ratio perturbations." *Combustion and Flame*, **157**(9):1731–1744. doi:[10.1016/j.combustflame.2010.04.006](https://doi.org/10.1016/j.combustflame.2010.04.006).
- [68] KIM, K. T., LEE, J. G., QUAY, B. D., & SANTAVICCA, D. A. (2011). "Reconstruction of Heat Release Response of Partially Premixed Flames." *Combustion Science and Technology*, **183**(2):122–137. doi:[10.1080/00102202.2010.503205](https://doi.org/10.1080/00102202.2010.503205).
- [69] KIRCHHOFF, G. (1868). "Ueber den Einfluß der Wärmeleitung in einem Gase auf die Schallbewegung." *Annalen der Physik und Chemie*, **210**(6):177–193. doi:[10.1002/andp.18682100602](https://doi.org/10.1002/andp.18682100602).
- [70] KOMAREK, T. & POLIFKE, W. (2010). "Impact of Swirl Fluctuations on the Flame Response of a Perfectly Premixed Swirl Burner." *Journal of Engineering for Gas Turbines and Power*, **132**(6):061503. doi:[10.1115/1.4000127](https://doi.org/10.1115/1.4000127).
- [71] KREBS, W., KREDIET, H., PORTILLO, E., HERMETH, S., POINSOT, T., SCHIMEK, S., & PASCHEREIT, C. O. (2013). "Comparison of Nonlinear to Linear Thermoacoustic Stability Analysis of a Gas Turbine Combustion System." *Journal of Engineering for Gas Turbines and Power*, **135**(8):081503. doi:[10.1115/1.4023887](https://doi.org/10.1115/1.4023887).
- [72] KREDIET, H. J., BECK, C. H., KREBS, W., & KOK, J. (2013). "Saturation mechanism of the heat release response of a premixed swirl flame using LES." *Proceedings of the Combustion Institute*, **34**(1):1223–1230. doi:[10.1016/j.proci.2012.06.140](https://doi.org/10.1016/j.proci.2012.06.140).
- [73] LAHIRI, C., ENGHARDT, L., BAKE, F., SADIG, S., & GERENDÁS, M. (2011). "Establishment of a High Quality Database for the Acoustic Modeling of Perforated Liners." *Journal of Engineering for Gas Turbines and Power*, **133**(9):091503. doi:[10.1115/1.4002891](https://doi.org/10.1115/1.4002891).
- [74] LAND, K. C. (1993). "S-Curves Everywhere." *Science*, **259**(5099):1349–1350. doi:[10.1126/science.259.5099.1349](https://doi.org/10.1126/science.259.5099.1349).
- [75] LECHNER, C. & BOTHIEN, M. R. (2005). "Measurement of the inlet gas temperature of a gas turbine." In: *Proceedings of ASME Turbo Expo 2005*. doi:[10.1115/GT2005-68138](https://doi.org/10.1115/GT2005-68138).
- [76] LEUCKEL, W. (1967). "Swirl intensities, swirl types and energy losses of different swirl generating devices." IFRF, IJmuiden, IFRF Doc. No. G02/a/16.
- [77] LEVINE, H. & SCHWINGER, J. (1948). "On the Radiation of Sound from an Unflanged Circular Pipe." *Physical Review*, **73**(4):383–406. doi:[10.1103/PhysRev.73.383](https://doi.org/10.1103/PhysRev.73.383).
- [78] LIEUWEN, T. (2003). "Modeling Premixed Combustion-Acoustic Wave Interactions: A Review." *Journal of Propulsion and Power*, **19**(5):765–781. doi:[10.2514/2.6193](https://doi.org/10.2514/2.6193).

- [79] LIEUWEN, T. & NEUMEIER, Y. (2002). "Nonlinear pressure-heat release transfer function measurements in a premixed combustor." *Proceedings of the Combustion Institute*, **29**:99–105. doi:[10.1016/s1540-7489\(02\)80017-7](https://doi.org/10.1016/s1540-7489(02)80017-7).
- [80] LIEUWEN, T. & YANG, V. (eds.) (2005). *Combustion Instabilities in Gas Turbine Engines: Operational Experience, Fundamental Mechanisms, and Modeling*, vol. 210 of *Progress in Astronautics and Aeronautics*. American Institute of Aeronautics and Astronautics, Reston, Va.
- [81] LIEUWEN, T., TORRES, H., JOHNSON, C., & ZINN, B. T. (2001). "A Mechanism of Combustion Instability in Lean Premixed Gas Turbine Combustors." *Journal of Engineering for Gas Turbines and Power*, **123**(1):182. doi:[10.1115/1.1339002](https://doi.org/10.1115/1.1339002).
- [82] LINSTONE, H. A. (1976). *Technological substitution: Forecasting, techniques and applications*. Elsevier, New York, NY.
- [83] LIPATNIKOV, A. N. & CHOMIAK, J. (2002). "Turbulent flame speed and thickness: phenomenology, evaluation, and application in multi-dimensional simulations." *Progress in Energy and Combustion Science*, **28**(1):1–74. doi:[10.1016/S0360-1285\(01\)00007-7](https://doi.org/10.1016/S0360-1285(01)00007-7).
- [84] MEADOWS, D. L. (1972). *The limits to growth*. Universe Books, New York.
- [85] MERK, H. (1957). "An analysis of unstable combustion of premixed gases." *Symposium (International) on Combustion*, **6**(1):500–512. doi:[10.1016/S0082-0784\(57\)80067-8](https://doi.org/10.1016/S0082-0784(57)80067-8).
- [86] MODIS, T. (1992). *Predictions: Society's telltale signature reveals the past and forecasts the future*. Simon & Schuster, New York.
- [87] MOECK, J. P. (2010). *Analysis, Modeling, and Control of Thermoacoustic Instabilities*. Ph.D. thesis, TU Berlin, Berlin.
- [88] MOECK, J. P. & PASCHEREIT, C. O. (2012). "Nonlinear interactions of multiple linearly unstable thermoacoustic modes." *International Journal of Spray and Combustion Dynamics*, **4**(1):1–28. doi:[10.1260/1756-8277.4.1.1](https://doi.org/10.1260/1756-8277.4.1.1).
- [89] MOECK, J. P., BOTHIEN, M. R., SCHIMEK, S., LACARELLE, A., & PASCHEREIT, C. O. (2008). "Subcritical thermoacoustic instabilities in a premixed combustor." In: *Proceedings of the 44th AIAA Aerospace Sciences Meeting and Exhibit*. doi:[10.2514/6.2008-2946](https://doi.org/10.2514/6.2008-2946).
- [90] MÖSER, M. (2009). *Technische Akustik*. Springer Berlin Heidelberg, Berlin, Heidelberg.
- [91] MUNJAL, M. L. (1987). *Acoustics of ducts and mufflers with application to exhaust and ventilation system design*. Wiley, New York.
- [92] NOACK, B. R., AFANASIEV, K., MORZYNSKI, M., TADMOR, G., & THIELE, F. (2003). "A hierarchy of low-dimensional models for the transient and post-transient cylinder wake." *Journal of Fluid Mechanics*, **497**:335–363. doi:[10.1017/S0022112003006694](https://doi.org/10.1017/S0022112003006694).
- [93] NOIRAY, N., DUROX, D., SCHULLER, T., & CANDEL, S. M. (2008). "A unified framework for nonlinear combustion instability analysis based on the flame describing function." *Journal of Fluid Mechanics*, **615**:139–167. doi:[10.1017/s0022112008003613](https://doi.org/10.1017/s0022112008003613).

- [94] OBERLEITHNER, K., SCHIMEK, S., & PASCHEREIT, C. O. (2012). "On the impact of shear flow instabilities on global heat release rate fluctuations: linear stability analysis of a cold and reacting swirling jet." In: *Proceedings of ASME Turbo Expo 2012*. doi:[10.1115/gt2012-69774](https://doi.org/10.1115/gt2012-69774).
- [95] OBERLEITHNER, K., SCHIMEK, S., & PASCHEREIT, C. O. (2014). "Shear flow instabilities in swirl-stabilized combustors and their impact on the amplitude dependent flame response: A linear stability analysis." *Combustion and Flame*. doi:[10.1016/j.combustflame.2014.07.012](https://doi.org/10.1016/j.combustflame.2014.07.012).
- [96] OSTER, D. & WYGNANSKI, I. (1982). "The forced mixing layer between parallel streams." *Journal of Fluid Mechanics*, **123**(-1):91. doi:[10.1017/S0022112082002973](https://doi.org/10.1017/S0022112082002973).
- [97] PALIES, P., DUROX, D., SCHULLER, T., & CANDEL, S. M. (2010). "The combined dynamics of swirler and turbulent premixed swirling flames." *Combustion and Flame*, **157**(9):1698–1717. doi:[10.1016/j.combustflame.2010.02.011](https://doi.org/10.1016/j.combustflame.2010.02.011).
- [98] PALIES, P., DUROX, D., SCHULLER, T., & CANDEL, S. M. (2011). "Nonlinear combustion instability analysis based on the flame describing function applied to turbulent premixed swirling flames." *Combustion and Flame*, **158**(10):1980–1991. doi:[10.1016/j.combustflame.2011.02.012](https://doi.org/10.1016/j.combustflame.2011.02.012).
- [99] PASCHEREIT, C. O., GUTMARK, E., & WEISENSTEIN, W. (1999). "Coherent structures in swirling flows and their role in acoustic combustion control." *Physics of Fluids*, **11**(9):2667. doi:[10.1063/1.870128](https://doi.org/10.1063/1.870128).
- [100] PASCHEREIT, C. O., GUTMARK, E., & WEISENSTEIN, W. (2000). "Excitation of Thermoacoustic Instabilities by Interaction of Acoustics and Unstable Swirling Flow." *AIAA Journal*, **38**(6):1025–1034. doi:[10.2514/3.14511](https://doi.org/10.2514/3.14511).
- [101] PASCHEREIT, C. O., SCHUERMANS, B., & POLIFKE, W. (2002). "Measurement of Transfer Matrices and Source Terms of Premixed Flames." *Journal of Engineering for Gas Turbines and Power*, **124**(2):239–247. doi:[10.1115/1.1383255](https://doi.org/10.1115/1.1383255).
- [102] PERACCHIO, A. A. & PROSCIA, W. M. (1999). "Nonlinear Heat-Release/Acoustic Model for Thermoacoustic Instability in Lean Premixed Combustors." *Journal of Engineering for Gas Turbines and Power*, **121**(3):415–421. doi:[10.1115/1.2818489](https://doi.org/10.1115/1.2818489).
- [103] PETERS, M. C. A. M., HIRSCHBERG, A., REIJNEN, A. J., & WIJNANDS, A. P. J. (1993). "Damping and reflection coefficient measurements for an open pipe at low Mach and low Helmholtz numbers." *Journal of Fluid Mechanics*, **256**:499. doi:[10.1017/S0022112093002861](https://doi.org/10.1017/S0022112093002861).
- [104] PETERS, N. (2004). *Turbulent combustion*. Cambridge monographs on mechanics. Cambridge University Press, Cambridge, repr. (with corr.) edn.
- [105] POINSOT, T., LE CHATELIER, C., CANDEL, S. M., & ESPOSITO, E. (1986). "Experimental determination of the reflection coefficient of a premixed flame in a duct." *Journal of Sound and Vibration*, **107**(2):265–278. doi:[10.1016/0022-460X\(86\)90237-3](https://doi.org/10.1016/0022-460X(86)90237-3).

- [106] POLIFKE, W., KOPITZ, J., & SERBANOVIV, A. (2001). "Impact of the fuel time lag distribution in elliptical premix nozzles on combustion stability." In: *7th AIAA/CEAS Aeroacoustics Conference and Exhibit*. doi:[10.2514/6.2001-2104](https://doi.org/10.2514/6.2001-2104).
- [107] POPE, S. B. (2000). *Turbulent flows*. Cambridge University Press, Cambridge and New York.
- [108] RÄMMAL, H. & LAVRENTJEV, J. (2008). "Sound reflection at an open end of a circular duct exhausting hot gas." *Noise Control Engineering Journal*, **56**(2):107. doi:[10.3397/1.2898681](https://doi.org/10.3397/1.2898681).
- [109] RAYLEIGH, J. W. S. (1878). "The explanation of certain acoustic phenomena." *Nature*, **18**:319–321. doi:[10.1038/018319a0](https://doi.org/10.1038/018319a0).
- [110] RIENSTRA, S. W. & HIRSCHBERG, A. (2006). "An introduction to acoustics." Eindhoven University of Technology.
- [111] RUPP, J., CARROTTE, J., & SPENCER, A. (2010). "Interaction Between the Acoustic Pressure Fluctuations and the Unsteady Flow Field Through Circular Holes." *Journal of Engineering for Gas Turbines and Power*, **132**(6):061501. doi:[10.1115/1.4000114](https://doi.org/10.1115/1.4000114).
- [112] SATTELMAYER, T. (2003). "Influence of the Combustor Aerodynamics on Combustion Instabilities From Equivalence Ratio Fluctuations." *Journal of Engineering for Gas Turbines and Power*, **125**(1):11. doi:[10.1115/1.1365159](https://doi.org/10.1115/1.1365159).
- [113] SATTELMAYER, T. & POLIFKE, W. (2003). "A novel method for the computation of the linear stability of combustors." *Combustion Science and Technology*, **175**(3):477–497. doi:[10.1080/00102200302387](https://doi.org/10.1080/00102200302387).
- [114] SATTELMAYER, T. & POLIFKE, W. (2003). "Assessment of methods for the computation of the linear stability of combustors." *Combustion Science and Technology*, **175**(3):453–476. doi:[10.1080/00102200302382](https://doi.org/10.1080/00102200302382).
- [115] SCARPATO, A., TRAN, N., DUCRUIX, S., & SCHULLER, T. (2012). "Modeling the damping properties of perforated screens traversed by a bias flow and backed by a cavity at low Strouhal number." *Journal of Sound and Vibration*, **331**(2):276–290. doi:[10.1016/j.jsv.2011.09.005](https://doi.org/10.1016/j.jsv.2011.09.005).
- [116] SCHADOW, K. C. & GUTMARK, E. (1992). "Combustion instability related to vortex shedding in dump combustors and their passive control." *Progress in Energy and Combustion Science*, **18**(2):117–132. doi:[10.1016/0360-1285\(92\)90020-2](https://doi.org/10.1016/0360-1285(92)90020-2).
- [117] SCHIMEK, S., MOECK, J. P., & PASCHEREIT, C. O. (2011). "An Experimental Investigation of the Nonlinear Response of an Atmospheric Swirl-Stabilized Premixed Flame." *Journal of Engineering for Gas Turbines and Power*, **133**(10):101502. doi:[10.1115/1.4002946](https://doi.org/10.1115/1.4002946).
- [118] SCHMID, M., BLUMENTHAL, R. S., SCHULZE, M., POLIFKE, W., & SATTELMAYER, T. (2013). "Quantitative Stability Analysis Using Real-Valued Frequency Response Data." *Journal of Engineering for Gas Turbines and Power*, **135**(12):121601. doi:[10.1115/1.4025299](https://doi.org/10.1115/1.4025299).
- [119] SCHUERMANS, B. (2003). *Modeling and Control of Thermoacoustic Instabilities*. Ph.D. thesis, Ecole Polytechnique Fédérale de Lausanne, Lausanne.

- [120] SCHUERMANS, B., BELLUCCI, V., GUETHE, F., MEILI, F., FLOHR, P., & PASCHEREIT, C. O. (2004). “A detailed analysis of thermoacoustic interaction mechanisms in a turbulent premixed flame.” In: *Proceedings of ASME Turbo Expo*. doi:[10.1115/GT2004-53831](https://doi.org/10.1115/GT2004-53831).
- [121] SCHUERMANS, B., GUETHE, F., PENNELL, D. A., GUYOT, D., & PASCHEREIT, C. O. (2010). “Thermoacoustic Modeling of a Gas Turbine Using Transfer Functions Measured Under Full Engine Pressure.” *Journal of Engineering for Gas Turbines and Power*, **132**(11):111503. doi:[10.1115/1.4000854](https://doi.org/10.1115/1.4000854).
- [122] SCHULLER, T., DUCRUIX, S., DUROX, D., & CANDEL, S. M. (2002). “Modeling tools for the prediction of premixed flame transfer functions.” *Proceedings of the Combustion Institute*, **29**(1):107–113. doi:[10.1016/S1540-7489\(02\)80018-9](https://doi.org/10.1016/S1540-7489(02)80018-9).
- [123] SCHULLER, T., DUROX, D., & CANDEL, S. M. (2003). “A unified model for the prediction of laminar flame transfer functions: comparisons between conical and V-flame dynamics.” *Combustion and Flame*, **134**(1–2):21–34. doi:[10.1016/S0010-2180\(03\)00042-7](https://doi.org/10.1016/S0010-2180(03)00042-7).
- [124] SCHULLER, T., TRAN, N., NOIRAY, N., DUROX, D., DUCRUIX, S., & CANDEL, S. M. (2009). “The role of nonlinear acoustic boundary conditions in combustion/acoustic coupled instabilities.” In: *Proceedings of ASME Turbo Expo 2009*. doi:[10.1115/GT2009-59390](https://doi.org/10.1115/GT2009-59390).
- [125] SEYBERT, A. F. & ROSS, D. F. (1977). “Experimental determination of acoustic properties using a two-microphone random-excitation technique.” *The Journal of the Acoustical Society of America*, **61**(5):1362–1370. doi:[10.1121/1.2016268](https://doi.org/10.1121/1.2016268).
- [126] SHREEKRISHNA, S. H. & LIEUWEN, T. (2010). “Premixed flame response to equivalence ratio perturbations.” *Combustion Theory and Modelling*, **14**(5):681–714. doi:[10.1080/13647830.2010.502247](https://doi.org/10.1080/13647830.2010.502247).
- [127] SMITH, S. H. & MUNGAL, M. G. (1998). “Mixing, structure and scaling of the jet in crossflow.” *Journal of Fluid Mechanics*, **357**:83–122. doi:[10.1017/S0022112097007891](https://doi.org/10.1017/S0022112097007891).
- [128] SOARES, C. (2008). *Gas turbines: A handbook of air, land, and sea applications*. Elsevier Butterworth-Heinemann, Amsterdam.
- [129] SOLOMON, S. (2007). *Climate change 2007 - the physical science basis: Contribution of Working Group I to the Fourth Assessment Report of the Intergovernmental Panel on Climate Change*. Cambridge Univ. Press, Cambridge [u.a.], first edn.
- [130] STAFFELBACH, G., GICQUEL, L., BOUDIER, G., & POINSOT, T. (2009). “Large Eddy Simulation of self excited azimuthal modes in annular combustors.” *Proceedings of the Combustion Institute*, **32**(2):2909–2916. doi:[10.1016/j.proci.2008.05.033](https://doi.org/10.1016/j.proci.2008.05.033).
- [131] SUN, X., JING, X., ZHANG, H., & SHI, Y. (2002). “Effect of Grazing-Bias Flow Interaction on Acoustic Impedance of Perforated Plates.” *Journal of Sound and Vibration*, **254**(3):557–573. doi:[10.1006/jsvi.2001.4110](https://doi.org/10.1006/jsvi.2001.4110).
- [132] TERHAAR, S., BOBUSCH, B. C., & PASCHEREIT, C. O. (2012). “Effects of Outlet Boundary Conditions on the Reacting Flow Field in a Swirl-Stabilized Burner at Dry and Humid Conditions.” *Journal of Engineering for Gas Turbines and Power*, **134**(11):111501: 1–9. doi:[10.1115/1.4007165](https://doi.org/10.1115/1.4007165).

- [133] TERHAAR, S., ĆOSIĆ, B., PASCHEREIT, C. O., & OBERLEITHNER, K. (2014). “Impact of Shear Flow Instabilities on the Magnitude and Saturation of the Flame Response.” *Journal of Engineering for Gas Turbines and Power*, **136**(7):071502. doi:[10.1115/1.4026530](https://doi.org/10.1115/1.4026530).
- [134] TERHAAR, S., PASCHEREIT, C. O., & OBERLEITHNER, K. (2014). “Impact of Steam-Dilution on the Flame Shape and Coherent Structures in Swirl-Stabilized Combustors.” *Combustion Science and Technology*, **186**(7):889–911. doi:[10.1080/00102202.2014.890597](https://doi.org/10.1080/00102202.2014.890597).
- [135] THUMULURU, S. K. & LIEUWEN, T. (2009). “Characterization of acoustically forced swirl flame dynamics.” *Proceedings of the Combustion Institute*, **32**(2):2893–2900. doi:[10.1016/j.proci.2008.05.037](https://doi.org/10.1016/j.proci.2008.05.037).
- [136] U.S. CENSUS BUREAU (2014). “International Programs Data.” URL: <http://www.census.gov/population/international/data/>, retrieved August 12, 2014.
- [137] WOLF, P., BALAKRISHNAN, R., STAFFELBACH, G., GICQUEL, L., & POINSOT, T. (2012). “Using LES to Study Reacting Flows and Instabilities in Annular Combustion Chambers.” *Flow, Turbulence and Combustion*, **88**(1-2):191–206. doi:[10.1007/s10494-011-9367-7](https://doi.org/10.1007/s10494-011-9367-7).
- [138] ZINN, B. T. (1970). “A theoretical study of non-linear damping by Helmholtz resonators.” *Journal of Sound and Vibration*, **13**(3):347–356. doi:[10.1016/s0022-460x\(70\)80023-2](https://doi.org/10.1016/s0022-460x(70)80023-2).
- [139] ZINN, B. T. & LIEUWEN, T. (2005). “Combustion Instabilities: Basic Concepts.” In: T. Lieuwen & V. Yang (eds.), *Combustion Instabilities in Gas Turbine Engines*, vol. 210 of *Progress in Astronautics and Aeronautics*, pp. 3–24. American Institute of Aeronautics and Astronautics, Reston, Va.